A Novel Dynamic Beam Steering-Based Architecture for Ultra-High-Speed Indoor Optical Wireless Communication Systems

A NOVEL ARCHITECTURE FOR ULTRA-HIGH SPEED INDOOR OPTICAL WIRELESS COMMUNICATION SYSTEMS WITH DYNAMIC BEAM STEERING

BY

HAMED HOSSEINNEJADAZAD, B.Sc.

A Thesis

Submitted to the Department of Electrical and Computer Engineering and the School of Graduate Studies of McMaster University

In Partial Fulfilment of the Requirements for the Degree of Master of Applied Science

© Copyright by Hamed Hosseinnejadazad, September 2025 All Rights Reserved Master of Applied Science (2025)
(Electrical and Computer Engineering)

 $\label{eq:McMaster University} \mbox{ McMaster University }$ $\mbox{ Hamilton, Ontario, Canada}$

TITLE: A Novel Architecture for Ultra-High Speed Indoor Optical

Wireless Communication Systems with Dynamic Beam

Steering

AUTHOR: HAMED HOSSEINNEJADAZAD

B.Sc. (Electrical Engineering),

Iran University of Science and Technology, Tehran, Iran

SUPERVISOR: Dr. Steve Hranilovic

NUMBER OF PAGES: xviii, 181

In loving memory of my mother, who left this world while I was away from home pursuing this work, and to my father.

Abstract

Indoor optical wireless links offer the potential for high data rates due to the wide and unregulated bandwidth of the optical spectrum. However, achieving ultra-high data rates in such systems requires using narrow infrared laser beams to focus optical power on the receiver. While narrow-beam links can enhance communication performance by concentrating power more effectively, they are subject to stricter eye safety constraints that limit the maximum allowable transmit power as the beam becomes narrower. Moreover, narrower beams are more susceptible to misalignment between the transmitter and receiver, as well as blockage by opaque objects. These factors restrict the mobility and range of such systems, limiting their adoption in commercial applications. Consequently, considerable research has focused on developing new configurations for indoor optical wireless links that utilize narrow laser beams to overcome these limitations.

This thesis presents a novel architecture for indoor optical wireless communication, referred to as the dynamic beam steering (DBS) system, which is designed to localize and track a mobile user while delivering high average data rates via a single ultra-narrow laser beam. Different from other indoor infrared communication systems that utilize multiple narrow beams, the proposed design employs a single emitter and achieves tracking and coverage through beam steering. Initially, a discrete multistage spiral search approach is developed to estimate the initial user location with sufficient precision to meet tracking requirements in the next phase while minimizing delay. Then, a tracking algorithm based on discrete beam scanning is developed along a circular pattern, enabling the prediction of the direction of the user movement and ensuring coverage during each scan cycle without the location information of the user. With a single bit feedback from the user, this system supports real-time tracking and communications.

This work proposes a theoretical model for the proposed DBS system, outlining its design and addressing considerations for tracking user movement while maintaining ultrahigh data rates. Computer simulations show average achievable data rates of up to 10 Gbps over a 1.5 GHz bandwidth for a randomly moving user, and the results are compared with existing architectures to highlight the effectiveness and simplicity of the proposed scheme.

Acknowledgements

I would like to express my deep gratitude to Dr. Steve Hranilovic for his guidance and mentorship. His unwavering support and confidence in my abilities allowed me to become a motivated researcher. I am grateful for the opportunity to work under his supervision at McMaster University.

I am deeply grateful to my parents, whose unwavering love and support have made all my achievements, including this Master's degree, possible. Their encouragement has been a constant source of inspiration. During my Master's studies, I faced the profound loss of my mother. Although she is no longer here, her strength, love, and belief in me continue to guide me every day. I dedicate this thesis to her memory, with gratitude for the inspiration she gave me. Her presence will forever remain in the deepest part of my heart.

I would like to thank my beloved friends, in particular, Alireza Barmaki and Mohammadreza Pashazanoosi. Thank you for your presence.

I would also like to thank Charlus Zhang for his support and the administrative team of the Electrical and Computer Engineering Department, particularly Cheryl Gies, for their assistance.

Contents

Lı	st or	Figure	es	X
Li	${f st}$ of	Tables	s x	viii
1	Intr	oducti	on	1
	1.1	Indoor	Optical Wireless Communications	3
		1.1.1	Optical Sources for Indoor OWC	5
		1.1.2	Classification of OWC Links	7
		1.1.3	Indoor OWC Receivers	9
		1.1.4	Hybrid Indoor Communication Layout	11
		1.1.5	Constraints and Challenges of OWC	12
		1.1.6	Overview of Beam Steering Technologies	15
		1.1.7	State-of-the-Art Indoor IRWC Architectures	16
		1.1.8	Localization and Tracking in Indoor Environments	20
		1.1.9	Beam Divergence Control and Adaptive Optics	25
	1.2	Resear	ch Objective and Problem Statement	26
	1.3	Contri	bution of the Thesis	26
	1.4	Thesis	Structure	29
2	Ind	oor Op	otical Wireless System	31
	2.1	System	n Model	31
	2.2	Gaussi	ian Beam	32

	2.3	Eye-Safety Constraints	
	2.4	Optical Receiver Architecture	
		2.4.1 Avalanche Photodetector	
		2.4.2 Receiver Noise	
	2.5	Geometry of Pointed Beam and Received	l Power 48
	2.6	Signaling and Modulation	
	2.7	Effect of Beamwidth on Received SNR a	nd Rate 53
	2.8	Uplink Feedback	
	2.9	Optical Beam Steering Hardware Solution	ns
	2.10	Conclusion	
3	Des	ign of Dynamic Beam Steering Syste	ems 69
	3.1	Introduction	
	3.2	Phase I: Initial Beam Searching Algorith	m
		3.2.1 Archimedean Spiral Search	
		3.2.2 Design Considerations for Spiral	Localization 81
		3.2.3 Localization Accuracy	
		3.2.4 Feedback Threshold Calculation	
		3.2.5 Multi-Stage Spiral Search	
	3.3	Phase II: Simultaneous Tracking and Co	mmunication with DBS 96
		3.3.1 Joint Scheduling, Tracking, and I	Delay Analysis 100
		3.3.2 DBS Algorithm	
		3.3.3 Average Achievable Data Rate pe	er Period of Scanning 107
	3.4	Conclusion	
4	Con	nparison of DBS System versus Ben	chmarks 109
	4.1	Design Considerations and Trade-offs in	DBS Architecture 110
		4.1.1 Effect of Feedback Threshold on	Rate of DRS Scheme 111

		4.1.2	Effect of Discrete Scanning Step Time on Rate of DBS Scheme	. 113
		4.1.3	Effect of Beam Divergence Angle on Rate of DBS Scheme	. 114
		4.1.4	Effect of Spot Numbers Per Scanning on Rate of DBS Scheme	. 117
		4.1.5	Effect of Scanning Radius on Rate of DBS Scheme	. 119
		4.1.6	Effect of Initial Localization Error on DBS Scheme Performance	. 120
		4.1.7	Effect of Noise in Beam Pointing on the Performance of DBS Schem	e123
	4.2	Param	eter Selection for DBS System	. 128
	4.3	Compa	arison of DBS Scheme with Cellular Scheme	. 132
	4.4	Conclu	ısion	. 139
5	Con	clusio	ns and Future Directions	142
\mathbf{A}	App	endix	DC Bias and Clipping Probability in DCO-OFDM	146
В	App	endix	Received Power Calculation (Exact Integration Method)	148
\mathbf{C}	Ana	llytical	Expression of Beam Spot and Localization Accuracy	155
D	App	endix	Simulation Results Comparing Approximate and Exact Re	;-
	ceiv	ed Pov	wer Calculations	163

List of Figures

1.1	Electromagnetic spectrum regions [18, Figure 1]	4
1.2	Geometry of infrared laser beam from a VCSEL	7
1.3	Hybrid indoor wireless communication architecture integrating optical	
	and RF links, including narrow IR beams for beam steering, an RIS for IR $$	
	beam redirection, a dashed line for the wireless IR backhaul, a fiber back-	
	bone interconnecting transmitters, diffuse point-to-point VLC links, and	
	millimeter-wave RF transmission to provide connectivity where optical	
	coverage is limited	12
1.4	$\label{two-dimensional} Two-dimensional\ steering\ of\ infrared\ beams\ using\ a\ high-port-count\ AWGR,$	
	[2, Figure 2]	17
1.5	Illustration of a LiDAR-assisted IRWC system. The θ_I is the scanning	
	field of view of the beam steering apparatus (BSA), and θ_R is the receiver	
	FoV at the user end, [57, Figure 1]	18
1.6	Indoor grid-based OWC network utilizing an array-of-arrays VCSEL for	
	AP, [1, Figure 1]	19
1.7	Example of the wide laser beam scanning system proposed in [66], where	
	the LD scans the coverage area A_C using a step-wise beam pattern of	
	resolution $A_R = A_B$	24
1.8	Cellular architecture with VCSEL array based on [11]	25
1.9	Dynamic beam steering strategy for indoor OWC for localization, track-	
	ing, and communication	28

2.1	Indoor OWC system model with IR beam pointed to the user	32
2.2	Geometry of Gaussian beam propagation	33
2.3	Beam waist radius at $d=2m$ vs initial beam waist based on (2.2) for	
	$\lambda = 1550 \mathrm{nm}; (\mathrm{a}) \mathrm{for} \omega_0 \ll \sqrt{\frac{d\lambda}{\pi}}; (\mathrm{b}) \mathrm{for} \omega_0 \gg \sqrt{\frac{d\lambda}{\pi}} \ldots \ldots \ldots \ldots $	35
2.4	Variation of the initial beam radius ω_0 with respect to θ_{FWHM} and beam	
	radius $\omega(d)$ at distance $d=2\mathrm{m}$ and operational wavelength of 1550 nm;	
	The blue curve represents θ_{FWHM} as a function of ω_0 and red curve shows	
	$\omega(d)$ as a function of ω_0	39
2.5	Maximum eye-safe transmit optical power for different $\theta_{\rm FWHM}$ at $850{\rm nm}$	
	and distance $d_{\rm mhp}=10{\rm cm}$	44
2.6	Maximum eye-safe transmit optical power for different $\theta_{\rm FWHM}$ at 1550 nm	
	and distance $d_{\rm mhp}=10{\rm cm}$	44
2.7	Spectral response of the Hamamatsu G8931 series APD	45
2.8	Illustration of the Gaussian beam directed towards the receiver	49
2.9	Block diagram of the DCO-OFDM-based OWC system	51
2.10	Illustration of the central beam vertically downward towards the user $(\theta=0)$	54
2.11	3D plot of data rate distribution on the XY plane at $z=1\mathrm{m}$ for different	
	θ_{FWHM} values at 1550 nm. The central beam is directed vertically down-	
	ward (fixed). User locations are swept over the XY plane at $z=1\mathrm{m}$, with	
	received power and data rate computed from (2.49) and (2.45), respec-	
	tively. For $\theta_{\rm FWHM}=1^{\circ},4^{\circ},$ and $6^{\circ},$ the corresponding maximum eye-safe	
	transmit powers are $10.25\mathrm{mW},60.18\mathrm{mW},\mathrm{and}129.13\mathrm{mW},\mathrm{respectively.}$.	55
2.12	Rate vs transmit optical power until maximum allowable eye-safe power	
	for different θ_{FWHM} values	56
2.13	System performance, (a) SNR in dB, and (b) data rate in [Gbps] as func-	
	tion of $\theta_{\text{FWHM}} \leq 0.4^{\circ}$, with $\omega(h)$ shown on the right y-axis	57

2.14	System performance, (a) SNR in [dB], and (b) data rate in [Gbps] as	
	function of $\theta_{\rm FWHM} \leq 10^{\circ}$, with $\omega(h)$ shown on the right y-axis	57
2.15	UL feedback with ODTx according to [11], and [89]	60
2.16	Motorized rotation stage (MOR-100-30) by Optics Focus with 360° range,	
	30mm aperture, and microstepping support for beam steering [91]	61
2.17	Thorlabs LSK-GR08 galvo-resonant scanner and controller for fast beam	
	steering applications [46]	62
2.18	Thorlabs GVS012 dual-axis MEMS mirror and controller system for high-	
	speed optical beam steering [46]	63
2.19	Thorlabs EXULUS-HD4 phase-only spatial light modulator with 1920×1200	
	resolution, optimized for 1550 nm applications [94]	64
2.20	TI DLPLCR55EVM evaluation module featuring the DLP5500 DMD	
	$(0.55^{\prime\prime}$ diagonal chip with a resolution of $1024{\times}768$ micromirrors, each	
	spaced $10.8\mu\mathrm{m}$ apart and capable of tilting $\pm12^{\circ}),$ capable of up to 5kHz	
	mirror switching for high-speed beam steering applications [51]	65
2.21	TECHSPEC Risley Prism Mount from Edmund Optics, enabling beam	
	steering through independent rotation of two wedge prisms [97]	65
2.22	Schematic illustration of a 64×64 nanophotonic phased array system,	
	as demonstrated by Sun et al. [53]. Light from an optical fiber is equally	
	distributed to 4,096 nanoan tennas via silicon waveguides. The inset shows $$	
	a unit cell with a directional coupler of length L_c and optical delay lines	
	that set the emission phase. This CMOS-compatible OPA enables high-	
	speed beam steering without mechanical inertia	67
3.1	Multi-stage Archimedean spiral search pattern on XY	72
3.2	Archimedean spiral search pattern on XY plane at $z_{rx} = 1 m$ above the	
	floor	74

3.3	Demonstration of pointed IR beam and XY user plane at $z=1m$ and	
	sample points on spiral with equal angular difference	75
3.4	Discrete spot positions on spiral pattern with fixed spot step length	76
3.5	Optimized points on the spiral pattern (compared to Fig. 3.3) on XY	
	user plane at $z=1\mathrm{m}$ with the pointed beam	77
3.6	Spiral search with $\theta_{\rm FWHM}=10^{\circ}$ for different α_s values; (a) $\alpha_s=0.4$; (b)	
	$\alpha_s = 0.841$; (c) $\alpha_s = 0.95$. Scanning spots may not cover the service area	
	for small values of α_s	78
3.7	Discrete spiral search pattern (black points) with beam spot footprints on	
	the XY plane (ellipses). The red points indicate the centers of the ellipses	
	(beam spots), the green point marks the user location, and $\theta_{\rm FWHM}=15^{\circ}$.	80
3.8	Minimum angular step size, $\Delta\theta_{s,\mathrm{min}}^{\circ}$, for different θ_{FWHM} values at the	
	farthest location $(2.5\mathrm{m},2.5\mathrm{m},1\mathrm{m})$	82
3.9	Maximum spot number, N_{spot} , and maximum localization error for differ-	
	ent $\theta_{\rm FWHM}$ values in the spiral search of stage 1 (see Fig. 3.1)	84
3.10	$\theta_{\text{FWHM,min}}$ required to achieve $D_{\text{max}} < \epsilon$	85
3.11	Beam spot geometry at the farthest position of PD, representing the min-	
	imum detectable received power for feedback as a threshold	87
3.12	Variation of SNR _{ref} versus δd_{rx} for different $\theta_{\rm FWHM}$ values	89
3.13	Multi-stage localization with $M=4$ total stages for $\epsilon=5\mathrm{cm}$ accuracy; (a)	
	cumulative spot numbers N and localization error D versus stage index	
	m , (b) corresponding optimal $\theta_{\mathrm{FWHM}}^{(i)}$ values at each stage index m	96
3.14	Cumulative N as a function of stage index m for different total stage	
	numbers M and localization accuracies ϵ : (a) $\epsilon=1\mathrm{cm},$ (b) $\epsilon=5\mathrm{cm}.$	97
3.15	Effect of stage number M and localization accuracy ϵ on cumulative N ;	
	$\epsilon = 10cm$	97

3.16	Geometry of dynamic beam steering on a circular path, where three dis-
	crete spot positions are selected as an example
3.17	Timing diagram showing the sequence of test signal (TS), reflected sig-
	nal (RS), short inter-frace space (SIFS), data transmission time (t_{data}) ,
	propagation delay t_{δ} , and packet time t_{packet} according to [11] 101
3.18	Timing diagram showing $t_{\text{step}}, T_{\text{scan}}$
4.1	Parameter dependencies of DBS scheme influencing achievable data rate $$. 111
4.2	Data rate vs radial distance of user from center $\theta_{\rm FWHM} = 0.4^{\circ}$ for differ-
	ence δd_{rx} values for tracking compared to ideal tracking
4.3	Data rate vs radial distance of user from center $\theta_{\rm FWHM}=4^{\circ}$ for difference
	δd_{rx} values for tracking compared to ideal tracking
4.4	Data rate vs radial distance of user from center with $\theta_{\rm FWHM} = 0.4^{\circ}$ for
	difference t_{step} times for tracking
4.5	Data rate vs radial distance of user from center with $\theta_{\rm FWHM}=1^{\circ}$ for
	difference t_{step} times for tracking
4.6	Data rate vs radial distance of user from center with $\theta_{\rm FWHM} = 4^{\circ}$ for
	difference t_{step} times for tracking
4.7	Data rate vs radial distance of user from center for different θ_{FWHM} values
	with $t_{\text{step}} = 0.1 \mu s$
4.8	Data rate vs radial distance of user from center for different θ_{FWHM} values
	with $t_{\text{step}} = 1 \text{ms}$
4.9	Data rate vs radial distance of user from center with $\theta_{\rm FWHM} = 0.4^{\circ}$ for
	different $n_{\rm spot}$ number per scanning; (a) $t_{\rm step}=0.1{\rm ms},$ (b) $t_{\rm step}=1{\rm ms}$ 118
4.10	Data rate vs radial distance of user from center with $\theta_{\rm FWHM}=2^{\circ}$ for
	different $n_{\rm spot}$ number per scanning; (a) $t_{\rm step}=1ms$, (b) $t_{\rm step}=3ms$ 119
4.11	Data rate vs radial distance of user from center with $\theta_{\rm FWHM}=0.4^{\circ}$ for
	difference $x_{\text{scan}} = \frac{r_{\text{scan}}}{r(h)}$ values for tracking with $t_{\text{step}} = 1 \text{ms}$ 120

4.12	Data rate vs radial distance of user from center with $\theta_{\mathrm{FWHM}} = 0.4^{\circ}$ for	
	difference $x_{\text{scan}} = \frac{r_{\text{scan}}}{\omega(h)}$ values for tracking with $t_{\text{step}} = 1.5 ms$	121
4.13	Data rate vs radial distance of user from center with $\theta_{\rm FWHM}=4^{\circ}$ for	
	difference $x_{\text{scan}} = \frac{r_{\text{scan}}}{\omega(h)}$ values for tracking with $t_{\text{step}} = 1ms$	122
4.14	Average data rate vs radial distance of user for different σ_s values for	
	initial localization error for DBS scheme with $\theta_{\rm FWHM} = 0.4^{\circ}$	122
4.15	Average data rate vs radial distance of user for different σ_s values for	
	initial localization error for DBS scheme with $\theta_{\rm FWHM} = 4^{\circ}$	123
4.16	Average data rate vs radial distance of user from center for θ_{FWHM} =	
	0.4° , considering noise in pointing for DBS scheme with different standard	
	deviation, σ_p values	126
4.17	Average data rate vs radial distance of user from center for θ_{FWHM} =	
	4° , considering noise in pointing for DBS scheme with different standard	
	deviation, σ_p values	126
4.18	Pointing error of DBS tracking (computed from (4.5)) considering $\sigma_p = 0$,	
	$\sigma_s = 0$, versus radial distance of user when moving linearly from center	
	to corner of room; (a) $\theta_{\rm FWHM}=0.4^{\circ}$, (b) $\theta_{\rm FWHM}=4^{\circ}$	127
4.19	Pointing error of DBS tracking (computed from (4.5)) considering $\sigma_s = 0$,	
	versus radial distance of user when moving linearly from center to corner	
	of room; (a) $\theta_{\rm FWHM}=0.4^\circ~\sigma_p=1{\rm mm},$ and (b) $\theta_{\rm FWHM}=4^\circ,~\sigma_p=30{\rm mm},$	128
4.20	Multi-stage localization with $M=6$ total stages for $\epsilon=1\mathrm{cm}$ accuracy:	
	(a) cumulative spot numbers N and localization error D versus stage	
	index m , (b) corresponding optimal $\theta_{\text{FWHM}}^{(i)}$ values at each stage index m .	129
4.21	Implementation of the DBS scheme considering pointing and initial lo-	
	calization errors, compared with the case without noise and with ideal	
	tracking	131
4.22	Downlink geometry of cellular architecture with VCSEL array based on [11]	133

4.23	Comparison between DBS, cellular, and ideal schemes in terms of average
	rate vs radial distance from the center of the room for linear user movement 135
4.24	User random movement following Brownian motion in $5\mathrm{s}$ time interval
	with $t_{\text{step}} = 1 ms$, i.e., 500 time steps
4.25	Monte-Carlo simulation with 10000 iterations for average rate when user
	moves randomly following Brownian model in $5\mathrm{s}$ for comparison between
	ideal tracking, DBS scheme (with $\sigma_s=0,\sigma_p=0$), and cellular schemes 139
4.26	Comparison between DBS considering noise in pointing and localization
	error $(\sigma_s = 1 ms, \sigma_p = 0.86 cm)$, cellular, and ideal schemes in terms of
	average rate vs radial distance from the center of the room for linear user
	movement
4.27	Average achievable rate from a 2000-run Monte Carlo simulation for a user
	following a Brownian-motion model over $1\mathrm{s}$; comparison of DBS tracking
	$(\sigma_s = 1 \text{ mm}, \sigma_p = 0.86 \text{ cm})$ with ideal and cellular schemes 140
B.1	Received power comparison between the approximation in (2.42) and the
	exact integration in (B.8), as the user moves from the room center to the
	corner with ideal AP tracking; (a) for $\theta_{\rm FWHM}=0.4^{\circ}$, (b) for $\theta_{\rm FWHM}=4^{\circ}$ 151
B.2	Intensity distribution ($\theta_{\rm FWHM}=0.4^{\circ}$) over the PD area at (2.5, 2.5, 1) [m],
	with the maximum intensity point $I_{\rm max}$, and the PD center (beam point-
	ing position) indicated
В.3	Difference between maximum intensity (included in Pr_{exact} according to
	(B.8)), and intensity at PD center (used for $P_{\rm r,approx}$ according to (2.42)) 152
B.4	Illustration of the integration area for computing $P_{r,\text{exact}}$ in (B.8), com-
	pared with the rectangular approximation used for $P_{r,approx}$ in (2.42) 153
B.5	Intensity distribution ($\theta_{\text{FWHM}} = 0.4^{\circ}$) over the PD area at (1.5, 1.5, 1) [m],
	with the maximum intensity point I_{max} , and the PD center (beam point-
	ing position) indicated

B.6	Intensity distribution ($\theta_{\rm FWHM}=0.4^{\circ}$) over the PD area at (0, 0, 1) [m],
	with the maximum intensity point I_{max} , and the PD center (beam point-
	ing position) indicated
C.1	Geometry of pointed beam and the intersection with XY plane at height
	z=h, resulting in elliptical beam spot footprint
C.2	The elliptical beam spot footprint on XY plane which is 2D demonstration
	of Fig. C.1
D.1	Comparison of DBS, cellular, and ideal schemes in terms of average rate
	versus radial distance from the room center. Results compare the exact
	received power calculated from (B.8) with the approximate received power
	estimated using (2.42)

List of Tables

2.1	MPE for different t_{exp} for $700 \text{nm} < \lambda < 1050 \text{nm}$ [15] 41
2.2	MPE for different t_{exp} for $1050 \text{nm} < \lambda < 1400 \text{nm}$ [15] 41
2.3	MPE for different t_{exp} for $\lambda > 1400 \text{nm}$ [15]
2.4	Limiting apertures for different spectral regions [15]
2.5	Simulation parameters for Fig. 2.5 and Fig. 2.6, [15], [11]
2.6	APD parameters used in the system [11], [76]
2.7	Noise parameters [76]
2.8	Comparison of Beam Steering Technologies
3.1	Delay time parameters for tracking [11]
4.1	System parameters for simulation setup
4.2	System Parameters for Proposed DBS Architecture
4.3	System Parameters for the Cellular Scheme based on [11]
4.4	Comparison of cellular and DBS schemes in terms of hardware and per-
	formance

Chapter 1

Introduction

The rapid advancement of digital technologies has driven an unprecedented demand for ultra-high-speed wireless connectivity [1], [2]. Internet-driven services such as 4K/8K ultra-high-definition (UHD) video streaming, immersive virtual reality (VR) and augmented reality (AR) applications, holographic telepresence, and multi-access edge computing are pushing existing wireless networks to their limits [3]. Supporting the real-time operation of these applications requires extremely high data rates, with next-generation systems targeting capacities beyond 1 Terabit per second (Tbps), particularly in short-range indoor scenarios such as immersive experiences and ultra-dense access point (AP) deployments [4]. These requirements are driven by emerging use cases such as extended reality, holographic communication, and digital twins. These scenarios have been highlighted by 3GPP under 5G-Advanced and are expected to evolve further in sixth-generation (6G) wireless systems [5]. Achieving such data rates remains a fundamental design challenge for future 6G networks [4], [5].

Latency is another vital performance metric in 6G, particularly for time-sensitive and mission-critical applications. As noted in early 6G vision work [4], end-to-end latencies below 0.1 ms are essential for high-precision manufacturing and holographic communication. More recent studies confirm that immersive services such as extended reality,

telepresence, and the tactile internet demand not only high throughput but also ultra-low latency to maintain consistent performance and system responsiveness [6]. Meeting these targets will require advances across the physical, MAC, and network layers, including edge computing, AI-driven control, and high-speed links.

To address these demands, optical wireless communication (OWC) has emerged as a promising alternative to radio-frequency (RF) systems, offering ultra-high data rates, reduced latency, and immunity to RF interference [7]. In particular, indoor OWC using infrared (IR) laser-based OWC has demonstrated significant potential in delivering multigigabit-per-second (Gb/s) data rates for multi-user environments, such as offices and conference rooms [1], [2], [8]–[11].

Indoor OWC systems offer low latency not only due to negligible light propagation delay, but also because their dedicated channels reduce signal processing and queuing delays, supporting higher throughput. The line-of-sight (LoS) OWC links with narrow beams exhibit negligible multipath components, unlike RF systems, which typically experience significant reflections and delay spread in indoor environments. As highlighted by [12], this results in much shorter channel impulse responses and enables sub-microsecond latency regimes. Furthermore, OWC links often employ intensity modulation with direct detection (IM/DD), where the transmitted information is carried by modulating the emitted optical power, and the receiver detects this power as a proportional electrical current [13]. This IM/DD approach yields simpler receiver architectures. These factors collectively allow OWC to outperform RF systems in latency-sensitive indoor applications. Moreover, while OWC is immune to RF interference, it remains sensitive to ambient optical emissions from natural and artificial sources, which must be carefully managed. On the positive side, optical beams are easily confined within indoor spaces, allowing for high spatial reuse and isolation that significantly improve spectral efficiency

[14]. Eye safety is another critical consideration in indoor OWC systems, where optical transmitters must comply with maximum permissible exposure limits to ensure safe operation for human occupants [15].

In the following, the fundamental concepts and challenges of indoor OWC systems are introduced, and the potential of narrow IR beams to achieve ultra-high data rates is examined, while the critical challenges of user localization, tracking, and beam alignment are addressed. The objective of this work is to develop a robust and efficient solution for next-generation indoor OWC systems that can deliver consistent, high-speed connectivity in dynamic environments.

1.1 Indoor Optical Wireless Communications

OWC offers various advantages over traditional RF communications, including utilizing the unlicensed optical spectrum, being electromagnetic interference-free, which thus can coexist with existing RF systems, and the potential to be integrated with indoor illumination systems to reduce the deployment cost and energy consumption. Since optical signals cannot pass through walls, indoor OWC systems are naturally more secure than their RF communication counterparts. This makes it possible to have optical devices that work worldwide without interfering with any other devices.

Indoor optical wireless links are typically short-range, spanning a few meters, and are categorized based on the light wavelength used, such as visible light communication (VLC) [16], [17], and IR wireless communication (IRWC) [13]. Fig. 1.1 illustrates the electromagnetic spectrum, highlighting the optical spectrum, which includes the infrared, visible, and ultraviolet regions. VLC systems operate in the 400–700 nm range, offering a bandwidth (BW) of over 320 THz.

VLC systems typically employ wide, diffused beams generated by indoor illumination

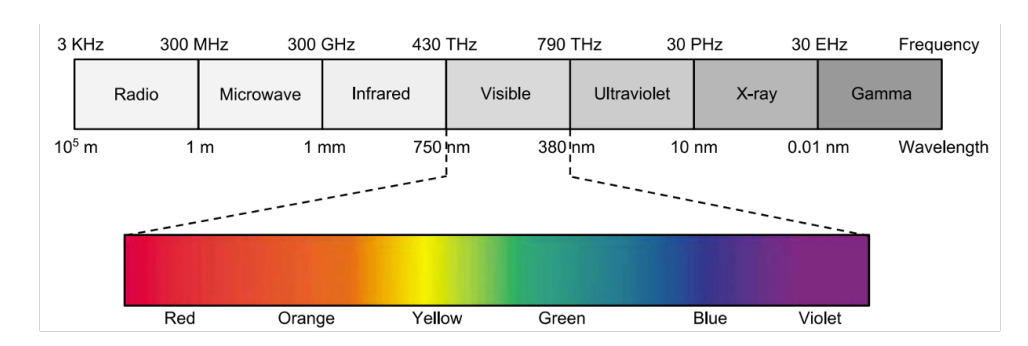


Figure 1.1: Electromagnetic spectrum regions [18, Figure 1]

sources, such as light-emitting diodes (LEDs), which serve the dual purpose of providing lighting and communication. In contrast, IRWC systems can utilize either narrow or wide beams but operate independently of visible light, thus providing no contribution to indoor illumination. Instead, IRWC systems rely on dedicated light emitters, such as laser diodes (LDs) or vertical-cavity surface-emitting lasers (VCSELs), to establish communication links.

Data transmission in VLC systems is primarily facilitated by LEDs, which modulate light intensity at high speeds without perceptible changes to human vision [19]. This allows VLC systems to achieve impressive data rates, with a single LED capable of reaching 10 Gb/s using orthogonal frequency division multiplexing (OFDM) [20]. Light Fidelity (LiFi), a bidirectional and fully networked extension of VLC, has further demonstrated data rates of up to 15.73 Gb/s using off-the-shelf LEDs [21]. The wide coverage of LEDs enables them to serve multiple users simultaneously, but this can lead to traffic congestion under high loads. Additionally, high-speed VLC systems rely on illumination being turned on, which may increase power consumption and limit flexibility in non-illumination scenarios.

IRWC offers a promising alternative to address these limitations. Using narrow IR beams for user-specific communication reduces traffic congestion and enhances user privacy by directing the beam solely toward the intended receiver. Furthermore, IR beams

are energy-efficient due to their high directivity, ensuring that a significant portion of the transmitted power reaches the user. The low beam divergence of VCSELs improves spatial reuse and minimizes interference, while their compatibility with array configurations enables scalable multi-user support in high-capacity optical wireless systems. Thus, utilizing VCSEL enables IRWC links to achieve data rates beyond 10 Gb/s and up to 100 Gb/s in advanced systems [22].

1.1.1 Optical Sources for Indoor OWC

White light LEDs, commonly used in VLC systems, are fundamentally limited by the slow response of the phosphor layer used to generate white light, restricting their modulation BW to a few megahertz. Even with advanced equalization techniques, their effective BW rarely exceeds tens of megahertz, resulting in data rates generally below 100 Mb/s [2], [4], [23]. In contrast, specialized high-speed visible light sources such as GaN-based micro-LEDs and RGB LED arrays have demonstrated data rates in the Gb/s range by utilizing high-speed modulation, spectral multiplexing, and advanced signal processing techniques [20], [21]. Furthermore, standard LEDs in VLC systems typically exhibit power conversion efficiencies of around 25%–50%, limiting their energy efficiency in communication applications [24]. Increasing the modulation BW of an LED typically leads to a reduction in its power conversion efficiency [13].

LDs are more expensive than LEDs but offer several advantages, including much higher modulation BW typically in the GHz range, and better power conversion efficiency ranging between 30–70% [13], [25]. LDs are well-suited for high-speed, long-distance applications such as free-space optics and fiber-optic communication systems. VCSELs, on the other hand, are solid-state micro-lasers that emit light vertically from the surface of a wafer in a narrow, cylindrical beam. Fabrication relies on standard microelectronic processes, and devices are available in both 1-D and 2-D array formats, enabling seamless integration with on-board components and reducing the complexity and cost of optical

transceivers [26], [27]. In comparison to edge-emitting LDs, alignment is simpler, and scalability is enhanced for parallel optical systems. VCSELs offer high modulation BW exceeding 10 GHz, power conversion efficiencies above 50%, and cost-effective large-scale manufacturability [28], [29]. These properties make VCSELs particularly attractive for short-reach applications such as indoor IRWC, LiFi, and high-speed optical interconnects. Despite these advantages, output power and modulation BW are generally lower than those of high-end LDs, which may constrain performance in long-range or high-throughput systems [27].

Among the various optical sources reviewed, VCSELs present an attractive tradeoff for indoor IRWC, offering high modulation BW, efficient power usage, and ease of integration in compact transceivers. Their array-based architecture and alignment flexibility make them particularly advantageous for dynamic, high-speed short-range applications. Therefore, a VCSEL is adopted in this work as the IR transmission source at the transmitter side, aligning with the system's performance goals and practical deployment considerations. Fig. 1.2 illustrates the geometry of the IR laser beam emitted by a VCSEL, where the beam radius $\omega(L)$ expands with increasing propagation distance L. As shown in the figure, the intensity profile follows a Gaussian distribution, meaning that the optical power is highest at the center of the beam and decreases toward the edges, resulting in a focused energy concentration around the beam axis. A detailed analysis of Gaussian beam characteristics is provided in Section 2.2. Narrow Gaussian beams concentrate optical power over a smaller area, resulting in higher received signal strength and improved SNR, which is advantageous for high-data-rate transmission. However, the reduced beam divergence limits the coverage area, necessitating more precise alignment between the transmitter and receiver.

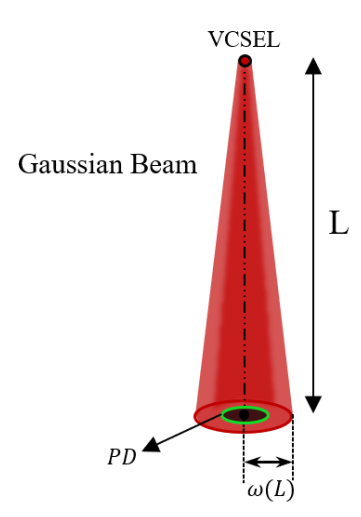


Figure 1.2: Geometry of infrared laser beam from a VCSEL

1.1.2 Classification of OWC Links

OWC links can be categorized based on the geometric relationship between the transmitter and receiver into three main types, including LoS, non-line-of-sight (NLoS), and diffuse links [13]. Each configuration presents trade-offs in alignment sensitivity, achievable data rates, receiver complexity, and robustness to blockage or mobility. Such factors influence the signal-to-noise ratio (SNR), defined as the ratio of received signal power to noise power within the system BW, and widely regarded as an indicator of link quality and data-carrying capability.

LoS links provide a direct optical path between transmitter and receiver, offering high coupling efficiency, minimal delay spread, and negligible inter-symbol interference (ISI). These features make LoS links well-suited for high-speed communication. However, their performance is highly sensitive to misalignment and obstructions (e.g., human bodies or furniture), which can result in link outages and limited mobility.

NLoS links rely on diffuse reflections from room surfaces to deliver the optical signal when a direct path is unavailable. This improves robustness to blockage and enables greater mobility, especially in dynamic indoor environments. However, with each reflection, a significant portion of the signal is scattered in undesired directions, and in IR-based systems, the attenuation per reflection is notably higher than in visible light systems [30], [31]. Common interior wall surfaces, such as painted plaster or wood, typically reflect around 70% to 85% of visible light [32]. In contrast, the reflectivity of these materials in the IR range is much lower. For opaque surfaces, the IR reflectivity is about 8% to 11% [33]. As a result, the receiver captures only a small fraction of the emitted power, leading to higher path loss, increased ISI, and lower SNR compared to LoS links [34]. Consequently, NLoS links typically support lower data rates and are less suited for ultra-high-speed indoor IRWC applications.

Reflections in indoor environments can be broadly classified as specular, where light is reflected in a mirror-like direction, and diffuse, where it is scattered across many angles. NLoS links rely mainly on diffuse reflections from room surfaces to deliver the optical signal when a direct path is unavailable. This improves robustness to blockage and enables greater mobility, especially in dynamic indoor environments. However, with each reflection, a significant portion of the signal is scattered in undesired directions, and in IR-based systems, the attenuation per reflection is notably higher than in visible light systems [30], [31]. Common interior wall surfaces, such as painted plaster or wood, typically reflect around 70% to 85% of visible light [32]. In contrast, the reflectivity of these materials in the IR range is much lower. For opaque surfaces, the IR reflectivity is about 8% to 11% [33], reported as a broadband value in the thermal infrared (approximately 2.5–25 μ m). Thus, the exact reflectivity depends on the specific wavelength within the IR spectrum. As a result, the receiver captures only a small fraction of the emitted power, leading to higher path loss, increased ISI, and lower SNR compared to LoS links [34]. Consequently, NLoS links typically support lower data rates and are less suited for ultra-high-speed indoor IRWC applications.

Diffuse links distribute light across a wide angle, allowing reception via multiple scattered paths. This link requires no alignment and is tolerant to user movement, making it ideal for low-speed applications, such as remote controls. However, it incurs significant power loss and delay spread, resulting in low SNR and limited support for high data rates [35].

1.1.3 Indoor OWC Receivers

At the receiver, a photodetector (PD), typically a photodiode, converts incident optical power into an electrical photocurrent signal [25]. Photodiodes are reverse-biased semiconductor devices, commonly made of silicon for operation in the near-infrared range between 700–1000 nm, offering high speed and low cost. For longer wavelengths (e.g., 1400 nm and above), compound semiconductor materials such as InGaAs are required due to the bandgap limitations of silicon. While InGaAs photodiodes offer excellent sensitivity and high BW, comparable to those used in optical fiber communication systems at 1550 nm, their use in indoor systems typically increases fabrication cost and packaging complexity [13], [25]. The responsivity of a PD, defined as the ratio of output electrical current to input optical power, depends on both the device material and the operating wavelength. An important spatial parameter of optical receivers is their field of view (FoV), defined as the angular range over which the receiver can effectively detect incoming optical signals.

Two widely used PD types are the p-i-n (p-type-intrinsic-n-type) PD and the avalanche PD (APD) [25]. A p-i-n PD incorporates a large intrinsic layer between the p+ and n+ regions to enhance photon absorption, but its BW is limited by junction capacitance. This issue is especially pronounced in OWC systems, where large-area detectors are needed to increase optical collection, leading to reduced BW due to increased capacitance. In contrast, APDs operate under high reverse bias and provide internal electrical

gain, making them more sensitive in low-light environments typical of indoor IR systems. This sensitivity improves SNR in IM/DD links, especially when thermal noise at the preamplifier dominates [13], [25]. However, APDs are more expensive than p-i-n diodes, require high-voltage biasing, and exhibit temperature-dependent gain. Beyond PD selection, the overall receiver design impacts system parameters. A compact, high-performance OWC receiver must efficiently capture and detect incident light with BW of several hundred megahertz to a few gigahertz and sub-nanosecond response times, as required for high-speed indoor communication links. For instance, APD has demonstrated sub-nanosecond time resolution, with response times as fast as approximately 100 ps in certain implementations [36]. A wide FoV is desirable for mobile users to avoid constant alignment, but widening the FoV increases vulnerability to ambient light and multipath interference. Increasing the active area of the PD improves optical power collection and thus SNR, but also increases junction capacitance, reducing response speed and BW [37]. This trade-off must be carefully considered when balancing SNR and data rate.

Optical receivers can be broadly classified into two categories, including the receiver architecture (single-element versus multi-element), and the optical configuration (imaging versus non-imaging) [37]–[39]. Single-element receivers use a single PD and are cost-effective and compact, but collect all light within their FoV, including ambient and reflected signals, which increases noise and reduces SNR. Multi-element receivers, such as angle diversity receivers (ADRs), employ multiple PDs pointed in different directions to enhance spatial selectivity and reduce interference. These architectures improve coverage and robustness, particularly in mobile environments, but introduce increased hardware and signal processing complexity. In terms of optical design, non-imaging receivers (e.g., those using compound parabolic concentrators (CPCs)) focus on maximizing optical power collection without resolving spatial information, offering a wide FoV and high optical gain with lower sensitivity to alignment errors. Imaging receivers, in contrast, use lenses to project spatially resolved light onto PD arrays, enabling improved angular

discrimination and multipath rejection. While imaging systems offer superior SNR and spatial filtering, precise alignment is required, with increased sensitivity to fabrication imperfections, as well as higher cost and bulk. Recent high-speed imaging receiver designs have demonstrated >20 Gb/s data rates, but often require complex configurations with thousands of detectors and lenses [38]. Therefore, the choice of receiver depends on the application requirements for mobility, alignment tolerance, size, and cost.

Given these trade-offs, this thesis adopts a single-element APD-based receiver. Compared to p-i-n PD, APD offers significantly higher sensitivity due to internal gain, which is advantageous in the low-power, IR-based indoor scenarios considered here. While multi-element receivers provide enhanced noise rejection and spatial resolution, increased complexity, cost, and integration overhead present practical challenges. Such designs are preferable when system constraints allow for higher design complexity and budget. However, for the scope of this work, an APD-based single-element receiver provides a practical and efficient solution that balances performance with system simplicity.

1.1.4 Hybrid Indoor Communication Layout

Fig. 1.3 illustrates an indoor communication scenario that integrates multiple communication technologies, including IRWC, VLC, and RF systems operating in the GHz band (millimeter-wave). The figure shows several APs connected via optical fibers, along with a wireless backhaul IR link between two APs to enable high-capacity data exchange without physical fiber. Ultra-narrow IR beams are depicted as red lines to represent their role in high-speed IRWC, although these beams are not visible to the human eye. VLC transmitters are illustrated using LEDs, while an RF AP is also shown to support areas where VLC and IRWC coverage may be limited. A reconfigurable intelligent surface (RIS) is mounted on the wall, implemented in this figure as an array of mirror elements with independently adjustable orientations to control the direction of reflected optical beams.

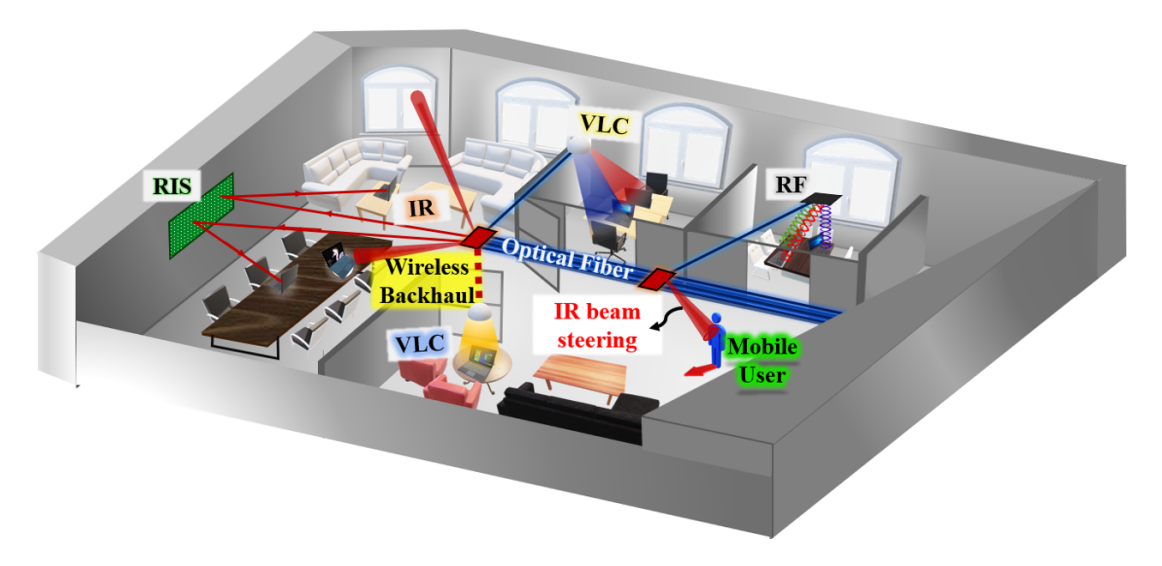


Figure 1.3: Hybrid indoor wireless communication architecture integrating optical and RF links, including narrow IR beams for beam steering, an RIS for IR beam redirection, a dashed line for the wireless IR backhaul, a fiber backbone interconnecting transmitters, diffuse point-to-point VLC links, and millimeter-wave RF transmission to provide connectivity where optical coverage is limited.

In this architecture, VLC employs LED-based transmitters to provide simultaneous data transmission and illumination. These transmitters communicate with user devices located within the FoV of the receiver. An RIS can passively perform beam shaping and steering, allowing it to redirect incident signals and improve coverage, particularly in NLoS areas [40]. IRWC supports ultra-high data rates for both static and mobile users, and also enables user localization and tracking through a dynamic beam-steering algorithm proposed in this thesis.

1.1.5 Constraints and Challenges of OWC

In indoor RF communication, the propagation of multipath signals will cause severe performance degradation and requires a high-complexity receiver design to properly handle multipath interference. In addition, interference from other users poses a significant challenge in RF links. Since RF signals easily penetrate walls and other objects, receivers can inadvertently detect and receive signals from neighboring links. Consequently, RF

transceivers must be designed to distinguish the desired signal from a background of interference. In contrast to radio frequency systems, OWC systems (VLC and IRWC) typically use IM/DD to ensure that transmitted optical signals are real and non-negative. Here, information is modulated onto the instantaneous optical power at the transmitter, and a PD converts the received optical power into an electrical photocurrent signal [13]. This approach simplifies transceiver design compared to RF systems. Moreover, the much shorter wavelength of optical signals compared to the active area of PD effectively eliminates multipath fading [13]. The PD integrates the received optical waveform over an area that spans thousands of square wavelengths, providing inherent spatial diversity. This characteristic mitigates fading and enables both VLC and IRWC links to support exceptionally high data rates using relatively simple and low-cost hardware.

While IM/DD is widely used in VLC and IRWC due to its simplicity, coherent detection, where both the amplitude and phase of the optical carrier are measured, offers higher spectral efficiency and potentially greater receiver sensitivity. Although IM/DD-based OWC systems can also achieve multi-gigabit data rates, coherent detection becomes advantageous in scenarios where optical power is limited or where advanced modulation and multiplexing techniques are employed. For example, system-level studies have shown that coherent IRWC can support high-speed links with reduced power requirements [41]. A metasurface-assisted coherent system has demonstrated 100 Gb/s bidirectional transmission over a 2 m indoor link, enabling multiuser communication via wavelength division multiplexing [42].

One of the constraints of OWC is compliance with eye and skin safety regulations, which require that the average transmitted optical power remains within safe limits as defined by established standards [15], [43]. Furthermore, optical signals cannot penetrate walls or opaque objects. Although this containment improves the security of the link within a room and reduces interference from external sources, it also introduces the

risk of signal blockage by objects within the room, including the human body. This limitation can restrict receiver mobility, as changes in the receiver position may lead to signal obstruction. Self-blockage by the user is also a significant concern, as the user movements or presence may block the optical signal. In the context of VLC, a mathematical model has been proposed to quantify the probability of link blockage and misalignment in indoor environments, highlighting the significant impact of device orientation and user-induced obstructions on system performance [44].

One of the challenges in OWC is the impact of intense ambient light from sources such as sunlight, incandescent bulbs, and fluorescent lighting, which generate high-intensity shot noise at the receiver. However, the transmitter cannot compensate for this noise by emitting arbitrary amounts of power due to safety restrictions [13]. In RF systems, SNR is directly proportional to the received signal power, as it is defined by the ratio of signal power to noise power within the system BW. In IM/DD optical systems, the electrical SNR is proportional to the square of the average received optical power [13]. This is because PD converts the incident optical power $P_{\rm opt}$ into an electrical current $I = R \cdot P_{\rm opt}$, where R is the responsivity of PD (in A/W). The electrical signal power is then proportional to $I^2 \propto R^2 P_{\rm opt}^2$, while the noise is often dominated by thermal or shot noise, which typically scales linearly with $P_{\rm opt}$ or remains approximately constant. This implies that a 1dB increase in received optical power results in an approximate 2dB increase in electrical SNR at the receiver. Conversely, a 1dB decrease in received optical power leads to an approximate 2dB reduction in electrical SNR. As a result, OWC links experience higher path loss compared to RF links [13].

Providing coverage while maintaining high SNR in indoor IRWC systems is particularly challenging when using narrow beams. Narrow-beam transmission is often employed in high-speed IR links to concentrate optical power over a small angular range, thereby increasing received power density, minimizing path loss, and reducing multipath

interference. However, the same narrow divergence that enables high spatial directivity and high SNR also makes the system highly sensitive to pointing errors and alignment mismatches between the transmitter and receiver. In addition, blockage of the signal by obstacles, such as the human body or other objects in the environment, further aggravates the problem, limiting mobility and reliability. A rigorous analysis of the relationship between beam directivity, received power, and SNR, including theoretical modeling and simulations, is presented in Chapter 2, which quantitatively demonstrates these trade-offs. These challenges necessitate precise user localization and continuous tracking to ensure stable and high-performance communication links.

1.1.6 Overview of Beam Steering Technologies

Optical beam steering is a function in IRWC and sensing systems, enabling dynamic alignment of narrow laser beams without requiring mechanical repositioning of the transmitter or receiver. Various technologies have been developed to implement beam steering, each offering different trade-offs in speed, precision, cost, and form factor. Traditional methods include stepper motors [45], and galvanometer scanners [46], which mechanically rotate mirrors or lenses to redirect the beam. While inexpensive and relatively easy to integrate, these approaches are limited by inertia, resulting in slow response times on the order of milliseconds. To overcome these limitations, modern solutions such as micro-electro-mechanical systems (MEMS) mirrors [47], [48], spatial light modulators (SLMs) [49], [50], and digital micromirror devices (DMDs) [51] offer faster scanning with sub-millidegree precision. However, these technologies often involve increased cost, limited steering range, or discrete angular resolution. Among emerging solid-state technologies, optical phased arrays (OPAs) represent a highly promising solution [52]. By electronically controlling the phase of light across an array of nanoantenna elements, OPAs achieve beam steering without any moving parts. This enables reconfiguration speeds on the order of microseconds or faster, along with a compact,

CMOS-compatible footprint [52]. Despite challenges such as limited steering angle and side lobes, recent advances have demonstrated OPAs capable of sub-degree precision and integration into LiDAR and optical wireless systems [53], [54]. A detailed comparison of beam steering technologies, including their performance metrics and use cases, is presented in Section 2.9.

1.1.7 State-of-the-Art Indoor IRWC Architectures

Recent indoor OWC systems achieve multi-Gb/s rates through the use of beam steering, VCSEL arrays, and LiDAR-based tracking. While enabling high throughput, these approaches involve trade-offs in complexity, mobility support, and scalability. This subsection reviews notable architectures, analyzing their strengths and limitations for high-speed indoor OWC networks.

The work in [2], [9], [55], and [56], has demonstrated that beam-steered IRWC can achieve multi-Gb/s data rates per user by accurately directing narrow IR laser beams toward mobile devices. In [2], Koonen et al. proposed a high-capacity indoor OWC system that achieves two-dimensional beam steering of narrow infrared beams using passive wavelength control, as illustrated in Fig. 1.4. The system uses an 80-port arrayed waveguide grating router (AWGR), with each port connected to a single-mode fiber arranged in a 2D grid. Placing this fiber array at the focal plane of a lens allows each fiber to emit a collimated beam in a unique direction. By tuning the laser wavelength at the transmitter, the AWGR routes the signal to a different output port, effectively steering the beam without any mechanical movement. The system demonstrated a perbeam transmission rate of up to 112 Gbit/s using PAM-4 modulation over distances of 2.5 to 3.4 meters, supported by a receiver with an 18 GHz PD and 8 GHz electrical BW. When all AWGR ports are active, the aggregate system capacity exceeds 8.9 Tbit/s. User localization is performed using a mechanically steerable 60 GHz horn antenna at the transmitter side, which scans the room to detect the uplink signal from the user

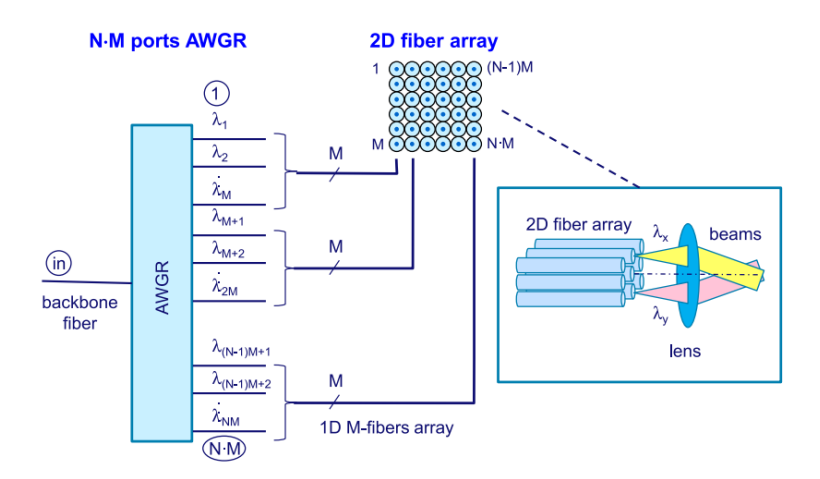


Figure 1.4: Two-dimensional steering of infrared beams using a high-port-count AWGR, [2, Figure 2]

terminal. The user device is equipped with its own 60 GHz horn antenna for transmitting this signal. By identifying the direction with the maximum received power, the system estimates the user position and selects the corresponding laser wavelength to steer the IR beam toward the user via the AWGR. However, this hybrid IR/RF system requires complex components such as fiber-linked APs, wavelength tuning, and horn antennas with mechanical scanning, making practical implementation challenging despite its high throughput.

In Fig. 1.5 and [57], a LiDAR-assisted indoor IRWC system is proposed, integrating a frequency-modulated continuous-wave (FMCW) LiDAR for calibration-free user localization. FMCW LiDAR enables millimeter-level ranging accuracy by continuously modulating the laser frequency and analyzing the beat frequency of the reflected signal. The system demonstrated 0.038° localization accuracy and achieved error-free on-off keying (OOK) data transmission at 17 Gbps over a 3 m link, with a maximum rate of 24 Gbps under the forward error correction threshold. However, the localization process relies on 3D point cloud reconstruction with offline data processing, introducing latencies ranging from tens to hundreds of milliseconds, depending on the hardware and acquisition setup, thereby limiting real-time performance.

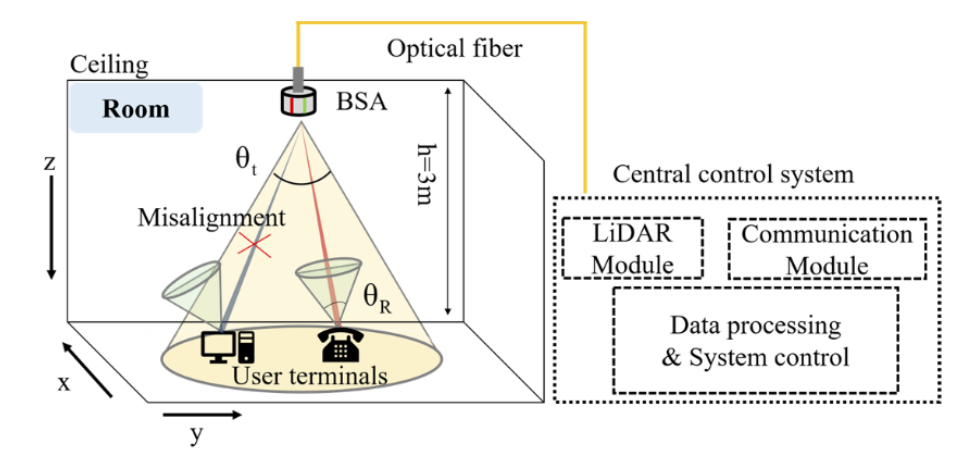


Figure 1.5: Illustration of a LiDAR-assisted IRWC system. The θ_I is the scanning field of view of the beam steering apparatus (BSA), and θ_R is the receiver FoV at the user end, [57, Figure 1]

In [58], a hybrid optical/RF network architecture is proposed that combines laser-based optical APs using VCSELs with a WiFi system to provide uplink support and offload users with poor optical connections [58]. The optical system uses a 2D grid of VCSELs arranged in an OPA configuration to generate narrow, directional beams aimed at multiple static users with known locations across the room. The beam direction and shape are controlled electronically by adjusting the amplitude and phase weights of individual VCSEL emitters, allowing for precise and simultaneous beam steering toward multiple users. To reduce multi-user interference and maximize throughput, the system optimizes these weights to create spatially isolated beams. Multiple optical APs are uniformly mounted on the ceiling, each covering a small attocell area, and each user is equipped with a reconfigurable receiver composed of multiple PDs arranged at different angles to provide angular diversity. Simulation results show that the system achieves a total downlink sum rate exceeding 50 bits/s/Hz when serving 20 users using the proposed beamforming approach. However, the study assumes that users are static and does not address localization, mobility, or real-time tracking.

In [1], [11], [59], the utilization of an array of VCSELs for the transmitter is proposed

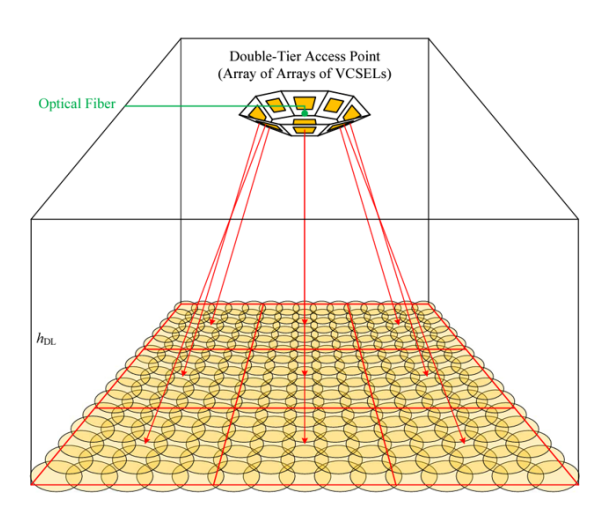


Figure 1.6: Indoor grid-based OWC network utilizing an array-of-arrays VCSEL for AP, [1, Figure 1]

for indoor OWC systems. In [59], a multiple-input multiple-output (MIMO) OWC system is designed using VCSEL arrays to achieve data rates exceeding 1 Tb/s for the backhaul of 6G indoor wireless networks with a system BW of 20 GHz. Their work focuses on the trade-off between channel gain and misalignment, and strategies to mitigate the effects of misalignment with a proposed reassociation method, aiming to effectively realign PDs with VCSELs. In [11], an atto-cell architecture is proposed, where the room is divided into small $10 \, \mathrm{cm} \times 10 \, \mathrm{cm}$ cells, and the corresponding transmitter element is activated based on the localized position of the user. The cell size is determined by the selected beam divergence, with a total of 2500 VCSELs deployed to ensure full coverage in a $5 \, \mathrm{m} \times 5 \, \mathrm{m} \times 3 \, \mathrm{m}$ room. Achieving higher data rates requires narrower beams, leading to smaller cells and an increased number of VCSELs, which adds complexity and introduces localization delays, especially for moving users. Notably, narrower beams restrict coverage to a single user per beam, making multi-user support challenging. This system thus involves a trade-off between beam coverage, received SNR, the number of cells, and the processing delay associated with the beam activation mechanism.

In [1], as illustrated in Fig. 1.6, the authors propose a double-tier AP design using an

array-of-arrays configuration, where each AP consists of 225 VCSELs arranged as a 3×3 grid of 5×5 sub-arrays. This design forms a dense grid of narrow, fixed-direction infrared beams, each capable of delivering multi-Gb/s data rates, and collectively enabling seamless room-wide coverage. On the receiver side, non-imaging ADRs are employed to enhance spatial selectivity. To manage the interference arising from such dense beam deployment, a static beam clustering strategy is introduced, where neighboring beams are grouped into fixed clusters. Within each cluster, the study compares non-orthogonal multiple access (NOMA) and orthogonal frequency-division multiple access (OFDMA) for user multiplexing, while space division multiple access (SDMA) is used as a baseline, where beams operate independently. The system is evaluated in a static indoor scenario with 100 randomly placed users. The results show that the proposed clustered beam deployment can achieve a total data rate of up to 15 Gb/s in the covered region using a 2 GHz system BW, outperforming the SDMA baseline under the same conditions.

1.1.8 Localization and Tracking in Indoor Environments

Indoor localization has become a critical enabler for a wide range of 6G applications, including smart environments, human-device interaction, and industrial automation. Accurate and low-latency positioning is also central to the broader vision of integrated sensing and communications (ISAC), where the same infrastructure supports both wireless communication and environmental awareness [60], [61]. Within this context, indoor OWC systems can greatly benefit from precise localization and tracking to optimize narrow IR beam pointing, thereby improving link reliability, data rates, and energy efficiency. This subsection reviews existing indoor localization and tracking approaches and their limitations, which motivate the design choices proposed in this work.

Localization of users in indoor environments can be performed using radio-based positioning technologies such as WiFi, Bluetooth, or radio frequency identification (RFID). However, Bluetooth and WiFi systems typically achieve localization accuracies in the range of 2-5 m and 1-7 m, respectively [62]. These methods fall short in applications that demand fine-grained spatial resolution. In emerging optical wireless systems, particularly those utilizing tightly confined IR, precise user positioning is critical to ensure reliable beam alignment and maintain a high SNR. In such contexts, localization accuracy on the order of a few centimeters is required, which conventional radio-based approaches cannot support. Visible light positioning (VLP) algorithms, including received signal strength (RSS), time difference of arrival (TDOA), and angle of arrival (AOA), provide centimeter-level accuracy with relatively low implementation cost compared to RF-based systems [63]. However, these methods rely on visible light transmitters, which may be unsuitable for applications limited to infrared sources.

The receiver in VLP systems typically falls into one of two categories, including PD-based systems and image sensor (IS)-based systems. PD-based VLP systems offer low latency but are highly sensitive to device orientation, which degrades positioning accuracy when the orientation of the user is not fixed. In contrast, IS-based VLP systems are more robust to device rotation but face challenges in real-time applications due to high computational latency. For example, Lin et al. [63] report an average processing delay of approximately 44 ms on embedded platforms when using convolutional neural networks for image-based localization. In addition, when image data must be transmitted to a server for remote processing, communication delays further increase the overall response time. Moreover, in many conventional VLP systems, there is no dedicated realtime feedback channel from the receiver to the APs for localization purposes. As a result, users often need to transmit their estimated location to the infrastructure, which can introduce additional latency, especially in systems relying on centralized processing [11]. Consequently, since VLP systems rely on illumination devices and uplink communication channels, this makes them unsuitable to support ultra-high-speed IR-based systems that demand low-latency and precise position information to support narrow beam links [11]. Therefore, to implement a narrow IR beam communication system, an alternative

localization and tracking method is needed.

In some systems, hybrid localization approaches combine RF or ultrasound signals for coarse user localization, followed by optical beam alignment for high-speed communication [64], [65]. For example, the system in [2] employs 60 GHz directional RF signals between steerable horn antennas to estimate the user position. This approach uses the well-established capabilities of millimeter-wave sensing for angular localization and avoids the need for real-time uplink transmission in the optical domain, which may not be reliable due to the narrow beam and limited FoV. However, relying on external RF components increases system complexity and cost. Alternatively, simpler techniques such as using received optical power feedback or narrow beam uplink signaling can enable real-time tracking without additional RF hardware.

The work in [57] further demonstrates the integration of FMCW LiDAR with an IRWC for high-precision user localization and gigabit-per-second data transmission. The system achieves millimeter-level ranging accuracy and an angular localization error as low as 0.038°, enabling precise beam alignment. While the approach eliminates the need for system calibration, it relies on 3D point cloud reconstruction and object detection techniques for tracking, which introduce processing delays due to the frame-by-frame nature of data acquisition. Although frame rates up to 30 Hz have been demonstrated using fast wavelength-swept sources, achieving consistent real-time tracking in dynamic environments with user mobility remains challenging. At 30 Hz, a new position is updated every 33 ms, which may be insufficient for fast-moving users or fine-grained beam tracking required in IRWC systems. The implementation requires specialized hardware, including a wavelength-swept tunable laser source, a blazed diffraction grating, a rotating mirror for 2D beam steering, and high-speed acquisition modules such as balanced PDs and oscilloscopes, which increase system complexity compared to camera- or retroreflector-based localization techniques [57].

Beam searching in indoor OWC systems involves rapidly identifying the optimal beam direction to align a narrow optical beam with a potentially mobile receiver. Traditional approaches assign discrete addresses to each beam direction and transmit them using packet-based communication that includes headers, synchronization bits, and error correction codes, introducing significant overhead and increasing localization delay. In contrast, [66] proposes a faster method that continuously transmits a pseudo-random bit sequence generated by a linear feedback shift register (LFSR), where each subsequence uniquely encodes a beam position. The receiver only needs to detect a short segment of this stream to determine alignment, eliminating the need for full packet decoding or synchronization and thus reducing search latency. As shown in Fig. 1.7, the system scans the coverage area A_C using a beam of area A_B , with resolution $A_R = A_B$, resulting in approximately $\frac{A_C}{A_B}=168{,}000$ scanning positions for $A_C=16.8~\mathrm{m}^2$ and $A_B=1~\mathrm{cm}^2$. In the analysis, it is assumed that the time required to redirect the beam from one position to the next is negligible compared to the symbol duration. Specifically, a modulation rate of $f_{\text{max}} = 100 \text{ MHz}$ is considered, corresponding to a bit duration of $T_b = 10 \text{ ns}$. This implies that the beam can be swept across all positions while transmitting the LFSR stream without pausing at each location, making the scan appear continuous. Under these assumptions, their approach achieves a total localization delay of approximately 25 ms to localize the receiver across the full coverage area, significantly faster than traditional stop-and-wait, packet-based methods.

An alternative localization approach is presented in [67], where IR camera networks are used to track users based on reflective markers or active IR LEDs. While this method offers high accuracy and real-time performance, it requires dense camera deployment, raising implementation cost and potential privacy concerns due to constant user monitoring.

In [11], the authors propose a user localization and beam activation scheme for indoor

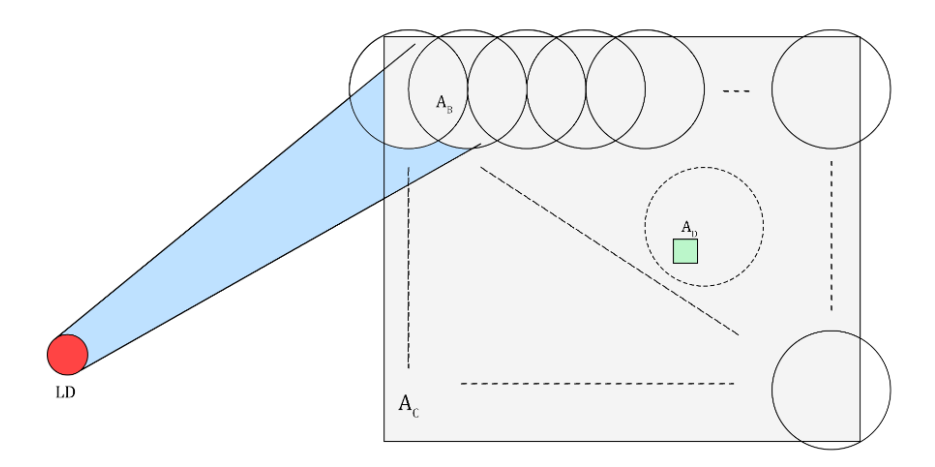


Figure 1.7: Example of the wide laser beam scanning system proposed in [66], where the LD scans the coverage area A_C using a step-wise beam pattern of resolution $A_R = A_B$.

OWC systems using a ceiling-mounted VCSEL array. The coverage area is divided into multiple square cells, each served by a VCSEL beam directed at the center of its corresponding cell, as shown in Fig.1.8. All VCSELs transmit test signals simultaneously, and the beam serving the user is activated based on the RSS at PDs co-located with each VCSEL. Two uplink feedback methods are explored for beam activation. The first uses a passive corner-cube reflector (CCR) placed near the receiver to retroreflect the incident light back to its source. This provides immediate feedback with latency in the order of a few microseconds with negligible power consumption. However, CCRbased feedback is not reliable under random device orientation, since the retroreflected signal may no longer return to the source beam, making detection at the transmitter inconsistent; thus, the need for omnidirectional CCR designs is highlighted. The second approach employs an omnidirectional transmitter (ODTx) at the user side. An artificial neural network (ANN) model at the AP side estimates the serving beam index based on the RSS measured at the ceiling PDs. This approach is well-suited for low-speed users with random orientation devices. However, for high-speed users, the delay introduced by the ANN processing (approximately 30 ms) could cause the location information to become outdated, potentially causing the AP to lose track of the user. While both

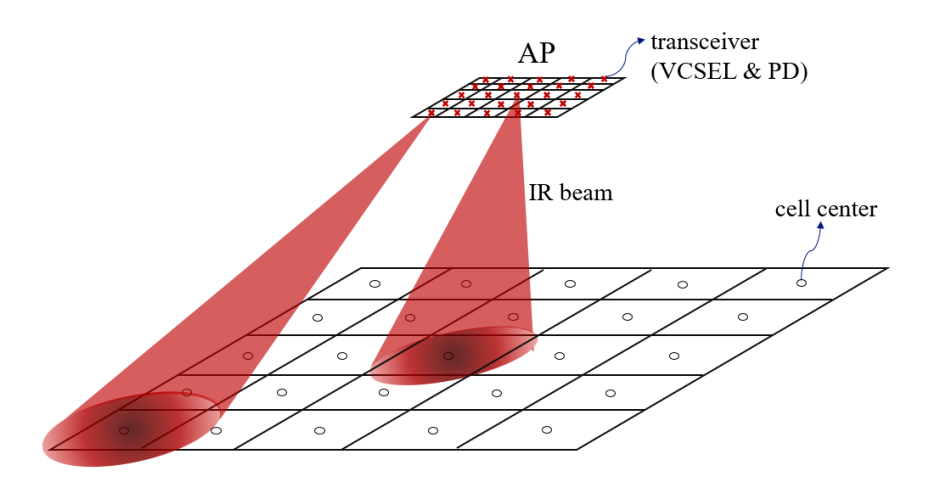


Figure 1.8: Cellular architecture with VCSEL array based on [11]

tracking methods proposed in [11] reduce the complexity and cost compared to IS-based systems (e.g., [9], with 44 ms latency), their scalability is limited. As cell sizes shrink, the number of VCSELs and PDs increases, leading to higher processing overhead and longer delays, especially for fast-moving users. For example, in a $5 \,\mathrm{m} \times 5 \,\mathrm{m}$ room with $10 \,\mathrm{cm} \times 10 \,\mathrm{cm}$ cells, 2,500 VCSELs and an equal number of co-located PDs are required to fully cover the area. Moreover, reducing beam divergence can theoretically increase the received SNR and data rate by concentrating more optical power within a smaller area. However, in this cellular system, the beam width must be sufficient to cover the entire cell $(10 \,\mathrm{cm} \times 10 \,\mathrm{cm})$, and therefore cannot be reduced beyond a certain point without causing coverage gaps. This constraint limits the potential gains from narrower beams and places trade-offs on system design and achievable data rates.

1.1.9 Beam Divergence Control and Adaptive Optics

While the VCSEL itself has a fixed initial divergence determined by its cavity design, external optics can reshape the beam profile. Tunable beam expanders and motorized zoom lenses can physically vary optical magnification to adjust divergence from narrow angles (e.g., 0.4°) to wider angles (up to 10°) within a single system [68]. Electrically tunable liquid lenses enable dynamic focal length control without moving mechanical

parts [69], while MEMS-based mirrors and optical systems allow rapid beam steering and divergence adjustment through micromechanical actuation [70]. Such adaptive optics technologies are widely used in fields like automotive LiDAR to support zoom and variable divergence operation [71], and can be integrated with a single VCSEL source in optical wireless AP designs to switch flexibly between beams with different divergence angles.

1.2 Research Objective and Problem Statement

In this thesis, a novel approach is proposed for localization, tracking, and communication in indoor OWC systems based on dynamic beam steering (DBS). Unlike prior grid-based schemes such as [11] and [1], which rely on dense arrays of VCSELs to statically cover the room, or fiber-based architectures such as [2], which require optical backplanes (i.e., AWGR, fiber arrays) and a UWB RF link for uplink feedback, the proposed design uses a single VCSEL and a beam steering device per user. While this introduces the cost and integration effort of a per-user steering mechanism, it eliminates the need for large-scale static emitter deployment and enables precise beam alignment to a single PD, allowing the transmitted power to be tightly focused on the receiver. This leads to stronger received signals and improved spectral efficiency per user. Overall, the proposed scheme offers a trade-off between hardware complexity and communication performance.

1.3 Contribution of the Thesis

To support centimeter-level user localization and efficient tracking with a single IR beam, this thesis proposes a two-phase approach that includes a multi-stage spiral beam searching for initial detection balancing delay, accuracy, and computational efficiency, followed by real-time tracking using a dynamic circular beam steering pattern with a one-bit uplink feedback mechanism. Fig. 1.9 illustrates the proposed system, which combines

these two stages to achieve reliable user localization and tracking. In this scheme, a dedicated beam steering device is required for each VCSEL beam to dynamically control its direction during both phases, with one beam allocated per user. Moreover, the AP is assumed to support dynamic adjustment of beam divergence during the localization phase while using a fixed divergence in the tracking stage. The proposed localization phase is designed as a general approach, with accuracy, delay, number of beam divergences, and stages all selectable to suit different room dimensions. Although a fixed beam divergence can be used for both localization and tracking phases, using adjustable beam divergence during localization improves performance by reducing delay and increasing accuracy.

In Fig. 1.9, two separate beams are shown for localization and tracking to highlight their distinct roles. In the proposed scheme, however, a single beam performs both localization and tracking for each user. For simplicity, the user position lies on a fixed XY plane and is equipped with a single PD. It is assumed that each user can respond with a 1-bit acknowledgment (ACK) through a low-latency (i.e., few μs) uplink upon detecting a test signal from the AP. A detection threshold is derived based on the minimum received power required for reliable signal detection. Once the user is localized, the AP switches to tracking. During this stage, the AP steers the beam through predefined positions along a circular path centered at the last estimated user location. At each position, the AP transmits a test signal with a narrow IR beam. If the beam enters the PD FoV and the received power exceeds the detection threshold, the user responds with an ACK; otherwise, the AP moves to the next position after a fixed time step. Upon receiving an ACK, the AP transmits the data signal during that time step before moving to the next position on the circular pattern. After completing a full cycle, the AP updates the circle center based on the ACK responses, enabling continuous user tracking and data transmission with a single steerable beam.

In contrast to existing methods that rely on high BW uplinks [2], or 3D vision-based

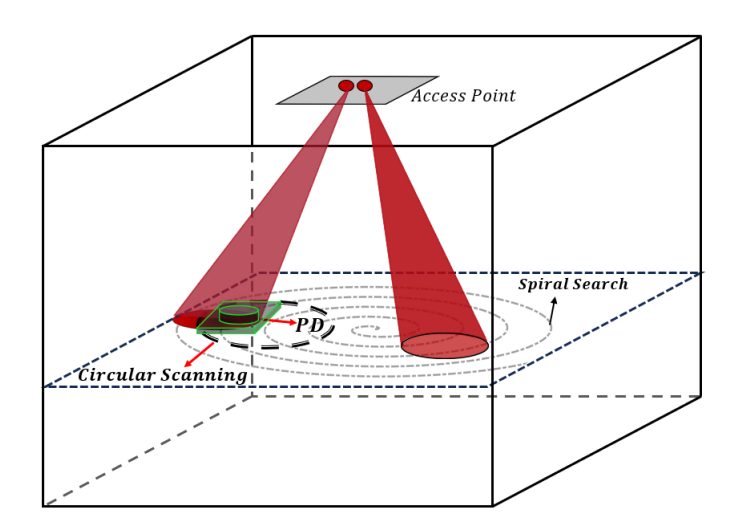


Figure 1.9: Dynamic beam steering strategy for indoor OWC for localization, tracking, and communication

systems [57], the proposed system operates using only one bit ACK signal from the user. It eliminates the need for RSS-based comparison, as in [11], and avoids upstream data transmission. Additionally, unlike [66], which encodes beam spot positions using pseudorandom address codes and requires maintaining a large set of addressable locations, the proposed system eliminates the need for address codes by dynamically steering a single beam to the user. The system also avoids the need for interference management techniques such as orthogonal multiple access or beam scheduling, as required in [1], since only one narrow beam is activated per user with no overlapping coverage. However, these advantages come at the cost of requiring a beam steering device for each VCSEL serving a user, along with the ability to adjust the beam divergence as needed.

Simulation results show that the proposed system achieves sub-centimeter localization and tracking accuracy using a single VCSEL and beam-steering device, with localization delay adjustable in the $\mu s-ms$ range depending on the steering step time. This exceeds the performance of [11], which only resolves the user position to a $10\,\mathrm{cm}\times10\,\mathrm{cm}$ grid cell (centimeter-level) using 2,500 VCSELs. Comparative simulations demonstrate that the proposed DBS setup achieves higher data rates, averaging 10 Gbps for a single user with

random movement using a single PD with 1.5 GHz BW, compared to the cellular-style architecture in [11], which achieves approximately 6 Gbps under the same conditions. Moreover, eye-safety constraints are addressed by limiting transmit power per beam to safe exposure levels. Specifically, results demonstrate that the proposed DBS approach achieves a higher data rate using approximately 10 mW per beam, compared to prior work such as [11], which relies on 60 mW per VCSEL with broader beam divergence.

The proposed DBS scheme inherently introduces channel fading due to the lack of exact knowledge of the instantaneous location of PD. Instead, the AP maintains a coarse estimate of the user position with centimeter-level accuracy and continuously steers the beam across a circular pattern to maintain alignment and update the estimated position of the user. This uncertainty leads to variations in received power as the beam periodically moves in and out of the PD FoV. Nevertheless, the sufficient localization and tracking accuracy achieved by the proposed method enables the use of a narrow IR beam with a divergence on the order of a few centimeters.

For multi-user scenarios, the system dynamically assigns a separate beam to each user for independent spiral-based localization and circular tracking. This eliminates the need for dense VCSEL arrays or static emitter grids and enables a fully cell-free indoor OWC architecture. Each beam operates independently, making the system scalable without requiring centralized beam coordination or resource partitioning.

1.4 Thesis Structure

Chapter 2 provides an overview of the indoor IR OWC channel and transceiver design. Key topics include Gaussian beam properties, eye-safe limits, optical modulation techniques, optical receiver design, the IM/DD channel model, and receiver noise considerations. Additionally, the effect of beam radius on the maximum eye-safe transmission power and the resulting received SNR is analyzed.

Chapter 3 introduces the DBS system, including the analytical framework for the proposed spiral search algorithm and the dynamic discrete beam-steering tracking mechanism. The chapter discusses spiral search localization, maximum delay, and localization error as metrics for evaluating localization accuracy, supported by simulation results. It also presents the discrete beam-steering algorithm, including tracking pattern selection, discrete spot step waiting time optimization, and determining the number of spot positions per cycle, along with their impact on tracking accuracy and average data rate.

Simulation results and performance trade-offs of DBS scheme are presented in Chapter 4. Furthermore, the cellular architecture and an ideal tracking method are discussed as benchmarks to compare the DBS system performance under user movement models, demonstrated through Monte Carlo simulations.

Chapter 5 concludes the thesis, summarizing key findings and proposing potential directions for future research.

Chapter 2

Indoor Optical Wireless System

This chapter focuses on the fundamental aspects of indoor OWC serving as prior knowledge before proposing the DBS design in Chapter 3, beginning with the system model, the characteristics of Gaussian beams emitted by VCSELs, and the impact of eye-safety constraints. It then covers the geometry of the pointed beam and the received power. The architecture of the optical receiver, along with receiver noise, is discussed. The chapter further examines the signaling and modulation scheme used in this work, the effect of beam width on received SNR and data rate, and, finally, the role of uplink feedback mechanisms.

2.1 System Model

For the balance of this work, consider a typical room where the AP is located at the center of the ceiling and the receiver (i.e., PD) is assumed to lie on the horizontal XY plane at z = 1 m (with -2.5 m $\leq x \leq 2.5$ m and -2.5 m $\leq y \leq 2.5$ m), yielding a vertical separation of h = 2 m. This height reflects the typical placement of handheld or desktop devices in indoor OWC models and is widely used as a prototypical scenario to ensure realistic link-budget analysis in room-scale OWC systems [72]. The user is considered vertically upward and its normal vector is $n_{Rx} = (0, 0, 1)$ [m]. Moreover, the footprint of

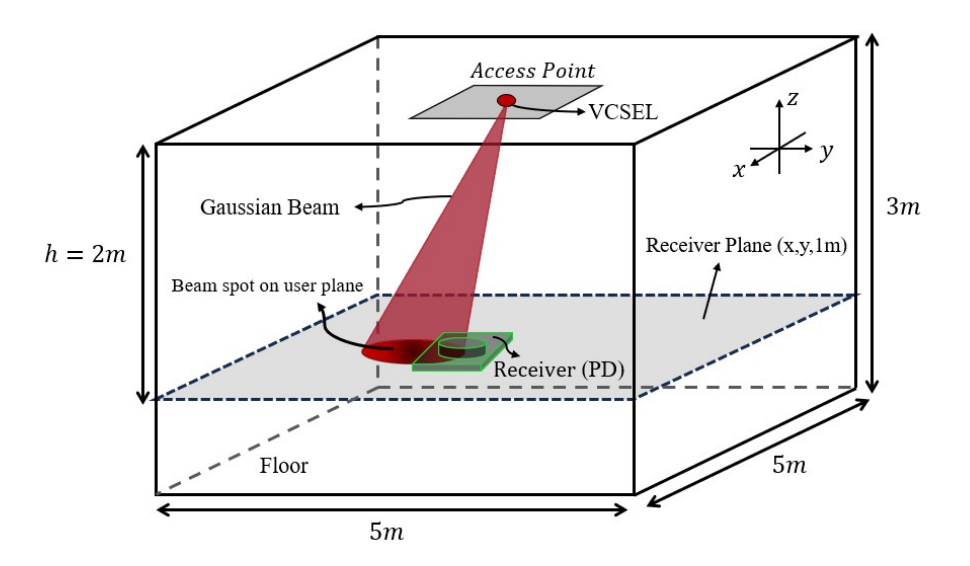


Figure 2.1: Indoor OWC system model with IR beam pointed to the user

the Gaussian beam, which represents the beam spot, is shown in the figure. In the next section, we discuss the propagation of the Gaussian beam from the VCSEL source and its characteristics, including the beam waist, divergence angle, and intensity distribution.

2.2 Gaussian Beam

Single-mode VCSELs that are considered as the optical source in this study, emit light in the fundamental transverse electromagnetic mode (TEM_{00}), producing a Gaussian intensity profile in the transverse plane [73, Ch. 3]. In this profile, the optical power is highest at the beam spot center and decreases exponentially with the square of the radial distance from the center. To analyze the propagation characteristics of the Gaussian beam, it is essential to first introduce the concept of wavefronts. A wavefront is an imaginary surface that connects all points in a medium where the wave is at the same phase of oscillation. It is always perpendicular to the direction of wave propagation. When waves travel a large distance from their source, the wavefront can appear flat over a small region, forming what is known as a plane wavefront. The wavefront of the Gaussian beam is planar at the beam waist, but it expands as it propagates. The radius

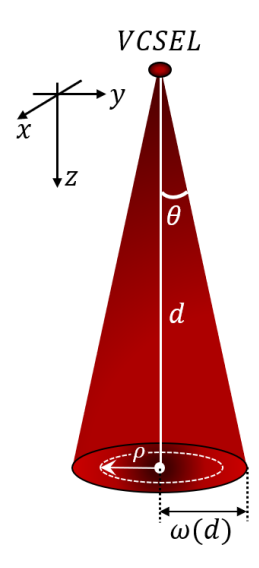


Figure 2.2: Geometry of Gaussian beam propagation

of curvature of the wavefront at a distance d from the source, and with laser operational wavelength of λ , can be described from [73] as

$$R(d) = d \left[1 + \left(\frac{\pi \omega_0^2}{\lambda d} \right)^2 \right] , \qquad (2.1)$$

where ω_0 is initial waist radius. The radius of the beam spot at a distance d from the source, is defined as the distance from the center of the beam to the point on the transverse plane. Thus, the effective beam radius at distance d is given by [73, Ch. 3]

$$\omega(d) = \omega_0 \sqrt{1 + \left(\frac{d}{d_R}\right)^2}, \qquad (2.2)$$

here, d_R represents the distance at which the beam radius $\omega(d_R)$ has expanded to $\sqrt{2}\omega_0$, indicating that the beam radius has increased by a factor of $\sqrt{2}$. Fig. 2.2 illustrates the propagation of a Gaussian beam emitted by a VCSEL, characterized by a beam radius $\omega(d)$ at a distance d and a half-angle beam divergence θ . In the far field, the circular-shaped beam spot is the base of a cone with its vertex positioned at the center of the beam waist.

In (2.2), d_R is defined as the Rayleigh range, and the beam spot area is twice that of the initial beam waist. The d_R can be described as [73, Ch. 3]

$$d_R = \frac{\pi \omega_0^2}{\lambda} \,. \tag{2.3}$$

When $d = d_R$,

$$d = \frac{\pi \omega_0^2}{\lambda}, \quad \omega(d) = \sqrt{2} \,\omega_0. \tag{2.4}$$

For $0 \le d < d_R$,

$$\omega_0 > \sqrt{\frac{d\lambda}{\pi}}, \quad and \quad \omega_0 \le \omega(d) < \sqrt{2}\,\omega_0.$$
 (2.5)

When $0 \le d \ll d_R$,

$$\omega(d) \approx \omega_0$$
. (2.6)

For $d \gg d_R$ (i.e., $\omega_0 \ll \sqrt{\frac{d\lambda}{\pi}}$), from (2.2), $\omega(d)$ can be approximated as

$$\omega(d) \approx \omega_0 \frac{d}{d_B} = \frac{\lambda d}{\pi \omega_0}. \tag{2.7}$$

Fig. 2.3 illustrates the relation between the beam waist radius $\omega(d)$ at a propagation distance $d=2\,\mathrm{m}$ and the initial waist radius ω_0 , based on (2.2). For this figure, $\sqrt{d\lambda/\pi}\approx 9.93\times 10^{-4}\,\mathrm{m}$ when $\lambda=1550\,\mathrm{nm}$. In subfigure (a), where $\omega_0\ll\sqrt{d\lambda/\pi}$, the beam exhibits strong diffraction spreading, indicating far-field behavior dominated by divergence. In contrast, subfigure (b) corresponds to the regime $\omega_0\gg\sqrt{d\lambda/\pi}$, where the beam maintains a nearly constant radius over the distance d, representing near-field propagation.

The half-angle divergence of the beam, θ_{beam} , at a distance $d \gg d_R$ is given by

$$\theta_{\text{beam}} = \arctan\left(\frac{\omega(d)}{d}\right) \approx \frac{\omega(d)}{d} \approx \frac{\lambda}{\pi\omega_0}$$
 (2.8)

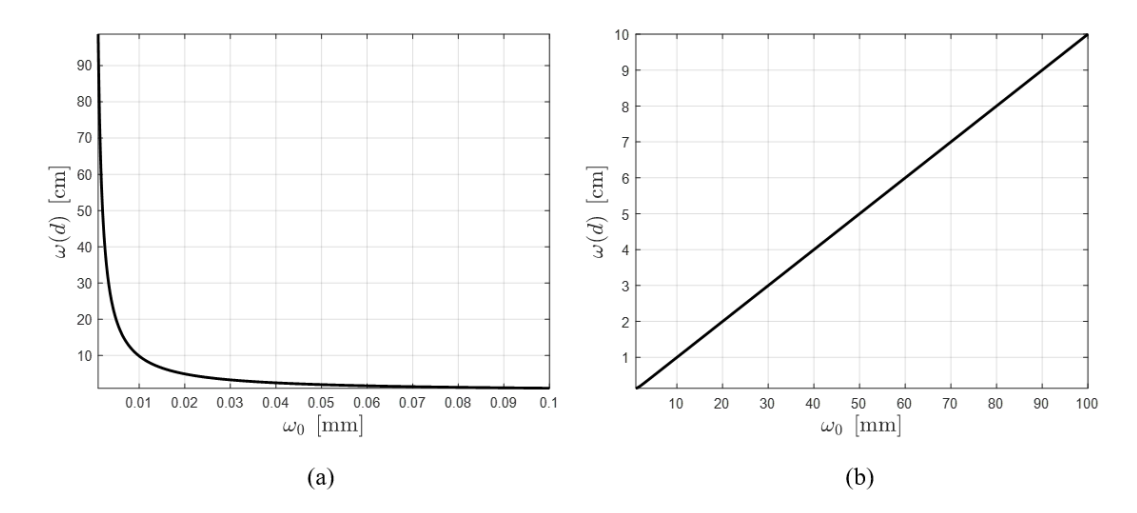


Figure 2.3: Beam waist radius at d=2m vs initial beam waist based on (2.2) for $\lambda=1550\,\mathrm{nm}$; (a) for $\omega_0\ll\sqrt{\frac{d\lambda}{\pi}}$; (b) for $\omega_0\gg\sqrt{\frac{d\lambda}{\pi}}$

Thus, the initial beam waist can be rewritten as

$$\omega_0 \approx \frac{\lambda}{\pi \theta_{\text{beam}}} \,.$$
 (2.9)

The spatial distribution of a Gaussian beam along its propagation axis is characterized by its intensity profile in the transverse plane, which describes the optical power per unit area at a given point perpendicular to the direction of propagation. Following [73, Ch. 3], the intensity distribution of a Gaussian beam at a distance d from the beam waist is given by

$$I(\rho, d) = I_0 \left(\frac{\omega_0}{\omega(d)}\right)^2 \exp\left(-\frac{2\rho^2}{\omega^2(d)}\right), \tag{2.10}$$

where $\rho = \sqrt{x^2 + y^2}$ is the radial distance from the beam spot center in the beam spot plane as demonstrated in Fig. 2.2. The peak intensity of the Gaussian beam for a given distance d is at $\rho = 0$, and continuously diminishes as ρ increases. The maximum intensity is at $(\rho = 0, d = 0)$, which is I_0 and can be determined as described in the following.

The total optical power of the beam at a distance d from the source is obtained by

integrating the optical intensity over any transverse plane located at that distance [73, Ch. 3]

$$P = \int_0^\infty \int_0^{2\pi} I(\rho, d) \rho \, d\rho \, d\phi$$

$$= \int_0^\infty I(\rho, d) \, 2\pi \rho \, d\rho$$

$$= I_0 \left(\frac{\omega_0}{\omega(d)}\right)^2 \, 2\pi \int_0^\infty \rho \, \exp\left(\frac{-2\rho^2}{\omega^2(d)}\right) \, d\rho$$
(2.11)

$$\Rightarrow P = I_0 \left(\frac{\omega_0}{\omega(d)}\right)^2 2\pi \frac{\omega^2(d)}{4} = \frac{1}{2}I_0 .(\pi\omega_0^2)$$
 (2.12)

$$\Rightarrow I_0 = \frac{2P}{\pi\omega_0^2}.\tag{2.13}$$

Therefore, the power carried by the beam is independent of distance d, and is equal to half of the peak intensity times the beam area, where the beam area is defined as $A_{\text{beam}} = \pi \omega^2(d)$. Accordingly, P can be replaced by the transmit optical power of the source in the room in Fig. 2.1, P_t . As a result by replacing (2.13) in (2.10) it follows that

$$I(\rho, d) = I_{max} \exp\left(-\frac{2\rho^2}{\omega^2(d)}\right) = \frac{2P_t}{\pi\omega^2(d)} \exp\left(-\frac{2\rho^2}{\omega^2(d)}\right) \quad \left[\frac{W}{m^2}\right]. \tag{2.14}$$

The ratio of the total power at distance d contained within a circle of radius ρ_0 in the transverse plane to transmit power is given by [73, Ch. 3]

$$\frac{1}{P_t} \int_0^{\rho_0} I(\rho, d) \, 2\pi \rho \, d\rho = 1 - \exp\left(\frac{-2\rho_0^2}{\omega^2(d)}\right) \,. \tag{2.15}$$

Considering a circle of radius $\rho_0 = \omega(d)$, the ratio of power is

$$\frac{P'}{P_t} = 1 - \exp\left(\frac{-2\omega^2(d)}{\omega^2(d)}\right) = 1 - e^{-2} = 0.86,$$
(2.16)

hence 86% of the total transmitted power is concentrated within a circle of radius $\rho_0=$

 $\omega(d)$, while nearly 99% of the power is enclosed within a circle of radius 1.5 $\omega(d)$ [73, Ch. 3]. One way to quantify the width of a function is by measuring its width at a specified fraction of its maximum value [73, App. A]. A widely used metric for this purpose is the full width at half maximum (FWHM), which represents the width of the function at half of its peak value. The angular width at which the intensity drops to half of its peak value is referred to as the FWHM of the intensity, denoted by $\theta_{\rm FWHM}$. The relation between beam divergence half-angle, $\theta_{\rm beam}$, and $\theta_{\rm FWHM}$ can be formulated as follows.

From Fig. 2.2, $\tan(\theta_{\text{beam}}) = \omega(d)/d$, and $\tan(\theta) = \rho/d$, where $0 \le \theta \le \theta_{\text{beam}}$, thus the Gaussian beam intensity profile in (2.14) can be rewritten in angular space as

$$I(\theta) = I_{max} \exp\left(-\frac{2\rho^2}{\omega^2(d)}\right)$$

$$= I_{max} \exp\left(-\frac{2(\tan(\theta) d)^2}{(\tan(\theta_{\text{beam}}) d)^2}\right)$$

$$= I_{max} \exp\left(-2\left(\frac{\tan(\theta)}{\tan(\theta_{\text{beam}})}\right)^2\right).$$
(2.17)

At $\theta_{\rm FWHM}$, the intensity drops to half of its maximum; therefore, $I(\theta_{\rm FWHM}/2) = I_{max}/2$. Hence $\theta_{\rm FWHM}$ can be derived as

$$\frac{I_{max}}{2} = I_{max} \exp\left(-2\left(\frac{\tan(\theta_{\text{FWHM}}/2)}{\tan(\theta_{\text{beam}})}\right)^2\right). \tag{2.18}$$

By taking natural logarithm, θ_{FWHM} can be found as

$$\ln \frac{1}{2} = -2 \left(\frac{\tan(\theta_{\text{FWHM}}/2)}{\tan(\theta_{\text{beam}})} \right)^2 \tag{2.19}$$

$$\Rightarrow \tan\left(\frac{\theta_{\text{FWHM}}}{2}\right) = \sqrt{\frac{\ln(2)}{2}} \tan(\theta_{\text{beam}})$$

$$= \sqrt{\frac{\ln(2)}{2}} \frac{\omega(d)}{d}$$
(2.20)

$$\Rightarrow \theta_{\text{FWHM}} = 2 \tan^{-1} \left(\sqrt{\frac{\ln(2)}{2}} \frac{\omega(d)}{d} \right)$$

$$= 2 \tan^{-1} \left(\sqrt{\frac{\ln(2)}{2}} \frac{\omega_0}{d} \sqrt{1 + \left(\frac{d\lambda}{\pi \omega_0^2}\right)^2} \right). \tag{2.21}$$

When $d = d_R$, the expression becomes

$$\theta_{\text{FWHM}} = 2 \tan^{-1} \left(\sqrt{\frac{\ln(2)}{2}} \frac{\omega_0 \sqrt{2}}{d} \right), \text{ where } \omega_0 = \sqrt{\frac{\lambda d}{\pi}}.$$
 (2.22)

For $d \gg d_R$, $\tan\left(\frac{\theta_{\text{FWHM}}}{2}\right) \approx \frac{\theta_{\text{FWHM}}}{2}$, and according to (2.8),

$$\theta_{\text{FWHM}} \approx 2\sqrt{\frac{\ln(2)}{2}} \frac{\lambda}{\pi \,\omega_0}.$$
 (2.23)

As a result

$$\omega_0 \approx \frac{\lambda\sqrt{2\ln(2)}}{\pi\,\theta_{\rm EWHM}}.\tag{2.24}$$

Thus, for $d \gg d_R$ (i.e., $\omega_0 \ll \sqrt{\frac{d\lambda}{\pi}}$), (2.7) can be rewritten as a function of θ_{FWHM} and distance from source d as

$$\omega(\theta_{\text{FWHM}}, d) \approx \frac{d \,\theta_{\text{FWHM}}}{\sqrt{2 \ln(2)}}.$$
 (2.25)

Fig. 2.4 illustrates the relation between the initial waist radius ω_0 , $\theta_{\rm FWHM}$ and the beam radius $\omega(d)$ at distance $d=2\,\mathrm{m}$ from the source with operational wavelength of 1550 nm. The curve corresponds to $\theta_{\rm FWHM}$, is obtained from (2.21), while the curve for $\omega(d)$ is computed using (2.2). The minimum of two curves is identified respectively and occurs at $\omega_0 = \sqrt{\frac{\lambda d}{\pi}}$. The minimum value occurs at $\omega_0 = 0.99\,\mathrm{mm}$ and for $\theta_{\rm FWHM}$ is 0.047°, whereas for $\omega(d)$ is 1.40 mm. The results demonstrate that there is a lower bound on achievable beam divergence at a given propagation distance due to diffraction. Specifically, even with ideal optical design, the divergence angle $\theta_{\rm FWHM}$, and beam radius $\omega(d)$, cannot be reduced below approximately 0.047°, and 1.40 mm respectively at $d=1.40\,\mathrm{mm}$

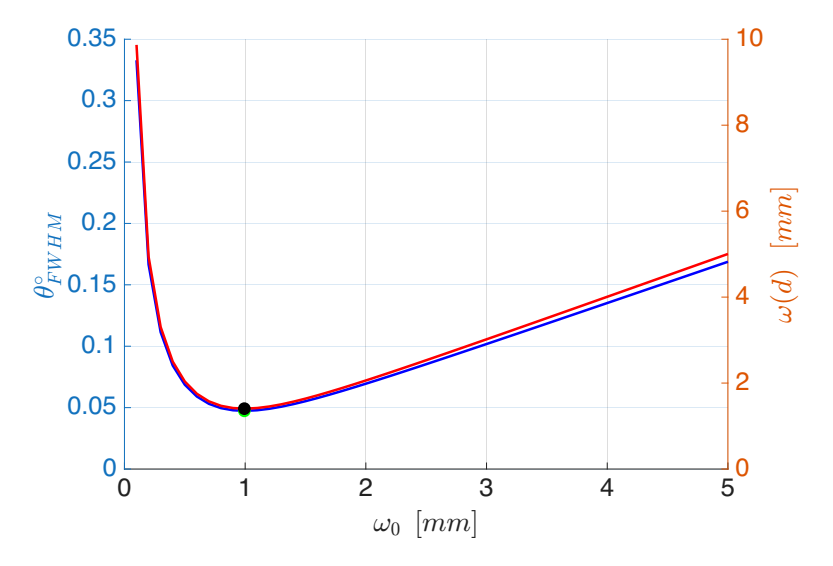


Figure 2.4: Variation of the initial beam radius ω_0 with respect to $\theta_{\rm FWHM}$ and beam radius $\omega(d)$ at distance $d=2\,\rm m$ and operational wavelength of 1550 nm; The blue curve represents $\theta_{\rm FWHM}$ as a function of ω_0 and red curve shows $\omega(d)$ as a function of ω_0

2 m for a wavelength of 1550 nm.

2.3 Eye-Safety Constraints

IR signals can pose risks to the human eye and skin, necessitating power restrictions to ensure safety. International laser safety standards, such as IEC 60825-1 [74], define maximum permissible exposure (MPE) levels, which are derived from the limits recommended by the International Commission for Non-ionizing Radiation Protection (ICNIRP) [75]. The MPE specifies the highest level of laser radiation to which the eye or skin can be exposed without harmful effects and serves as the basis for determining safe emission thresholds and product classifications.

The source size is often described using its angular diameter, measured from the point where the source is observed. This angular subtense defines the size of the optical image formed by a focusing system, such as the eye. The smallest spot size that can be focused onto the retina is characterized by the minimum angular subtense, defined as

 $\alpha_{\min} = 1.5 \,\text{mrad}$ [15]. Even if the source has an angular subtense smaller than 1.5 mrad, the retinal spot size cannot be reduced below 1.5 mrad due to diffraction and scattering effects. Retinal thermal exposure limits depend on the angular subtense of the apparent source via the factor C_6 , defined as

$$C_6 = \frac{\alpha}{\alpha_{min}} = \frac{\alpha}{1.5 \,\text{mrad}},\tag{2.26}$$

where the unit of α is mrad, and its values are constrained between α_{\min} and $\alpha_{\max} = 100 \,\mathrm{mrad}$. An apparent source with an angular subtense below α_{\min} is classified as a small source. For $\alpha < 1.5 \,\mathrm{mrad}$, $C_6 = 1$, which can be disregarded. For large sources, where $\alpha > 100 \,\mathrm{mrad}$, $C_6 = 66.6$. Consequently, if the MPE is 1 mW for an exposure duration of 0.25 s, multiplying the MPE by the area of the aperture results in a limit that remains 1 mW for small sources ($\alpha < 1.5 \,\mathrm{mrad}$). In the case of large sources, the exposure limit increases, reaching up to 66.6 mW [15].

The exposure level at a distance d, $E_{\text{exp}}(d)$, is the ratio of average optical density (irradiance) on the pupil with diameter d_a , to pupil area. From (2.14), the cornea exposure level at a distance d can be written as

$$E_{\text{exp}}(d) = \frac{1}{\pi (d_a/2)^2} \int_0^{\frac{d_a}{2}} I(\rho, d) \, 2\pi \rho \, d\rho$$

$$= \frac{1}{\pi (d_a/2)^2} \int_0^{\frac{d_a}{2}} \frac{2P_t}{\pi \omega^2(d)} \exp\left(-\frac{2\rho^2}{\omega^2(d)}\right) \, 2\pi \rho \, d\rho$$

$$= \frac{P_t}{\pi (d_a/2)^2} \left(1 - \exp\left(-\frac{d_a^2}{2\omega^2(d)}\right)\right). \tag{2.27}$$

The MPE represents the maximum permissible level of laser radiation that does not pose a hazard to the eyes or skin, with its value determined by the wavelength and the exposure duration. The most hazardous position (MHP) is defined as a position of 10 cm from the source, the standardized distance at which the eye is at greatest risk of exposure because it can accommodate and focus the beam onto the retina most

Table 2.1: MPE for different $t_{\rm exp}$ for $700 \, {\rm nm} < \lambda < 1050 \, {\rm nm}$ [15]

Exposure duration t_{exp}	MPE value
$t_{\rm exp} < 100 {\rm fs}$	$1.5 \times 10^9 \times C_4 \mathrm{W} \mathrm{m}^{-2}$
$100 \mathrm{fs} - 10 \mathrm{ps}$	$1.5 \times 10^{-4} \times C_4 \mathrm{J} \;\mathrm{m}^{-2}$
$10\mathrm{ps}-1\mathrm{ns}$	$2.7 \times 10^4 t_{\rm exp}^{3/4} \times C_4 \mathrm{J} \mathrm{m}^{-2}$
$1 \mathrm{ns} - 18 \mu\mathrm{s}$	$0.005 \times C_4 \mathrm{J} \;\mathrm{m}^{-2}$
$18 \mu \text{s} - 10 \text{s}$	$18 t_{\rm exp}^{3/4} \times C_4 { m J m}^{-2}$

Table 2.2: MPE for different $t_{\rm exp}$ for $1050\,{\rm nm} < \lambda < 1400\,{\rm nm}$ [15]

Exposure duration t_{exp}	MPE value
$t_{\rm exp} < 100{\rm fs}$	$1.5 \times 10^{10} \times C_7 \mathrm{W} \mathrm{m}^{-2}$
$100 \mathrm{fs} - 10 \mathrm{ps}$	$1.5 \times 10^{-3} \times C_7 \mathrm{J} \;\mathrm{m}^{-2}$
$10\mathrm{ps}-1\mathrm{ns}$	$2.7 \times 10^5 t_{\rm exp}^{3/4} \times C_7 \mathrm{J} \;\mathrm{m}^{-2}$
$1 \mathrm{ns} - 18 \mu\mathrm{s}$	$0.005 \times C_7 \mathrm{J} \;\mathrm{m}^{-2}$
$18 \mu s - 10 s$	$90 t_{\rm exp}^{3/4} \times C_7 { m J m}^{-2}$

effectively, producing the highest retinal irradiance [15]. Accordingly, the exposure level at $d_{mhp} = 10 \,\text{cm}$, $E_{\text{exp}}(d_{\text{mhp}})$, must be less than MPE at a certain exposure duration t_{exp} [15], i.e.,

$$E_{\text{exp}}(d_{\text{mhp}}) \le \text{MPE}(t_{\text{exp}})$$
 (2.28)

As a result, using (2.27), and (2.28), the maximum eye-safe transmit optical power $P_{\rm t,max}$, can be calculated as

$$P_{\text{t,max}}(t_{\text{exp}}) = \frac{\pi d_{\text{a}}^2 \text{ MPE}(t_{\text{exp}})}{4\left(1 - \exp\left(-\frac{d_a^2}{2\omega^2(d_{\text{mhp}})}\right)\right)}.$$
 (2.29)

MPE values for the retina for $t_{\rm exp} < 10\,{\rm s}$ for a single exposure within the wavelength range of $700\,{\rm nm} < \lambda < 1050\,{\rm nm}$, and $1050\,{\rm nm} < \lambda < 1400\,{\rm nm}$, are demonstrated in Table. 2.1, and 2.2 respectively [15]. Note that MPE values are specified for both pulsed and continuous-wave lasers as a function of exposure duration [15]

Wavelength	Exposure duration	MPE
1400–1500 nm	1 ns-1 ms 1 ms-10 s	1000 J m ⁻²
1500–1800 nm		$5600 t_{\text{exp}}^{0.25} \text{ J m}^{-2}$ 10000 J m^{-2}
1800–2600 nm	1 ns-1 ms 1 ms-10 s	1000 J m^{-2} $5600 t_{\text{exp}}^{0.25} \text{ J m}^{-2}$
$2600\!\!-\!\!10^6~{\rm nm}$	1–100 ns 100 ns–10 s	100 J m^{-2} $5600 t_{\text{exp}}^{0.25} \text{ J m}^{-2}$

Table 2.3: MPE for different $t_{\rm exp}$ for $\lambda > 1400\,{\rm nm}$ [15]

where C_4 , and C_7 can be calculated as

$$C_4 = \begin{cases} 1 & \text{for } \lambda < 700 \text{ nm} \\ 10^{0.002(\lambda - 700)} & \text{for } 700 \text{ nm} \le \lambda < 1050 \text{ nm} \\ 5 & \text{for } 1050 \text{ nm} \le \lambda < 1400 \text{ nm} \end{cases}$$
 (2.30)

$$C_7 = \begin{cases} 1 & \text{for } \lambda < 1150 \text{ nm} \\ 10^{0.018(\lambda - 1150)} & \text{for } 1150 \text{ nm} \le \lambda < 1200 \text{ nm} \\ 8 & \text{for } 1200 \text{ nm} \le \lambda < 1400 \text{ nm}. \end{cases}$$
 (2.31)

For the operational wavelength of $\lambda > 1400 \,\mathrm{nm}$, and exposure duration between 1 nm and 10 s, the MPE values are shown in Table. 2.3 [15]. Table 2.4 presents the limiting apertures used to average irradiance or radiant exposure for comparison with the MPE values for the eye. Since 1 Watt = 1 J/s, the MPE values in Jm⁻² must be divided by $t_{\rm exp}$ to be converted to Wm⁻².

Figures 2.5, and 2.6, compare maximum eye-safe transmit power for wavelengths 850 nm, and 1550 nm respectively based on parameters in Table. 2.5. For an operational wavelength of 850 nm, the maximum eye-safe power is much less than that permitted at 1550 nm. In this work, as is the case in most indoor high-speed optical wireless links, a

Table 2.4: Limiting apertures for different spectral regions [15]

Spectral region	Limiting eye aperture diameter d_a
180-400 nm	1 mm
400 – 1400 nm	$7~\mathrm{mm}$
$\geq 1400\mathrm{nm}0.1~\mathrm{mm}$	1 mm for $t_{\rm exp} \leq 0.35 {\rm s}$
	$1.5 t_{\rm exp}^{3/8} \text{ mm for } 0.35 \text{ s} < t_{\rm exp} \le 10 \text{ s}$
	$3.5 \text{ mm for } t_{\text{exp}} \geq 10 \text{ s}$
0.1-1 mm	11 mm

Table 2.5: Simulation parameters for Fig. 2.5 and Fig. 2.6, [15], [11].

	$\lambda = 1550\mathrm{nm}$		$\lambda = 850 \mathrm{nm}$	
Exposure duration, t_{exp} [s]	0.35 to 10	$10 \text{ to } 10^3$	10^{-3} to 10	$10 \text{ to } 10^3$
MPE, E_{MPE} [W m ⁻²]	$10^4/t_{\rm exp}$	1000	$18 t_{\rm exp}^{0.75} C_4 / t_{\rm exp}$	$10C_4C_7$
Aperture diameter, $d_{\rm a}$ [mm]	$1.5 t_{\rm exp}^{3/8}$	3.5	7	7

wavelength of 1550 nm is selected due to the wide availability of mature telecommunication components and equipment at this band. Furthermore, the maximum allowable eye-safe transmit power at 1550 nm is significantly higher than at 850 nm for the same $\theta_{\rm FWHM}$, which directly translates into a higher received SNR at the receiver. Note also that, smaller beam width, i.e., $\theta_{\rm FWHM}$, results in lower maximum allowable eye-safe transmit power. For example, at 1550 nm, the maximum allowable eye-safe power is 9.62 mW for $\theta_{\rm FWHM} = 0.5^{\circ}$, whereas for $\theta_{\rm FWHM} = 6^{\circ}$, it is 129.13 mW.

2.4 Optical Receiver Architecture

2.4.1 Avalanche Photodetector

As discussed in Chapter 1, this work adopts an APD-based receiver architecture for its superior sensitivity in low-power, IR-based indoor environments, benefiting from internal gain that enhances signal detection. For simulation purposes, a specific APD model is selected, namely the indium gallium arsenide (InGaAs) APD (G8931-10) [11], [76]. This device operates over 950 nm–1700 nm with peak sensitivity at 1550 nm, matching the

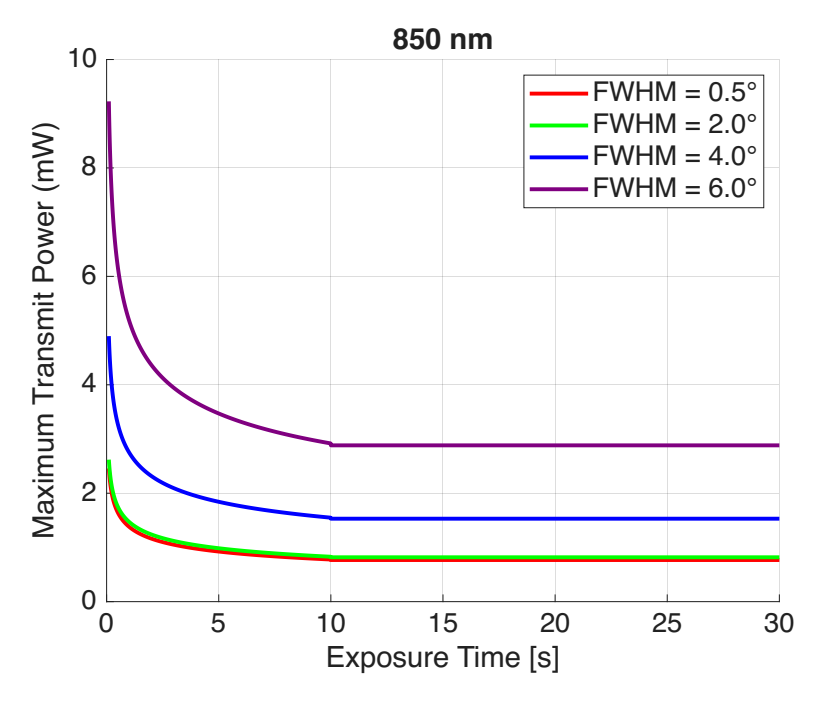


Figure 2.5: Maximum eye-safe transmit optical power for different $\theta_{\rm FWHM}$ at 850 nm and distance $d_{\rm mhp}=10\,{\rm cm}$

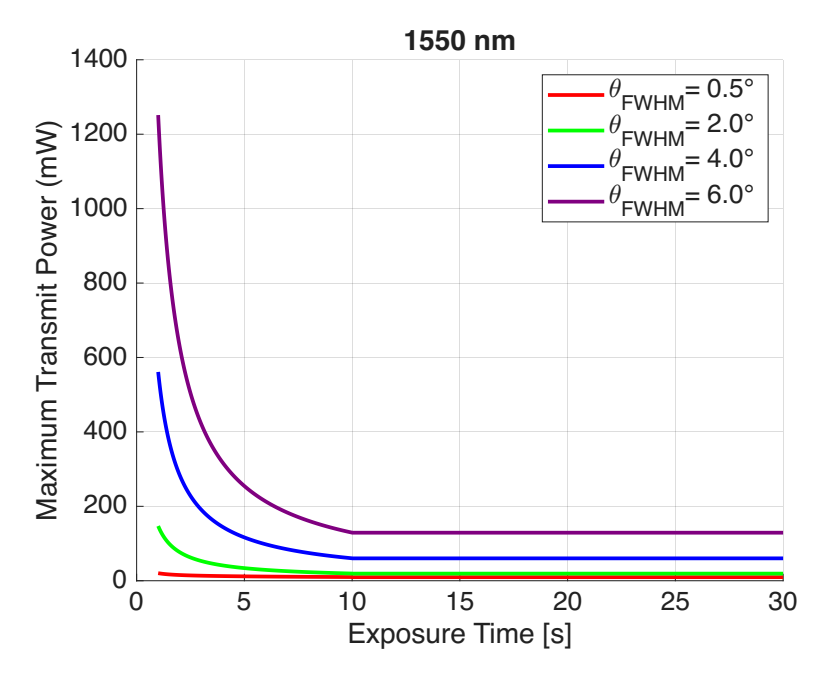


Figure 2.6: Maximum eye-safe transmit optical power for different $\theta_{\rm FWHM}$ at 1550 nm and distance $d_{\rm mhp}=10\,{\rm cm}$

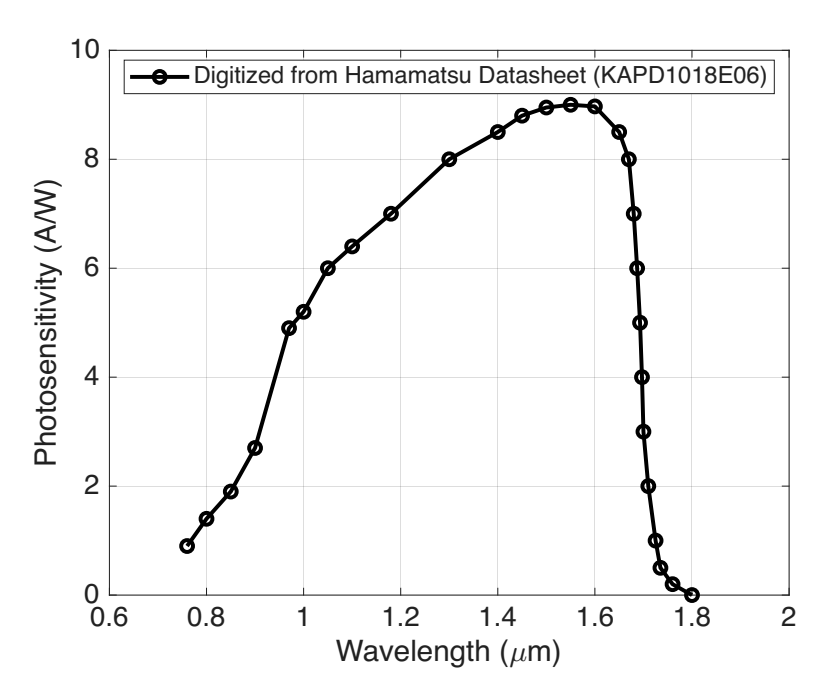


Figure 2.7: Spectral response of the Hamamatsu G8931-10 InGaAs APD measured at an internal gain of M=10 and ambient temperature of 25 °C. Digitized and reproduced from [76].

chosen optical source, as illustrated by its digitized spectral response in Figure 2.7. The receiver BW is inversely proportional to the capacitance of APD [11] and can be computed from

$$BW = \frac{1}{2\pi R_F C_T},$$
 (2.32)

where C_T is APD capacitance, and R_F is transimpedance amplifier feedback resistor. Since the APD terminal capacitance C_T increases with the detector area, higher area devices exhibit higher capacitance and therefore reduced BW. As a result, there is a trade-off between the PD area and its BW. For a small-area PD with high bandwidth, an optical concentrator can be used at the receiver to collect optical power and improve the received SNR. The internal gain of APD, denoted as $G_{\rm APD}$, can improve SNR. The SNR improvement by the APD is limited by receiver noise and is less than $G_{\rm APD}^2$ [77]. The APD parameters are summarized in table 2.6 [11], [76].

Parameter Symbol Value Bandwidth BW $1.5~\mathrm{GHz}$ 950 to 1700 nm Spectral response range Peak sensitivity wavelength λ 1550 nm $\pi \times 0.25 \times 0.25 \times 10^{-4} \text{ m}^2$ Effective area of APD A_{eff} Receiver FOV 60° $\Psi_{
m c}$ $\overline{G}_{\mathrm{APD}}$ Gain of APD 30 Responsivity $0.9~\mathrm{A/W}$ $R_{\rm PD}$ -155 dB/HzLaser noise RIN Terminal capacitance C_T 0.7 pFFeedback resistor $151.58\,\Omega$ R_F

Table 2.6: APD parameters used in the system [11], [76]

2.4.2 Receiver Noise

The receiver noise is composed of three factors, including thermal noise, shot noise, and relative intensity noise (RIN) [11]. The thermal noise arises from the random thermal motion of charge carriers in a resistor and is directly proportional to temperature T. The power spectral density (PSD) of thermal noise is defined as [13]

$$S_{\text{thermal}}(f) = \frac{4K_{\text{B}}T}{R_{\text{E}}},\tag{2.33}$$

where K_B is the Boltzmann constant, T is the absolute temperature in Kelvin.

The shot noise arises from the inherent randomness of photon arrivals, with the average arrival rate being determined by the incident optical power. For an APD, the PSD of the shot noise is expressed as [11]

$$S_{\text{shot}}(f) = 2 q G_{\text{APD}}^2 F_{\text{A}} R_{\text{PD}} (P_r + P_{\text{n}}),$$
 (2.34)

where q is electron charge, G_{APD} is APD internal gain, R_{PD} is responsivity of PD, P_n is average ambient power, P_r is received optical power, and F_A is excess noise factor which

is given by [11]

$$F_{\rm A} = k_{\rm A} G_{\rm APD} + (1 - k_{\rm A}) \left(2 - \frac{1}{G_{\rm APD}} \right),$$
 (2.35)

where $0 < k_A < 1$ is a dimensionless parameter. It is important to note that when $P_n \gg P_r$, the shot noise can be considered to be dependent solely on the ambient light power and is therefore independent of the signal.

The RIN is a type of noise primarily caused by fluctuations in the transmitted optical power of the VCSEL. These fluctuations arise mainly due to variations in the laser cavity and instabilities in the laser gain. The variance of the resulting photocurrent fluctuations at the APD can be expressed as [78]

$$\sigma_{\rm I}^2 = (R_{\rm PD} P_r r_{\rm I})^2, \tag{2.36}$$

where the parameter $r_{\rm I}$ quantifies the noise level in the optical signal and is defined as

$$r_{\rm I}^2 = \int_{-\infty}^{\infty} \text{RIN}(f) \, \mathrm{d}f, \tag{2.37}$$

here, RIN(f) denotes the power spectral density (PSD) of the relative intensity noise (RIN). Note that r_I is the inverse of the transmit optical power [11]. For a receiver with limited BW, the integral above should be computed over the receiver BW. For simplicity, it is assumed that RIN(f) remains constant across the entire BW, i.e., RIN(f) = RIN [11]. Thus, the PSD of the RIN is expressed as

$$S_{\text{RIN}}(f) = \text{RIN} \left(R_{\text{APD}} P_{\text{r}} \right)^2. \tag{2.38}$$

Consequently, the total noise power at the receiver can be derived as

$$\sigma_{\rm n}^2 = BW \left(\frac{4 K_{\rm B} T}{R_{\rm F}} + 2 q G_{\rm APD}^2 F_{\rm A} R_{\rm PD} (P_{\rm n} + P_{\rm r}) + \text{RIN} (R_{\rm PD} P_{\rm r})^2 \right).$$
 (2.39)

 $\begin{array}{|c|c|c|c|c|} \hline \textbf{Parameter} & \textbf{Symbol} & \textbf{Value} \\ \hline Boltzmann constant & K_B & 1.38 \times 10^{-23} \, \text{J/K} \\ \hline Temperature & T & 298 \, \text{K} \\ \hline Elementary charge & q & 1.602 \times 10^{-19} \, \text{C} \\ \hline Average ambient power & P_n & 47 \mu W \ [13], \ [76] \\ \hline \end{array}$

Table 2.7: Noise parameters [76]

The noise parameters at $1550 \, nm$ are summarized in Table 2.7.

2.5 Geometry of Pointed Beam and Received Power

The geometry of the Gaussian beam pointed to the PD of the receiver is illustrated in Fig. 2.8. According to the figure, the beam center is pointed towards the location $(x_s, y_s, 1)$ [m] and has an angle of θ with respect to the Z axis which is $\theta = \cos^{-1}\left(\frac{h}{\sqrt{x_s^2+y_s^2}}\right)$, where h=2 m. Furthermore, the vector between AP and PD is denoted by $\mathbf{d}_{Rx} = R\dot{x} - T\dot{x}$ where $T\dot{x} = (0,0,3)$ [m], and $R\dot{x}$ is the position vector of the user. Note that for perfect pointing, $(x_s, y_s) = (x_{rx}, y_{rx})$. The AP normal vector is $n_{Tx} = \frac{\mathbf{d}_{Tx}}{||\mathbf{d}_{Tx}||}$, where $d_{Tx} = ||\mathbf{d}_{Tx}|| = ||\mathbf{d}_{Rx}|| \cos(\varphi)$, and $||\cdot||$ is norm of a vector. Moreover, $\rho = ||\mathbf{d}_{Rx}|| \sin(\varphi)$, and $\cos(\varphi) = \frac{n_{Tx} \cdot \mathbf{d}_{Rx}}{||\mathbf{d}_{Rx}||}$. The beam radius at distance $||\mathbf{d}_{Tx}||$ from AP can be written from (2.2) as

$$\omega(d_{Tx}) = \omega_0 \sqrt{1 + \left(\frac{\lambda d_{Tx}}{\pi \omega_0^2}\right)^2},\tag{2.40}$$

where ω_0 can be calculated from (2.24). The Gaussian beam intensity can be obtained using (2.14) as

$$I(\rho, d_{Tx}) = \frac{2P_t}{\pi\omega^2(d_{Tx})} \exp\left(-\frac{2\rho^2}{\omega^2(d_{Tx})}\right),\tag{2.41}$$

where d_{ρ} is the distance from AP to the (x, y) point on the beam spot along the beam axis as shown in Fig. 2.8, and P_t is maximum eye-safe power which can be obtained from (2.29). Assuming the beam spot intensity is uniform over the effective PD area,

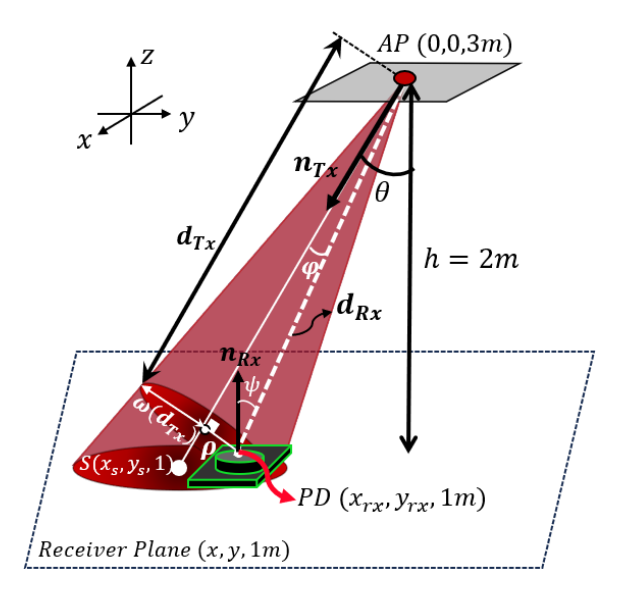


Figure 2.8: Illustration of the Gaussian beam directed towards the receiver

 A_{eff} (which is common in many previous studies [11], [38], [79]), the received optical power for APD can be approximated as [11]

$$P_{r}(\rho, d_{Tx}) = I(\rho, d_{Tx}) A_{\text{eff}} G_{\text{APD}} \cos(\psi) \operatorname{rect}\left(\frac{\psi}{\Psi_{c}}\right)$$

$$= \frac{2\cos(\psi) P_{t} A_{\text{eff}} G_{\text{APD}}}{\pi \omega^{2}(d_{Tx})} \times \exp\left(-\frac{2(||\mathbf{d}_{Rx}||\sin(\varphi))^{2}}{\omega^{2}(d_{Tx})}\right) \operatorname{rect}\left(\frac{\psi}{\Psi_{c}}\right),$$
(2.42)

where G_{APD} is APD gain, ψ is the received beam incident angle with respect to PD normal vector, thus $\psi = \cos^{-1}\left(\frac{n_{Rx}\cdot(-\mathbf{d}_{Rx})}{||\mathbf{d}_{Rx}||}\right)$, Ψ_c is receiver FoV, and a logic function is defined as $rect\left(\frac{\psi}{\Psi_c}\right) = 1$ for $0 \le \psi \le \Psi_c$ and zero otherwise. In (2.42), as the beam spot size increases, especially at greater distances from the AP where the spot widens, the variation in intensity across the detector area becomes more significant. For narrower beam divergence, the intensity distribution is more tightly focused, resulting in a larger fraction of the beam power being captured by the PD. Consequently, the uniform-intensity approximation becomes closer to the exact integration over the detector area. For comparison, the exact calculation of the received power is provided in Appendix B.

2.6 Signaling and Modulation

Modulation techniques used in conventional RF systems are generally not directly applicable to OWC because the optical intensity must remain non-negative, and the transmitter output is subject to average optical power limits for eye safety and power efficiency. Consequently, specialized modulation schemes have been developed for OWC systems to satisfy these constraints. Among these, orthogonal frequency division multiplexing (OFDM) is attractive for its ability to handle channel distortion and to support high data rates. OFDM divides the data stream into multiple parallel subcarriers with overlapping spectra that remain mathematically orthogonal, ensuring separation at the receiver without interference [80]. By converting a frequency-selective fading channel into multiple flat subchannels, OFDM reduces ISI and simplifies equalization to a per-subcarrier gain adjustment. This design achieves high spectral efficiency. In OWC, DC-biased optical OFDM (DCO-OFDM) ensures the transmitted signal is real and positive to meet IM/DD requirements by adding a DC bias. These features, along with adaptive modulation on individual subcarriers to match channel conditions, make OFDM well-suited for high-data-rate indoor OWC systems [59], [80].

The overall processing flow for DCO-OFDM in an OWC system is illustrated in Fig. 2.9. The diagram shows how the transmitter maps data to symbols and allocates them to subcarriers with Hermitian symmetry, ensuring the time-domain signal is real-valued. A DC bias is then added to make the signal positive before transmission. At the receiver, the PD captures the optical intensity, the DC bias is removed, and the subcarrier data is demapped to recover the original data stream. The total number of OFDM subcarriers is $m \in \{0, ..., M_s - 1\}$, where M_s is positive integer and even. The signals must be positive, thus $X(0) = X(M_s/2) = 0$, and real, therefore, $X(m) = X^*(M_s - m)$, for $m \neq 0$, where $(\cdot)^*$ is complex conjugate operator [81]. Therefore, the effective of subcarriers carrying information are $\mathcal{M}_s = \{m \mid m \in [1, M_s/2 - 1], m \in \mathbb{N}\}$, where

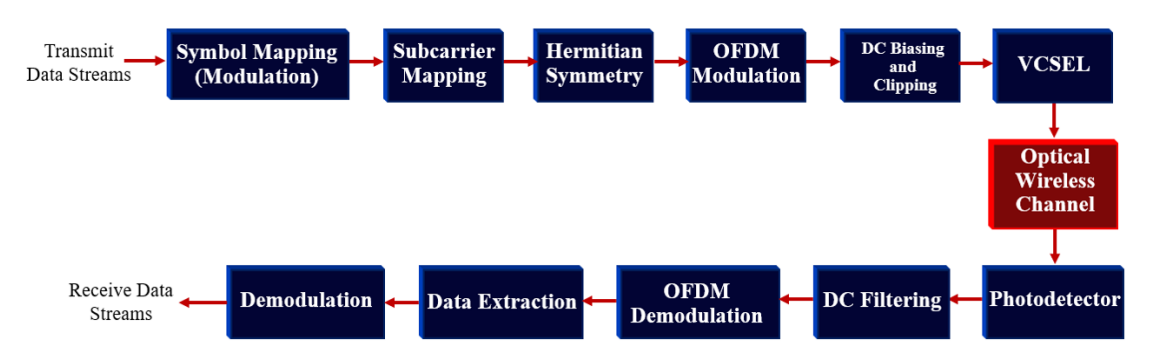


Figure 2.9: Block diagram of the DCO-OFDM-based OWC system

N is set of natural numbers. For a DCO-OFDM signal, the DC bias $x_{\rm DC}$ is defined as $x_{\rm DC} = \kappa \sqrt{P_{\rm elec}}$, where $P_{\rm elec}$ is the electrical power, and κ is a conversion factor. Choosing $\kappa = 3$ ensures that less than 1% of the signal samples are clipped, making the clipping noise negligible [82]. This value is based on modeling the DCO-OFDM time-domain signal as approximately Gaussian distributed (as shown in [83]). For a Gaussian distribution, setting the DC bias to three times the standard deviation places over 99% of the probability mass above zero, resulting in negligible clipping distortion. The detailed proof is provided in Appendix A.

The received SNR of the user for each effective subcarrier m can be denoted as

$$SNR_m = \frac{(R_{PD}P_r)^2}{(M_s - 2)\kappa^2 \sigma_n^2}, \quad m \in \{1, 2, \dots, \frac{M_s}{2} - 1\},$$
 (2.43)

where $P_{\rm r}$ is given in (2.42), and $\sigma_{\rm n}^2$ is the total noise power for each subcarrier [11].

In this work, the VCSEL-based optical wireless channel is modeled as a time-varying IM/DD channel with additive white Gaussian noise (AWGN). Perfect channel state information (CSI) is assumed at both the transmitter and receiver, enabling instantaneous tracking of channel variations caused by user motion. The front-end is operated with DC biasing to satisfy the non-negativity requirement of intensity modulation, with the bias level chosen to limit clipping distortion as previously discussed. Under this design

condition, the channel can be approximated as parallel AWGN subchannels, and following the Shannon capacity for a given channel realization, the instantaneous user rate is given by [84]

$$R = \sum_{m=1}^{\frac{M_s}{2} - 1} \frac{BW}{M_s} \log_2 (1 + SNR_m)$$
 (2.44)

$$= \frac{\left(\frac{M_s}{2} - 1\right)}{M_s} BW \log_2 \left(1 + \frac{(R_{PD}P_r)^2}{(M_s - 2)\kappa^2 \sigma_n^2}\right). \tag{2.45}$$

The noise variance expression in (2.46) follows directly from the general receiver noise model presented in Section 2.4.2 [(2.39)], with the total bandwidth BW replaced by the per-subcarrier bandwidth BW/M_s to account for the M_s OFDM subcarriers. Thus, the total noise power for each subcarrier at the receiver is given by [11]

$$\sigma_{\rm n}^2 = \frac{BW}{M_s} \left(\frac{4 k_{\rm B} T}{R_{\rm F}} + 2 q G_{\rm APD}^2 F_{\rm A} R_{\rm PD} (P_{\rm n} + P_{\rm r}) + {\rm RIN} (R_{\rm PD} P_{\rm r})^2 \right). \tag{2.46}$$

To select the number of subcarriers, M_s , the effect on the data rate in (2.45) is first investigated. From (2.46), the noise variance per subcarrier scales as $1/M_s$ since the total thermal, shot, and RIN power is distributed across all subcarriers. Substituting σ_n^2 from (2.46) into the SNR expression yields

$$SNR = \frac{(R_{PD}P_r)^2}{(M_s - 2)\kappa^2 \sigma_n^2}$$
(2.47)

$$= \frac{M_s}{(M_s - 2)\kappa^2 \sigma_n^2} \cdot \frac{(R_{PD}P_r)^2}{\kappa^2 BW \left(S_{\text{thermal}}(f) + S_{\text{shot}}(f) + S_{\text{RIN}}(f)\right)}, \tag{2.48}$$

demonstrating that the per-subcarrier SNR remains approximately independent of M_s for large M_s . Therefore, increasing the number of subcarriers does not significantly reduce the per-subcarrier SNR but improves the spectral efficiency prefactor $\frac{M_s/2-1}{M_s}$, which approaches its asymptotic limit of 0.5 as M_s increases at the cost of increased system complexity, and potentially greater sensitivity to synchronization and phase noise

impairments.

The choice of M_s in VCSEL-based DCO-OFDM systems can be guided by emerging standards in OWC. IEEE 802.11bb, the recently released LiFi specification, adapts the OFDM framework from traditional WiFi for operation over optical carriers, supporting data rates from approximately 10 Mb/s up to 9.6 Gb/s in the near-infrared band [85]. In this work, the scalable OFDM parameterization of IEEE 802.11ax is taken as a practical reference point, consistent with prior LiFi simulation studies that explicitly employ $M_s = 128$ subcarriers [86], [87], thereby ensuring a balance between spectral efficiency, subcarrier spacing, and implementation complexity.

2.7 Effect of Beamwidth on Received SNR and Rate

From Fig. 2.8, by selecting $\theta=0$, the beam is directed vertically downward, as illustrated in Fig. 2.10. This beam is referred to as the central beam and has the shortest distance between the AP and the user plane (i.e., at $(x,y,1\,\mathrm{m})$), resulting in the highest received power. In this case, $d_{\mathrm{Tx}}=h$, and ρ is replaced by r, which denotes the distance between the beam center and the user location, defined as $r=\sqrt{(x_s-x_{rx})^2+(y_s-y_{rx})^2}$, where (x_s,y_s) and (x_{rx},y_{rx}) are the beam center and the user location, respectively according to the figure. Since the central beam is aimed at the center of the XY plane, $(x_s,y_s)=(0,0)$, leading to $r=\sqrt{x_{rx}^2+y_{rx}^2}$. Furthermore, for the vertically downward central beam, the angles satisfy $\cos(\varphi)=\cos(\psi)=\frac{h}{\sqrt{h^2+r^2}}$, $\sin(\varphi)=\frac{r}{\sqrt{h^2+r^2}}$, and the distance between the AP and the user is $||\mathbf{d}_{Rx}||=\sqrt{r^2+h^2}$. As a result, (2.42) can be rewritten as

$$P_r(r) = \frac{2P_t A_{\text{eff}} G_{\text{APD}}}{\pi \omega^2(h)} \frac{h}{\sqrt{h^2 + r^2}} \exp\left(-\frac{2r^2}{\omega^2(h)}\right). \tag{2.49}$$

Hence SNR from (2.43) can be express as

$$SNR(r) = \left(\frac{2R_{PD} P_{t} A_{\text{eff}} G_{APD}}{\pi \omega^{2}(h)\sqrt{M-2} \kappa \sigma_{n}}\right)^{2} \cdot \frac{h^{2}}{h^{2}+r^{2}} \cdot \exp\left(-\frac{4r^{2}}{\omega^{2}(h)}\right). \tag{2.50}$$

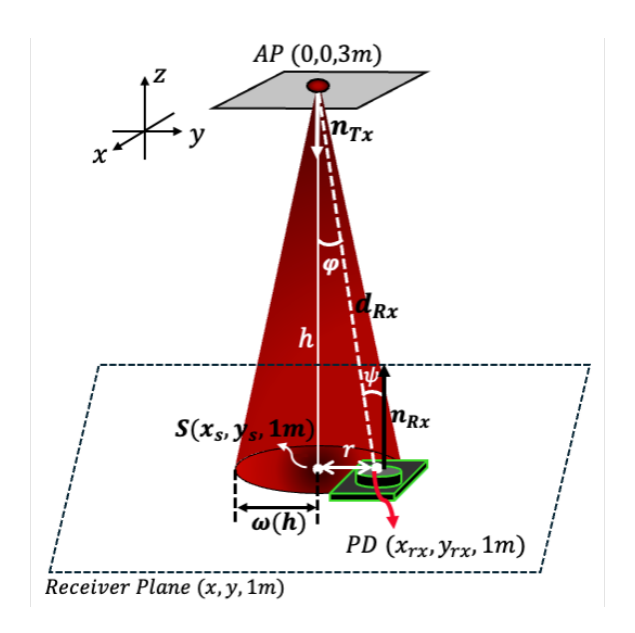


Figure 2.10: Illustration of the central beam vertically downward towards the user $(\theta = 0)$

Fig. 2.11 presents a three-dimensional illustration of the data rate distribution on the XY plane at $z=1\,\mathrm{m}$ above the floor for the central beam. The beam is oriented vertically downward toward the center $(x_s,y_s)=(0,0)$, while the user location is swept over the XY plane at $z=1\,\mathrm{m}$. For each θ_{FWHM} , the maximum eye-safe transmit power is determined using (2.29). Specifically, for $\theta_{\mathrm{FWHM}}=1^\circ$, 4° , and 6° , the corresponding maximum transmit powers are 10.25 mW, 60.18 mW, and 129.13 mW, respectively. The simulation parameters are provided in Tables 2.6, 2.7. The received power for each θ_{FWHM} is calculated using (2.49), the noise variance is obtained from (2.39), and the data rate is computed via (2.45), assuming M=128 subcarriers for DCO-OFDM. It can be observed that the maximum data rate occurs when the user is positioned at $(0,0,1\,\mathrm{m})$, representing the shortest distance between the access point and the user on the XY plane at $z=1\,\mathrm{m}$. The figure also illustrates the trade-off between maximum data rate and coverage area for a fixed beam direction. Additionally, a lower θ_{FWHM} achieves higher data rates with reduced eye-safe transmit power, but results in a smaller

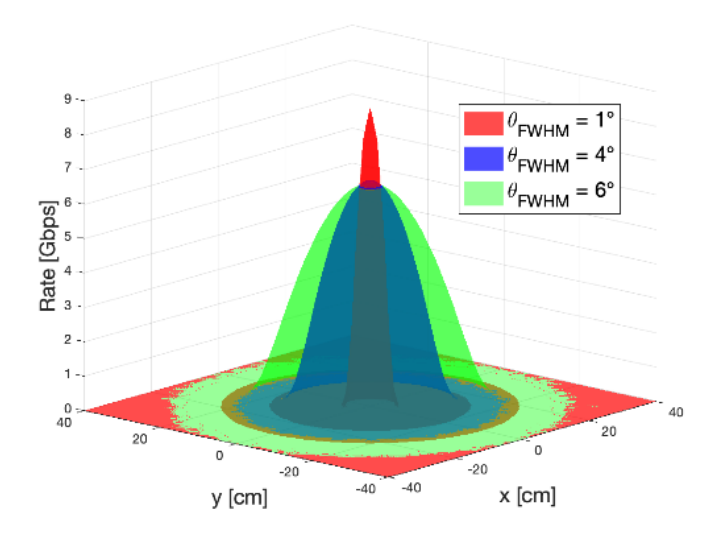


Figure 2.11: 3D plot of data rate distribution on the XY plane at $z=1\,\mathrm{m}$ for different θ_{FWHM} values at 1550 nm. The central beam is directed vertically downward (fixed). User locations are swept over the XY plane at $z=1\,\mathrm{m}$, with received power and data rate computed from (2.49) and (2.45), respectively. For $\theta_{\mathrm{FWHM}}=1^\circ, 4^\circ,$ and $6^\circ,$ the corresponding maximum eye-safe transmit powers are 10.25 mW, 60.18 mW, and 129.13 mW, respectively.

coverage area. Larger $\theta_{\rm FWHM}$ results in higher allowable eye-safe transmitted power. This is because a higher $\theta_{\rm FWHM}$ leads to a larger $\omega(d_{\rm mhp})$ in (2.29), resulting in a higher $P_{\rm t,max}$.

Using the same simulation parameters from Tables 2.6 and 2.7, with the central beam directed vertically downward toward $(x_s, y_s) = (0,0)$ and the user located at (0,0,1 m) above the floor, the AP-to-user distance is set to 2 m. The transmit power varies up to the maximum eye-safe level for each θ_{FWHM} . Figure 2.12 illustrates the relationship between the achievable data rate and transmit power for different θ_{FWHM} values. From this figure, it can be observed that a narrower beam enables higher data rates with lower transmit power. As θ_{FWHM} increases, the data rate approaches a constant value slightly above 6 Gbps. Therefore, employing a wider beam results in significantly higher power consumption, but provides coverage over a larger is (according to Fig. 2.11).

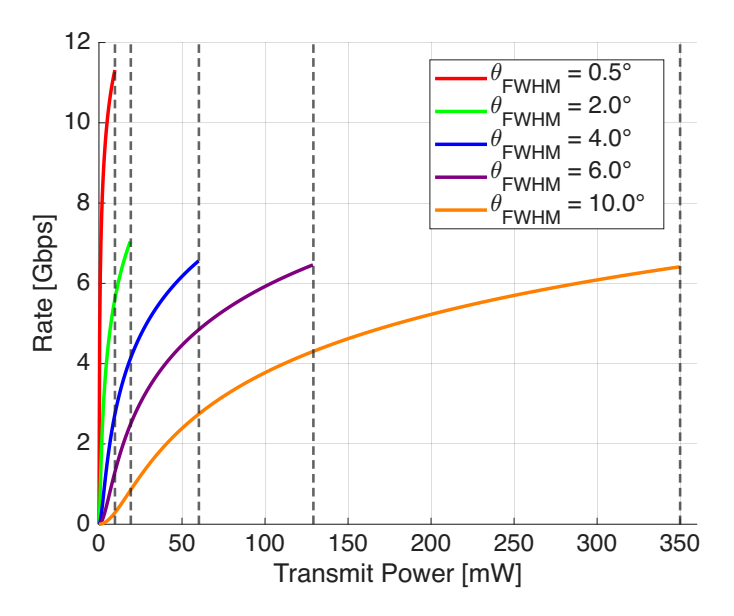


Figure 2.12: Rate vs transmit optical power until maximum allowable eye-safe power for different $\theta_{\rm FWHM}$ values

For the same simulation setup as in Fig. 2.12, except with the transmit power set to the maximum eye-safe level computed from (2.12) for each $\theta_{\rm FWHM}$, Figures 2.13 and 2.14 show the variations of SNR, data rate, and $\omega(h)$ as functions of $\theta_{\rm FWHM}$ (computed from (2.21)). In Fig. 2.13, $\theta_{\rm FWHM}$ varies from near zero to 0.4°. It is observed that both SNR and rate do not change significantly for $\theta_{\rm FWHM} < 0.2^{\circ}$. Moreover, the maximum SNR and data rate are shown in the figure. The maximum SNR occurs at $\theta_{\rm FWHM} = 0.047^{\circ}$ which is 53.76 dB, whereas maximum rate is 13.19 Gbps. $\theta_{\rm FWHM} = 0.047^{\circ}$ corresponding to the maximum directivity as shown in Fig. 2.4. This result follows directly from (2.50), where the narrow divergence (minimum $\omega(h)$) yields the highest received power and thus the peak SNR in the evaluated scenarios. It is interesting to note that given this $\theta_{\rm FWHM}$, the $\omega(h)$ is 1.4 mm. Furthermore, in Fig. 2.14, SNR and rate are not significantly changing for $\theta_{\rm FWHM} \geq 6^{\circ}$.

To achieve higher data rates, potentially approaching the Tb/s range, the system design must simultaneously address both BW and spatial multiplexing. One approach is to employ a receiver with substantially larger BW; for example, increasing the BW from

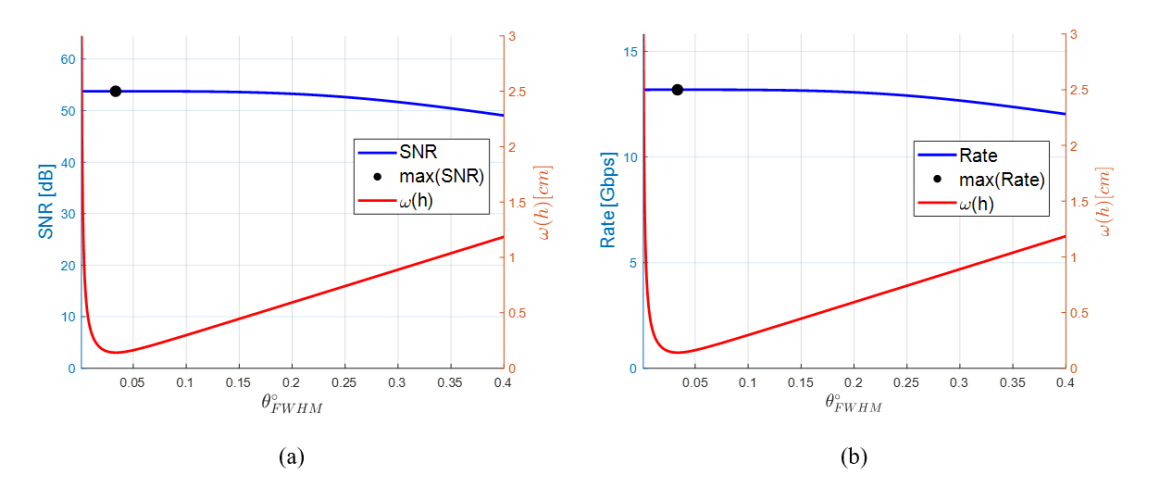


Figure 2.13: System performance, (a) SNR in dB, and (b) data rate in [Gbps] as function of $\theta_{\rm FWHM} \leq 0.4^{\circ}$, with $\omega(h)$ shown on the right y-axis

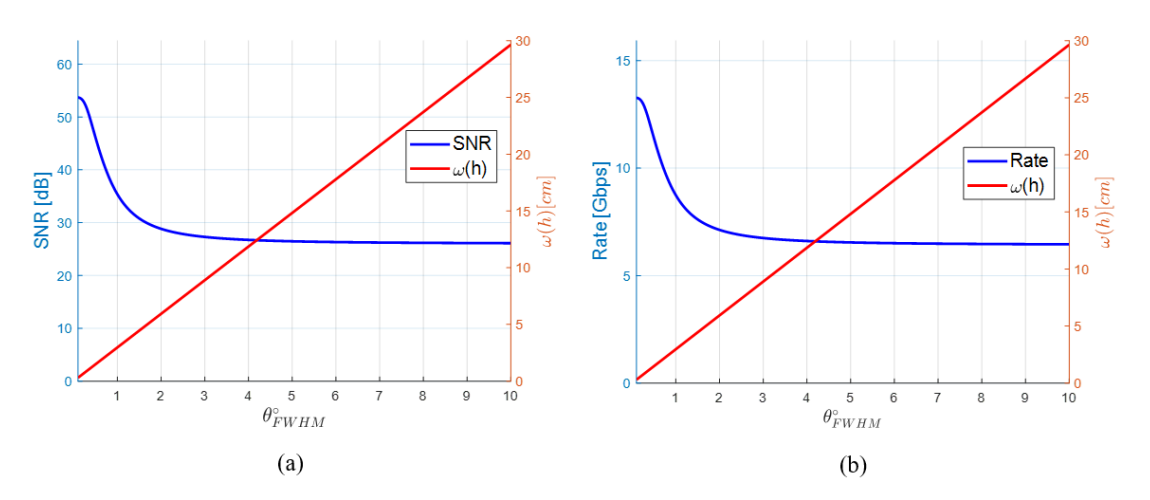


Figure 2.14: System performance, (a) SNR in [dB], and (b) data rate in [Gbps] as function of $\theta_{\rm FWHM} \leq 10^{\circ}$, with $\omega(h)$ shown on the right y-axis

1.5 GHz to 20 GHz expands the number of channel uses per second. In the simulated system, shot noise is the dominant impairment, and its variance grows proportionally with BW, thereby reducing the SNR. It should be emphasized that increasing BW does not unconditionally improve capacity. While BW appears linearly in the capacity expression (see (2.45)), the concurrent SNR reduction introduces a fundamental trade-off between power-limited and bandwidth-limited operating regimes. For the simulated

scenarios considered here, the multiplicative effect of increasing BW yields a net capacity gain, but this behavior is not general and must be interpreted within the specific operating regime of the system. Additionally, deploying multiple PD elements and multiple VCSEL transmitters in a MIMO configuration enables parallel data streams while maintaining eye safety per beam. This approach divides the total power across multiple narrower beams, each remaining within eye-safe limits but collectively delivering much higher aggregate throughput. For example, Kazemi $et\ al.$ demonstrated a 64×64 indoor optical wireless MIMO system using VCSEL arrays with 20 GHz bandwidth at 850 nm wavelength, with AP-to-receiver distance of 2 m, achieving nearly 3 Tb/s while ensuring eye-safe operation for each channel [59].

2.8 Uplink Feedback

Efficient user tracking requires frequent and low-latency updates of the user location at the AP. Without such feedback, the AP cannot accurately steer or adjust its narrow optical beams toward the moving user, which would result in beam misalignment and degraded communication performance. In practice, there are many ways to realize this uplink feedback channel, including using an RF link with low-rate signaling (for example, one-bit beam presence feedback), optical retroreflectors (CCR designs as discussed in Section 1.1.8), or dedicated ODTx at the user side. Each approach has trade-offs in terms of complexity, cost, power consumption, and orientation sensitivity.

A CCR is a passive optical device that reflects incident light back toward its source with minimal scattering, but only within a limited range of incident angles (for example, effective up to approximately 30° in the design studied in [88]). A CCR enables feedback by returning a portion of the AP optical test signal along the incoming path with latency on the order of a few microseconds. This occurs because the beam spot size at the CCR location is typically much larger than the CCR itself, so only the portion of the

beam incident on the CCR aperture is retroreflected. This passive reflection eliminates the need for an active uplink transmitter or dedicated illumination equipment on the user device. However, a single CCR is sensitive to the device orientation because it only retroreflects effectively when its reflective face is approximately aligned with the incoming beam [11]. To mitigate this limitation, an omnidirectional CCR design can employ multiple CCR elements arranged in different orientations to maintain reflection performance even as the user device orientation changes [11]. Moreover, in [10], Koonen et al. implemented circular retroreflective foils (approximately 4 cm diameter) containing embedded arrays of miniature CCR elements to enable device localization via beam reflection. This design reflected part of the narrow, steered optical beam directly back to the transmitter with minimal scattering and a small lateral offset, enabling precise round-trip detection. Each 4 cm diameter foil included a central 3 cm hole allowed for the placement of the downstream optical receiver without blocking the localization return path.

The ODTx feedback for uplink to assist AP for tracking is proposed in [11], and ODTx was initially proposed in [89]. The ODTx architecture is demonstrated in Fig. 2.15 where the uplink signal sent from ODTx can be detected from the AP detector. It is shown in [89] that using six orthogonal infrared LEDs with $\phi_{1/2} = 45^{\circ}$ forms an omnidirectional transmitter, where $\phi_{1/2}$ is transmitter semi-angle at half power [13]. Moreover, since the uplink and downlink operate on distinct wavelengths, users can simultaneously transmit data on the uplink and receive data on the downlink without interference.

2.9 Optical Beam Steering Hardware Solutions

Multiple technologies are available for implementing IR beam steering, ranging from low-cost rotating optics to high-precision MEMS mirrors and SLMs. Each technology offers a trade-off between cost, speed, precision, and complexity. In this section, the

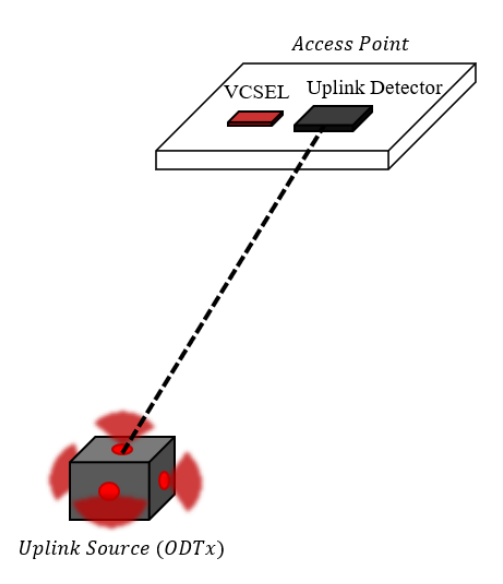


Figure 2.15: UL feedback with ODTx according to [11], and [89]

main beam steering solutions, along with their specifications, are described.

The simplest approach to beam steering is using stepper motors with rotating mirrors. In this method, a stepper motor rotates a mirror or lens to steer the beam. Each step corresponds to a discrete angular displacement, allowing for both continuous and discrete steering. The angular resolution depends on the motor precision (e.g., 1.8° per step, or finer with microstepping). Low-cost modular systems, such as those based on NEMA 23 stepper motors, are available in the \$50 to \$300 USD range [90]. Alternatively, off-the-shelf motorized stages, like the MOR-100-30 from Optics Focus, offer integrated control with improved mechanical stability, as illustrated in Fig. 2.16 [91] with a cost of \$280 USD. For higher-precision tasks requiring sub-microdegree resolution and excellent stability, high-end motorized rotation stages from established optics manufacturers are commonly employed [45]. For example, some models can achieve angular resolution down to 0.0005° with appropriate microstepping and encoder feedback, though the stages are significantly more expensive (\$3,300-\$5,750 USD) [45].

Another solution is a galvanometer scanner, which rotates a small mirror in response

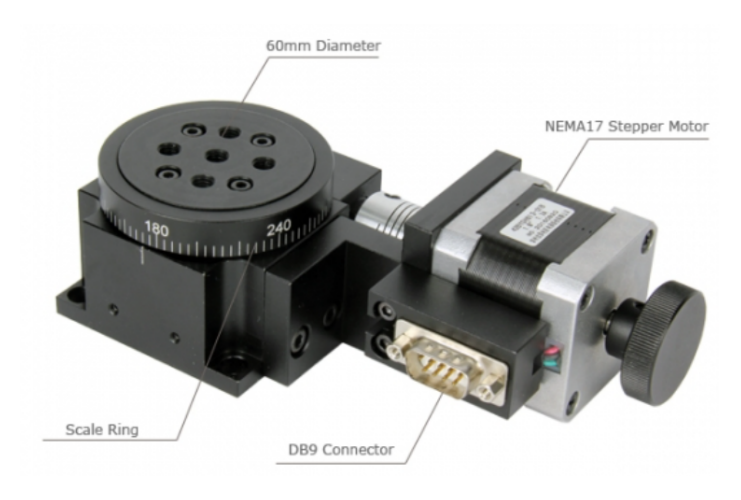


Figure 2.16: Motorized rotation stage (MOR-100-30) by Optics Focus with 360° range, 30mm aperture, and microstepping support for beam steering [91].

to an input voltage, enabling beam steering at speeds of several kHz with sub-millidegree precision. These systems are compact, reliable, and well-suited for applications requiring faster scanning rates. A representative example is shown in Fig. 2.17 [46]. However, galvo-resonant scanners are more expensive than stepper motors, with costs typically ranging from \$3,000 to \$15,000 USD [46], [92]. The main limitation of galvanometer scanners is their restricted rotation range, usually limited to $\pm 20^{\circ}$. The controller for representative galvo-resonant systems (e.g., Thorlabs LSK-GR08/12) accepts 90–264 VAC and is rated at 120 VA (max)¹, with the galvo motor drawing up to 2.4 A average and 8.0 A peak. Some standalone galvo drivers require ± 24 V_{DC} supplies at a few amperes [46], [92].

MEMS mirrors represent a cutting-edge solution for compact, high-speed, and high-precision beam steering [47], [48]. These devices employ microelectromechanical systems to tilt or rotate a mirror, allowing for sub-millidegree precision at speeds up to 10 kHz. A representative device is the GVS012 dual-axis MEMS mirror from Thorlabs, shown

¹Volt-amperes (VA) measure apparent power, which is the product of RMS voltage and RMS current without accounting for the phase angle between them. In practice, the actual power consumed in watts is lower when the power factor is less than one. Thus, "120 VA max" indicates the upper limit of the apparent power draw of the supply, not necessarily the real power dissipated.



Figure 2.17: Thorlabs LSK-GR08 galvo-resonant scanner and controller for fast beam steering applications [46].

in Fig. 2.18 [93], which offers sub-millidegree angular precision, scanning speeds up to 10 kHz, and is priced at approximately \$20,000 USD depending on configuration and driver options. MEMS mirrors are well-suited for advanced optical communication systems, including LiDAR and spiral scanning, as they can achieve sub-millidegree positioning accuracy with scanning frequencies up to 10 kHz in a compact, solid-state form factor without macroscopic moving parts. Their small moving mass enables bidirectional scanning with minimal mechanical wear and long service lifetimes. Compared to stepper motors and galvanometers, MEMS devices offer smaller physical size, higher angular precision, and the ability to implement complex two-dimensional scan trajectories.

For applications requiring high flexibility in beam shaping or dynamic control of light, SLMs and liquid crystal on silicon (LCoS) devices are commonly used [49], [50]. These systems manipulate the phase or amplitude of coherent light, typically from laser sources, enabling precise beam shaping and steering in applications where wavefront



Figure 2.18: Thorlabs GVS012 dual-axis MEMS mirror and controller system for high-speed optical beam steering [46].

control is critical. A representative device is the EXULUS-HD4, which provides a high-resolution 1920×1200 pixel grid for shaping a laser beam, where each pixel can change the beam phase with 256 levels of precision, and the entire pattern can be updated 60 times per second, enabling dynamic optical control in real-time applications, as shown in Fig. 2.19 [94]. The device is priced at approximately \$20,000 USD. While SLMs and LCoS systems can achieve phase modulation resolutions of $\pi/128$ to $\pi/256$ radians per pixel and angular beam steering steps on the order of 0.05-0.5 mrad in the far field, their update rates are generally slower than MEMS mirrors, ranging from a few Hz to 1 kHz. The angular pointing resolution for Gaussian beam steering in the far field is determined by the ratio of the optical wavelength to the clear aperture size [95]. For a wavelength of 1550 nm and a typical active aperture width of 10-20 mm, the smallest achievable beam deflection is on the order of 0.08-0.15 mrad, corresponding to sub-milliradian steering steps. Costs for these devices vary widely, from \$13k to \$20k USD [49], depending on resolution and modulation capabilities.

Digital Micromirror Devices (DMDs) offer a high-speed approach to beam steering using arrays of micro-scale mirrors that tilt in discrete angular steps, typically $\pm 12^{\circ}$,



Figure 2.19: Thorlabs EXULUS-HD4 phase-only spatial light modulator with 1920×1200 resolution, optimized for 1550 nm applications [94].

to redirect light. In beam steering applications, a pulsed or continuous laser source illuminates the DMD, and rapid switching of the mirror array patterns can create programmable diffraction gratings, enabling discrete steering angles with control over the direction and intensity of the output beam. For instance, the TI DLP5500 DMD can switch binary patterns at up to 5 kHz and grayscale patterns at 500 Hz when operated with the DLPC200 controller [51]. The micromirror array provides a tilt range of $\pm 12^{\circ}$, with far-field steering precision determined by the array size (1024×768 micromirrors at 10.8 μ m pitch), corresponding to a diffraction-limited angular step of approximately 0.15 mrad at 1550 nm. The DLPLCR55EVM evaluation module has a typical electrical power consumption of ~ 30 W and is priced at approximately \$700 USD. A representative image of the module is shown in Fig. 2.20. Low-cost DMD modules (\$100) support simple steering, while industrial-grade systems employing evaluation boards or complete optical engines can cost over \$10,000 USD [96].

Rotating optics with prisms or Risley prisms offer another option for beam steering. These systems are mechanically simple and can steer beams continuously or discretely by rotating a pair of wedge prisms. A representative example is shown in Fig. 2.21, where the TECHSPEC Risley Prism Mount from Edmund Optics (part #33-431) accommodates 25 mm diameter prisms with wedge angles up to 26°. This configuration

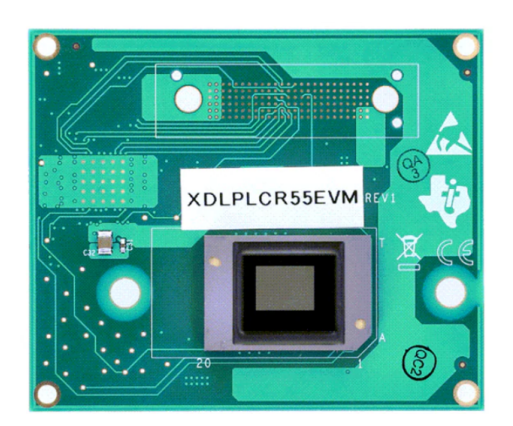




Figure 2.20: TI DLPLCR55EVM evaluation module featuring the DLP5500 DMD (0.55" diagonal chip with a resolution of 1024×768 micromirrors, each spaced $10.8 \,\mu\mathrm{m}$ apart and capable of tilting $\pm 12^{\circ}$), capable of up to 5kHz mirror switching for high-speed beam steering applications [51].

allows for angular beam deflection over a wide range, with a typical precision of tens to hundreds of microradians, depending on the motorization and alignment accuracy. However, mechanical constraints limit the dynamic response to around 20–30 Hz, making it slower than MEMS or DMD-based systems. The cost of such a setup is approximately \$468 USD [97], with complete custom systems ranging up to \$1,000 USD or more.



Figure 2.21: TECHSPEC Risley Prism Mount from Edmund Optics, enabling beam steering through independent rotation of two wedge prisms [97].

OPAs are solid-state beam steering devices that control the direction of emitted light

by precisely manipulating the phase of signals across an array of waveguides or nanoantenna elements. By electronically tuning the phase of each element, using thermo-optic, electro-optic or carrier injection mechanisms, OPAs steer the far-field beam through constructive and destructive interference, entirely without mechanical movement [52]. This enables high-speed beam steering without mechanical inertia, with switching times ranging from a few microseconds for thermo-optic tuning to tens of nanoseconds for electro-optic or carrier-based implementations [53], [98], [99]. Compared to traditional mechanical or MEMS-based beam steering systems, which are limited by inertia and millisecond-scale response times, OPAs offer significantly faster reconfiguration, higher reliability, and a more compact form factor. CMOS-compatible OPAs further enhance scalability and manufacturability by using mature, high-volume semiconductor processes [52]. The typical cost of a fabricated OPA chip can range from approximately \$100 in high-volume CMOS production to \$10,000+ for research-grade or customized systems, depending on complexity, packaging, and array size. In terms of angular precision, OPAs generally achieve sub-degree resolution, with reported beam steering accuracies on the order of $<0.1^{\circ}$ in recent demonstrations [53], [54]. For example, the 64×64 nanophotonic phased array by Sun et al. and the fully integrated LiDAR-on-chip system by Tan et al. demonstrate sub-degree angular resolution with beam steering speeds on the order of 1–10 µs using integrated thermal phase shifters [53], [98]. However, OPAs also face challenges, including limited steering range, reduced output power, and sidelobe artifacts, which must be addressed through phase calibration, thermal stabilization, or array design optimization [53], [99]. Recent developments such as multispectral photonic integration [100] and wavelength-diverse large-scale OPAs [54] are actively overcoming these limitations. As fabrication costs decline and performance improves, OPAs are becoming increasingly viable for a wide range of applications in LiDAR, OWC, and compact tracking systems, offering an attractive balance of speed, precision, and integration potential.

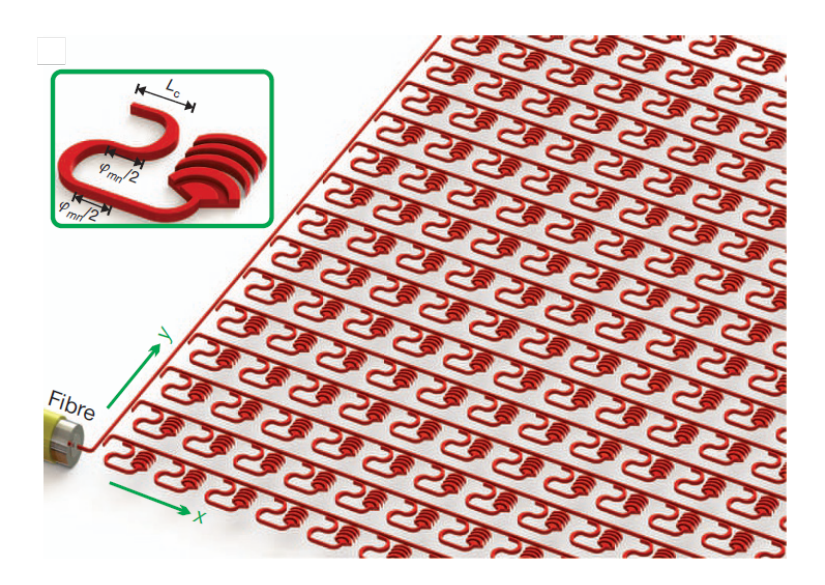


Figure 2.22: Schematic illustration of a 64×64 nanophotonic phased array system, as demonstrated by Sun et al. [53]. Light from an optical fiber is equally distributed to 4,096 nanoantennas via silicon waveguides. The inset shows a unit cell with a directional coupler of length L_c and optical delay lines that set the emission phase. This CMOS-compatible OPA enables high-speed beam steering without mechanical inertia.

A prominent example of a fabricated OPA is the 64×64 nanophotonic phased array system demonstrated by Sun et al. [53]. As illustrated in Fig. 2.22, this OPA consists of 4,096 nanoantennas arranged in a two-dimensional array, where light from a single optical fiber is split and delivered to each antenna through silicon waveguides. Each antenna element, or pixel, includes a directional coupler with length L_c that adjusts coupling efficiency, and two optical delay lines that modulate the output phase. This architecture enables precise beamforming through phase control, supporting angular resolution below 0.2° and beam reconfiguration in microseconds via thermal tuning. Fabricated using CMOS-compatible processes, the OPA demonstrates a clear path to scalable, low-cost integration for high-speed beam steering applications in LiDAR and free-space optics. A comparative summary of the beam steering hardware solutions is presented in Table 2.8. Note that the discrete scanning step time is defined as $t_{\rm steep} = 1/f_{\rm steering}$, where $f_{\rm steering}$ is the angular switching frequency of beam steering device.

Table 2.8: Comparison of Beam Steering Technologies

Technology	Cost (USD)	Speed	Precision	Remarks
Stepper Motors	\$50-\$5,000	Low (Hz)	$\sim 1^{\circ} \text{ (to } 0.1^{\circ}\text{)}$	Cheap, bulky, slow
Galvanometer	\$3,000-\$15,000	Moderate (kHz)	Sub-millidegree	Fast, limited FoV
MEMS Mirrors	\$20,000+	High (up to 10 kHz)	Sub-millidegree	Compact, precise, costly
SLMs / LCoS	\$13,000-\$20,000	Low (Hz to 1 kHz)	Sub-millidegree	Precise, slow, bulky
DMDs	\$100-\$10,000+	High (>10 kHz)	Discrete	Fast, binary resolution
Risley Prisms	\$1,000 (custom)	Low	Moderate	Simple, slow
OPAs	\$100-\$10,000+	Very High (MHz)	Sub-degree	Fast, solid-state, narrow FoV

2.10 Conclusion

This chapter provides an overview of the system model, Gaussian beam properties, and eye-safety constraints that limit transmit power and beam design. The architecture of the optical receiver was described in detail, including the characteristics of the APD and relevant noise sources. The geometric relationship between the pointed beam and received power was examined, along with the implications of signaling, modulation choices, and the impact of beam divergence on received SNR and data rate. Additionally, the chapter discussed uplink feedback mechanisms, presenting timing and delay considerations for enabling accurate user tracking and beam steering. Finally, different hardware solutions for optical beam steering were briefly reviewed.

These foundational topics establish the context and motivate the need for a beam steering approach to enable localization, tracking, and communication. The next chapter builds on this background by presenting the theory of the proposed DBS scheme, beginning with initial user localization using a multi-stage spiral search, followed by the integrated tracking and communication approach employing beam steering.

Chapter 3

Design of Dynamic Beam Steering Systems

3.1 Introduction

This chapter introduces the proposed dynamic beam steering (DBS) scheme, starting with an overview of the hardware solutions for beam steering, an initial beam-searching process in a multi-stage spiral method, and then introducing the DBS tracking algorithm. Unlike conventional cell grid architectures (e.g., [1], [2], [11]) that rely on static beams directed at predefined positions, the DBS scheme employs dynamic beams to serve users in a cell-free manner while simultaneously tracking their movements. The trade-offs between tracking precision and data rate for the DBS system are then analyzed, which is presented through simulations in Chapter 4, and the parameters are selected to achieve optimized performance. The proposed architecture is then compared with cellular-based design based on the work in [11], in terms of achievable rate, and efficiency in chapter 4. The system model considered for simulation is discussed in Chapter 2, and the DBS system architecture refers to Fig. 1.9.

3.2 Phase I: Initial Beam Searching Algorithm

In the proposed architecture for this work, a purely optical scheme is considered for localization, tracking, and communication, meaning both the transmitter and receiver are optical rather than using a hybrid RF/IR approach. To track the user movement, an initial estimation of the user is required. There can be different approaches to searching and finding the initial approximate location of the user within the room, which are discussed in Chapter 1. Among various beam-searching patterns, the Archimedean spiral search is particularly efficient for circular uncertainty regions [101]. While this represents a reasonable design choice, other search strategies also exist and could be investigated. It should be noted that the spiral cannot be formally proven to be optimal; however, its mechanical implementation is straightforward and practical. In this work, the spiral pattern is considered to begin searching at the center and progresses outward toward the edges at a constant velocity, ensuring continuous coverage without gaps or redundant overlap. This pattern is well-suited to cases where the prior uncertainty region is roughly circular, offering continuous coverage that avoids unnecessary overlap or missed regions [101]. It should be noted that although starting from center of the room is chosen here as a natural starting point, the search could alternatively be initialized from any region if prior information about the probable location of the user within the room is available.

The Archimedean spiral can be described mathematically in polar coordinates by the equation

$$r(\theta_s) = a + \beta \,\theta_s,\tag{3.1}$$

where a controls the initial radius of the spiral at $\theta = 0$ (the starting distance from the center), β determines the radial spacing between successive turns, and θ is the polar angle that increases as the spiral progresses outward from the center.

Spiral scans have been extensively analyzed in free-space optical (FSO) for space-based systems, where they are shown to minimize average acquisition time by matching the scan geometry to the uncertainty cone and maintaining uniform dwell times across the region [102]–[105]. In satellite optical links, spiral scanning has also proven effective for acquisition using the same narrow beam that is later used for tracking, removing the need for a separate wide-beam search system [102]. This work adapts the spiral search concept to the indoor OWC context, where such patterns have not been applied or studied to the best of the authors knowledge. It can be implemented by steering a narrow IR beam along a predefined spiral path to cover the room and localize the user.

Assuming the AP can adjust $\theta_{\rm FWHM}$, starting with a large beam width allows the room to be scanned more quickly, with corners covered efficiently and minimal excessive overlap compared to using a narrow beam. The AP stops scanning as soon as it receives feedback from the user, allowing it to initiate a narrower beam search centered on the spot position corresponding to the feedback. This approach refines the search, scanning the user probable location with greater precision. As illustrated in Fig. 3.1, the multistage spiral search process begins with a wide beam in stage 1, and progressively reduces the beam width with each subsequent spiral scan in stages 2 and 3, until a predefined minimum beam width is reached (stage 4 in Fig. 3.1). Once feedback is received in each stage, the AP refines its search using a narrower beam and continues the spiral scan within the probable region. This multi-stage strategy reduces localization delay compared to scanning with an ultra-narrow beam from the start. There is a trade-off between localization accuracy and delay, which is explored further in this chapter. In the following section, the theory and algorithm for the proposed localization approach are discussed.

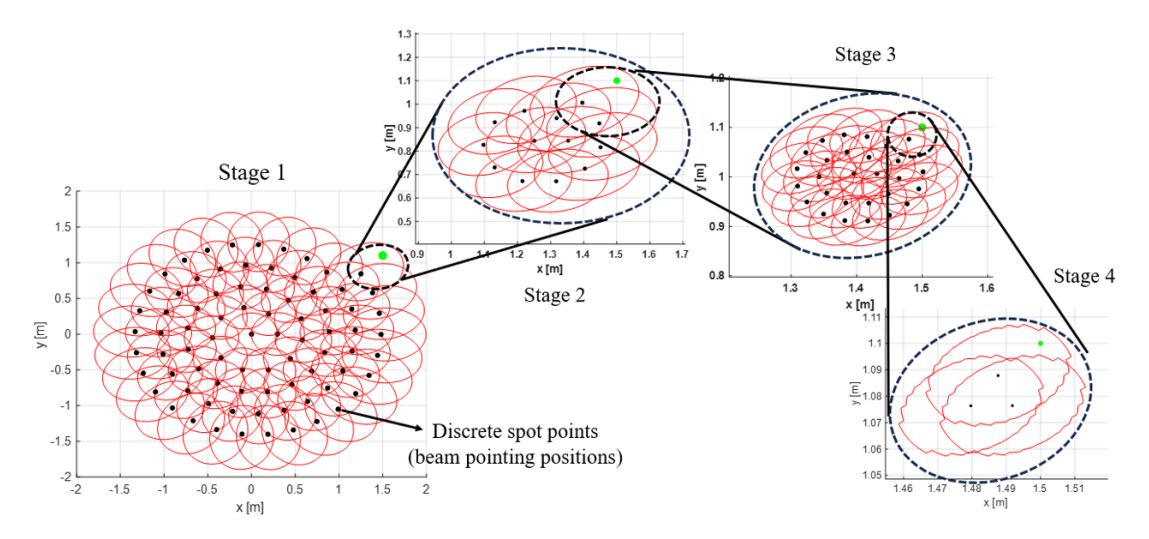


Figure 3.1: Multi-stage Archimedean spiral search pattern on XY

3.2.1 Archimedean Spiral Search

In this section, the Archimedean spiral search is first explained, as illustrated in stage 1 in Fig. 3.1, and in Fig. 3.2. Next, the relationship between the beam divergence angle, $\theta_{\rm FWHM}$, and the spiral parameters is derived, followed by a discussion on tuning the spiral parameter. Finally, the delay of a single spiral search and the localization error are analyzed, examining their relationship with the beam divergence angle through simulations.

According to Fig. 3.2, the spiral search is on XY plane at $z = z_{rx}$ since it is assumed that the user is positioned in this plane with a vertically upward orientation. The search starts from (0,0,1) [m], which is the center of the XY plane in the room, thus the parameter a in (3.1) is zero. In this design, the beam spot positions along the spiral path are defined as a finite set of discrete points. The beam steering device sequentially directs the beam toward these predefined positions. These predefined angular steps will be computed in the following to design the spiral pattern with respect to the θ_{FWHM} , as introduced in Chapter 2, ensuring there are no gaps between successive spiral rounds. This discretization also enables practical implementation with a finite number

of beam steering positions and allows for optimizing the search process. Moreover, at each discrete position, the AP sends a test signal and waits to receive an ACK from the user within the dwell time of each spot position (on the order of milliseconds to microseconds). If no ACK is received, it proceeds to the next position along the spiral.

Each beam spot position on the spiral corresponds to a polar angle $\theta_s^{(i)}$ at spot number (i). According to Fig. 3.2, each discrete spot position on spiral path on XY plane is $(r_s^{(i)}, \theta_s^{(i)})$, where

$$r_s^{(i)} = \beta \,\theta_s^{(i)} = \sqrt{\left(x_s^{(i)}\right)^2 + \left(y_s^{(i)}\right)^2},$$
 (3.2)

where β is a factor that controls the overlap between adjacent spots and also the gaps between each round of spiral. Moreover, each position on the spiral pattern in XYZcoordinates can be shown with a spherical coordinate system, $(r^{(i)}, \theta^{(i)}, \varphi^{(i)})$, which is equivalent to $(x_s^{(i)}, y_s^{(i)}, z_{rx})$, where

$$r^{(i)} = \sqrt{\left(x_s^{(i)}\right)^2 + \left(y_s^{(i)}\right)^2 + z_{rx}^2} = \sqrt{\left(r_s^{(i)}\right)^2 + z_{rx}^2}$$
(3.3)

$$\theta^{(i)} = \tan^{-1} \left(\frac{r_s^{(i)}}{h} \right) \tag{3.4}$$

$$\varphi^{(i)} = \tan^{-1} \left(\frac{y_s^{(i)}}{x_s^{(i)}} \right). \tag{3.5}$$

The spiral scanning angles, $\theta_s^{(i)}$, are known to AP, and once AP receives feedback, it stops and calculates $r_s^{(i)}$ to obtain an initial estimate of the heading of the user, under the assumption that the user lies on the known plane. Using a vector of discrete angles for spiral pattern, $\theta_s^{(i)}$, with equal angular difference (i.e., $\Delta\theta_s = \theta_s^{(i+1)} - \theta_s^{(i)}$, is independent of i), results in smaller distances between spot positions for lower (i) values, which gradually increase as i grows (see Fig. 3.3). Thus, the density of spots around the origin is much greater than at distant positions. This causes gaps between

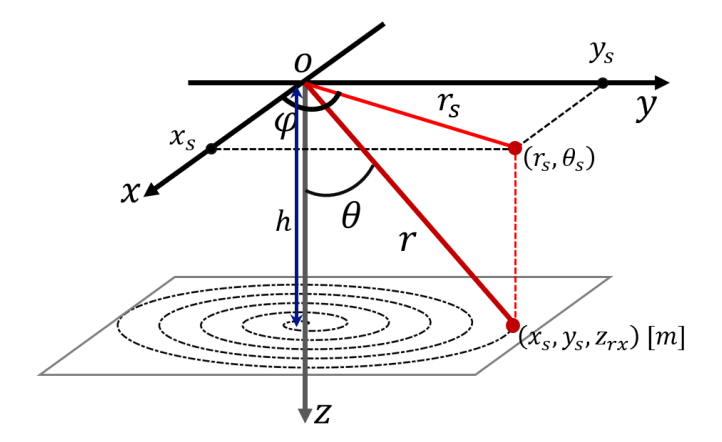


Figure 3.2: Archimedean spiral search pattern on XY plane at $z_{rx} = 1 m$ above the floor

spots farther from the center of the spiral and more delay in scanning regions close to the center since the AP must scan more spots in a small area around $(0,0,1\,m)$ before reaching the corners. Since $r_s^{(i)}$ varies along the spiral, the separation between successive beam pointing positions can be defined either by maintaining a constant angular increment (see Fig. 3.3) or by maintaining a constant separation between adjacent pointing positions, denoted $\omega(h)$ in Fig. 3.5. In the constant-angular-increment approach, the azimuthal angle is increased by a fixed step size $\Delta\theta_s$ at each point on the spiral. This method is straightforward to implement, particularly with servo-based beam steering as described in Section 2.9, but the lateral spacing between pointing positions increases with radius, reducing coverage density toward the outer region. In the constant-separation approach, $\omega(h)$ is kept the same for all positions, ensuring uniform angular coverage along the spiral. This requires $\Delta\theta_s^{(i)} = \theta_s^{(i+1)} - \theta_s^{(i)}$ to vary with radius, larger for positions near the center and smaller for those farther out, imposing higher pointing resolution and more precise control compared to the constant-angular-increment method.

Since it is assumed that the user is located at $z=1\,\mathrm{m}$ on XY plane, the minimum distance between AP and the XY plane is $h=2\,\mathrm{m}$ which corresponds to the minimum beam radius $\omega(h)$ as shown in Fig. 3.4. In defining the spiral scan, $\omega(h)$ is used as the

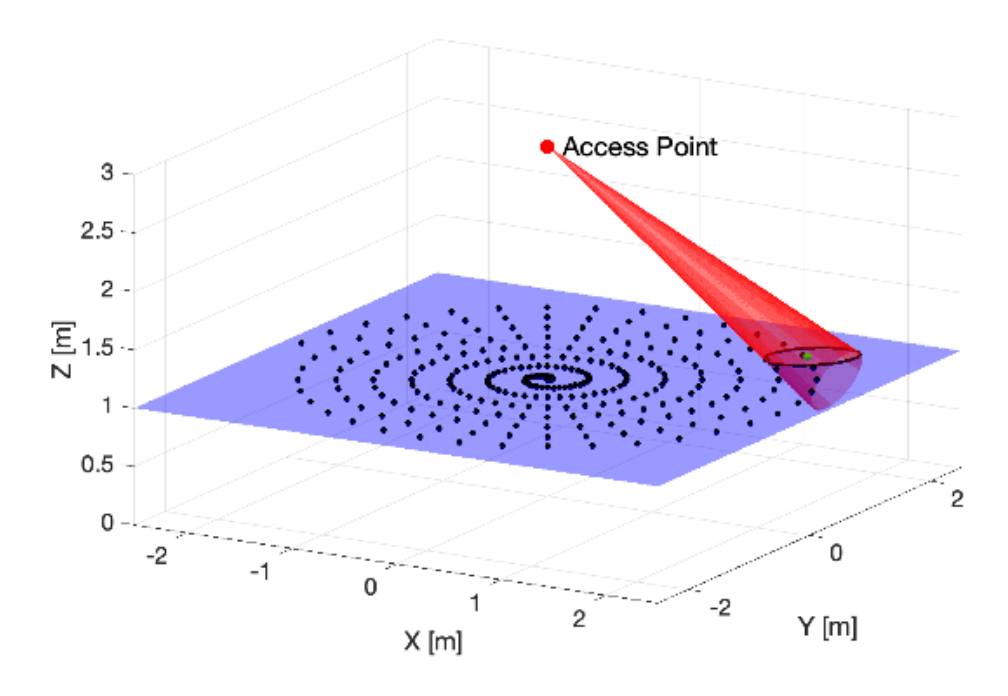


Figure 3.3: Demonstration of pointed IR beam and XY user plane at z = 1m and sample points on spiral with equal angular difference

reference separation between adjacent beam pointing positions, calculated from (2.40) for this minimum range. Although the beam footprint may change slightly with steering angle θ_s due to the projection effect, this fixed $\omega(h)$ value serves as a design reference to ensure adequate coverage while simplifying the scanning pattern generation. The constant spot step length can be controlled by a factor of $(1 - \alpha_s)$ where $0 < \alpha_s < 1$. Also, α_s controls the tightness of the spiral scanning pattern, determining how closely the spiral loops are spaced. Consequently, the discrete spot centers on the spiral path in polar coordinates can be formulated as

$$r_s^{(i)} = \beta \, \theta_s^{(i)} = (1 - \alpha_s) \, \omega(h) \, \theta_s^{(i)}.$$
 (3.6)

To determine the optimal incremental change in $\Delta \theta_s^{(i)}$, an equation based on the geometry of beam spot positions according to Fig. 3.4 is derived as

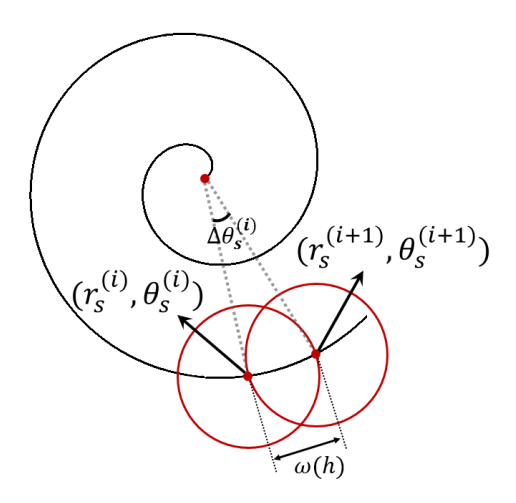


Figure 3.4: Discrete spot positions on spiral pattern with fixed spot step length

$$\omega^{2}(h) = (r_{s}^{(i)})^{2} + (r_{s}^{(i+1)})^{2} - 2 r_{s}^{(i)} r_{s}^{(i+1)} \cos (\theta_{s}^{(i+1)} - \theta_{s}^{(i)})$$

$$= ((1 - \alpha_{s}) \omega(h) \theta_{s}^{(i)})^{2} + ((1 - \alpha_{s}) \omega(h) \theta_{s}^{(i+1)})^{2}$$

$$- 2 ((1 - \alpha_{s}) \omega(h) \theta_{s}^{(i)}) ((1 - \alpha_{s}) \omega(h) \theta_{s}^{(i+1)})$$

$$\times \cos (\theta_{s}^{(i+1)} - \theta_{s}^{(i)}).$$
(3.7)

The equation (3.7) can be rewritten and simplified as

$$\omega^{2}(h) = (1 - \alpha_{s})^{2} \omega(h)^{2} \times \left(\left(\theta_{s}^{(i)} \right)^{2} + \left(\theta_{s}^{(i)} + \Delta \theta_{s}^{(i)} \right)^{2} - 2\theta_{s}^{(i)} \left(\theta_{s}^{(i)} + \Delta \theta_{s}^{(i)} \right) \cos(\Delta \theta_{s}^{(i)}) \right)$$
(3.8)

$$\Rightarrow 2\,\theta_s^{(i)}\,\left(1-\cos(\Delta\theta_s^{(i)})\right)\left(\theta_s^{(i)}+\Delta\theta_s^{(i)}\right)+\left(\Delta\theta_s^{(i)}\right)^2-\frac{1}{(1-\alpha_s)^2}=0. \tag{3.9}$$

The optimal $\Delta \theta_s^{(i)}$ given the $\theta_s^{(i)}$ can be obtained by numerically solving the equation (3.9), and $\theta_s^{(i+1)}$ can be obtained accordingly. This process continues until AP receives feedback from the user and stops the search. As an example for $\theta_{\text{FWHM}} = 8^{\circ}$, the optimized angles are demonstrated in Fig. 3.5. Note that $\theta_s^{(1)} = 0$, if the spiral search

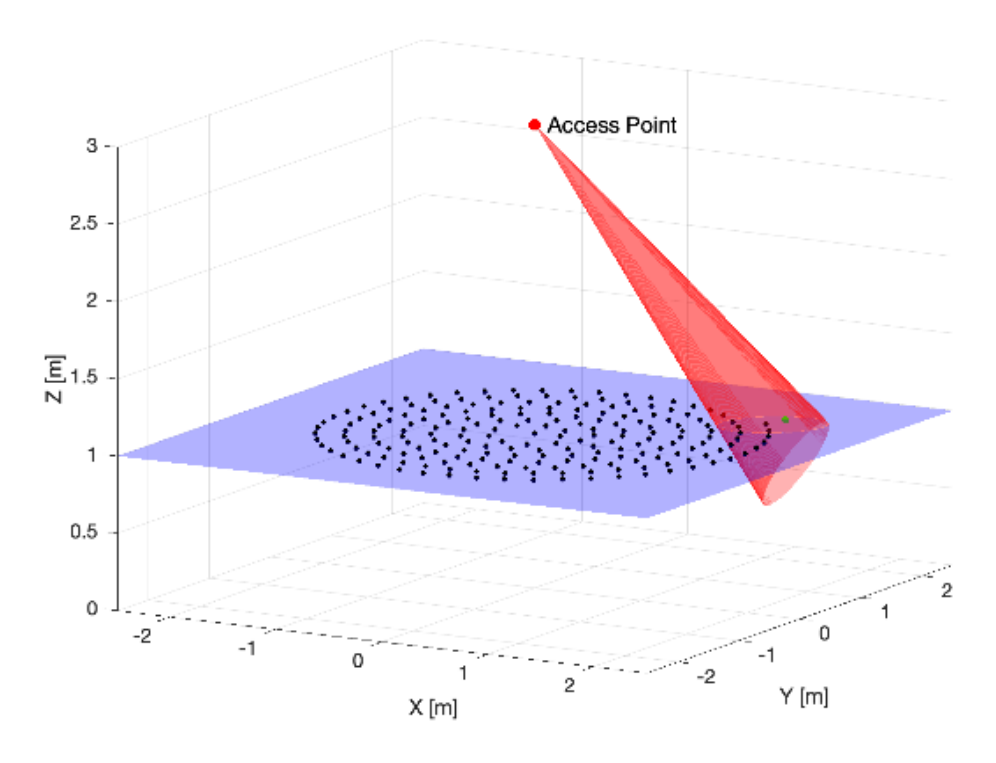


Figure 3.5: Optimized points on the spiral pattern (compared to Fig. 3.3) on XY user plane at $z=1\,\mathrm{m}$ with the pointed beam

starts from the center of the room. Considering the actual beam spot size, the spot shape near the origin is approximately circular. However, at greater distances from the origin, the spot shape on the XY plane transforms into a rotated ellipse, as illustrated in Fig. 3.5, and beam spot size increases. This transformation occurs because the 3D beam shape resembles a cone, with the cone axis forming an angle θ with the Z-axis (see Fig. 3.5). To determine the precise spot shape on the XY plane, where the user is positioned, a horizontal plane at z = 1 m intersects the rotated cone, resulting in an elliptical overlap that represents the beam spot shape. The equations for the actual beam spot shape are derived in the Appendix C.

Fig. 3.6 illustrates the spiral search pattern for different values of α_s . Lower values of α_s (e.g., $\alpha_s = 0.4$) produce a wider, more open spiral, increasing the radial separation between consecutive loops. This creates coverage gaps that can lead to missed

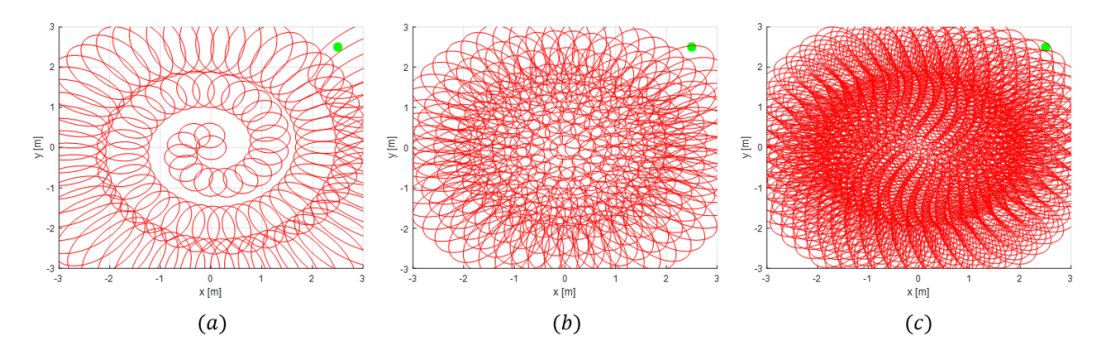


Figure 3.6: Spiral search with $\theta_{\rm FWHM}=10^{\circ}$ for different α_s values; (a) $\alpha_s=0.4$; (b) $\alpha_s=0.841$; (c) $\alpha_s=0.95$. Scanning spots may not cover the service area for small values of α_s

user detection, as seen in Fig. 3.6a. Conversely, higher values of α_s (e.g., $\alpha_s = 0.95$) produce a tighter and denser spiral, reducing the risk of coverage gaps but increasing the total number of beam positions and, consequently, the localization time (Fig. 3.6c). The total number of steps required to complete the spiral depends on the search area (room dimension), the beam radius $\omega(h)$, and α_s . Higher α_s values (close to 1) yield proportionally more steps and greater overlap between successive loops.

To find a proper selection for α_s , the condition of no gaps between rounds of the spiral must be satisfied. In this context, a round refers to one complete 2π rotation of the spiral in the angular coordinate θ_s . The radial separation between two consecutive rounds (i.e., between round k with $\theta_s = 2\pi k$ and round (k+1) with $\theta_s = 2\pi (k+1)$, k = 1, 2, 3, ...) is defined as

$$\Delta r_{\text{rounds}} = r_s^{(k+1)} - r_s^{(k)},$$
 (3.10)

where

$$r_s^{(k)} = (1 - \alpha_s) \,\omega(h) \cdot (2\pi(k)),$$

$$r_s^{(k+1)} = (1 - \alpha_s) \,\omega(h) \cdot (2\pi(k+1)).$$
(3.11)

Thus, substituting (3.11) into (3.10) yields

$$\Delta r_{\text{rounds}} = r_s^{(k+1)} - r_s^{(k)} = (1 - \alpha_s) \ \omega(h) \cdot 2\pi k.$$
 (3.12)

To have no gap between rounds, the radial separation between adjacent rounds Δr_s must be less than $\omega(h)$. Therefore,

$$(1 - \alpha_s) \ \omega(h) \cdot 2\pi k < \omega(h) \tag{3.13}$$

$$\Rightarrow \alpha_s > 1 - \frac{1}{2\pi k}.\tag{3.14}$$

By setting k = 1, the minimum value for α_s can be found as

$$\alpha_s > 1 - \frac{1}{2\pi} = 0.8408. \tag{3.15}$$

Consequently, to ensure no gaps between spiral rounds and sufficient overlap without excessive density, $\alpha_s = 0.841$ is selected for all of the simulations and for all $\theta_{\rm FWHM}$ values. The result of selection is also demonstrated in Fig. 3.6.

It is observed from Fig. 3.7 that there is an offset between the actual center of the beam spot footprint on the XY plane (red points within each ellipse) and the nominal beam pointing positions $(x_s^{(i)}, y_s^{(i)})$ in the spiral pattern (black points). This offset occurs because the projected footprint of the beam on the XY plane is an ellipse whose center is generally displaced from the geometric intersection point of the beam axis with the plane (see Fig. 3.5). The displacement is negligible near the center of the room, where the beam axis is nearly perpendicular to the XY plane, but becomes more pronounced toward the corners, where the beam strikes the plane at a larger incidence angle. In such cases, the elliptical footprint is elongated and its centroid shifts laterally relative to the beam axis intersection point. This shift increases the localization error, particularly when the user lies near the edge of the beam footprint (see Fig. 3.7). A larger θ_{FWHM}

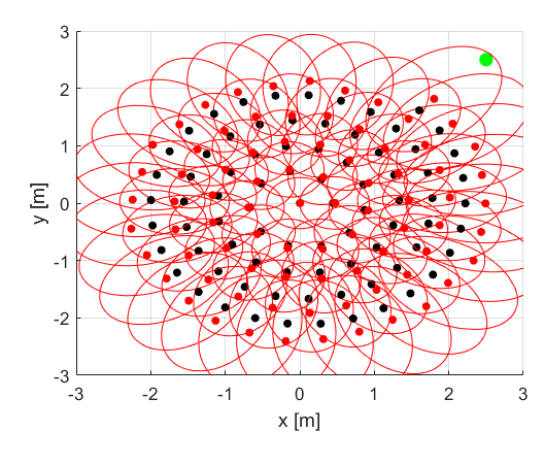


Figure 3.7: Discrete spiral search pattern (black points) with beam spot footprints on the XY plane (ellipses). The red points indicate the centers of the ellipses (beam spots), the green point marks the user location, and $\theta_{\rm FWHM}=15^{\circ}$.

increases both the footprint size and the angular spread, thereby amplifying the offset for positions farther from the room center.

It should be noted that at distant positions within the room, the beam spot becomes larger and the received power decreases, particularly at the edges of the spot. Since the beam has a Gaussian profile, the intensity distribution is lower at its edges. A detection threshold is therefore derived in Section 3.2.4 for a given $\theta_{\rm FWHM}$, taking into account the room dimensions. To make the spiral search more robust and ensure that the user can detect the received power even at the corners of the room where the beam spot is wide, one can increase α_s to enhance the overlap between successive spiral rounds. For larger rooms (e.g., $10 \, {\rm m} \times 10 \, {\rm m} \times 3 \, {\rm m}$), if the user is positioned in a corner, the communication link can become very weak due to low SNR, or the AP may fail to detect uplink feedback because of excessive attenuation. In such cases, for very large office spaces, reliable communication can be achieved by deploying multiple APs, each covering, for example, a $(5 \, {\rm m} \times 5 \, {\rm m})$ region, thereby effectively clustering the room.

3.2.2 Design Considerations for Spiral Localization

In the spiral search method (see stage 1 in Fig. 3.1), the step angles, $\theta_s^{(i)}$, are first calculated for one time based on the input θ_{FWHM} before AP starts scanning. When a user sends a test signal to the AP for the first time to indicate its presence in the room, the AP initiates scanning to localize the device. If AP receives no feedback after searching the entire room due to the blockage of the LoS path, it will increase α_s to scan the room with more resolution, which leads to more lateral spot overlap. Note that if the receiver is located at $z_{rx} < 1 \,\mathrm{m}$, the vertical distance between the AP and the XY plane where the user is located increases. Consequently, the beam radius at the XY plane also increases. The user can still be covered with the same selection of $(1-\alpha_s)\,\omega(h)$ as the coefficient for $\theta_s^{(i)}$. The difference, however, is that the beam size becomes larger, resulting in increased overlap between adjacent spots. In contrast, if the user is located at the XY plane at $z_{rx} > 1 \,\mathrm{m}$, the beam radius decreases, potentially causing gaps between the inner rounds of the spiral. In this case, the AP may miss the user position while scanning the room. To avoid this issue, if the AP reaches the corners of the room and receives no feedback, despite knowing that the user is in the room due to the uplink test signal received, it can restart scanning from the center of the room with higher precision (i.e., larger α_s). When feedback is eventually received, the user height remains unknown, but the angles (θ, φ) determines the direction towards the approximate location of the user. The AP can then point the beam toward this direction to cover the user position and track it.

The spiral search begins with larger angular steps $\Delta\theta_s^{(i)}$ and concludes with the minimum step size, $\Delta\theta_{s,\text{min}}$, at the room corner (2.5 m, 2.5 m, 1 m) for a given θ_{FWHM} . To assess the steering resolution required to achieve $\Delta\theta_{s,\text{min}}$ for a given θ_{FWHM} , Fig. 3.8 presents the values of $\Delta\theta_{s,\text{min}}^{\circ}$ for various $\theta_{\text{FWHM}}^{\circ}$ at the most distant location in the room. It can be observed from the figure that the $\Delta\theta_{s,\text{min}}$ increases as θ_{FWHM} grows. The $\Delta\theta_{s,\text{min}}$ at $\theta_{\text{FWHM}} = 0.047^{\circ}$, 0.4° , 1° , 4° are 0.02° , 0.19° , 0.49° , 2.11° , respectively.

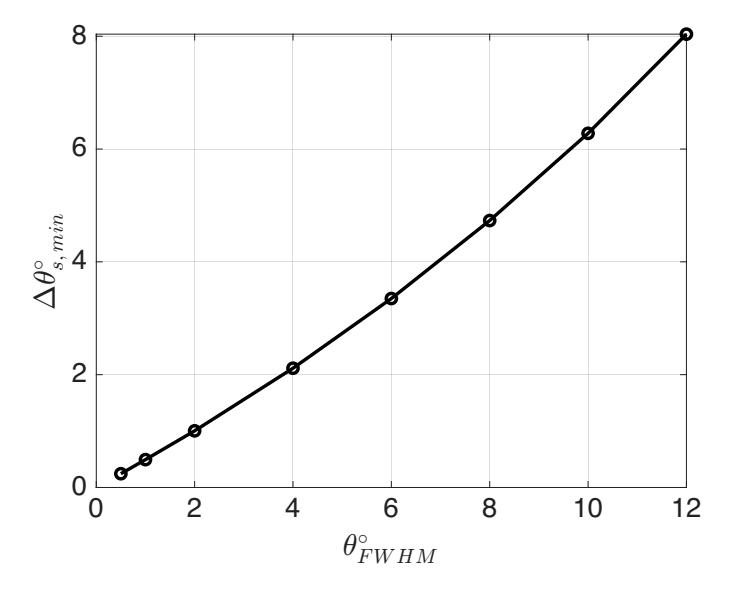


Figure 3.8: Minimum angular step size, $\Delta\theta_{s, \min}^{\circ}$, for different θ_{FWHM} values at the farthest location (2.5 m, 2.5 m, 1 m)

Thus, achieving higher-precision localization at the centimeter level requires more accurate dynamic beam width control and a higher-precision beam steering device capable of providing the necessary $\Delta\theta_{s,\,\mathrm{min}}$.

The total delay of scanning until localizing the user is $t_{tot} = N_{\text{spot}} t_{\text{spiral}}$, where N_{spot} is the total number of spot positions until AP receives feedback. Furthermore, t_{spiral} , is the spot step time for the discrete spiral search and can be selected from

$$t_{\text{spiral}} = t_r + 2t_{\delta},\tag{3.16}$$

where t_r is receiver response time and $2t_{\delta}$ is twice the optical signal propagation time (according to [106], $t_{\delta} = 3 \, ns$). Note that t_r mainly affects the spot dwell time. Also, depending on the beam steering device speed for transitioning from one spot position to another, $t_{\rm spiral}$ can be determined (in the order of few μs to ms), but it must be greater than the receiver response time to allow the receiver to send the feedback once it receives the signal for localization. Smaller $t_{\rm spiral}$, and larger $\theta_{\rm FWHM}$ results in less localization

delay. However, with a larger beam width, localization accuracy decreases since the user is detected within a larger spot area, and the maximum distance between the spot center and the user location can be in the range of the spot radius. For distant positions from the center of the room, the spot size increases, which results in larger localization errors. The spiral search must provide an initial location estimation for the dynamic beam tracking algorithm in the next phase. With a smaller selection of beam width for the DBS scheme, the spiral search must be more accurate at the cost of increased delay. Therefore, there is a trade-off between initial localization accuracy and delay of localization. The maximum delay corresponds to the most distant position within the room and can be calculated for a given $\theta_{\rm FWHM}$ as

$$t_{\rm spiral, \ max} = \max \left(N_{\rm spot}(\theta_{\rm FWHM}) \right) \times t_{\rm spiral},$$
 (3.17)

where $\max(N_{\text{spot}}(\theta_{\text{FWHM}}))$ is the maximum spot number within the room that is required to locate the most distant user (i.e., (2.5m, 2.5m, 1m)) with a spiral pattern with fixed θ_{FWHM} , and α_s . As shown in Fig. 3.9, the dual-axis plot provides a comparison of localization error and maximum spot number for localization (i.e., $\max(N)$) with respect to θ_{FWHM} .

For $\theta_{\rm FWHM}=0.5^{\circ}$, maximum spot numbers until reaching the user is 173508 spots with roughly 5.36 cm localization error. Moreover, by choosing $\theta_{\rm FWHM}=10^{\circ}$, the user is localized with 260 spots, and the localization error is 83.54 cm. $\theta_{\rm FWHM}$ higher than 10° can also be considered, which can lower the required number of spots for detection at the cost of increased localization error. As an example, choosing $\theta_{\rm FWHM}=12^{\circ}$ leads to the localization error of $100\,\rm cm$, and 158 required spots.

Note that power consumption and hardware implementation constraints must be carefully considered when selecting larger values of θ_{FWHM} . While the dominant power consumption often comes from the mechanisms required to adjust beam width and steer

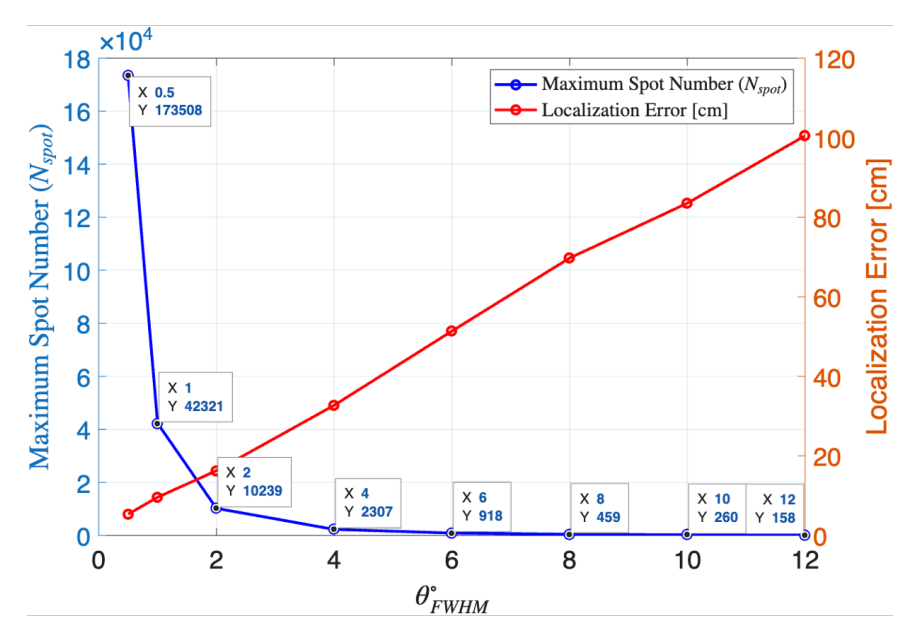


Figure 3.9: Maximum spot number, $N_{\rm spot}$, and maximum localization error for different $\theta_{\rm FWHM}$ values in the spiral search of stage 1 (see Fig. 3.1).

the beam, increasing the beam divergence angle also necessitates higher transmit eye-safe power to ensure sufficient intensity at the edge of the beam spot for user detection and feedback. For example, achieving $\theta_{\rm FWHM}=10^{\circ}$ may require eye-safe transmit power on the order of 350 mW, though this level is needed only for a few milliseconds during the search phase. As a result, there is a clear trade-off between localization delay, accuracy, transmit power requirements, and hardware complexity.

3.2.3 Localization Accuracy

The localization error is defined as the distance between the beam pointing position (x_s, y_s) , and the actual location of the user, (x_{rx}, y_{rx}) , on XY plane, which can be expressed as

$$D = \sqrt{(x_s - x_{rx})^2 + (y_s - y_{rx})^2}.$$
 (3.18)

The required initial localization accuracy is defined as ϵ . In order to localize the user with an accuracy of ϵ , it is required that $D < \epsilon$. The maximum localization error, D_{max} ,

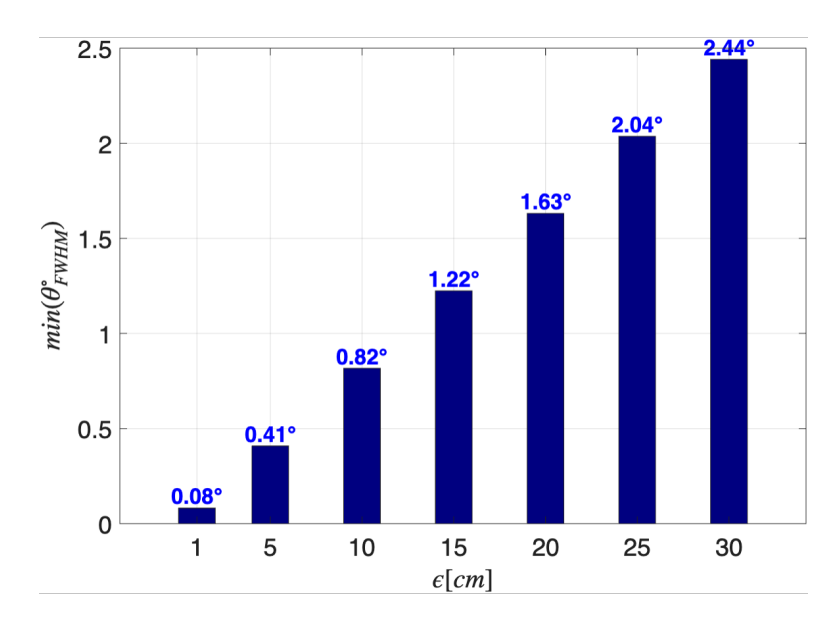


Figure 3.10: $\theta_{\mathrm{FWHM,min}}$ required to achieve $D_{\mathrm{max}} < \epsilon$

corresponds to the largest beam spot footprint in the room, corresponding to the user being located at the edge of the beam spot in the farthest position from the center of the room. If $D_{\text{max}} \leq \epsilon$, then it guarantees that the actual localization error, D from (3.18), will be less than ϵ throughout the entire room for all spot positions at the given θ_{FWHM} . In Appendix C, the mathematical expression for the elliptical beam spot shape is derived, from which D_{max} is obtained (see (C.27)). The required θ_{FWHM} to achieve the desired localization accuracy ϵ is then derived in (C.29). Fig. 3.10 illustrates the minimum θ_{FWHM} given by (C.30) in Appendix C, which is required to ensure that the maximum localization error D_{max} remains below the specified localization accuracy ϵ .

3.2.4 Feedback Threshold Calculation

In this subsection, we establish the condition for feedback transmission from the receiver to the AP. When the beam spot lies within the receiver FoV, the receiver measures the incident optical power P_r and compares it against a threshold. Rather than employing a separate light source or header sequence, the threshold is modeled as a tunable fraction

of the transmit power, i.e., the receiver sends feedback if

$$P_r > \rho_{\rm th} P_t, \tag{3.19}$$

where P_t is the eye-safe transmit power (function of θ_{FWHM} , and ρ_{th} is a coefficient determined by system geometry and receiver sensitivity. This formulation captures the effect of receiver sensitivity and link geometry on feedback triggering. In the following, after deriving the threshold received power, the corresponding detectable SNR is also obtained directly from this condition. This provides a clear link between the minimum received optical power required for detection and the achievable SNR at the receiver. In practice, detection is typically carried out either by monitoring whether the received optical power exceeds a given sensitivity threshold, or by evaluating the SNR to ensure it meets a target level associated with reliable demodulation and decoding. More advanced and robust schemes may employ header-based detection loops or pilot-assisted sequences to further enhance synchronization and reliability, but such methods are beyond the scope of this work and may be considered in future studies.

The coefficient $\rho_{\rm th}$ is defined to be

$$\rho_{\rm th} = \frac{P_{\rm r, ref}}{P_t},\tag{3.20}$$

where $P_{\rm r, ref}$ is the tunable reference power received in the room that corresponds to the corner position of the room. The formulation of $P_{\rm r, ref}$ is given in the following. To enable tunable thresholding and evaluate the impact of receiver sensitivity on detection, a parameter δd_{rx} is introduced to represent the receiver edge offset position, as illustrated in Fig. 3.11. Therefore, the user is assumed to be located at

$$C = (2.5 - \delta d_{rx}, 2.5 - \delta d_{rx}, 1) [m]. \tag{3.21}$$

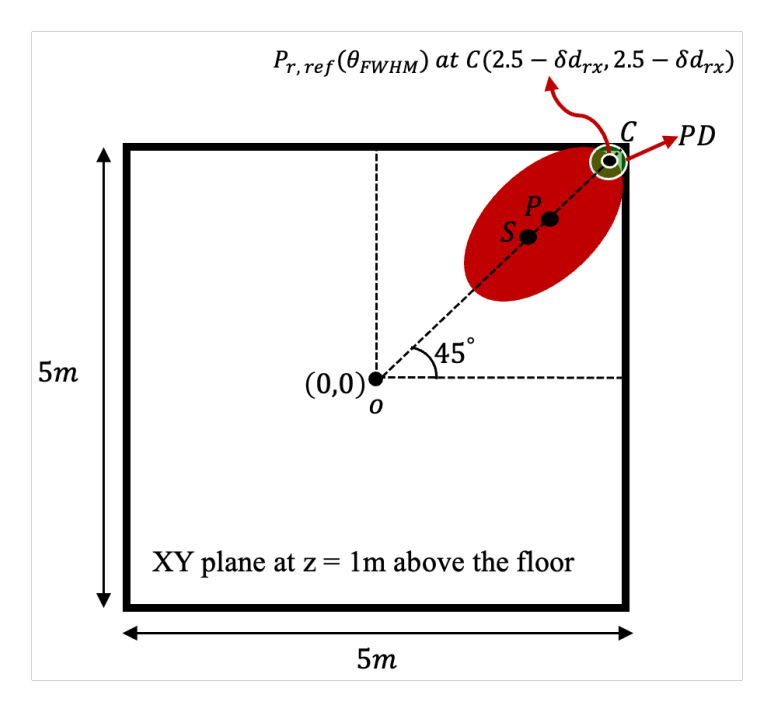


Figure 3.11: Beam spot geometry at the farthest position of PD, representing the minimum detectable received power for feedback as a threshold.

According to Fig. 3.11, the user position is shown with point C and the received power at this point is $P_{\rm r,ref}$. The maximum incident angle is defined at the farthest position where

$$\psi_{max} = \cos^{-1} \left(\frac{n_{Rx} \cdot (-\mathbf{d}_{Rx,\text{max}})}{\|\mathbf{d}_{Rx,\text{max}}\|} \right). \tag{3.22}$$

For $\psi < \Psi_c$, where Ψ_c denotes the receiver FoV, the relation in (3.22) yields a boundary condition for $\delta d_{\rm rx}$ as

$$d_{Rx,\max} = \vec{Rx} - \vec{Tx} = (2.5 - \delta d_{rx}, 2.5 - \delta d_{rx}, -2),$$

$$\Rightarrow \psi_{\max} = \cos^{-1} \left(\frac{2}{\sqrt{2 \times (2.5 - \delta d_{rx})^2 + 4}} \right) < \Psi_c,$$

$$0 < \psi_{\max} < \frac{\pi}{2} \left(\frac{2}{\sqrt{2 \times (2.5 - \delta d_{rx})^2 + 4}} \right) > \cos(\Psi_c),$$
(3.23)

$$\Rightarrow 2.5 - \sqrt{\frac{2}{\cos^2(\Psi_c) - 2}} < \delta d_{rx} < 2.5 [m]. \tag{3.24}$$

By substituting $\Psi_c = 60^{\circ}$ from Table 2.6 in (3.24), it follows that $\delta d_{rx} > 0.05 \,\mathrm{m}$. To calculate the $P_{\rm r, ref}$, the user must be at the edge of the beam spot (with pointing position $S = (x_s, y_s, 1) \, [m]$) as indicated in Fig. 3.11. In this figure, it is assumed that the user is located at point C on the elliptical beam spot. The distance between the user position and the center of the beam spot, $P = (C_x, C_y)$, is b, where b can be calculated from (C.26) in Appendix C. The objective is to find the pointing position vector S as a function of δd_{rx} . The points C, P, S, are considered according to Fig. 3.11 to be on the same line that passes through the origin O. Therefore, $x_s = y_s$, and $C_x = C_y$. Hence,

$$\sqrt{(x_c - C_x)^2 + (y_c - C_y)^2} = \frac{h \sin(\alpha_b)}{\cos(2\theta) + \cos(\alpha_b)}$$
 (3.25)

where $(x_c, y_c) = (2.5 - \delta_{rx}, 2.5 - \delta_{rx})$, and (C_x, C_y) can be obtained according to Appendix C from (C.22) and (C.5), while α_b is derived from (C.7). Consequently, x_s , y_s , and the relative position vector $\mathbf{d}_{Rx} = \vec{Rx} - \vec{Tx}$ are computed. Using these results, $\omega(\|\mathbf{d}_{Rx}\|)$ from (2.2) and $P_{r,ref}$ from (2.42) are determined. The feedback condition ρ_{th} that depends on θ_{FWHM} and δd_{rx} , is then can be computed from (3.20). Due to symmetry, all room corners yield identical results. Note that δd_{rx} represents the FoV margin offset and determines the sensitivity of the feedback threshold. A larger δd_{rx} results in a more restrictive threshold (i.e., a higher value of ρ_{th}).

To evaluate the threshold for a detectable SNR, the relation between the SNR and $\rho_{\rm th}P_{\rm r,ref}$ must be derived. The receiver can detect the test signal if the resulting SNR exceeds the minimum detectable SNR. Recalling from (2.48), and SNR definition in IM/DD systems from [13], since the test signal is an unmodulated waveform, the received SNR can be expressed as

$$SNR = \frac{\left(R_{PD} P_r\right)^2}{\sigma_n^2},\tag{3.26}$$

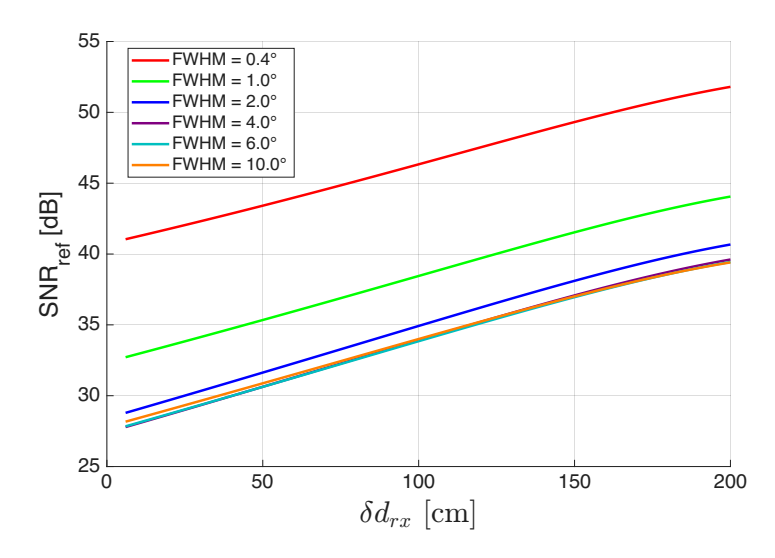


Figure 3.12: Variation of SNR_{ref} versus δd_{rx} for different $\theta_{\rm FWHM}$ values

where σ_n can be computed from (2.39). Using (3.19), the minimum detectable SNR can be derived as

$$P_r > \rho_{\text{th}} P_t$$

$$\Rightarrow P_r > \frac{P_{r,\text{ref}}}{P_t} P_t$$

$$\Rightarrow \frac{\left(R_{\text{PD}} P_r\right)^2}{\sigma_n^2} > \frac{\left(R_{\text{PD}} P_{r,\text{ref}}\right)^2}{\sigma_n^2}$$

$$\Rightarrow \text{SNR} > \text{SNR}_{\text{ref}}.$$
(3.27)

The impact of δd_{rx} on SNR_{ref} for different $\theta_{\rm FWHM}$ values is illustrated in Fig. 3.12, based on the simulation parameters summarized in Table 2.6. As observed, even for $\theta_{\rm FWHM} = 10^{\circ}$ at the corner of the room, the minimum received SNR at $\delta d_{rx} = 5 \, {\rm cm}$ is on the order of 28 dB. This SNR level corresponds to the case of operating at the maximum eye-safe transmit power of $P_t = 350 \, {\rm mW}$ (computed from (2.29)). Therefore, a lower transmit power can be used while still ensuring that the minimum received SNR remains above the detectable threshold.

3.2.5 Multi-Stage Spiral Search

To improve both accuracy and delay in spiral search, the spiral search can be implemented in multiple stages (see Fig. 3.1). The search begins with a large beam radius, allowing the room to be scanned with fewer spots until feedback is received from the user. The beam is then narrowed and pointed to the (θ, φ) corresponding to the feedback, and a new spiral search is initiated from this updated center with higher resolution (i.e., smaller $\theta_{\rm FWHM}$). This procedure is repeated, progressively reducing the beam radius and search region in each stage, until the user location is determined with the desired precision. In this multi-stage spiral search, $i=1,2,\ldots,M$ denotes the search stage, and the beamwidth $\theta_{\rm FWHM}$ at each stage is selected to minimize the total number of spots $N_{\rm tot}$ required to meet a target localization accuracy ϵ . The localization delay is minimized when $N_{\rm tot}$ is smallest, given the constraint $D_{\rm max} \leq \epsilon$ by the final stage. Since the first-stage delay is greatest when the user is at the farthest point from the transmitter, the analysis assumes the user is located at $(2.5\,\mathrm{m},\,2.5\,\mathrm{m},\,1\,\mathrm{m})$ in this setup.

The localization accuracy ϵ is determined based on the required user position estimation accuracy for DBS tracking. For example, if DBS tracking employs a specific beamwidth $\theta_{\text{FWHM},\text{DBS}}$ that produces a minimum beam radius $\omega(h)$ at the smallest AP-user separation in the XY plane, the initial user location must be estimated with an accuracy of at least $\omega(h)$. This requirement imposes $\epsilon \leq \omega(h)$, from which the minimum beamwidth $\theta_{\text{FWHM},\text{min}}$ can be calculated using (C.29), ensuring $D_{\text{max}} \leq \epsilon$. Once $\theta_{\text{FWHM},\text{min}}$ is obtained, and for a given number of search stages M, the optimal beamwidths $\theta_{\text{FWHM}}^{(i)}$ for each stage i must be computed to minimize the total spot count N_{tot} while satisfying the final-stage accuracy constraint. The localization error at stage i is defined as

$$D^{(i)} = \sqrt{\left(x_{sf}^{(i)} - x_{rx}\right)^2 + \left(y_{sf}^{(i)} - y_{rx}\right)^2},$$
(3.28)

where $\left(x_{sf}^{(i)}, y_{sf}^{(i)}\right)$ is the beam spot position when feedback is received by the AP during

the spiral search. Although $D^{(i)}$ is not known to the AP in practice, it is used within the optimization framework to evaluate performance and determine the optimal sequence $\{\theta_{\text{FWHM}}^{(i)}\}_{i=1}^{M}$.

A smaller θ_{FWHM} leads to better localization accuracy but requires a higher number of spot positions. The optimization problem can be formulated as follows

$$\min_{\theta_{\text{FWHM}}^{(i)}} \sum_{i=1}^{M} N_i \left(\theta_{\text{FWHM}}^{(i)}, x_{sf}^{(i-1)}, y_{sf}^{(i-1)}, x_{rx}, y_{rx} \right)$$
(3.29a)

s.t.,
$$D^{(M)}\left(\theta_{\text{FWHM}}^{(M)}, x_{sf}^{(M)}, y_{sf}^{(M)}, x_{rx}, y_{rx}\right) \le \epsilon,$$
 (3.29b)

$$D^{(i+1)} < D^{(i)}, (3.29c)$$

$$\theta_{\text{FWHM}}^{(1)} = \theta_{\text{FWHM,max}}, \qquad (3.29d)$$

$$\theta_{\text{FWHM}}^{(M)} = \theta_{\text{FWHM,min}}, \tag{3.29e}$$

$$\theta_{\text{FWHM}}^{(i+1)} < \theta_{\text{FWHM}}^{(i)}, \tag{3.29f}$$

where N_i is the maximum number of spots at stage i within the room, and is a function of the final spot position of the previous stage $\left(x_{sf}^{(i-1)}, y_{sf}^{(i-1)}\right)$. This is because the next stage starts from the spot center corresponds to the previously received feedback. Also $\left(x_{sf}^{(0)}, y_{sf}^{(0)}\right)$ is (0,0) since at the beginning AP starts scanning from the center of the room. N_i is also function of user position (x_{rx}, y_{rx}) and θ_{FWHM} . Note that $N_{\text{tot}} = \sum_{i=1}^{M} N_i$. Moreover, M is the total number of stages required for convergence to the accuracy ϵ . Note that the localization error is also function of θ_{FWHM} , and final spot position (x_{sf}, y_{sf}) . The bound for θ_{FWHM} must be selected such that AP starts with a large beam radius to locate the user with the minimum number of spots and begin the next stage of spiral scanning with a narrower beam.

For the selection of $\theta_{\text{FWHM, max}}$, there is a trade-off among several factors, including transmit eye-safe power, the number of discrete beam spot positions, and hardware constraints. A higher $\theta_{\text{FWHM, max}}$ requires a higher maximum eye-safe transmit power

to ensure that the user can detect the signal even at the farthest positions in the room. Additionally, hardware limitations must be considered, such as the AP ability to tune θ_{FWHM} between its maximum and minimum values, the range over which it can adjust the beam width, its angular precision, the maximum achievable eye-safe transmit power, and the speed at which it can switch between different FWHM settings.

The optimization problem (3.29f) can be classified as a constrained optimization problem. Specifically, the objective is to minimize N_{tot} while ensuring that the localization error at the last stage $(D^{(M)})$ remains below a predefined accuracy (ϵ) , and $\theta_{\text{FWHM}}^{(i)}$ is reduced from its initial value, denoted as $\theta_{\text{FWHM, max}}$, to the target value, $\theta_{\text{FWHM, min}}$, over a predetermined number of steps, M.

To simplify the problem in (3.29f) and enable a practical real-time implementation, a heuristic progression is adopted for updating $\theta_{\text{FWHM}}^{(i)}$ across stages. The goal is to gradually reduce θ_{FWHM} from a wide search beam to a narrow tracking beam in a controlled manner, avoiding computationally expensive optimization while maintaining acceptable localization accuracy. The update rule is chosen as a geometric progression

$$\theta_{\text{FWHM}}^{(i)} = \theta_{\text{FWHM,max}} \cdot q^{i-1}, \tag{3.30}$$

where q is the progression factor. At the final stage M,

$$\theta_{\text{FWHM}}^{(M)} = \theta_{\text{FWHM,min}}$$

$$= \theta_{\text{FWHM max}} \cdot q^{M-1}.$$
(3.31)

This yields

$$q = \left(\frac{\theta_{\text{FWHM,min}}}{\theta_{\text{FWHM,max}}}\right)^{\frac{1}{M-1}},\tag{3.32}$$

and therefore

$$\theta_{\text{FWHM}}^{(i)} = \theta_{\text{FWHM,max}} \cdot \left(\frac{\theta_{\text{FWHM,min}}}{\theta_{\text{FWHM,max}}} \right)^{\frac{i-1}{M-1}}.$$
 (3.33)

This heuristic provides a simple and predictable reduction of $\theta_{\rm FWHM}$ between $\theta_{\rm FWHM,max}$ and $\theta_{\rm FWHM,min}$, balancing localization accuracy and scanning delay without solving the optimization problem explicitly. The choice of $\theta_{\rm FWHM,max}$ is based on the beam divergence capability of AP and maximum eye-safe transmit power, while $\theta_{\rm FWHM,min}$ is set according to the required localization accuracy. In practice, suitable values range from approximately 0.4° for fine tracking to 4°–10° for wide-area search, with corresponding transmit powers from about 10 mW to 350 mW.

Algorithm 1 summarizes the proposed multi-stage spiral search strategy used for initial user localization (as introduced in Fig. 3.1) in the simulation framework. The algorithm begins with a wide beam (corresponding to $\theta_{\text{FWHM.max}}$), and progressively narrows the beam width over multiple stages (up to M stages) to refine localization accuracy. At each stage i, the beam divergence angle $\theta_{\text{FWHM}}^{(i)}$ and corresponding spot radius $r_s^{(i)}$ are computed to define the spiral. For each spot in the current spiral pattern, the AP sends a test signal at calculated coordinates (x_s, y_s) and waits for an ACK signal from the user for t_{step} . The search proceeds by updating the spiral angle θ_s and counting the number of spot positions, $N_{\rm spot}$, until an ACK is received. Upon receiving an ACK (i.e., when the received power P_r exceeds the detection threshold $\rho_{\rm th}P_t$), the algorithm updates the estimated user location (x_{s0}, y_{s0}) and stores the final estimate (x_{sf}, y_{sf}) . If the search spiral exceeds the room boundaries without finding the user, the algorithm resets the spiral center and increases the overlap factor α_s by 10% (heuristically chosen) to improve coverage in subsequent iterations. The search continues until the final stage M. The output of the algorithm consists of the final estimated user coordinates (x_{sf}, y_{sf}) and the total number of scanning steps $N_{\rm spot}$, providing an initial localization estimate suitable for the tracking and communication phase.

In terms of practical implementation, key considerations include the ability of the AP to operate at high steering speeds, achieve fine angular precision, and maintain

Algorithm 1: Multi-Stage Spiral Search for Initial Localization (Simulation)

```
Input: \epsilon, \theta_{\text{FWHM,max}}, t_{\text{step}}, M, \alpha_s, h, room dimensions (x_{\text{room}}, y_{\text{room}}, z_{\text{room}})[m],
                \theta_s = 0, \, \rho_{\text{th}} \, (\text{from } (3.20)), \, x_{s0}, \, y_{s0} = (0,0), \, \lambda = 1550 \, \text{nm}
     Output: Estimated user location (x_{sf}, y_{sf}), total delay N \times t_{step}
 1 Compute \theta_{\text{FWHM,min}} using (C.29)
 2 Initialize i \leftarrow 1
    while i \leq M do
         Compute \theta_{\text{FWHM}}^{(i)} using (3.33)
 4
         Compute \omega(h) from (2.21) according to \theta_{\text{FWHM}}^{(i)}
 5
         Compute r_s^{(i)} using (3.6)
 6
          Compute P_t from (2.29) with respect to \lambda for sending test signal at each spot
 7
          ACK \leftarrow \emptyset
 8
          while ACK = \emptyset do
 9
               Update \theta_s from (3.9)
10
              Update r_s^{(i)} from (3.6)
11
               N_{\text{spot}} \leftarrow N_{\text{spot}} + 1
12
              Compute x_s = r_s^{(i)} \cos(\theta_s) + x_{s0}
13
              Compute y_s = r_s^{(i)} \sin(\theta_s) + y_{s0}
14
               Compute (\theta, \varphi) from (3.4) and (3.5) for beam steering
15
               Wait t_{\text{step}} for possible ACK
16
              if P_r > \rho_{th} P_t then
17
                    ACK = 1
18
                    (x_{s0}, y_{s0}) \leftarrow (x_s, y_s)
19
                   (x_{sf}, y_{sf}) \leftarrow (x_s, y_s)
20
21
               end
               else if x_s > x_{room}/2 \lor y_s > y_{room}/2 then
22
                   \theta_s \leftarrow 0 (restart spiral from the last (x_{s0}, y_{s0}))
\mathbf{23}
                    \alpha_s \leftarrow \alpha_s \times 1.1 (increase spiral overlap by 10%)
24
               end
25
          end
26
          i \leftarrow i+1
27
28 end
29 Output (x_{sf}, y_{sf}), N \times t_{\text{step}}
```

eye-safe power levels. As discussed in Section 2.9, most of the surveyed beam steering technologies (e.g., stepper motors, galvanometers, DMDs, SLMs/LCoS) are designed for directing a narrow beam from one point to another and are not inherently suited for high-speed, high-precision operation. Among these, MEMS-based systems and OPAs stand out as the most suitable for high-performance applications. MEMS mirrors combine sub-millidegree precision with switching speeds up to 10 kHz, while offering compact form factors compatible with integrated systems. OPAs provide solid-state operation with steering speeds in the MHz range and fine angular resolution, though their usable FoV is typically limited to about $\pm 6^{\circ}$ ($\approx 12^{\circ}$ total) [53]. Moreover, dynamic beam divergence control can be achieved using additional optics, such as liquid lenses, tunable beam expanders, or adaptive optics, which are already employed in commercial LiDAR and indoor localization systems.

The required precision for selecting $\theta_{\rm FWHM}^{(i)}$ is not critical, as small deviations have a limited impact on the search process. Only the choice of $\theta_{\rm FWHM,\,min}$ (i.e., final stage) is critical to guarantee the required precision for the tracking phase. The design is adaptive with respect to $\theta_{\rm FWHM,\,min}$, allowing flexibility in balancing accuracy, delay, and the choice of M. For example, a single $\theta_{\rm FWHM} = 0.4^{\circ}$ can be used for localization, tracking, and communication. A single-stage spiral scan with this $\theta_{\rm FWHM}$ is also possible, though it results in increased localization delay (see Fig. 3.9). This study presents a generalized system design along with its limitations, trade-offs, and achievable best performance.

Fig. 3.13a shows the cumulative spot numbers N after each stage and the corresponding localization error D at each stage. The optimium $\theta_{\rm FWHM}^{(i)}$ values at each stage are demonstrated in Fig. 3.13b. In this figure, M=4 stages with localization accuracy of $\epsilon=5$ cm, and initial $\theta_{\rm FWHM,max}=10^\circ$ are considered for the simulation. At the final stage, $N_{\rm tot}=617$ spots, $D_{\rm max}^{(4)}=3.47$ cm, and $\theta_{\rm FWHM,min}=0.4^\circ$.

Fig. 3.14, and 3.15, demonstrate the cumulative N at each stage for M=2,3,...,10,

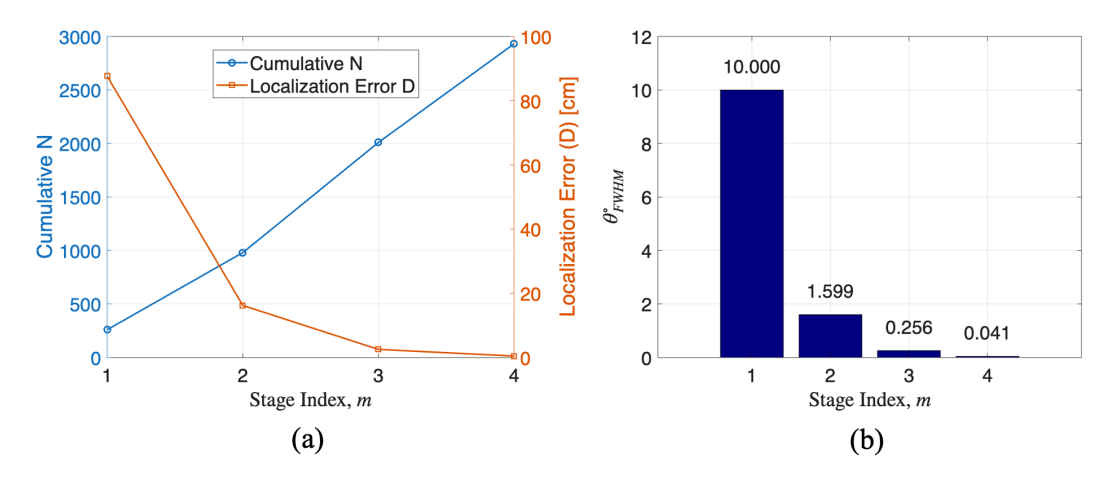


Figure 3.13: Multi-stage localization with M=4 total stages for $\epsilon=5$ cm accuracy; (a) cumulative spot numbers N and localization error D versus stage index m, (b) corresponding optimal $\theta_{\rm FWHM}^{(i)}$ values at each stage index m.

for $\epsilon=1\,\mathrm{cm}$, 5 cm, 10 cm respectively. Each curve represents a multi-stage spiral search until maximum stage number M with given fixed ϵ . It can be observed from the figures that by increasing the M stages, N_{tot} decreases. Note that in Fig. 3.14b, the multi-stage with M=9 achieves the $D_{\mathrm{max}}<\epsilon=5\,\mathrm{cm}$ at the 8th stage and stops with fewer N_{tot} compared to M=8. Moreover, it reaches the threshold at the 9th stage when M=10. Similar effect happened in Fig. 3.15 for M=8,9. Also M=10 does not decrease N_{tot} compared to M=9.

3.3 Phase II: Simultaneous Tracking and Communication with DBS

The aim is to provide a high average data rate while the user is moving randomly. An ideal indoor OWC architecture with an IR narrow beam can perfectly point the beam toward the exact location of the user and track its movement without any error in positioning. However, a narrower beam is more sensitive to user random movements and vibrations for tracking due to the smaller coverage area of the beam spot. Thus,

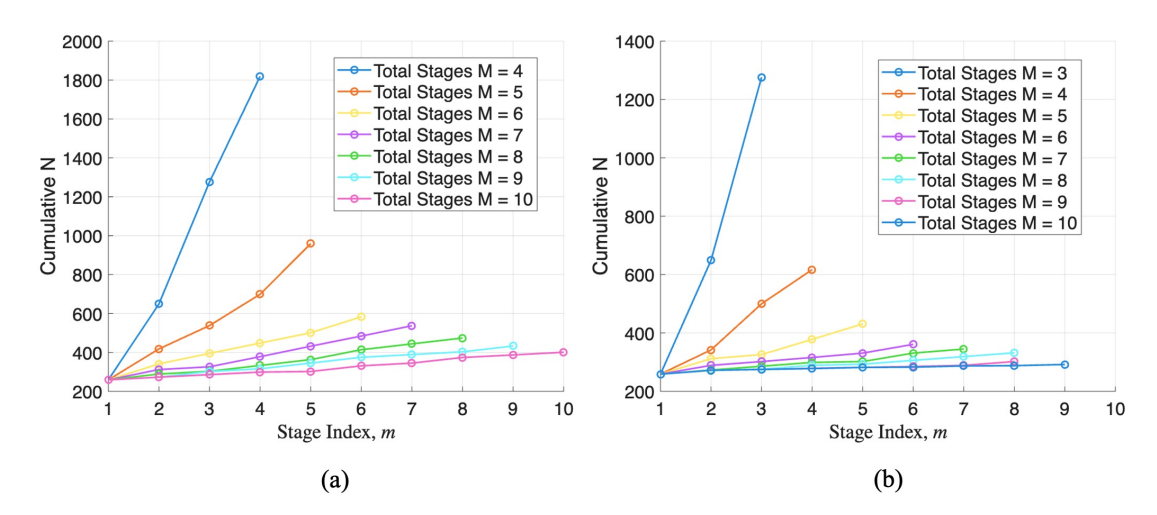


Figure 3.14: Cumulative N as a function of stage index m for different total stage numbers M and localization accuracies ϵ : (a) $\epsilon=1\,\mathrm{cm}$, (b) $\epsilon=5\,\mathrm{cm}$.

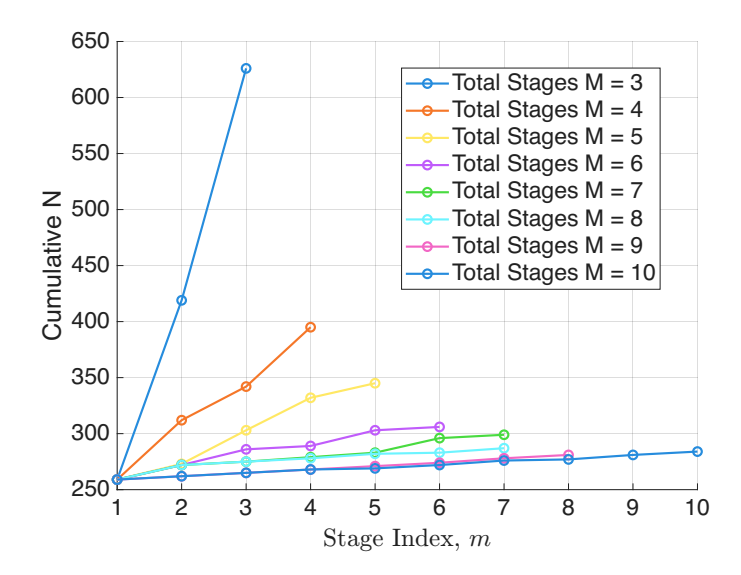


Figure 3.15: Effect of stage number M and localization accuracy ϵ on cumulative N; $\epsilon=10cm$

it is required for AP to track the user location with real-time precision on the order of a fraction of the beam spot size, ensuring the user remains within the beam coverage region to sustain the required SNR and data rate. This motivates the proposed DBS design and is the focus of this section.

Consider the case where an initial estimated location of the user is obtained from the

multi-stage spiral search described in Section 3.2. Given this initial location, the AP can point the IR beam and begin data transmission to the user. However, the user position is assumed to exhibit vibration or movement in random directions with a certain velocity. Therefore, the AP must estimate the direction of user movement to maintain alignment. Initially, the AP knows the user location from the localization phase, points the beam toward it, and sends a test signal to receive an ACK from the user, ensuring the user is within the beam coverage at the start. As the user moves, the AP must estimate the user next position for beam steering. In this work, a circular pattern with finite beam pointing positions is considered for tracking user movement, as illustrated in Fig. 3.16. The reason for circular pattern selection is its symmetry, which allows the AP to estimate the direction of updates based on uniform feedback from multiple predefined beam spot positions around the pattern. The center of the circular scanning pattern at time step t is denoted by $c_s^{(t)}$, where t represents a discrete time index. The initial center, $c_s^{(1)}$, is obtained from the estimated user location provided by the multi-stage spiral search described in Section 3.2. The overall circular scanning pattern is illustrated by the black dashed line in Fig. 3.16. Additionally, $\theta_{s,i}$ denotes the discrete beam steering angles on this circular pattern, representing the pointing directions within a single scanning cycle, where i ranges from 1 to n_{spot} discrete spot positions ($n_{\text{spot}} = 3$ in Fig. 3.16 since there are 3 spot positions). To uniformly distribute $n_{\rm spot}$ beam positions on a circular trajectory, the discrete beam steering angles θ_{si} can be computed from

$$\theta_{si} = \frac{2\pi(i-1)}{n_{\text{spot}}}, \quad i = 1, 2, \dots, n_{\text{spot}}.$$
 (3.34)

For example, when $n_{\rm spot}=3$, the angular phases become $\theta_{si}\in\{0^{\circ}, 120^{\circ}, 240^{\circ}\}$. This construction ensures equal angular separation of $2\pi/n_{\rm spot}$ between consecutive scanning directions. Each solid circle in Fig. 3.16 indicates the beam spot footprint with its corresponding center (i.e., $\theta_{s,i}$ where i = 1,2,3) on the circular path. The radius of the circular path is fixed at $r_{\rm scan}$. Note that in this figure, the beam radius is denoted by

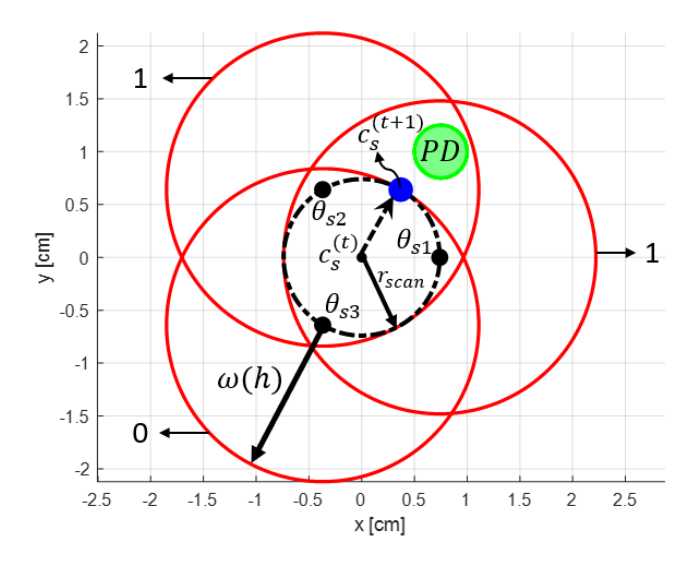


Figure 3.16: Geometry of dynamic beam steering on a circular path, where three discrete spot positions are selected as an example

 $\omega(h)$, which represents the minimum beam radius in the XY plane at $z=1\,\mathrm{m}$ above the floor. Here, $h=2\,\mathrm{m}$ is the minimum distance between the AP and the user XY plane. In other positions on XY plane, beam radius is greater, and the overlap between spot positions increases. The scanning circular pattern radius r_{scan} must be selected such that there is no empty place in the center of the scanning pattern; thus, $r_{\mathrm{scan}} \leq \omega(h)$. Therefore, r_{scan} can be expressed as

$$r_{\rm scan} = x_{\rm scan} \,\omega(h),\tag{3.35}$$

where $0 \le x_{\text{scan}} \le 1$ determines the coverage area that the dynamic beam is scanning. Higher x_{scan} results in higher scanning coverage that makes the tracking algorithm more robust to random movement with higher user speed, but decreases the average rate since the overlap between spot positions decreases, and fewer spots may receive feedback. Thus, there is a trade-off between the accuracy of tracking and the average rate. Selecting a larger $\omega(h)$ makes the tracking more robust against vibration, but this decreases the instantaneous data rate, and more power will be consumed.

3.3.1 Joint Scheduling, Tracking, and Delay Analysis

The general process of downlink transmission and uplink feedback begins with the AP transmitting a test signal (through a narrow IR beam with VCSEL in this work), typically an unmodulated optical beam, to probe the user location [11]. Upon receiving this signal, the user device returns an ACK feedback signal, which can be implemented using various methods such as CCR-based retroreflection, ODTx, or an RF uplink. In the case of using CCR, the incoming optical test signal is passively retroreflected back to the AP along the incoming path with a latency denoted by t_{RS} . The mean signal propagation delay is represented as t_{δ} . Following this, a data frame is transmitted after a short inter-frame space (SIFS) [11]. Once the data packet is transmitted, the AP sends another test signal after the next SIFS. The time required for the AP to transmit a single data packet, denoted by t_{DL} , is given as

$$t_{\rm data} = \frac{L_{\rm data}}{R_{\rm DL}},\tag{3.36}$$

where L_{data} is the packet length and R_{DL} is the downlink rate calculated from (2.45). The relevant delay parameters are summarized in Table 3.1, as detailed in [11]. Thus, the total required time for packet transmission can be calculated as

$$t_{\text{packet}} = t_{\text{TS}} + t_{\delta} + t_{\text{RS}} + t_{\text{SIFS}} + t_{\text{data}} + t_{\text{SIFS}}. \tag{3.37}$$

The effective throughput of the system, assuming no collision, can be calculated as [11] [11]

$$\tau_{\text{eff}} = \frac{t_{\text{data}}}{t_{\text{packet}}}.$$
(3.38)

Note that, as mentioned previously, other uplink feedback approaches can also be considered, with the value of $t_{\rm RS}$ adjusted to reflect the specific latency characteristics of the chosen method.

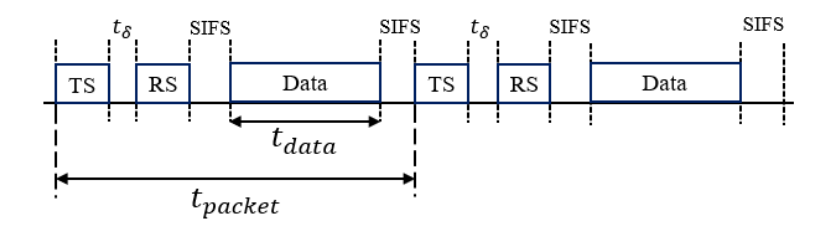


Figure 3.17: Timing diagram showing the sequence of test signal (TS), reflected signal (RS), short inter-frace space (SIFS), data transmission time ($t_{\rm data}$), propagation delay t_{δ} , and packet time $t_{\rm packet}$ according to [11]

Table 3.1: Delay time parameters for tracking [11]

Parameter	Symbol	Value
Test signal time	$t_{ m TS}$	$0.3\mu\mathrm{s}$
Reflected signal time from CCR	$t_{ m RS}$	$0.3\mu\mathrm{s}$
Average length of data packet [107]	$L_{ m data}$	64 Kbytes
Mean propagation delay [106]	t_{δ}	$3\mathrm{ns}$
Short Inter-Frame Space (SIFS) [107]	SIFS	$2\mu\mathrm{s}$

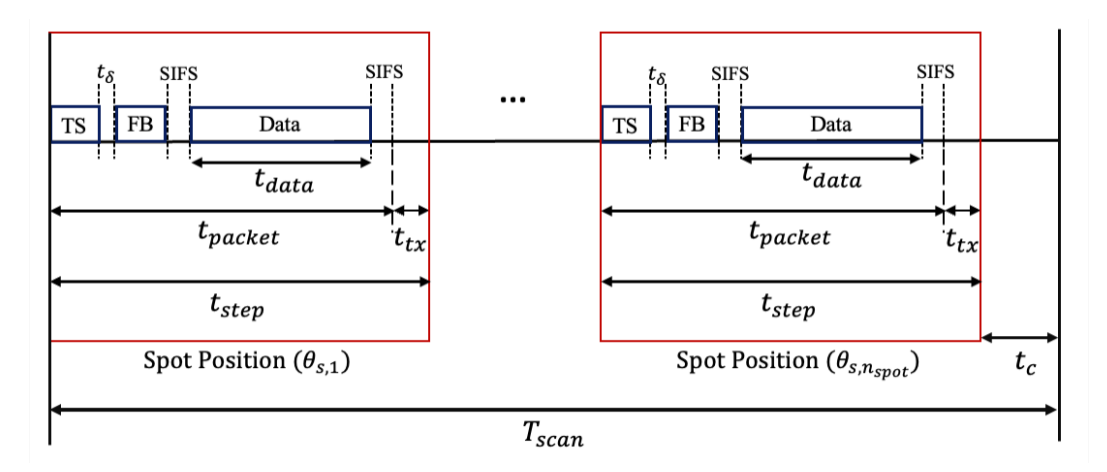


Figure 3.18: Timing diagram showing $t_{\rm step},\,T_{\rm scan}$

According to the Fig. 3.16, 3 spot positions are considered on the circular path in one period of DBS tracking, denoted by T_{scan} . It is assumed that t_{step} represents the time required to move from spot s_i to spot s_{i+1} as illustrated in Fig. 3.18. From this figure, t_{step} is given by

$$t_{\text{step}} = t_{\text{packet}} + t_{tx}. (3.39)$$

where t_{packet} can be computed from (3.37), and t_{tx} is transmitter processing time for pointing the beam towards the next spot position which depends on the beam steering device as explained in Table 2.8 in Chapter 2. Note that, feedback response time of receiver, t_{FB} , affects the t_{step} selection. In this process, the AP first sends a test signal through the beam pointed at θ_{s1} . If an ACK is received, it transmits data during the time slot of t_{data} and then proceeds to the next spot position. If no ACK is received within the feedback duration t_{FB} , it is considered as no feedback (NACK), and the AP moves to the next spot position. This process continues sequentially until $\theta_{s, n_{\text{spot}}}$ is reached. The total scan period from the figure is given by

$$T_{\text{scan}} = n_{\text{spot}} t_{\text{step}} + t_c, \tag{3.40}$$

where t_c is AP processing time to update the center of scanning for the next scanning period, which also depends on the beam steering device. In Fig. 3.16, the PD is covered by the beam spots corresponding to θ_{s1} and θ_{s2} , where a 1-bit ACK is assumed for these positions. For θ_{s3} , a 0 is considered to indicate no feedback. To update the scanning center (i.e., $c_s^{(t)} = (c_{s,1}^{(t)}, c_{s,2}^{(t)})$) for the next period, AP can take the average of θ_{s1} and θ_{s2} angles and update the center of scanning to $c_s^{(t+1)} = (c_{s,1}^{(t+1)}, c_{s,2}^{(t+1)})$ which denotes the updated estimation of the user location, as shown by the blue point in the Fig. 3.16. In the discrete-time t, the spot positions $(x_{s,i}^{(t)}, y_{s,i}^{(t)})$ corresponds to θ_{si} on the circular pattern can be computed from

$$\begin{bmatrix} x_{s,i}^{(t)} \\ y_{s,i}^{(t)} \end{bmatrix} = r_{\text{scan}} \begin{bmatrix} \cos(\theta_{si}) \\ \sin(\theta_{si}) \end{bmatrix} + \begin{bmatrix} c_{s,1}^{(t)} \\ c_{s,2}^{(t)} \end{bmatrix}, \quad i = 1, 2, ..., n.$$
 (3.41)

The feedback vector at the AP side in one period can be constructed as $\Theta \in \{0,1\}^{n_{\text{spot}}}$, and spot position angles corresponds to positive feedback can be stored in vector Θ^+ .

Then $c_s^{(t)}$ can be updated as,

$$\begin{bmatrix} c_{s,1}^{(t+1)} \\ c_{s,2}^{(t+1)} \end{bmatrix} = \frac{r_{\text{scan}}}{|\mathbf{\Theta}^+|} \sum_{j=1}^{|\mathbf{\Theta}^+|} \begin{bmatrix} \cos(\mathbf{\Theta}^+(j)) \\ \sin(\mathbf{\Theta}^+(j)) \end{bmatrix} + \begin{bmatrix} c_{s,1}^{(t)} \\ c_{s,2}^{(t)} \end{bmatrix}, \tag{3.42}$$

where $|\cdot|$ is cardinality. Note that during each $t_{\rm step}$, the user moves with a velocity of $v_{\rm rx}$ [m/s], and its movement is $t_{\rm step}$ v_{rx} . Assume user is in the spot center, if its movement after one $t_{\rm step}$ is still in the coverage area of spot, then user looks nearly static from the AP viewpoint in one $t_{\rm step}$. The $t_{\rm step}$ must be sufficient such that the distance moved by the user is less than $(\omega(h) + r_{\rm scan})$, thus,

$$t_{\text{step}} \ll \frac{(\omega(h) + r_{\text{scan}})}{v_{\text{user}}}.$$
 (3.43)

Note that $\omega(h)$ is function of θ_{FWHM} (see (2.21)). This allows the AP to react before the user moves out of the scanning range, and it can update the scanning center accordingly. Moreover, another more strict condition for T_{scan} can also be considered as

$$T_{\rm scan} \ll n_{\rm spot} \, \frac{(\omega(h) + r_{\rm scan})}{v_{\rm user}}.$$
 (3.44)

Since $\omega(h)$ is the smallest beam radius in this system at the receiver plane, other positions have a larger beam size, resulting in a larger spot coverage within $t_{\rm step}$. The selection of $\theta_{\rm FWHM}$ determines the sensitivity of tracking. If feedback and response system is not fast, then larger value of $\theta_{\rm FWHM}$ must be selected to guarantee that within $t_{\rm step}$, user is still in the coverage of beam spot with high probability. Therefore the choice of $\theta_{\rm FWHM}$ depends on $t_{\rm step}$. Furthermore, $n_{\rm spot}$ determines the accuracy of the direction of the update. Assuming a fast operating system, i.e., $t_{\rm step}$ is very small, with larger $n_{\rm spot}$, AP receives feedback corresponding to more angles close to each other and takes the average of them for center update. Furthermore, a number of discrete spots, $n_{\rm spot}$, must be selected such that it does not increase $T_{\rm scan}$ to avoid having unnecessary spots.

The AP may fail to receive any feedback from the user during a full scanning cycle due to several factors. For instance, the user might move abruptly outside the scanning coverage, the LoS link could be temporarily obstructed, or the user could be near the edge of the coverage area and exit it after a scanning cycle. In such scenarios, if the AP receives no feedback during a scanning interval of duration T_{scan} , the parameter $c_s^{(t)}$ can be updated in a direction same as the previous direction of update as

$$c_s^{(t+1)} = c_s^{(t)} + \varepsilon_c \cdot \zeta, \tag{3.45}$$

$$\varepsilon_c = 2|\delta d_{rx}|_{\text{max}},\tag{3.46}$$

$$|\delta d_{rx}|_{\text{max}} = v_{\text{user, max}} \cdot T_{\text{scan}},$$
 (3.47)

$$\zeta = \frac{c_s^{(t)} - c_s^{(t-1)}}{\|c_s^{(t)} - c_s^{(t-1)}\|},\tag{3.48}$$

where $v_{\text{user, max}}$ [m/s] is considered to be the user maximum speed, and ζ is the direction of center update in the previous scan. Note that $||(c_s^{(t)} - c_s^{(t-1)})|| \neq 0$, otherwise the center of scanning can be updated randomly according to

$$c_s^{(t+1)} = c_s^{(t)} + \varepsilon_c Z,$$
 (3.49)

where $Z \sim \mathcal{N}(0,1)$. Since user speed is random, to evaluate ε_c , a maximum speed of $v_{\text{user,max}}$ is considered to consider the worst-case scenario, which is a movement with maximum speed. Therefore, if the user is out of scanning coverage in one period, it is possible that the user may be found again in subsequent scans. Otherwise, if the user is not found in multiple periods of scanning center update, then the spiral search with the same beam divergence, i.e., θ_{FWHM} , can start searching according to section. 3.2.1 from the center $c_s^{(t)}$, where $c_s^{(t)}$ corresponds to the last received feedback.

3.3.2 DBS Algorithm

The summary of DBS tracking scheme is demonstrated in Algorithm 2. The inputs of this algorithm are the simulation time interval $t_{\rm tot}$, beam divergence $\theta_{\rm FWHM}$, feedback threshold coefficient $\rho_{\rm th}$ that determines minimum acceptance power by the receiver and can be derived from (3.11), number of spot positions $n_{\rm spot}$, vector of angles on the circular scanning pattern Θ_s , scanning step time $t_{\rm step}$, initial center of scanning pattern $c_s^{(0)}$ obtained from initial multi-stage spiral search, ε_c is derived from (3.46), and the receiver edge threshold δd_{rx} from (3.21). The output of the algorithm is $c_s^{(t+1)}$, which is the next center of the discrete circular scanning pattern at time step (t+1). Note that in Algorithm 2, it is assumed that t_c is negligible and $T_{\rm step} \approx n_{\rm spot} t_{\rm step}$ for simplicity in the simulations.

When the user is lost during tracking, the AP updates the direction according to (3.48) and (3.49). In the simulations and in Algorithm 2, only DBS tracking is implemented, and the spiral search is not used to recover a lost user. A sufficiently small $t_{\rm step}$ relative to the chosen $\theta_{\rm FWHM}$ proves in the following simulation that the data rate can be maintained while the user is randomly moving. The following simulations will demonstrate that if t_{step} is insufficient for tracking, the data rate drops to zero. In practical implementations, a spiral search can be incorporated into the tracking phase to guarantee user recovery if the AP loses the signal after multiple attempts. In a scenario where the user does not move significantly (i.e., remains within a circle of center $c_s^{(t)}$ and radius $r_{\rm scan}$, see Fig. 3.16), the circular scanning pattern remains active; however, its center is not updated since all beam spot positions satisfy $P_r > \rho_{\rm th} P_t$, resulting in $n_{\rm spot}$ ACKs per scan cycle. The user is still required to provide periodic ACK feedback to confirm continued coverage within the beam FoV. This requirement arises not only from user movement but also from small-scale vibration effects, such as structural vibrations in the environment, which become relevant when operating with very low θ_{FWHM} values. The frequency of feedback transmission is determined by $1/t_{\text{step}}$.

Algorithm 2: Tracking and Communication with DBS for Simulation

```
Input: t_{\text{tot}}, \theta_{\text{FWHM}}, \rho_{\text{th}}, n_{\text{spot}}, \Theta_{\text{s}}, t_{\text{step}}, x_{\text{scan}}, c_{\text{s}}^{(0)}, \varepsilon_{\text{c}}, \delta d_{rx}
      Output: c_s^{(t+1)}
  1 Calculate \omega(h), and P_t, from (2.40), and (2.42) respectively
  2 T_{\rm scan} \approx n_{\rm spot} t_{\rm step}, r_{\rm scan} = x_{\rm scan} \omega(h)
     while t \leq t_{tot} do
              for i = 1 : n_{spot} do
  4
                    Calculate x_{si}^{(t)}, y_{si}^{(t)} based on (3.41)
  5
                    S_i^{(t)} = [x_{s,i}^{(t)} y_{s,i}^{(t)} z_s], \ n_{tx,i}^{(t)} = \frac{S_i^{(t)} - Tx}{||S_i^{(t)} - Tx||}, \ \varphi_i^{(t)} = \cos^{-1} \left( \frac{n_{tx,i}^{(t)} d_{rx}^{(t)}}{||d_{rx}^{(t)}||} \right)
  6
                    Calculate \omega\left(d_{rx}^{(t)}\cos(\varphi_i^{(t)})\right), based on (2.40)
  7
                    Calculate \psi^{(t)} = \cos^{-1} \left( \frac{n_{rx}.(-d_{rx}^{(t)})}{||d_{rx}^{(t)}||} \right)
  8
                    Calculate P_{r,i}^{(t)} based on (2.42)
  9
                    if P_{r,i}^{(t)} > \rho_{th} P_t then
10
                            \Theta(i) = 1, receiver sends 1-bit feedback
11
                            \Theta^+(i) = \Theta_s(i)
12
                    else
                      \Theta(i) = 0
13
                     Update user position after one t_{\text{step}} to model its movement:
14
                    d_{\mathrm{rx}}^{(t)} \leftarrow d_{\mathrm{rx}}^{(t)} + \frac{(d_{\mathrm{rx}}^{(t+1)} - d_{\mathrm{rx}}^{(t)})}{n_{\mathrm{spot}}}
15
             if \Theta^+ \neq \emptyset then
16
                    if |\Theta^+| = n_{spot} then c_s^{(t+1)} = c_s^{(t)}
17
18
                     else
                           Update c_s^{(t)} to c_s^{(t+1)} based on (3.42)
19
                    end
              else
                    if ||c_s^{(t)} - c_s^{(t-1)}|| \neq 0 then
c_s^{(t+1)} = c_s^{(t)} + \varepsilon_c \frac{c_s^{(t)} - c_s^{(t-1)}}{||c_s^{(t)} - c_s^{(t-1)}||}
20
21
                    else c_s^{(t+1)} = c_s^{(t)} + \varepsilon_c \cdot Z
\mathbf{22}
                    end
              \mathbf{end}
             t \leftarrow t + T_{\text{scan}}
23
      end
```

3.3.3 Average Achievable Data Rate per Period of Scanning

The AP can only determine whether the spot is within the receiver FoV based on a 1-bit ACK. Since the receiver either sends a signal upon detection or nothing if undetected, the AP cannot measure the full channel. At the receiver side, the received power can be measured, providing knowledge of the link gain but not the beam pointing direction; thus, the receiver does not have complete channel state information. According to Fig. 3.18, in each spot position during t_{step} , the AP first transmits a TS and transmits data only when 1-bit ACK is received. This process repeats for n_{spot} spot positions within one scanning cycle of duration T_{scan} . The data is not retransmitted within the same scanning cycle. Therefore, the average data rate per cycle is the total data rate from all spot positions divided by the number of spot positions. For the DBS scheme, the average data rate after each period of scanning can be calculated as

$$R_{\text{DBS, avg}}^{(i)} = \frac{1}{|\mathbf{\Theta}|} \sum_{j=1}^{|\mathbf{\Theta}_{i}^{+}|} R_{ij}, \quad for \quad i = 1, 2, \dots, m,$$
 (3.50)

where R_{ij} is the j-th instantaneous rate at the i-th scanning cycle, which is defined in the equation (2.45), and Θ_i^+ is the set of angles in which a positive feedback is obtained in the i-th scanning cycle. Note that the total simulation time interval is obtained using $t_{\text{tot}} = m T_{\text{scan}}$, where T_{scan} is defined in (3.40).

3.4 Conclusion

This chapter has presented the design framework for DBS systems in indoor OWC. The design was divided into two main phases, including initial beam searching using a multi-stage spiral scanning approach, and simultaneous tracking and communication with periodic feedback to maintain sufficiently high-precision alignment. Detailed modeling and algorithm development were provided for defining the beam steering geometry,

M.A.Sc. Thesis - Hamed Hosseinnejadazad McMaster University - ECE Department

feedback threshold calculation, and the tracking strategy based on discrete beam steering positions. The performance evaluation and simulation results in an indoor scenario demonstrating the trade-offs in DBS parameter selection for different user movement scenarios, along with comparisons to a cellular-style design from [11] and an idealized case, is presented in the next chapter.

Chapter 4

Comparison of DBS System versus Benchmarks

In this chapter, the DBS tracking algorithm (Algorithm 2) is evaluated through simulations to illustrate parameter trade-offs, their dependencies, and their impact on tracking and communication performance. In each simulation, the performance of the DBS scheme is benchmarked against an ideal tracking scenario in which the AP has perfect knowledge of the user location and can instantaneously steer the beam with zero pointing error. For this purpose, the user motion model for these simulations is defined as linear movement in the XY plane at z = 1 m, starting from the center of the room and moving toward the corner at (2.5 m, 2.5 m, 1 m) with a user speed of 1 m/s. The parameters of the simulation environment (see also Fig. 2.1) are summarized in Table 4.1.

After analyzing the parameter trade-offs, suitable values are selected for the DBS configuration, and its communication performance is compared with the cellular-style architecture introduced in Chapter 1 (also see Fig. 1.8), which follows the atto-cell design of [11]. As discussed previously, this scheme divides the room into cells of size $10 \, cm \times 10 \, cm$ determined by the beam divergence ($\theta_{\rm FWHM} = 4^{\circ}$) and activates the corresponding transmitter element based on the localized position of the user. The

Table 4.1: System parameters for simulation setup.

Parameter	Value / Description
Room dimensions	$(2.5\mathrm{m},2.5\mathrm{m},3\mathrm{m})$
AP location	$(0,0,3\mathrm{m})$
Vertical separation	$h=2\mathrm{m}$
User motion model	Linear trajectory from center to corner of the
	room on XY plane at $z_{\rm rx} = 1 \rm m$
User velocity	$v_{\rm user} = 1 {\rm m/s}$
Receiver parameters	According to Table 2.6
Receiver noise parameters	According to Table 2.7
Wavelength	$\lambda = 1550\mathrm{nm}$
Eye-safety parameters	From Table 2.5
Number of subcarriers	$M_s = 128$

comparison is carried out under two user motion scenarios. One is a linear movement from the center to the corner of the room, and another is a Brownian motion model representing random movement in random directions. All simulation parameters are selected based on Table 2.6 and Table 2.7. The transmit eye-safe power is calculated using (2.29) and Table 2.3 for a given θ_{FWHM} , the received power is computed from (2.42), noise power is derived from (2.46), and the resulting data rate is obtained from (2.45) (considering $M_s = 128$ subcarriers).

4.1 Design Considerations and Trade-offs in DBS Architecture

The DBS architecture depends on several design parameters, including the beam divergence angle $\theta_{\rm FWHM}$, scanning step time $t_{\rm step}$, circular scanning radius $r_{\rm scan} = x_{\rm scan} \, \omega(h)$, number of spot positions per scan $n_{\rm spot}$, feedback threshold coefficient $\rho_{\rm th}$ (see (3.20)) determined by the receiver edge threshold δd_{rx} from (3.21), the AP–receiver plane distance h, and the maximum user velocity $v_{\rm user,max}$. To evaluate the effect of each parameter, one variable is varied while the others are held fixed; unless otherwise stated, $h=2\,{\rm m}$ and $v_{\rm user,max}=1\,{\rm m/s}$ are assumed. Since the user displacement within each $t_{\rm step}$ is

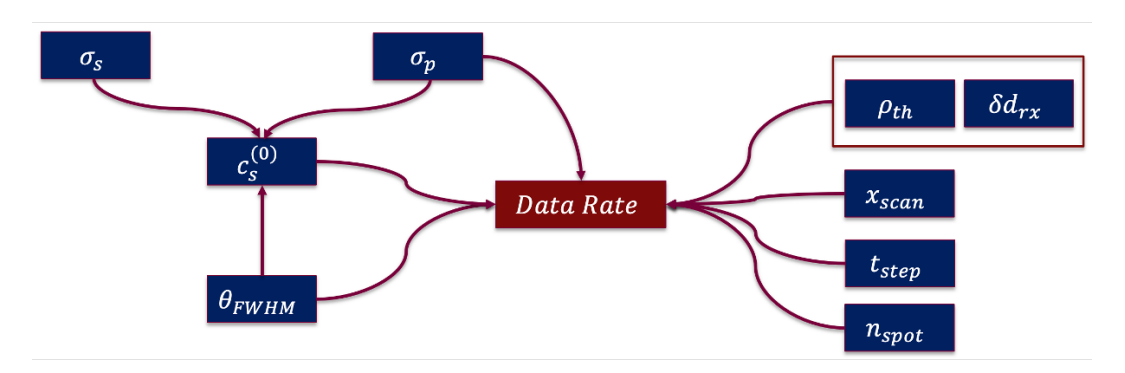


Figure 4.1: Parameter dependencies of DBS scheme influencing achievable data rate

 $v_{\text{user,max}} t_{\text{step}}$, this parameter directly affects the rate of user position change. Furthermore, the analysis assumes that the user location is initially known to the AP at the beginning of scanning (i.e., $c_s^{(0)} = (0,0)$).

Figure 4.1 summarizes the interaction of these parameters to determine the achievable data rate. Specifically, beam divergence θ_{FWHM} , scanning strategy variables x_{scan} , t_{step} , n_{spot} , feedback sensitivity $(\rho_{\text{th}}, \delta d_{rx})$, and the initial estimated location $c_s^{(0)}$ obtained through multi-stage spiral search jointly affect alignment accuracy and system performance. In addition, noise in beam pointing and initial localization error further influence the achievable rate by perturbing tracking accuracy. This integrated view highlights the design trade-offs and parameter interdependencies explored through the simulations and compared with an ideal tracking method, where AP can exactly track the position of the user.

4.1.1 Effect of Feedback Threshold on Rate of DBS Scheme

First, the effect of $\rho_{\rm th}$, $\delta d_{\rm rx}$, and $\theta_{\rm FWHM}$, is examined. Considering $\theta_{\rm FWHM}=2^{\circ}$, $t_{\rm step}=1\,{\rm ms}$, $r_{\rm scan}=0.5\,\omega(h)$, and $n_{\rm spot}=3$, the parameter $\delta d_{\rm rx}$ is swept to determine $\rho_{\rm th}$ for different $\theta_{\rm FWHM}$ values. Moreover, user movement is assumed to be linear at height $1\,m$ above the floor from center of XY plane to the corner at $(2.5\,m, 2.5\,m)$. Therefore the radial distance from center, $r=\sqrt{x_{rx}^2+y_{rx}^2}$ is changing.

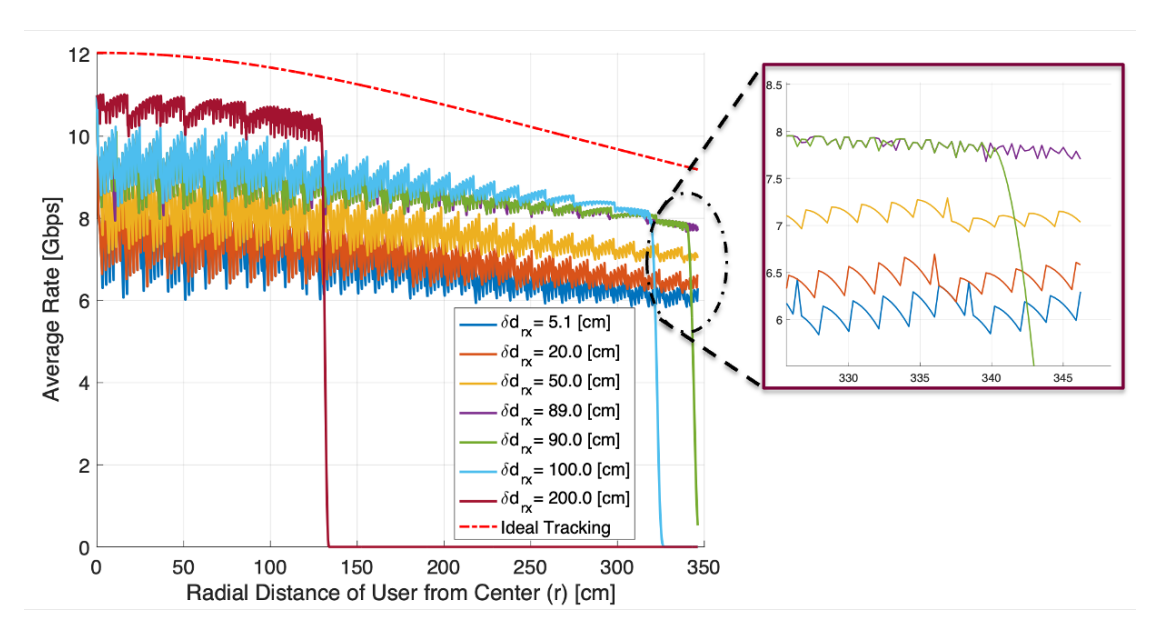


Figure 4.2: Data rate vs radial distance of user from center $\theta_{\rm FWHM} = 0.4^{\circ}$ for difference δd_{rx} values for tracking compared to ideal tracking

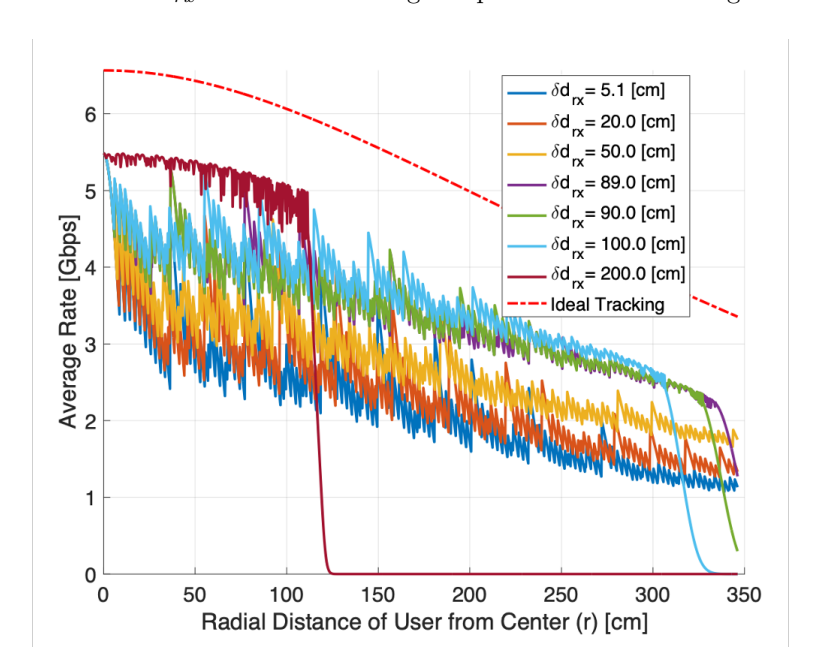


Figure 4.3: Data rate vs radial distance of user from center $\theta_{\rm FWHM} = 4^{\circ}$ for difference δd_{rx} values for tracking compared to ideal tracking

It is evident from Figures 4.2 and 4.3 that increasing δd_{rx} from 5.1 cm to 89 cm leads to a higher data rate, whereas further increases (e.g., $\delta d_{rx} = 90$ cm or larger) cause the

rate to drop as the radial distance grows. This behavior can be explained through the effect of δd_{rx} on the feedback threshold $\rho_{\rm th}$. A larger δd_{rx} corresponds to a stricter sensitivity requirement, such that the receiver does not send an ACK unless the received power exceeds a higher threshold. If the threshold is set too high (e.g., $\delta d_{rx} = 200 \,\mathrm{cm}$), the condition is rarely satisfied during user motion, resulting in lost ACKs, disrupted tracking, and a sharp reduction in rate at radial distance equal to almost 133.5 cm in Fig. 4.2. On the other hand, a high threshold ($\delta d_{rx} = 200 \,\mathrm{cm}$) can improve performance by enforcing stricter ACK conditions. In this case, the circular scanning pattern is adapted more accurately to the user location in each cycle of circular scanning. For instance, if a user lies within the overlap of two spots, with one spot covering the user in the spot center and the other only at the spot edge, the stricter threshold ensures that only the first spot triggers an ACK. This guides the beam update toward the spot that provides better alignment, and after several scanning cycles, the user becomes covered by all $n_{\rm spot} = 3 \,\mathrm{close}$ to center of circular pattern (i.e., $c_s^{(t)}$, see Fig. 3.16), thereby achieving a higher data rate than with a less strict threshold.

Both Figures 4.2, and 4.3 exhibits the same trend compared to $\delta d_{\rm rx}$ values for different $\theta_{\rm FWHM}$ values, i.e., 0.4°, 4° respectively. Note that selecting δd_{rx} higher than 200 cm results in almost the same data rate as for the curve corresponding to $\delta d_{rx} = 200$ cm. In Fig. 4.2, selecting $\delta d_{\rm rx} > 89$ cm results in data rate drop before reaching the corner of the room. Also for $\theta_{\rm FWHM} = 4^{\circ}$, rate drops at $\delta d_{rx} = 89$ cm, but before it reaches zero, the farthest distance will be reached.

4.1.2 Effect of Discrete Scanning Step Time on Rate of DBS Scheme

The next trade-off is to investigate the effect of t_{step} (as introduced in Subsection 3.3.1 and defined in (3.39)) on the average data rate for different θ_{FWHM} values using Algorithm 2. Figures 4.4, 4.5, 4.6 show the average data rate compared to radial distance of user from center of XY plane when user moves from center of the room to the corner with

 $\theta_{\rm FWHM} = 0.4^{\circ}, 1^{\circ}, 4^{\circ},$ respectively. Note that the figures are shown with radial distance at most 25 cm from the center. Moreover, similar to the previous comparison, $n_{\rm spot}=3$ is considered for the tracking and $\delta d_{\rm rx} = 89\,{\rm cm}$ is selected for threshold calculation for all θ_{FWHM} values. In Fig. 4.4, selecting $t_{\text{step}} = 0.01 \,\text{ms}$, 0.1 ms results in a higher average data rate since the AP can track the user movement with higher precision due to shorter periods for full scanning cycles. This means that $\Delta r_{\rm user} = v_{\rm user} \times t_{\rm step}$ is smaller within one t_{step} for lower values of t_{step} , leading to more precise tracking. Note that selecting $t_{\rm step} = 0.001\,{\rm ms}$ results in the same performance as $t_{\rm step} = 0.01\,{\rm ms}$. In contrast, for $t_{\rm step} = 1 \, \text{ms}$, the data rate decreases, and greater fluctuations occur in the average data rate. Larger values of $t_{\rm step}$ result in losing track of the user, as $\Delta r_{\rm user}$ becomes large compared to the scanning coverage. Consequently, the user is frequently positioned at the edge of the scanning coverage and eventually moves out of the scanning range. For Figs. 4.5 and 4.6, similar trends are observed. A larger θ_{FWHM} provides wider scanning coverage, making tracking more robust against larger values of $\Delta r_{\rm user}$. For instance, in Fig. 4.4, tracking fails at $t_{\text{step}} = 1.1 \,\text{ms}$ for $\theta_{\text{FWHM}} = 0.4^{\circ}$. In contrast, in Fig. 4.5, tracking fails after $t_{\rm step} > 2 \, \text{ms}$ for $\theta_{\rm FWHM} = 1^{\circ}$, and in Fig. 4.6, it fails after $t_{\rm step} > 5 \, \text{ms}$ for $\theta_{\text{FWHM}} = 4^{\circ}$.

4.1.3 Effect of Beam Divergence Angle on Rate of DBS Scheme

The effect of $\theta_{\rm FWHM}$ on the average achievable data rate is now investigated for a user moving linearly from the center to the corner of the room. Figures 4.7, and 4.8 represent the results for $t_{\rm step} = 0.1\,\mu s$, and $t_{\rm step} = 1\,\rm ms$ respectively. In this simulation, $n_{\rm spot} = 3$, $\delta d_{\rm rx} = 89\,\rm cm$, and $x_{\rm scan} = 0.5$ are considered. It can be observed from Fig. 4.7 that $\theta_{\rm FWHM} = 0.047^{\circ}$ yields the highest average data rate, consistent with the expectation based on Fig. 2.4 in the previous chapter. The choice of $\theta_{\rm FWHM} = 0.047^{\circ}$ gives the minimum beam divergence and highest SNR, thus maximum rate can be achieved if the tracking precision is extremely high. Increasing $\theta_{\rm FWHM}$ results in degradation in the

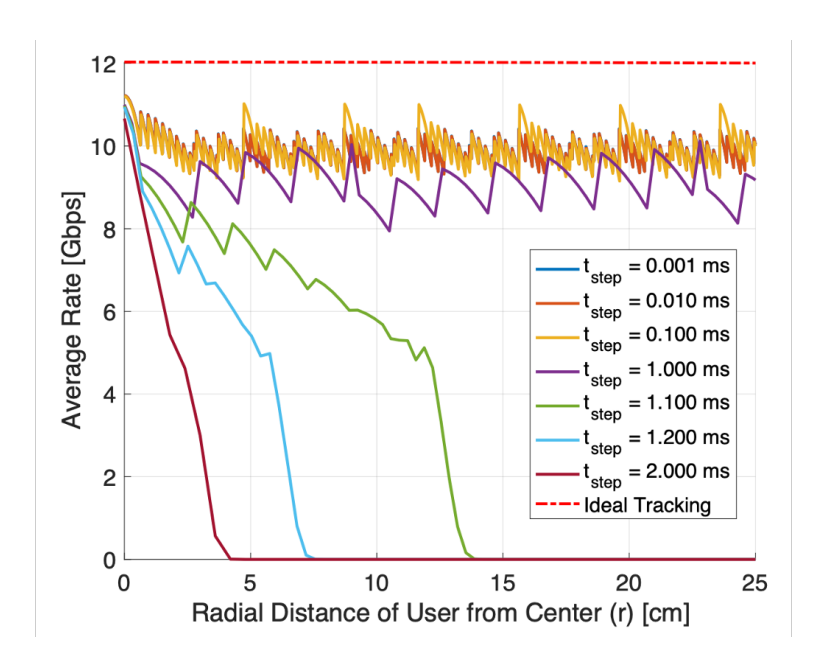


Figure 4.4: Data rate vs radial distance of user from center with $\theta_{\rm FWHM}=0.4^{\circ}$ for difference $t_{\rm step}$ times for tracking

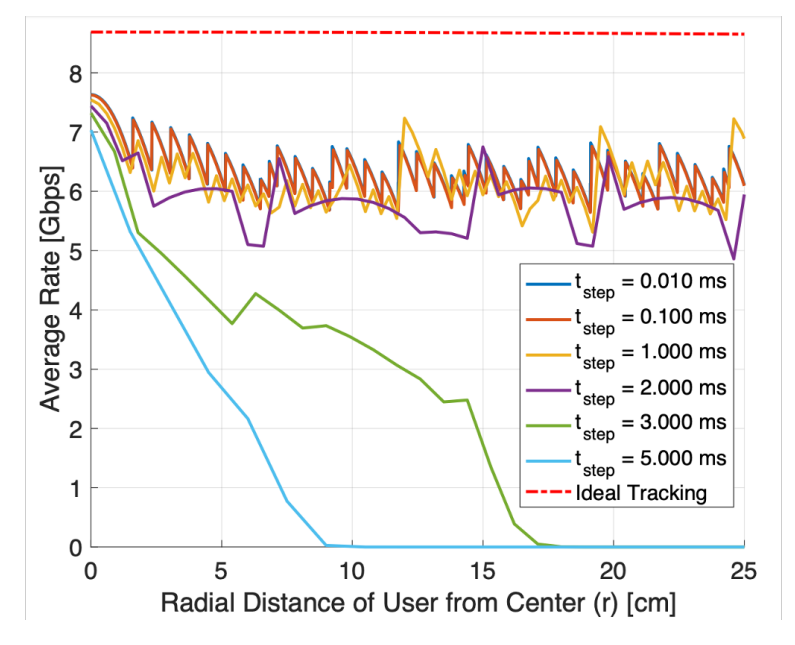


Figure 4.5: Data rate vs radial distance of user from center with $\theta_{\rm FWHM}=1^{\circ}$ for difference $t_{\rm step}$ times for tracking

average rate. Moreover, in Fig. 4.8, tracking is done with larger t_{step} and communication is lost when the user moves. Only with $\theta_{\text{FWHM}} = 0.4^{\circ}$, 0.5° the tracking is successful

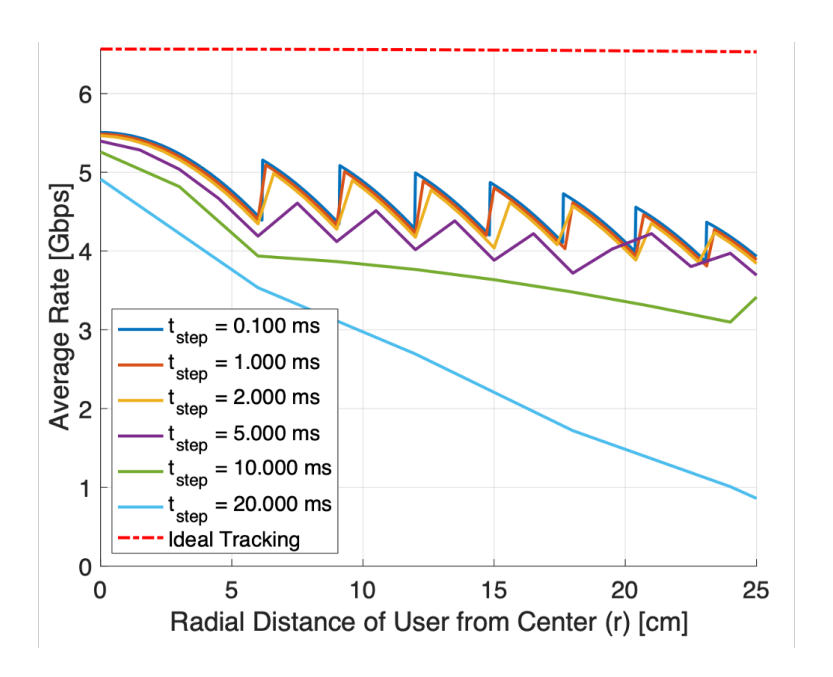


Figure 4.6: Data rate vs radial distance of user from center with $\theta_{\rm FWHM}=4^{\circ}$ for difference $t_{\rm step}$ times for tracking

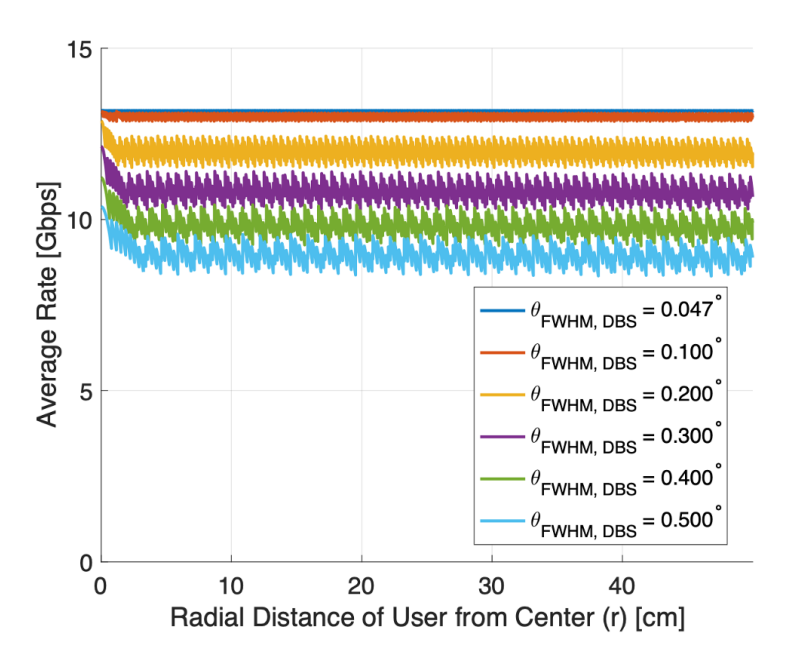


Figure 4.7: Data rate vs radial distance of user from center for different $\theta_{\rm FWHM}$ values with $t_{\rm step}=0.1\mu s$

and $\theta_{\rm FWHM}=0.4^{\circ}$ gives the better performance. Therefore, in the following simulations, $\theta_{\rm FWHM}=0.4^{\circ}$ is considered when $t_{\rm step}=1\,{\rm ms}$ is selected.

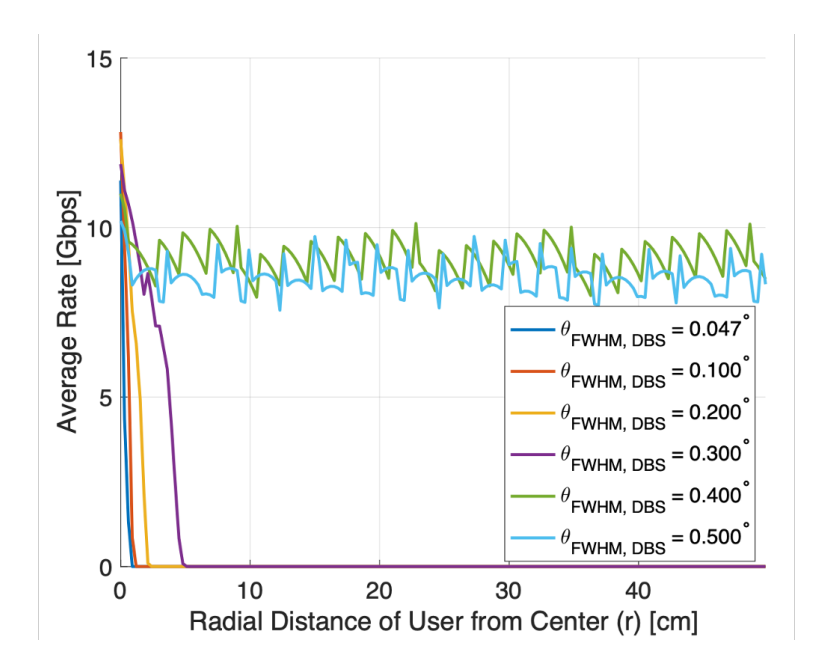


Figure 4.8: Data rate vs radial distance of user from center for different $\theta_{\rm FWHM}$ values with $t_{\rm step}=1\,{\rm ms}$

4.1.4 Effect of Spot Numbers Per Scanning on Rate of DBS Scheme

The effect of the number of beam spot positions per scanning cycle, $n_{\rm spot}$, is illustrated in Figs. 4.9 and 4.10. In both figures, $\delta d_{\rm rx}=89\,{\rm cm}$, the user moves linearly from the center to the corner. In Fig. 4.9, $\theta_{\rm FWHM}=0.4^{\circ}$, while in Fig. 4.10, $\theta_{\rm FWHM}=2^{\circ}$. It can be observed from Fig. 4.9(a) that with $t_{\rm step}=0.1\,{\rm ms}$, larger fluctuations occur when $n_{\rm spot}=3$, while the curve of the average data rate becomes smoother as $n_{\rm spot}$ increases. This behavior can be explained as follows. With high-precision tracking ($t_{\rm step}=0.1\,{\rm ms}$), a larger number of spot positions $n_{\rm spot}$ enables more accurate updates of the circular scanning pattern center. As a result, the user remains closer to the pattern center, which yields $n_{\rm spot}$ ACKs in each cycle and thus a higher data rate. In contrast, for $t_{\rm step}=1\,{\rm ms}$ (see Fig. 4.9(b)), corresponding to lower tracking precision, setting $n_{\rm spot}=3$ provides a better average data rate. In this case, the AP scans fewer spots per cycle, allowing faster updates of the pattern center and improving responsiveness compared to configurations with larger $n_{\rm spot}$.

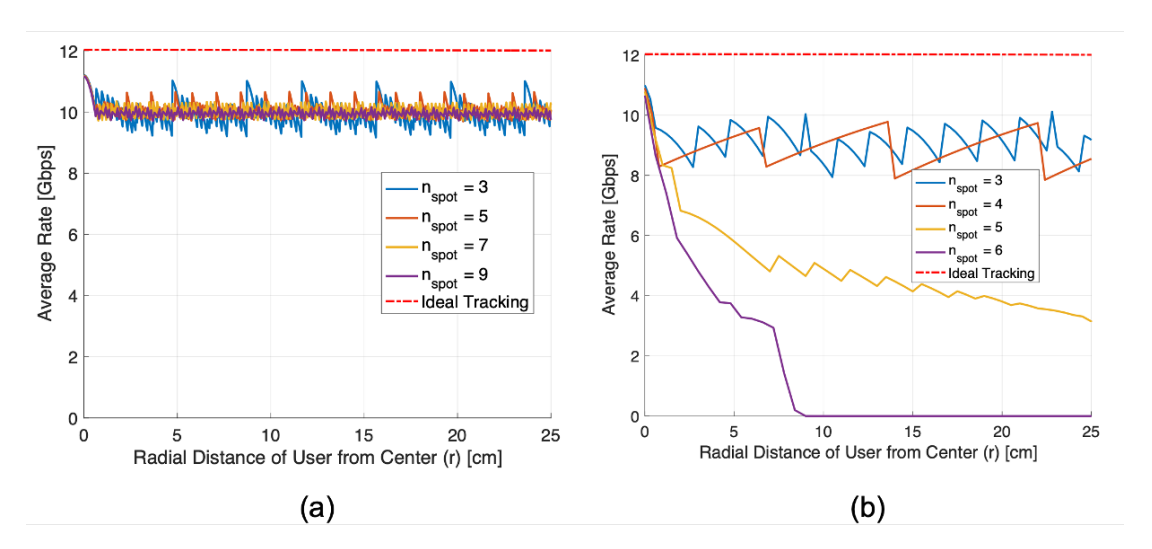


Figure 4.9: Data rate vs radial distance of user from center with $\theta_{\rm FWHM} = 0.4^{\circ}$ for different $n_{\rm spot}$ number per scanning; (a) $t_{\rm step} = 0.1 \, \rm ms$, (b) $t_{\rm step} = 1 \, \rm ms$

The average of achievable rate when user moves from center to the corner of the room on XY plane, is 8.97, 9.13, 9.08, 9.07, 9.01 [Gbps] for $n_{\rm spot}=3$, 4, 5, 6, 9, respectively. Therefore selecting $n_{\rm spot}=4$ results in better performance for high precision tracking depending on $\theta_{\rm FWHM}$. Also for $t_{\rm step}=0.01\,{\rm ms}$, selecting $n_{\rm spot}=4$ leads to the higher average data rate. In contrast, in Fig. 4.9(b), selecting $n_{\rm spot}=3$ provides better tracking performance compared to $n_{\rm spot}=4$ where average of data rate is 8.61 [Gbps] and 8.56 [Gbps] for $n_{\rm spot}=3$ and $n_{\rm spot}=4$ respectively. Moreover, for $n_{\rm spot}\geq 5$, tracking fails, and the AP cannot maintain communication. This failure occurs because when the AP points the beam to multiple spot positions within one cycle, the user moves to the edge of the scanning coverage and eventually moves out of the scanning range for larger radial distances, making it difficult for the AP to predict the next tracking direction. Therefore, for lower precision tracking, i.e., larger $t_{\rm step}$, selecting a smaller $n_{\rm spot}$, particularly $n_{\rm spot}=3$, leads to better results in terms of achievable data rate.

Fig. 4.10(a) shows tracking with $t_{\text{step}} = 1 \text{ ms}$, which represents high tracking precision for $\theta_{\text{FWHM}} = 2^{\circ}$. Selecting $n_{\text{spot}} = 4$ results in a higher average data rate compared to

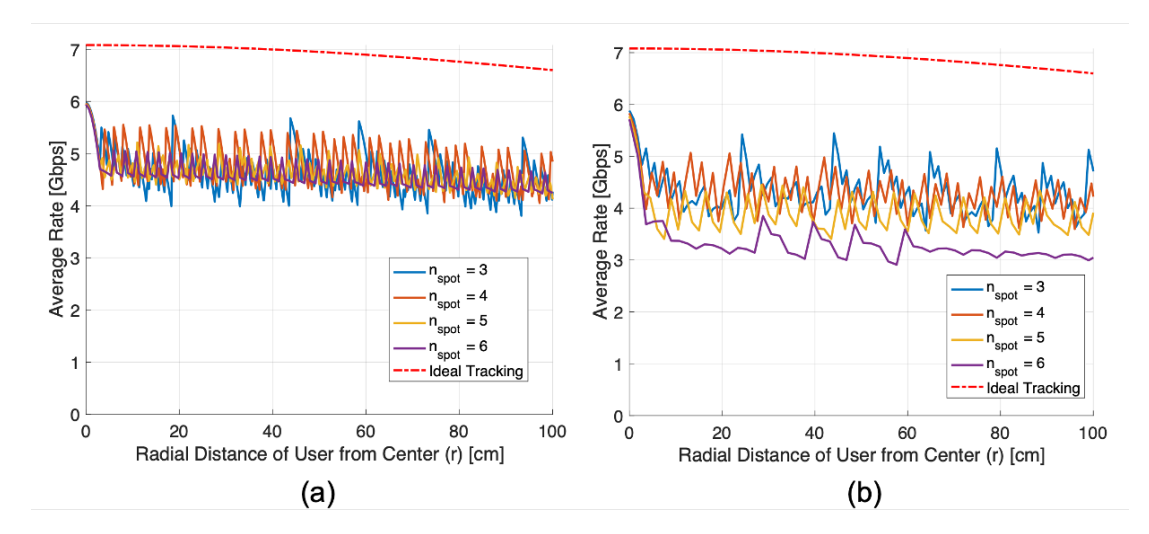


Figure 4.10: Data rate vs radial distance of user from center with $\theta_{\text{FWHM}} = 2^{\circ}$ for different n_{spot} number per scanning; (a) $t_{\text{step}} = 1 \, ms$, (b) $t_{\text{step}} = 3 \, ms$

 $n_{\rm spot}=3$. However, selecting $n_{\rm spot}=5$ or 6 degrades performance, since the AP must scan more spot positions in each cycle. During this longer scanning process, the user, moving linearly toward the corner, shifts closer to the edge of the coverage region, reducing alignment accuracy and thus lowering the achievable rate. Selecting $t_{\rm step}=3$ ms in Fig. 4.10(b) results in a higher average rate for $n_{\rm spot}=3$ and a lower rate for $n_{\rm spot}\geq 4$.

4.1.5 Effect of Scanning Radius on Rate of DBS Scheme

In Figs. 4.11, 4.12, and 4.13, the effect of $x_{\text{scan}} = r_{\text{scan}}/\omega(h)$ is investigated for $\theta_{\text{FWHM}} = 0.4^{\circ}, 4^{\circ}$ respectively, where $\delta d_{\text{rx}} = 89 \,\text{cm}$, and $n_{\text{spot}} = 3$. In Fig. 4.11, it can be observed that the curves corresponding to $x_{\text{scan}} = 0.5, 0.6, 0.7$ result in higher average data rates compared to other curves when $t_{\text{step}} = 1 \,\text{ms}$. More precisely, the average data rates when the user moves from the center to $(2.5 \,\text{m}, 2.5 \,\text{m})$ are $9.02, 9.26, 9.19 \,\text{Gbps}$ for $x_{\text{scan}} = 0.5, 0.6, 0.7$ respectively. Selecting $t_{\text{step}} = 0.1 \,\text{ms}$ results in the same trend for the mentioned x_{scan} values, with $x_{\text{scan}} = 0.6$ showing slightly superior performance. In Fig. 4.12, $t_{\text{step}} = 1.5 \,\text{ms}$ is selected for $\theta_{\text{FWHM}} = 0.4^{\circ}$. Only with $x_{\text{scan}} = 0.9, 1$ does tracking not fail to maintain communication. This is due to the higher scanning coverage area of

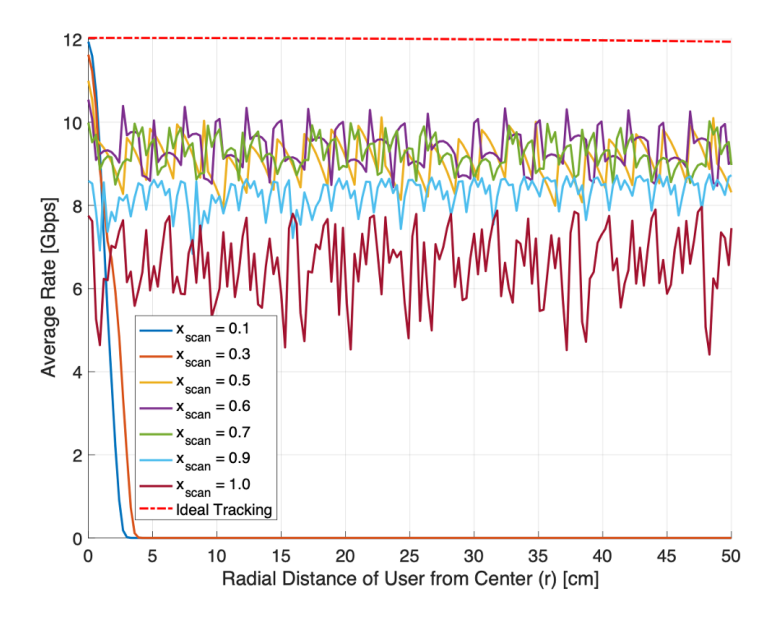


Figure 4.11: Data rate vs radial distance of user from center with $\theta_{\rm FWHM}=0.4^{\circ}$ for difference $x_{\rm scan}=\frac{r_{\rm scan}}{\omega(h)}$ values for tracking with $t_{\rm step}=1\,{\rm ms}$

the AP compared to smaller values of $x_{\rm scan}$. This demonstrates that if tracking precision is low for $\theta_{\rm FWHM}$, increasing $x_{\rm scan}$ to 1 allows tracking to be maintained. Moreover, Fig. 4.13 shows the performance comparison for $\theta_{\rm FWHM}=4^{\circ}$ when $t_{\rm step}=1\,{\rm ms}$. Since the tracking precision of $t_{\rm step}$ is high for $\theta_{\rm FWHM}=4^{\circ}$, selecting $x_{\rm scan}=0.5$ balances the trade-off between scanning coverage and data rate. When $x_{\rm scan}$ is larger, the user is close to the edges of the scanning coverage in a cycle, similar to the case when $x_{\rm scan}<0.5$.

4.1.6 Effect of Initial Localization Error on DBS Scheme Performance

In previous simulations, it is assumed that there is no initial localization error for the starting position of DBS tracking. The user starts from the position $(0,0,1\,m)$, and the DBS scheme knows the exact initial location of the user. In practice, the initial location must be estimated using a multi-stage spiral search, which introduces errors in the initial position estimation. To incorporate this error into the tracking analysis, it is assumed that the initial position has an error modeled by a Gaussian distribution with

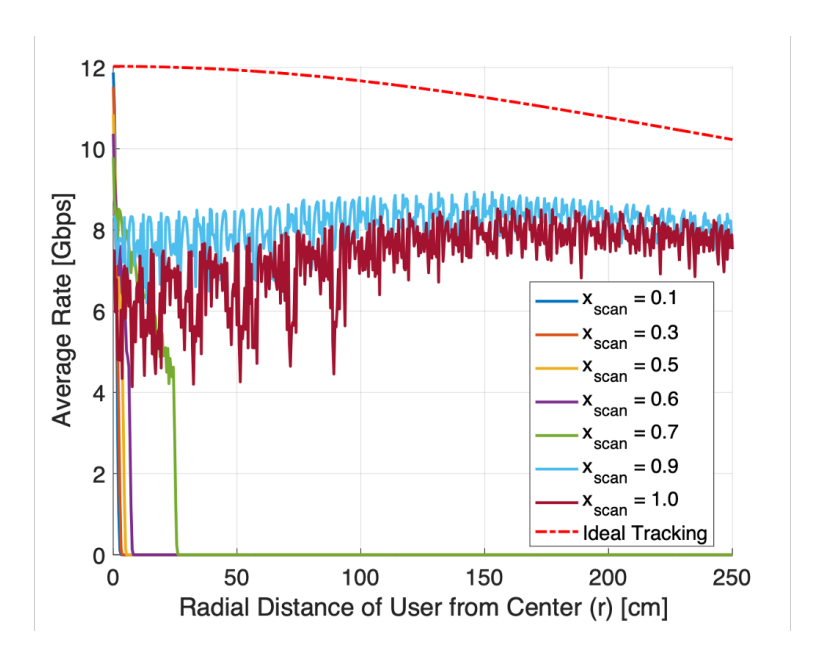


Figure 4.12: Data rate vs radial distance of user from center with $\theta_{\rm FWHM}=0.4^{\circ}$ for difference $x_{\rm scan}=\frac{r_{\rm scan}}{\omega(h)}$ values for tracking with $t_{\rm step}=1.5\,ms$

zero mean and standard deviation σ_s . A Monte Carlo simulation with 1000 iterations is then performed for tracking with a given standard deviation, and the average of the average data rate is computed as the user moves from the center to the corner of the room. In this simulation, $t_{\text{step}} = 1 \,\text{ms}$, $n_{\text{spot}} = 3$, $\delta d_{\text{rx}} = 89 \,\text{cm}$, and $x_{\text{scan}} = 0.5$ are considered, and the DBS scheme is compared across different σ_s values for a θ_{FWHM} .

Fig. 4.14 illustrates the performance comparison of the DBS scheme for different values of σ_s in a Monte Carlo simulation. The figure shows the average of the average data rate after 1000 iterations. The curve corresponding to zero initial localization error $(\sigma_s = 0)$, is obtained from a single simulation. In contrast, the other curves represent the average of 1000 simulations and appear smoother. It can be observed that the curves for $\sigma_s = 0.1 \,\mathrm{cm}, 0.5 \,\mathrm{cm}$ maintain a data rate similar to the case with no initial localization error $(\sigma_s = 0)$. The minimum beam radius for $\theta_{\mathrm{FWHM}} = 0.4^{\circ}$ is $\omega(h) = 1.19 \,\mathrm{cm}$, and the minimum radius of the scanning coverage is $r_{\mathrm{scan}} + \omega(h) \approx 1.78 \,\mathrm{cm}$. Therefore, when $\sigma_s > 1.78 \,\mathrm{cm}$, the data rate deteriorates, and the AP may lose track of the user. For

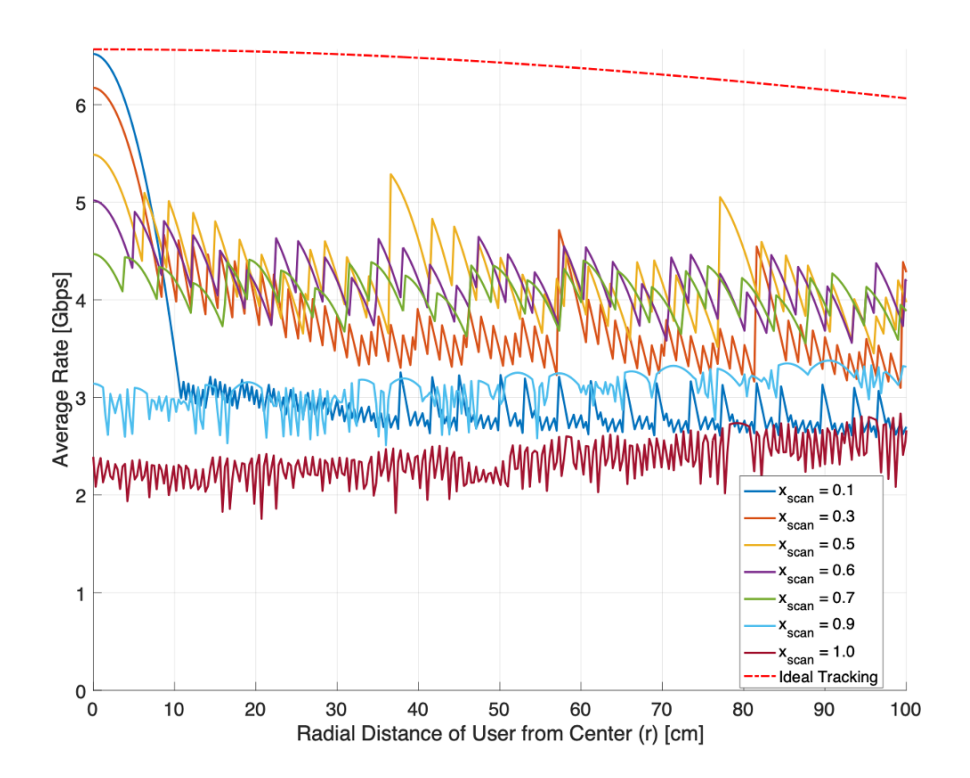


Figure 4.13: Data rate vs radial distance of user from center with $\theta_{\rm FWHM} = 4^{\circ}$ for difference $x_{\rm scan} = \frac{r_{\rm scan}}{\omega(h)}$ values for tracking with $t_{\rm step} = 1\,ms$

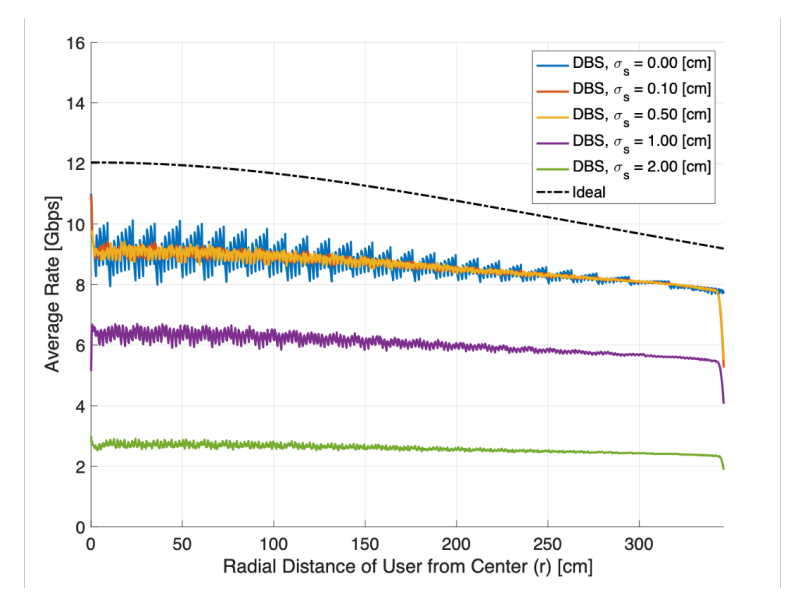


Figure 4.14: Average data rate vs radial distance of user for different σ_s values for initial localization error for DBS scheme with $\theta_{\rm FWHM}=0.4^\circ$

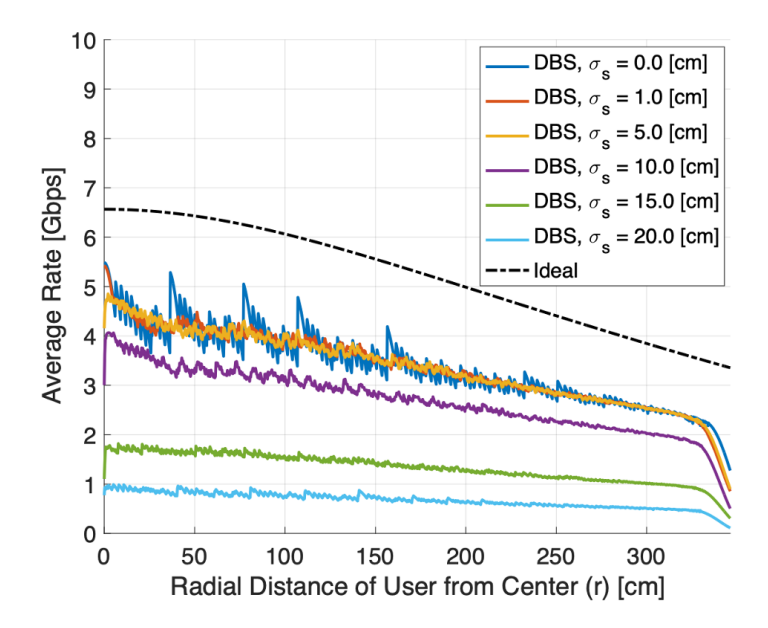


Figure 4.15: Average data rate vs radial distance of user for different σ_s values for initial localization error for DBS scheme with $\theta_{\rm FWHM}=4^{\circ}$

 $\sigma_s=1\,\mathrm{cm}, 2\,\mathrm{cm}$, tracking is still maintained, but the average data rate drops significantly. Moreover, Fig. 4.15 represents the similar performance comparison for $\theta_{\mathrm{FWHM}}=4^\circ$ which is more robust against initial localization error since $\omega(h)+r_{scan}=17.79\,\mathrm{cm}$. It can be seen that $\sigma_s=1\,\mathrm{cm}, 5\,\mathrm{cm}$ gives the same average data rate. Furthermore, with $\sigma_s\geq 10\,\mathrm{cm}$, the average data rate drops.

4.1.7 Effect of Noise in Beam Pointing on the Performance of DBS Scheme

In practice, there will be noise in pointing due to imperfections of the beam steering device or vibrations of the building, which introduces inaccuracy in pointing. To examine this effect, zero-mean Gaussian additive noise is considered for the beam pointing vector $S^{(t)} = \left(x_s^{(t)}, y_s^{(t)}\right)$ at time t. Therefore,

$$S'^{(t)} = \left(x_s^{(t)} + n_x^{(t)}, y_s^{(t)} + n_y^{(t)}\right),\tag{4.1}$$

is obtained, indicating random noise in pointing position with a standard deviation of σ_p [m]. The parameter σ_p is linked to the intrinsic angular pointing noise specified for the beam steering device. Conceptually, this relationship can be expressed by comparing the noiseless angles $\theta^{(t)}$ and $\varphi^{(t)}$ at time step t (from (3.4) and (3.5)) with their noisy counterparts $\theta'^{(t)}$ and $\varphi'^{(t)}$ derived from (4.1) on the XY plane at z=1 m. Thus, σ_p should be regarded as a free parameter determined by the characteristics of the steering device, rather than a value computed from the simulation. The elevation and azimuth errors can then be defined as

$$\Delta \theta^{(t)} = \theta'^{(t)} - \theta^{(t)},$$

$$\Delta \phi^{(t)} = \varphi'^{(t)} - \varphi^{(t)}.$$
(4.2)

Since the pointing-angle noise is modeled as zero-mean additive Gaussian noise, the standard deviation is given by

$$\sigma_{\theta} = \sqrt{\frac{1}{N_t - 1} \sum_{i=1}^{N_t} (\Delta \theta_i)^2}, \tag{4.3}$$

$$\sigma_{\varphi} = \sqrt{\frac{1}{N_t - 1} \sum_{i=1}^{N_t} (\Delta \varphi_i)^2},\tag{4.4}$$

where $N_t = t_{\text{tot}}/t_{\text{step}}$ is the number of total simulation time steps.

Fig. 4.16, and 4.17 shows the performance comparison for different σ_p values for $\theta_{\rm FWHM}=0.4^{\circ}$, 4° respectively. Note that the Monte-Carlo simulation is performed with 1000 iterations, and the average of the data rate is demonstrated in the figures. It can be observed from Fig. 4.16 that having $\sigma_p=1$ mm degrades the data rate slightly compared to the curve corresponding to $\sigma_p=0$. Given $\sigma_p=1$ mm, and using (4.3) and (4.4), the angular standard deviations σ_{θ} and σ_{φ} can be obtained in the simulation and averaged over multiple Monte Carlo iterations. In this case, $\sigma_{\theta}=69.63\,\mu{\rm rad}$ and $\sigma_{\varphi}=258.61\,\mu{\rm rad}$ were computed by averaging across 10,000 Monte Carlo runs. These results indicate that a tracking system with $\theta_{\rm FWHM}=0.4^{\circ}$ is highly sensitive and strongly dependent on the

pointing accuracy of the beam steering device.

Moreover, in Fig. 4.17, the DBS tracking is robust against standard deviations of $\sigma_p=10\,\mathrm{mm},\,20\,\mathrm{mm},\,30\,\mathrm{mm}$ and the data rate degrades with $\sigma_p\geq40\,\mathrm{mm}$. It can be observed that a higher θ_{FWHM} reduces the sensitivity of the DBS scheme to pointing errors. For example, in this figure, with $\sigma_p=50\,\mathrm{mm}$, the average data rate is still maintained at a level comparable to the case with $\sigma_p=0$. In this figure, the curve corresponding to $\sigma_p=30\,\mathrm{mm}$ maintains the tracking and communication, whereas curves with larger σ_p values exhibit a significant performance drop. Therefore, for $\theta_{\mathrm{FWHM}}=4^\circ$, the system remains robust to pointing noise up to approximately $\sigma_p=30\,\mathrm{mm}$, which corresponds to $\sigma_\theta=0.95\,\mathrm{mrad}$ and $\sigma_\varphi=3.5\,\mathrm{mrad}$, computed from (4.3) and (4.4) and averaged over 10,000 Monte Carlo iterations.

Angular pointing noise varies with the steering technology. MEMS micromirrors specify point-to-point precision as a proxy for jitter, with reported values of about $3.5\,\mu\mathrm{rad}$ per axis [108] which is equivalent to $\sigma_p = 0.05\,\mathrm{mm}$ for $\theta_{\mathrm{FWHM}} = 0.4^\circ$ from simulation. OPAs have demonstrated root-mean-square (RMS) pointing precision of $8.1\,\mu\mathrm{rad}$ ($\approx \sigma_p = 0.12\,\mathrm{mm}$ for $\theta_{\mathrm{FWHM}} = 0.4^\circ$) at $1550\,\mathrm{nm}$ under active phase locking [109]. In contrast, SLMs specify phase stability rather than angular noise. For example, Meadowlark Optics reports phase ripple of $0.002\pi-0.02\pi\,\mathrm{rad}$, corresponding to 6.3-62.8 mrad of phase variation [110]. The impact of angular pointing noise on the proposed DBS system depends on the selected θ_{FWHM} . For narrow beams, such as $\theta_{\mathrm{FWHM}} = 0.4^\circ$, the angular noise standard deviations of $\sigma_\theta > 69.63\,\mu\mathrm{rad}$ and $\sigma_\varphi > 258.61\,\mu\mathrm{rad}$ (equivalent to $\sigma_p > 1\,\mathrm{mm}$ obtained from simulation) become significant and noticeably degrade tracking and communication performance, as shown in Fig. 4.16. For this beam divergence, both OPAs and MEMS mirrors are capable of supporting DBS tracking and communication since their σ_θ and σ_φ values remain well below these thresholds.

Let the pointing error of DBS tracking at time step t on XY plane at z = 1 m is

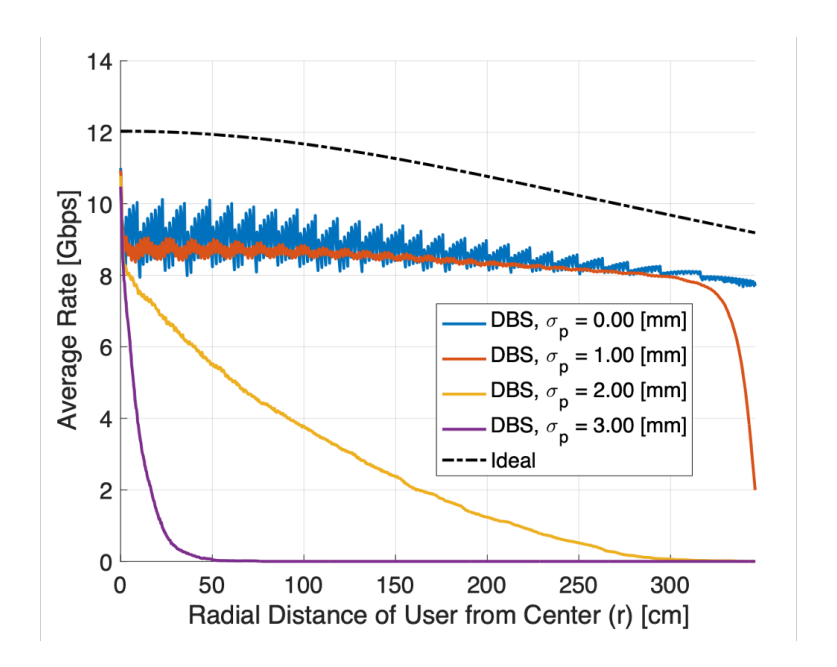


Figure 4.16: Average data rate vs radial distance of user from center for $\theta_{\rm FWHM}=0.4^{\circ}$, considering noise in pointing for DBS scheme with different standard deviation, σ_p values

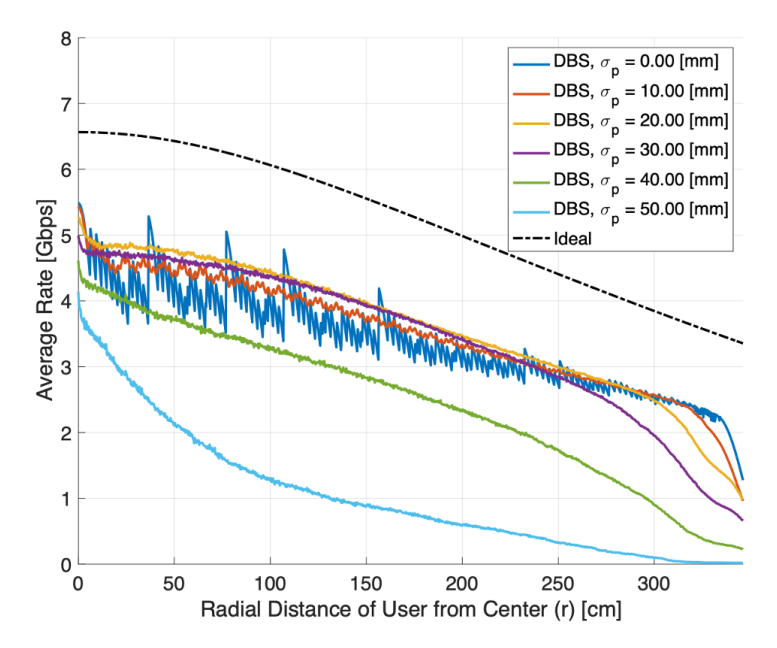


Figure 4.17: Average data rate vs radial distance of user from center for $\theta_{\rm FWHM} = 4^{\circ}$, considering noise in pointing for DBS scheme with different standard deviation, σ_p values

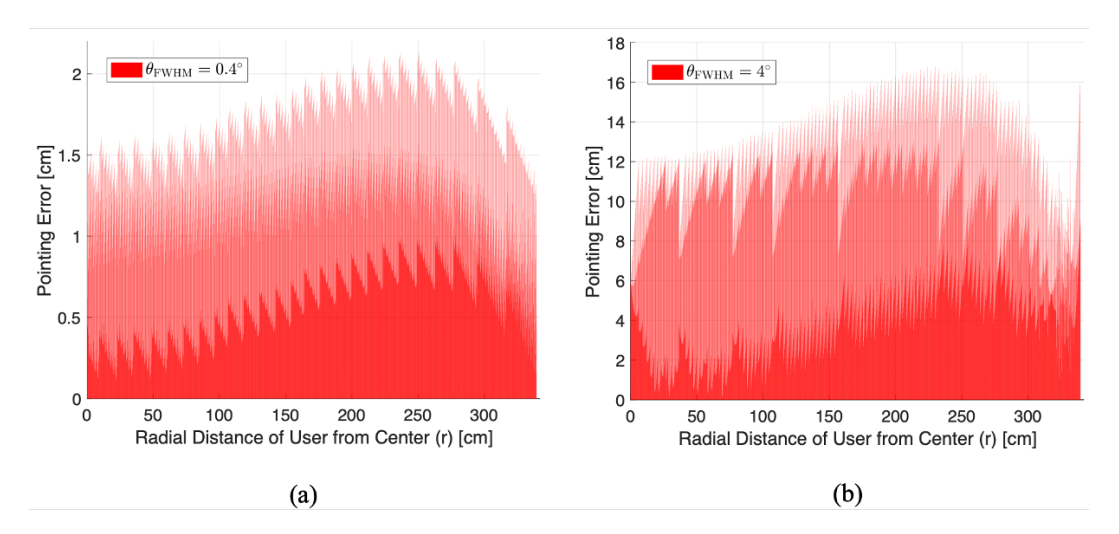


Figure 4.18: Pointing error of DBS tracking (computed from (4.5)) considering $\sigma_p = 0$, $\sigma_s = 0$, versus radial distance of user when moving linearly from center to corner of room; (a) $\theta_{\text{FWHM}} = 0.4^{\circ}$, (b) $\theta_{\text{FWHM}} = 4^{\circ}$

defined as difference between pointing position $(x_s^{(t)}, y_s^{(t)})$ and user position (x_{rx}, y_{rx}) , and can be computed as

$$err_{DBS}^{(t)} = \sqrt{(x_s^{(t)} - x_{rx}^{(t)})^2 + (y_s^{(t)} - y_{rx}^{(t)})^2}.$$
 (4.5)

Figure 4.18 illustrates the pointing error err_{DBS} for $\theta_{FWHM} = 0.4^{\circ}$ and 4° under noiseless beam steering ($\sigma_p = 0$) and zero initial localization error ($\sigma_s = 0$). The maximum error is 2.13 cm in Fig. 4.18(a) and 16.77 cm in Fig. 4.18(b).

Figure 4.19 shows the DBS pointing error for (a) $\theta_{\rm FWHM} = 0.4^{\circ}$, $\sigma_p = 1 \, \rm mm$ and (b) $\theta_{\rm FWHM} = 4^{\circ}$, $\sigma_p = 30 \, \rm mm$, averaged over 1000 Monte Carlo iterations. Compared with Fig. 4.18(a) (noiseless case), panel (a) exhibits a similar overall pattern, except for a pronounced error growth near the room corner, which reduces the data rate (cf. Fig. 4.16, curve for $\sigma_p = 1 \, \rm mm$). Panel (b) demonstrates lower sensitivity to pointing noise, consistent with the results in Fig. 4.17 (curve for $\sigma_p = 30 \, \rm mm$).

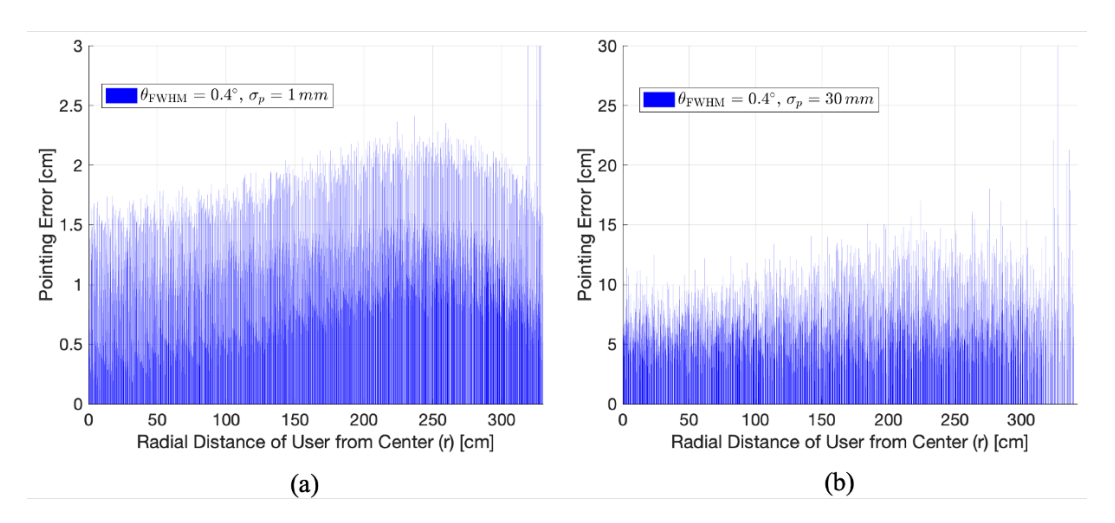


Figure 4.19: Pointing error of DBS tracking (computed from (4.5)) considering $\sigma_s = 0$, versus radial distance of user when moving linearly from center to corner of room; (a) $\theta_{\rm FWHM} = 0.4^{\circ}$ $\sigma_p = 1$ mm, and (b) $\theta_{\rm FWHM} = 4^{\circ}$, $\sigma_p = 30$ mm,

4.2 Parameter Selection for DBS System

In Section 4.1, the impact of the design parameters on the proposed DBS scheme is analyzed (see also Fig. 4.1). To balance the inherent trade-offs, the DBS parameters are selected to provide a complete system design while accounting for practical constraints. The chosen parameters are summarized in Table 4.2.

According to the table, the selection of $\delta d_{\rm tx}=89\,{\rm cm}$ is examined in Subsection 4.1.1, yielding $\rho_{\rm th}=0.316$ for $\theta_{\rm FWHM}=0.4^{\circ}$ as computed from (3.20). The parameters $\theta_{\rm FWHM}=0.4^{\circ}$ and $t_{\rm step}=1\,{\rm ms}$ are chosen based on the results presented in Subsections 4.1.3, and 4.1.2. The number of discrete spot positions on the circular tracking pattern, $n_{\rm spot}=3$, is selected according to the trade-off discussed in Subsection 4.1.4, with respect to $t_{\rm step}=1\,{\rm ms}$ and $\theta_{\rm FWHM}=0.4^{\circ}$. The scanning radius, defined as $r_{\rm scan}=x_{\rm scan}\,\omega(h)$, where $x_{\rm scan}=0.5$ is determined from the analysis in Subsection 4.1.5 for $\theta_{\rm FWHM}=0.4^{\circ}$. Noise in pointing, σ_p , and initial localization error, σ_s , are discussed in Subsections 4.1.7, and 4.1.6 respectively. For $\theta_{\rm FWHM}=0.4^{\circ}$, the results in Subsection 4.1.7 show that values of $\sigma_p>1\,{\rm mm}$ cause significant rate degradation; therefore,

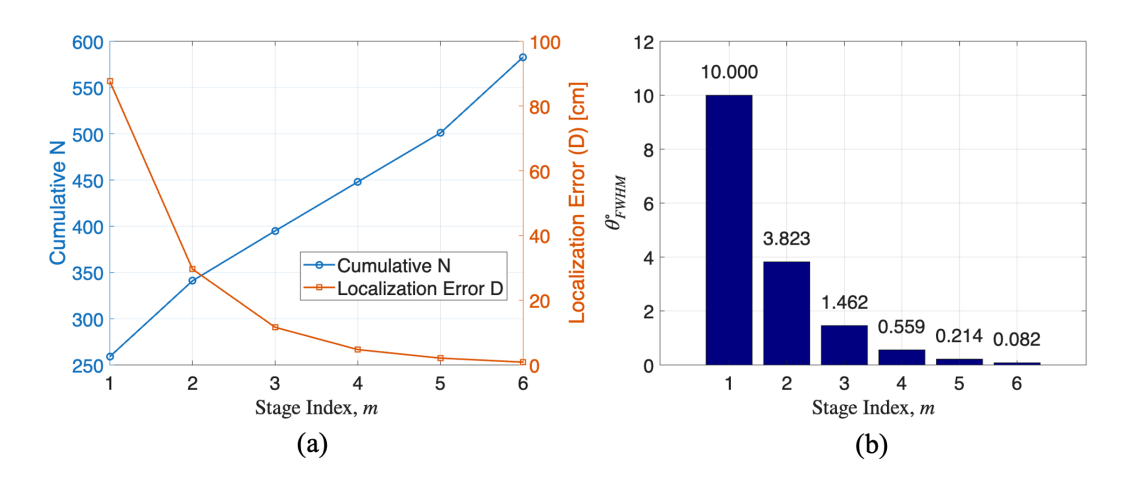


Figure 4.20: Multi-stage localization with M=6 total stages for $\epsilon=1\,\mathrm{cm}$ accuracy: (a) cumulative spot numbers N and localization error D versus stage index m, (b) corresponding optimal $\theta_{\mathrm{FWHM}}^{(i)}$ values at each stage index m.

 $\sigma_p = 1 \,\mathrm{mm}$ is adopted for the simulations.

The results for the initial localization algorithm are presented in Fig. 4.20. In Fig. 4.20(a), M=6 stages are considered, following the observation from Fig. 3.14(a) that increasing the number of stages to 6 significantly reduces the maximum localization delay compared to smaller values of M. From Fig. 4.20(a), the localization error at the most distant point, i.e., (2.5, 2.5, 1) [m], corresponding to the worst-case scenario, is 0.86 cm at the final stage. Based on this finding, a standard deviation of $\sigma_s = 0.86$ cm is adopted for the initial localization error (as shown in Table 4.2) in the Monte Carlo simulations of DBS tracking. In addition, the total number of beam spots required to achieve the target accuracy of $\epsilon = 1$ cm at this location is 583, which results in a maximum localization delay of 583 ms given the step time of $t_{\rm step} = 1$ ms. Furthermore, Fig. 4.20(b) illustrates the computed $\theta_{\rm FWHM}$ values for each stage. It is important to note that, for the required accuracy of $\epsilon = 1$ cm (at the most distant location), the divergence angle $\theta_{\rm FWHM,min}$ in Table 4.2 for the final spiral stage is obtained from (C.30).

Figure 4.21 compares the DBS scheme with and without considering pointing and

Table 4.2: System Parameters for Proposed DBS Architecture

Category	Parameter	Value
Transmitter	Beam steering device	MEMS / OPA
	Angular speed	$1/t_{ m step} = 1{ m kHz}$
	Beam configuration	Single beam with lens (adjustable divergence)
	Step time	$t_{\rm step} = 1{\rm ms}$
Room & User Model	Room dimensions	(2.5, 2.5, 3) [m]
	AP-user vertical distance	$h=2\mathrm{m}$
	User motion	Linear, $v_{\text{user}} = 1 \text{ m/s}$ on XY plane at $z = 1 \text{ m}$
Receiver & Link	Power threshold edge offset	$\delta d_{rx} = 89 \mathrm{cm}$
	$\rho_{\rm th}$ (threshold factor)	0.316
	Receiver parameters	From Table 2.6
	Receiver noise parameters	From Table 2.7
	Uplink feedback	ODTx / CCR / RF
	Wavelength	$\lambda = 1550\mathrm{nm}$
	Transmit eye-safe power	Computed from Table 2.5
Multi Stage Spiral Search	Number of stages	M = 6
	Spiral factor	$\alpha_s = 0.841$
	Initial Beam divergence	$\theta_{\mathrm{FWHM,max}} = 10^{\circ}$
	Final Beam Divergence	$\theta_{\mathrm{FWHM,min}} = 0.082^{\circ}$
	Target accuracy	$\epsilon = 1\mathrm{cm}$
DBS Tracking	Beam divergence	$\theta_{\mathrm{FWHM}} = 0.4^{\circ}$
	Transmit power	$P_t = 9.6 \mathrm{mW}$
	Scanning radius	$x_{\rm scan} = 0.5$
	Number of spots	$n_{\rm spot} = 3$
	Initial localization std	$\sigma_s = 0.86 \mathrm{cm}$
	Noise in pointing std	$\sigma_p = 1 \mathrm{mm}$

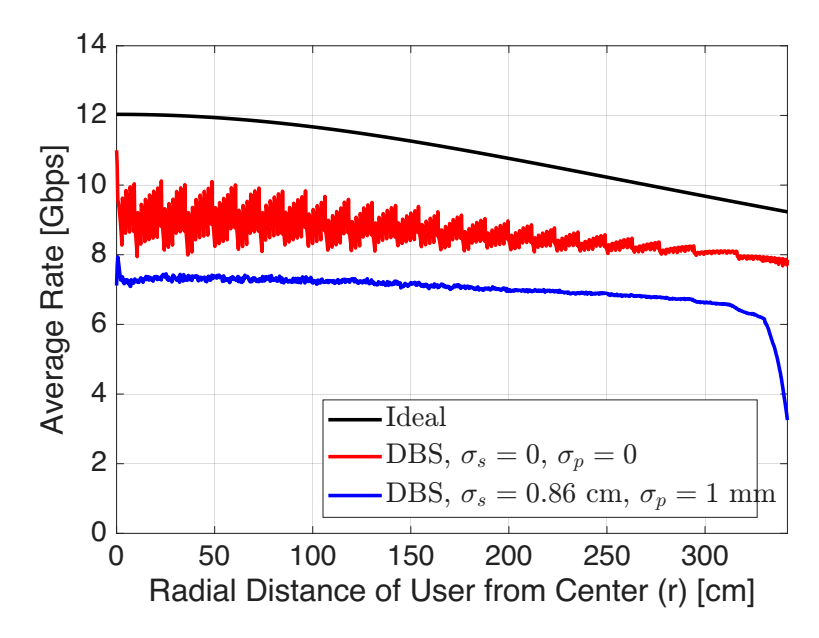


Figure 4.21: Implementation of the DBS scheme considering pointing and initial localization errors, compared with the case without noise and with ideal tracking.

localization noise (σ_s , σ_p from Table 4.2), alongside the ideal tracking performance. In this simulation, the user moves linearly at a constant speed of $v_{\rm user}=1\,\mathrm{m/s}$ from the center to the corner of the room on the XY plane. The curve corresponding to DBS with noise is averaged over 10,000 Monte Carlo simulations. As expected, smaller values of σ_s and σ_p cause the performance to approach that of the DBS scheme without noise. The feasibility of achieving beam divergence angles $\theta_{\rm FWHM}$ below 0.082° (see Fig. 4.20(b)) with available hardware reduces the initial localization error, thereby improving the performance and yielding a higher average data rate, closer to the noise-free DBS curve in Fig. 4.21. For instance, targeting a localization accuracy of $\epsilon=0.5\,\mathrm{cm}$ results in an error of 0.42 cm for $\theta_{\rm FWHM}=0.041^\circ$.

It is important to note that this level of precision in $\theta_{\rm FWHM}$ corresponds to the most distant point in the room, representing the worst-case scenario. In practice, achieving beam divergences well below $\theta_{\rm FWHM} = 0.4^{\circ}$ is feasible with current devices. Commercial compact fiber collimators specify full-angle beam divergence < 0.50 mrad (i.e., $\approx 0.029^{\circ}$),

which is already an order of magnitude tighter than 0.4°. At the integrated module level, state-of-the-art MEMS/Fourier beam scanners report measured far-field FWHM divergences on the order of 0.05°, demonstrating what is achievable with careful optical design and alignment [111].

Furthermore, depending on the capabilities of the selected beam steering device (see Table 2.8), the step time t_{step} can be further reduced, which would also enhance the overall performance. Note that the parameters in Table 4.2 are selected to illustrate the upper-limit performance of the DBS scheme while accounting for hardware constraints and impairments. The DBS scheme can be adapted to more relaxed conditions (e.g., larger θ_{FWHM} , higher localization error, reduced sensitivity to pointing noise, or larger t_{step}). However, such adaptations result in a lower average data rate (for given BW of 1.5 GHz) when the user is moving.

4.3 Comparison of DBS Scheme with Cellular Scheme

For comprehensive evaluation, this section benchmarks the DBS scheme against two scenarios, including an ideal case, where the AP perfectly tracks the user location with zero error and no feedback, and an atto-cell architecture, which assumes an ideal algorithm that activates a beam toward the user cell without delay, as described in [11]. This architecture is called the cellular scheme (see also Fig. 1.8) in the simulations, where 2500 VCSEL elements are considered, each pointed at its corresponding cell. Note that a PD is allocated next to each VCSEL element to enable activation based on the received feedback signal strength [11]. From Fig. 4.22, the position of i^{th} VCSEL element is \mathbf{P}_{tx}^i and it is slightly tilted towards the center of its corresponding cell, which is denoted as \mathbf{P}_{cell}^i . Thus the normal vector of i^{th} transmitter element is $\mathbf{n}_{tx}^i = (\mathbf{P}_{cell}^i - \mathbf{P}_{tx}^i) / \|\mathbf{P}_{cell}^i - \mathbf{P}_{tx}^i\|$ as shown in the figure. The parameters of the cellular scheme are listed in Table 4.3 based on [11]. From the table, a cell size of $10\,\mathrm{cm} \times 10\,\mathrm{cm}$ is selected, which is appropriate

Table 4.3: System Parameters for the Cellular Scheme based on [11]

Parameter	Value
Number of VCSEL elements	2500
Cell size	$10\mathrm{cm} \times 10\mathrm{cm}$
Beam divergence	$ heta_{ m FWHM} = 4^\circ$
Receiver parameters	From Table 2.6
Receiver noise	From Table 2.6
Spacing between VCSEL ele-	$12\mathrm{mm}$
ments	

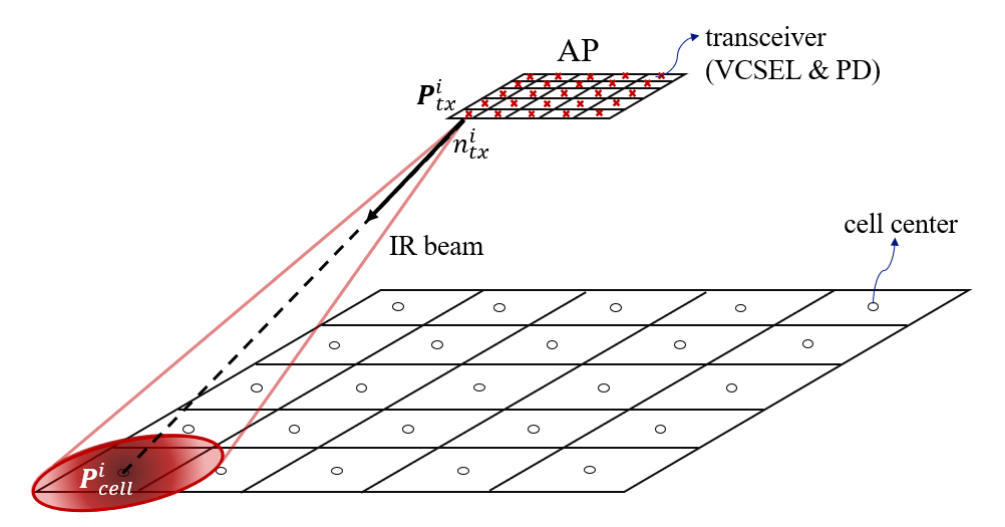


Figure 4.22: Downlink geometry of cellular architecture with VCSEL array based on [11]

for $\theta_{\text{FWHM}} = 4^{\circ}$ [11]. For simplicity and considering the cellular scheme from [11] to be ideal, it is assumed that the user can be perfectly tracked and if the user is in a certain cell, the corresponding beam will be activated with zero delay.

To enable a fair comparison between the proposed DBS scheme and the cellular architecture in [11], the following assumptions are made. First, no noise in pointing $(\sigma_p = 0)$ and no error in initial localization $(\sigma_s = 0)$ are considered in both schemes, since the cellular baseline from [11] did not include these impairments. This ensures that both schemes are benchmarked under equivalent conditions. Second, the DBS beam divergence $\theta_{\rm FWHM}$ and step time $t_{\rm step}$ are selected from Table 4.2, which represent feasible

values given hardware constraints. For the cellular scheme, a cell size of $10 \,\mathrm{cm} \times 10 \,\mathrm{cm}$ corresponding to $\theta_{\mathrm{FWHM}} = 4^{\circ}$ is chosen in line with [11], where 2500 VCSEL and PD elements are assumed to cover the room. In contrast, the DBS scheme employs a single beam steering device and one detector at the AP with transmit power of 9.6 mW. It is important to highlight that if the cellular scheme were designed with the same narrow beam divergence as DBS, i.e., $\theta_{\mathrm{FWHM}} = 0.4^{\circ}$, the required number of cells would increase to about $211 \times 211 = 44{,}521$, each with its own VCSEL and PD. Such a configuration is clearly impractical due to excessive hardware and power demands. Hence, following [11], the cellular scheme is evaluated with $\theta_{\mathrm{FWHM}} = 4^{\circ}$.

The simulation results are presented in Fig. 4.23. According to this figure, the curve corresponding to the cellular architecture is simulated for $\theta_{\rm FWHM}=4^{\circ}$ (according to [11]), the ideal system as a benchmark has the highest SNR value in each position and corresponds to $\theta_{\rm FWHM}=0.047^{\circ}$. This ideal case is compared with DBS architecture with $\theta_{\rm FWHM}=0.047^{\circ}$ with $t_{step}=0.1\,{\rm ms}$ for tracking precision to make the tracking for this $\theta_{\rm FWHM}$ value possible. Note that the maximum eye-safe power for this beam divergence is also 9.6 mW.

It can be observed that by having an extremely high precision tracking system (e.g., $t_{\rm step}=0.1\,{\rm ms}$), the DBS and ideal case give almost the same achievable data rate. In this figure, the DBS scheme with $\theta_{\rm FWHM}=0.4^{\circ}$, and $t_{\rm step}=1\,{\rm ms}$ is also demonstrated and compared with the ideal scheme gives the same beam divergence. By comparing the curves for DBS, $\theta_{\rm FWHM}=0.4^{\circ}$, and Cellular, $\theta_{\rm FWHM}=4^{\circ}$, it can be concluded that the DBS scheme outperforms the cellular architecture with only one IR beam, beam steering device, single detector at AP, and transmit power of 9.6 mW, whereas the transmit power for cellular architecture for each of the 2500 cells is 60 mW and a PD element is considered next to a VCSEL which means 2500 PDs are considered for cellular scheme. Moreover, the ideal tracking scheme and DBS scheme for $\theta_{\rm FWHM}=4^{\circ}$ are also

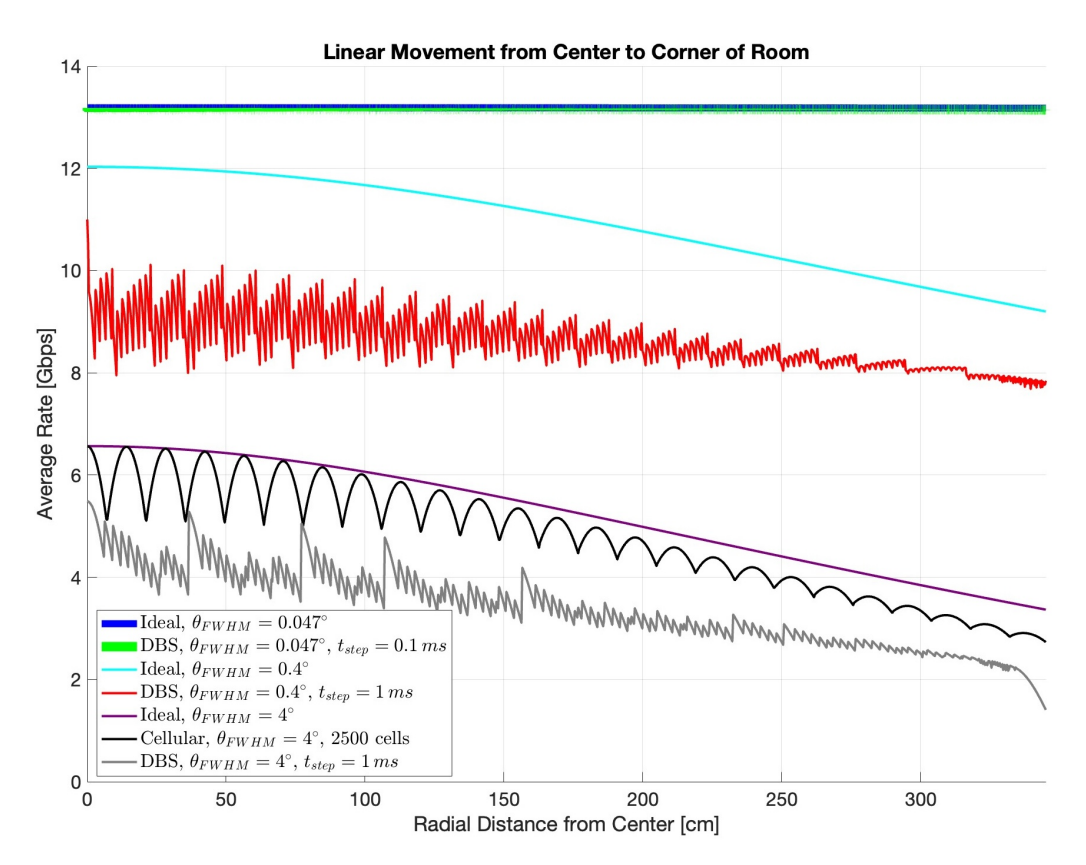


Figure 4.23: Comparison between DBS, cellular, and ideal schemes in terms of average rate vs radial distance from the center of the room for linear user movement

simulated in this figure. It is worth noting that the performance of cellular architecture and ideal tracking for the same beam divergence are very close. This comes at the cost of utilizing a large number of transmitter elements and detectors. For completeness, Appendix D provides a comparison between the exact P_r calculation (Appendix B) and the approximate method using (2.42) for the same setup, confirming the validity of the approximation used in the above analysis.

A comparison between the cellular scheme and the DBS scheme is presented in Table 4.4 for three cases that include basic DBS, intermediate DBS, and advanced DBS. The basic DBS corresponds to a lower-cost and performance design with less stringent tracking requirements, characterized by $t_{\rm step} < 5\,{\rm ms}$. The intermediate DBS represents

TABLE 4.4: Comparison of cellular and DBS schemes in terms of hardware and performance

Scheme	Details
Cellular	θ _{FWHM} : 4°
	Hardware: Array of 2500 VCSELs and PDs Power per VCSEL: 60 mW
	Maximum achievable rate (BW=1.5 GHz, room center): 6.57 Gbps
DBS (Basic)	$\theta_{\rm FWHM}\colon 4^{\circ}$ Hardware: Stepper motor / Galvo, 1 VCSEL, 1 PD, $t_{\rm step}$ up to 5 ms Power per VCSEL: 60 mW
	Maximum achievable rate (BW=1.5 GHz, room center): 5.49 Gbps
DBS (Intermediate)	$\theta_{\rm FWHM}$: 0.4° Hardware: Galvo/SLM/MEMS, 1 VCSEL, 1 PD, lens, $t_{\rm step}=1$ ms Power per VCSEL: ~ 10 mW
	Maximum achievable rate (BW=1.5 GHz, room center): 11 Gbps
DBS (Advanced)	$\theta_{\rm FWHM}$: 0.047° Hardware: MEMS/SLM/OPA, 1 VCSEL, 1 PD, lens, $t_{\rm step}=0.1$ ms Power per VCSEL: ~10 mW Maximum achievable rate (BW=1.5 GHz, room center): 13.19 Gbps

a moderate performance solution with improved beam steering capability, achieving $t_{\rm step}=1\,{\rm ms}$. The advanced DBS corresponds to a high-complexity beam steering configuration, targeting $t_{\rm step}=0.1\,{\rm ms}$. Achieving this performance requires a highly accurate and fast steering device, which comes at a higher cost. The comparison is made in terms of hardware requirements, power consumption, and maximum achievable rate. The performance of these three DBS schemes, relative to the cellular scheme, can be observed from Fig. 4.23.

The second motion model for comparing DBS, cellular, and ideal architectures is Brownian movement. It is assumed that the user moves randomly following Brownian motion on XY plane in $z=1\,m$ with an average speed of $v_{\rm user}=1\,m/s$. Brownian motion, or random walk, describes an unpredictable path in space. In practical scenarios, user movement can follow a random waypoint model, such as the one analyzed in [112], which characterizes user mobility with randomly selected destinations and pause times. This type of model is also employed in [11] to evaluate system performance. In contrast, Brownian motion is a more constrained form of random movement without defined waypoints, used here to demonstrate the robustness of the proposed tracking algorithm

under continuous, highly variable motion. Since discrete time steps for tracking are considered, it is assumed that the user is moving randomly at each $t_{\rm step}$. The distance moved by user in one $t_{\rm step}$ and the direction of movement is random and can be modeled as

$$X(t) = (x(t), y(t)) \tag{4.6}$$

$$\Rightarrow X(t + t_{\text{step}}) = X(t) + W(t), \tag{4.7}$$

where $W(t) = (\Delta x, \Delta y)$ is random vector corresponding to displacement in X, Y directions at time (t) with Gaussian distribution at each step and $\Delta x, \Delta y \sim N(0, \sigma^2)$. Moreover, to ensure that user speed does not exceed a maximum speed of v_{rx} , the maximum absolute value of displacement must be limited to

$$||W(t)|| \le v_{\text{user}} t_{\text{step}}. \tag{4.8}$$

Fig. 4.24 shows the Brownian motion in 0.5 s time interval considering $t_{\rm step}=1\,ms$ which results in 500 step times across the room. Fig. 4.25 shows the average rate when the user moves following the Brownian motion in the simulation time interval with an average speed of $1\,m/s$. A Monte-Carlo simulation with 10000 iterations is performed, and the average rate is calculated. The simulation time interval, i.e, $t_{\rm tot}$, is 5 s, which means at each iteration of the Monte-Carlo simulation, the user is moving randomly until 5 s and AP is tracking its movement. Note that the random seed for user movement is changed after each iteration of Monte-Carlo simulations. The ideal tracking case with perfect knowledge of user location is implemented for $\theta_{\rm FWHM}=0.4^{\circ}$ as a benchmark comparison in this figure. Performance of the proposed DBS scheme with $\theta_{\rm FWHM}=0.4^{\circ}$ and $t_{\rm step}=1\,{\rm ms}$, and cellular-style architecture with $\theta_{\rm FWHM}=4^{\circ}$ and 2500 cells are shown in the figure. With only one scanning beam, the DBS scheme can show its superior performance for integrated communication and tracking with less power consumption over cellular architecture. Moreover, 4° DBS case is included in this

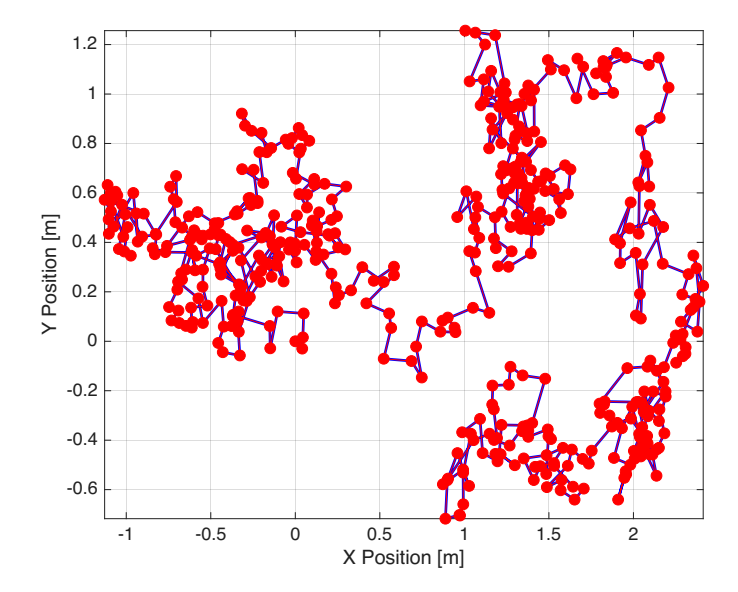


Figure 4.24: User random movement following Brownian motion in 5 s time interval with $t_{\text{step}} = 1 \, ms$, i.e., 500 time steps.

comparison, and the performance is lower than the cellular baseline under the same user motion conditions. The simulation focuses on demonstrating that the proposed DBS approach can exceed the best cellular performance by using its optimal configuration with a single narrow beam that can be implemented with a practical beam steering device, as summarized in Table 2.8.

Building on the noise-free comparison presented previously (see Fig. 4.23), the robustness of DBS is then assessed by including pointing noise $\sigma_p = 0.86$ cm and an initial localization error $\sigma_s = 1$ mm for the DBS scheme only. A Monte Carlo simulation with 1000 iterations is conducted while the user moves linearly from the room center to a corner, and the resulting tracking performance is compared against the cellular and ideal schemes in Fig. 4.26. Relative to this figure, the DBS achievable rate continues to outperform the cellular scheme across the trajectory. Furthermore, Fig. 4.27 shows the average achievable rate over 2000 Monte Carlo runs for a user following a 1s Brownian trajectory, comparing DBS ($\sigma_s = 1$ mm, $\sigma_p = 0.86$ cm) with ideal and cellular baselines. DBS consistently outperforms the cellular scheme, even when considering impairments

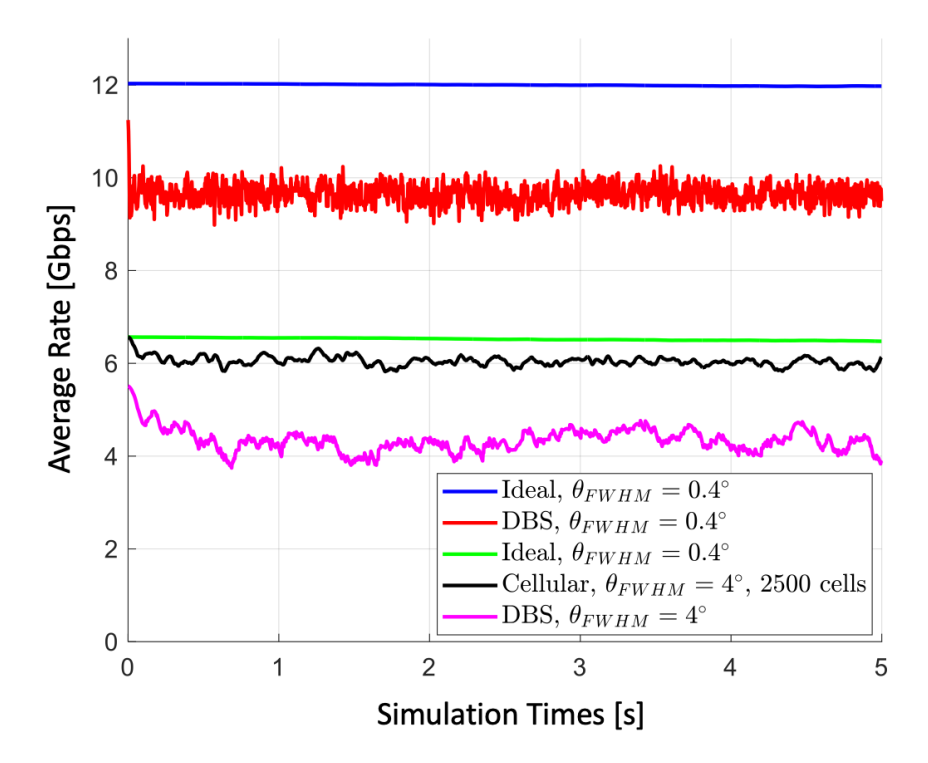


Figure 4.25: Monte-Carlo simulation with 10000 iterations for average rate when user moves randomly following Brownian model in 5s for comparison between ideal tracking, DBS scheme (with $\sigma_s = 0$, $\sigma_p = 0$), and cellular schemes.

such as initial localization error and noise in pointing.

4.4 Conclusion

This chapter has presented a detailed simulation-based evaluation of the proposed DBS scheme for indoor OWC, with a focus on quantifying design trade-offs. Various system parameters were examined, including feedback threshold, discrete scanning step time, beam divergence angle, number of beam spots per scan, scanning radius, initial localization error, and noise in beam pointing. Their individual and combined effects on the achievable data rate were analyzed to guide the selection of practical operating points.

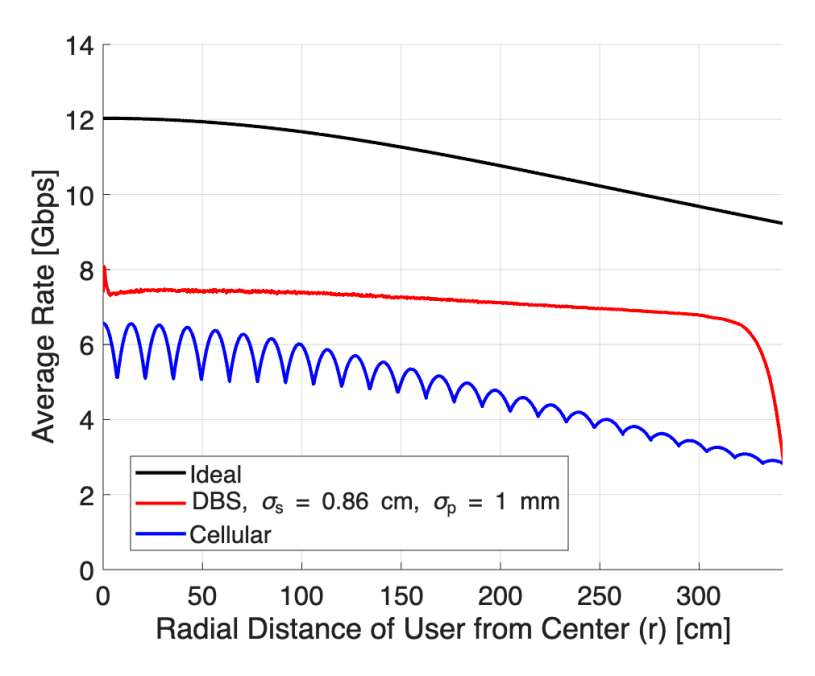


Figure 4.26: Comparison between DBS considering noise in pointing and localization error ($\sigma_s = 1 \, ms$, $\sigma_p = 0.86 \, cm$), cellular, and ideal schemes in terms of average rate vs radial distance from the center of the room for linear user movement

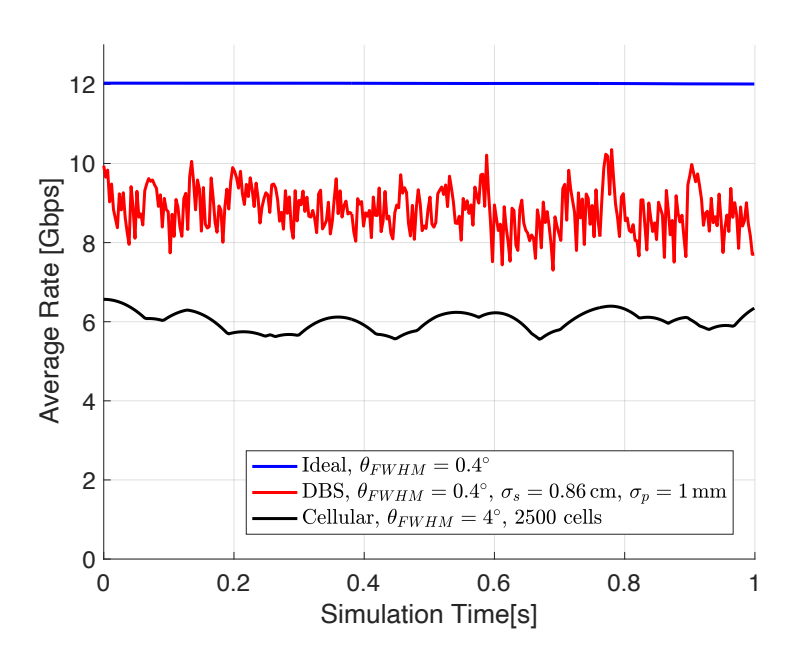


Figure 4.27: Average achievable rate from a 2000-run Monte Carlo simulation for a user following a Brownian-motion model over 1 s; comparison of DBS tracking ($\sigma_s = 1 \text{ mm}$, $\sigma_p = 0.86 \text{ cm}$) with ideal and cellular schemes.

Simulation results demonstrated that by carefully tuning these parameters, particularly adopting a narrow beam divergence ($\theta_{\rm FWHM}=0.4^{\circ}$) and feasible update spot step dwell time, ($t_{\rm step}=1\,{\rm ms}$), the DBS scheme can deliver reliable user tracking and high-speed data transmission using a single steerable beam. Importantly, the performance of the DBS approach was benchmarked against an ideal tracking scenario as an upper bound, and a cellular-style design with dense, wide-divergence beams as a practical baseline. The comparison showed that the optimized DBS configuration can match or exceed the best cellular performance under identical user motion conditions, while using fewer resources and offering greater adaptability.

In the next chapter, this study is brought to a close by reflecting on its key insights and outcomes. Looking ahead, ways to refine the DBS scheme are explored, along with considerations for its evolution to address practical scenarios and large-scale deployments.

Chapter 5

Conclusions and Future

Directions

Indoor OWC systems face major challenges such as user mobility, narrow beam alignment requirements, eye-safety power limits, and the complexity and cost of hardware when trying to deliver high data rates reliably. State-of-the-art cellular-style optical systems address mobility by using many wide-divergence beams and dense cell deployments, which increase power consumption and system complexity while limiting achievable data rates due to broader beam spreading. This work targets these challenges by proposing a DBS approach that uses a single, narrow beam with integrated localization and tracking algorithms, reducing power transmit power for communications and the number of emitters. By requiring only simple 1-bit feedback, the system enables precise, low-latency beam alignment suitable for high-speed users without needing multi-element transmitters. While the proposed DBS scheme shows significant performance advantages in simulations, practical deployment still requires addressing issues such as reliable feedback design in real environments, integration with existing infrastructure, practical implementation, and scaling for multi-user scenarios. Future work will explore these challenges, refine beam steering algorithms under more realistic mobility models,

and develop prototypes to validate the approach in practical settings.

To enhance the DBS scheme, adopting a multi-beam approach instead of a single beam can be beneficial. For example, a single spot position could consist of a combination of n narrower spots formed using a lens. Additionally, the receiver can be upgraded to an array of PD elements. Utilizing an imaging angle diversity receiver, as proposed in [37], is an example that can significantly improve communication throughput. Furthermore, receiver designs presented in [113], [114], [115], and [38] offer valuable insights for further investigation and enhancement. By designing a multi-beam AP for a single-user scenario and integrating a multi-element receiver with high BW, it becomes possible to achieve higher data rates while effectively tracking the user movement.

For more predictable user movement patterns, the design of Kalman filters and particle filters can be investigated and compared with the proposed DBS scheme in terms of tracking algorithm complexity and tracking efficiency. The closer the data rate is to that achieved under ideal tracking, the better the tracking algorithm is. It is worth noting that for unpredictable motion patterns, such as Brownian motion, the DBS scheme proves robust due to its simplicity in estimating the user position after each scanning period. However, for more predictable motion models, training a dataset encompassing various possible user movements, along with the application of Kalman filters and reinforcement learning methods, could be explored for further optimization [116], [117], [118].

In this work, a single-user scenario is considered. For future work, a multi-user system can be implemented where each user is allocated a dedicated beam, since a single narrow beam can only cover one PD. This would require multiple VCSELs, each equipped with a beam steering device. An alternative approach is to design a central beam steering device capable of independently controlling the beams from multiple VCSEL elements.

This could reduce hardware redundancy and improve scalability. Potential implementations include OPAs [119], SLMs [120], [7], or MEMS mirrors [121], which allow precise and dynamic beam control (as discussed in Section 2.9). However, challenges such as synchronization, latency, and optical efficiency must be addressed to ensure reliable performance in a high-speed communication system.

In a multi-user scenario, allocating a dedicated beam steering device for each transmitter element may be impractical or inefficient, particularly in environments with high user density. To address this, users with lower Quality of Service (QoS) requirements can be served using a wider beam that covers multiple adjacent users. Multiple-access techniques such as OFDMA, SDMA, or NOMA can be employed to efficiently share resources among these users while ensuring continuous tracking of their movement. For users with higher QoS demands, a narrow beam can be allocated to enable simultaneous tracking and ultra-high data rate communication. Additionally, in larger indoor environments, a multi-AP architecture can be implemented, where each AP manages a designated cluster of users to improve coverage and system scalability. To optimize resource allocation in a multi-cluster, multi-user scenario, strategies such as beam allocation, modulation selection, transmit power optimization, and beam divergence control can be dynamically adjusted based on user QoS requirements. In this context, machine learning techniques, particularly reinforcement learning-based approaches such as the one proposed in [122], can be explored to enable adaptive resource management and system-level optimization.

This work assumes a fixed user orientation. In practical scenarios, random device orientations must be considered [123], [124], and the performance of the DBS scheme should be evaluated in such conditions. Improving the receiver architecture and employing an angle diversity receiver and ODTx for feedback can mitigate the effects of random user orientations. Moreover, in this research, the user position is assumed to lie on a fixed XY plane at $z=1\,\mathrm{m}$. A more realistic scenario would involve random

M.A.Sc. Thesis - Hamed Hosseinnejadazad McMaster University - ECE Department

user movement in XYZ coordinates, modeling the uncertainty region as a sphere, and adapting the proposed localization and tracking algorithms to provide full 3D coverage for communication.

To improve SNR, liquid crystal technology can be investigated to be considered at the receiver side to amplify the received signal strength as demonstrated in [125], [126]. To further address LoS blockage, deploying mirror-array RIS on walls to create NLoS channels can be investigated based on the works in [40], [127], [128], [129], and [130].

Appendix A

Appendix: DC Bias and Clipping Probability in DCO-OFDM

In this Appendix, it is noted that for DCO-OFDM systems with a large number of subcarriers, the time-domain signal obtained after the inverse fast Fourier transform (IFFT) can be well approximated by a Gaussian random process. This approximation follows from the central limit theorem, since the IFFT output represents the superposition of many independent subcarrier contributions [131]. Consequently, the time-domain signal is modeled as

$$s \sim \mathcal{N}(0, \sigma^2),$$
 (A.1)

where σ^2 denotes the variance of the signal. To ensure non-negativity for optical intensity modulation, a DC bias $x_{\rm DC}$ is added

$$x = s + x_{DC}. (A.2)$$

The clipping distortion arises when x becomes negative and is clipped to zero at the transmitter. The probability of this event is

$$P(x < 0) = P(s + x_{DC} < 0) = P(s < -x_{DC}).$$
(A.3)

By standardizing the Gaussian variable

$$z = -\frac{s}{\sigma} \sim \mathcal{N}(0, 1), \tag{A.4}$$

this leads to

$$P(x < 0) = P\left(z < -\frac{x_{\rm DC}}{\sigma}\right) = Q\left(\frac{x_{\rm DC}}{\sigma}\right),$$
 (A.5)

where $Q(\cdot)$ denotes the complementary cumulative distribution function of the standard normal distribution

$$Q(a) = \int_{a}^{\infty} \frac{1}{\sqrt{2\pi}} e^{-\frac{t^2}{2}} dt.$$
 (A.6)

By choosing

$$x_{\rm DC} = 3\sigma, \tag{A.7}$$

the clipping probability becomes

$$P(x<0) = Q(3) \approx 0.00135,\tag{A.8}$$

which is approximately 0.13%. This ensures that over 99.8% of the signal samples remain unaltered after biasing, rendering the clipping distortion negligible for practical purposes.

Appendix B

Appendix: Received Power Calculation (Exact Integration Method)

To accurately determine the received power, integration over the circular avalanche PD area, \mathcal{A} , is performed based on [59], considering the Gaussian intensity distribution, $I(\rho, d_{Tx})$, as

$$P_{r} = \iint_{(x,y)\in\mathcal{A}} I(x,y,z) G_{\text{APD}} n_{\text{Tx}} \cdot n_{\text{Rx}} dx dy,$$

$$= \iint_{(x,y)\in\mathcal{A}} \frac{2 P_{t}}{\pi \omega^{2}(z)} \exp\left(-\frac{2\rho(x,y)}{\omega^{2}(z)}\right) n_{\text{Tx}} \cdot n_{\text{Rx}} dx dy,$$
(B.1)

where $n_{\text{Tx}} \cdot n_{\text{Rx}}$ incorporates the effect of Lambert cosine law [59], and

$$\mathcal{A} = \{ (x, y) \in \mathbb{R}^2 \mid x^2 + y^2 \le r_{PD}^2 \}, \tag{B.2}$$

M.A.Sc. Thesis - Hamed Hosseinnejadazad McMaster University - ECE Department

where r_{PD} denotes PD radius [59]. To solve the integral (B.8), we express it in terms of polar coordinates (r, θ) . The points on the circular PD are

$$\begin{cases} x_{\text{Rx}}(r,\theta) = r\cos(\theta) + x_{\text{rx}} \\ y_{\text{Rx}}(r,\theta) = r\sin(\theta) + y_{\text{rx}} \end{cases}, \quad 0 \le \theta \le 2\pi, \quad 0 \le r \le r_{\text{PD}}.$$
 (B.3)

Thus, the distance between AP and PD can be rewritten as

$$\mathbf{d}_{Rx}(r,\theta) = \vec{Rx}(r,\theta) - \vec{Tx}$$

$$= (x_{Rx}(r,\theta), y_{Rx}(r,\theta), 1 m) - (0,0,3 m)$$

$$= (x_{Rx}(r,\theta), y_{Rx}(r,\theta), -2 m)$$

$$= (x_{Rx}(r,\theta), y_{Rx}(r,\theta), -h).$$
(B.4)

Moreover, the AP vector, \mathbf{d}_{Tx} is the difference between target pointing vector, $\vec{S} = (x_s, y_s, 1)$ [m], and \vec{Tx} vector, which can be evaluated as

$$\mathbf{d}_{\mathrm{Tx}} = \vec{S} - \vec{Tx}$$

$$= (x_s, y_s, -h)$$
(B.5)

The term $n_{\text{Tx}} \cdot n_{\text{Rx}}$ can be calculated as

$$n_{\text{Tx}} \cdot n_{\text{Rx}} = \cos(\varphi(r, \theta))$$

$$= \frac{\mathbf{d}_{\text{Tx}}}{||\mathbf{d}_{\text{Tx}}||} \cdot \frac{\mathbf{d}_{\text{Rx}}(r, \theta)}{||\mathbf{d}_{\text{Rx}}(r, \theta)||}$$

$$= \frac{(x_s, y_s, -h)}{\sqrt{x_s^2 + y_s^2 + h^2}} \cdot \frac{(x_{\text{Rx}}(r, \theta), y_{\text{Rx}}(r, \theta), -h)}{\sqrt{x_{\text{Rx}}^2(r, \theta) + y_{\text{Rx}}^2(r, \theta) + h^2)}}$$

$$= \frac{x_s x_{\text{Rx}}(r, \theta) + y_s y_{\text{Rx}}(r, \theta) + h^2}{\sqrt{x_s^2 + y_s^2 + h^2} \sqrt{x_{\text{Rx}}^2(r, \theta) + y_{\text{Rx}}^2(r, \theta) + h^2)}}$$
(B.6)

The distance ρ which is the distance between \mathbf{d}_{Tx} and PD surface, as shown in Fig. 2.8, can be found as

$$\rho(r,\theta) = ||\mathbf{d}_{Rx}(r,\theta)|| \sin(\phi(r,\theta))$$
(B.7)

In this case, the equation (B.8) can be rewritten as

$$P_{r} = \int_{0}^{2\pi} \int_{0}^{r_{\text{PD}}} I(r,\theta) G_{\text{APD}} n_{Tx}(r,\theta) \cdot n_{Rx}(r,\theta) r dr d\theta$$

$$= \int_{0}^{2\pi} \int_{0}^{r_{\text{PD}}} \frac{2P_{t} G_{\text{APD}}}{\pi \omega^{2} (||\mathbf{d}_{\text{Tx}}||)} \exp\left(-\frac{2\rho^{2}(r,\theta)}{\omega^{2} (||\mathbf{d}_{\text{Tx}}||)}\right) n_{Tx}(r,\theta) \cdot n_{Rx}(r,\theta) r dr d\theta \qquad (B.8)$$

$$= \int_{0}^{2\pi} \int_{0}^{r_{\text{PD}}} \frac{2P_{t} G_{\text{APD}}}{\pi \omega^{2} (||\mathbf{d}_{\text{Tx}}||)} \exp\left(-\frac{2||\mathbf{d}_{\text{Rx}}||^{2} \sin^{2}(\phi(r,\theta))}{\omega^{2} (||\mathbf{d}_{\text{Tx}}||)}\right) \cos(\varphi(r,\theta)) r dr d\theta$$

The equation (B.8) accounts for the gradual intensity variation across the detector area. The integral in (B.8) can be numerically calculated using Python or MATLAB. For a small beam spot size compared to PD area (i.e., $r_{\rm PD} \approx \omega(d_{\rm Tx})$), the expressions (B.8), and (2.42), yield similar results. However, when the detector area very small compared to the beam spot (e.g., for $\theta_{\rm FWHM} > 4^{\circ}$), especially for distant locations, the integral approach becomes necessary to avoid overestimating the received power.

The simulation results in Fig. B.1 compare the received power obtained from the approximate expression in (2.42) with the exact value computed from (B.8), as the user moves from the center of the room to the corner while the AP ideally tracks the motion. In Fig. B.1(a), corresponding to $\theta_{\text{FWHM}} = 0.4^{\circ}$, the approximate expression in (2.42) yields a higher received power than the exact integration for radial distances less than 50 cm. Beyond this point, the exact method produces larger values. In contrast, for Fig. B.1(b), corresponding to $\theta_{\text{FWHM}} = 4^{\circ}$, the exact computation of P_r remains consistently greater than the approximation across the entire range of user positions. It is noteworthy that, at the position (2.5, 2.5, 2.5) [m], the ratio of the exact power computation to the approximation is 1.98 for both $\theta_{\text{FWHM}} = 0.4^{\circ}$ and $\theta_{\text{FWHM}} = 4^{\circ}$.

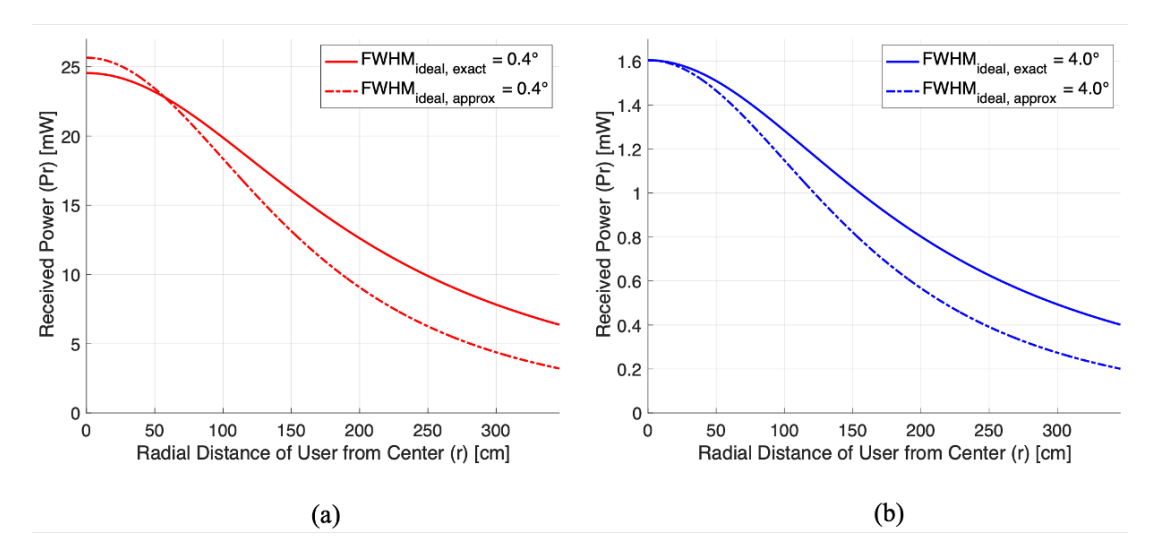


Figure B.1: Received power comparison between the approximation in (2.42) and the exact integration in (B.8), as the user moves from the room center to the corner with ideal AP tracking; (a) for $\theta_{\rm FWHM} = 0.4^{\circ}$, (b) for $\theta_{\rm FWHM} = 4^{\circ}$

To explain the behavior observed in Fig. B.1, consider Fig. B.2, where the user is located at (2.5, 2.5, 1) [m] and the intensity distribution across the PD area is shown. The figure reveals an offset between the maximum intensity, I_{max} , and the PD center, i.e., the beam pointing position. This difference is further illustrated in Fig. B.3, which compares the peak intensity with the center intensity. Although the difference is small, its impact becomes significant when multiplied by the APD gain, $G_{\text{APD}} = 30$ (see Table 2.6).

Building on this, Fig. B.4 compares $P_{r,\text{exact}}$, obtained from integration in (B.8), with $P_{r,\text{approx}}$, computed using the center intensity approximation in (2.42). The figure highlights how the actual area under the Gaussian curve differs from the rectangular approximation, which explains the discrepancy observed in Fig. B.1.

The position (2.5, 2.5, 2.5) [m] is selected because it yields the largest offset between the point of maximum intensity and the PD center. At locations nearer the room center, this offset diminishes. For comparison, Figs. B.5 and B.6 show the intensity maps and the

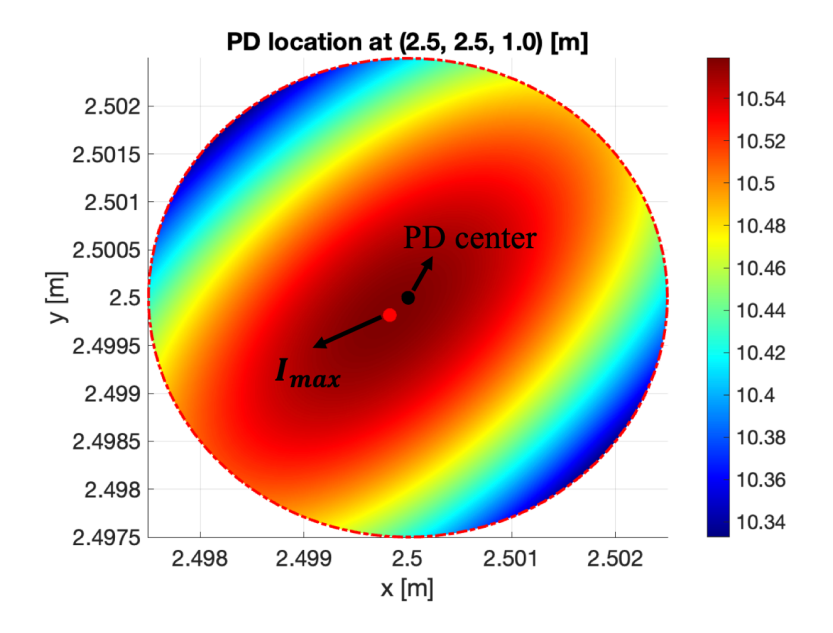


Figure B.2: Intensity distribution ($\theta_{\text{FWHM}} = 0.4^{\circ}$) over the PD area at (2.5, 2.5, 1) [m], with the maximum intensity point I_{max} , and the PD center (beam pointing position) indicated.

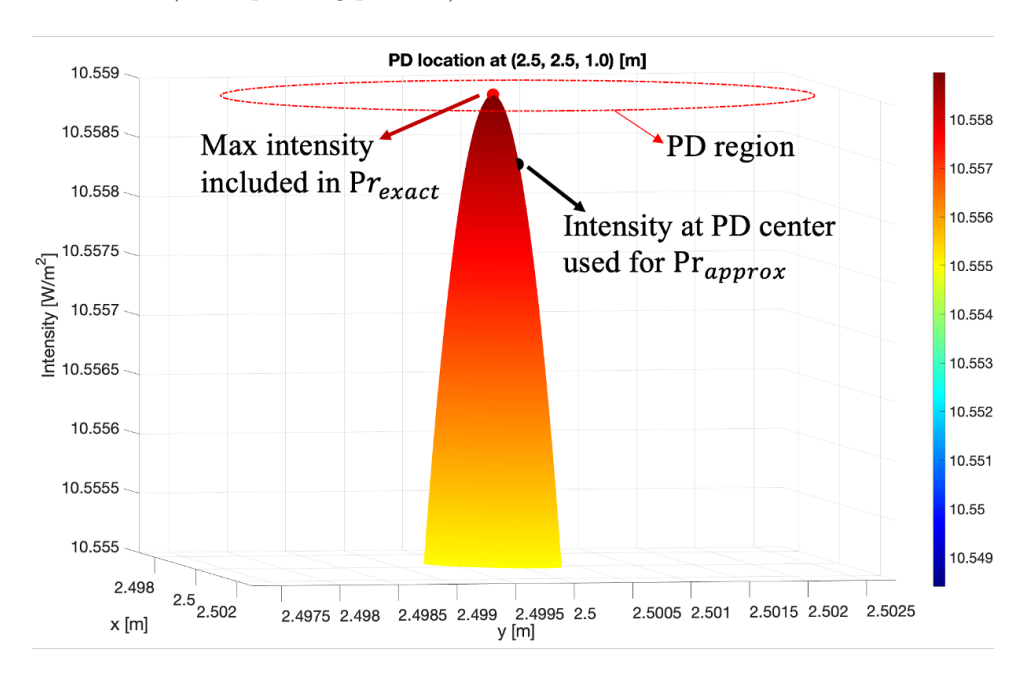


Figure B.3: Difference between maximum intensity (included in Pr_{exact} according to (B.8)), and intensity at PD center (used for $P_{\text{r,approx}}$ according to (2.42))

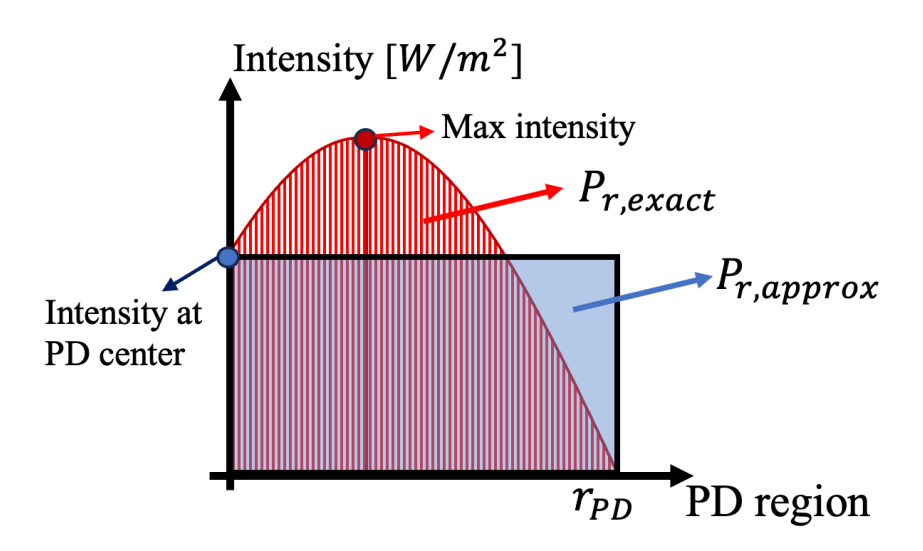


Figure B.4: Illustration of the integration area for computing $P_{r,\text{exact}}$ in (B.8), compared with the rectangular approximation used for $P_{r,\text{approx}}$ in (2.42).

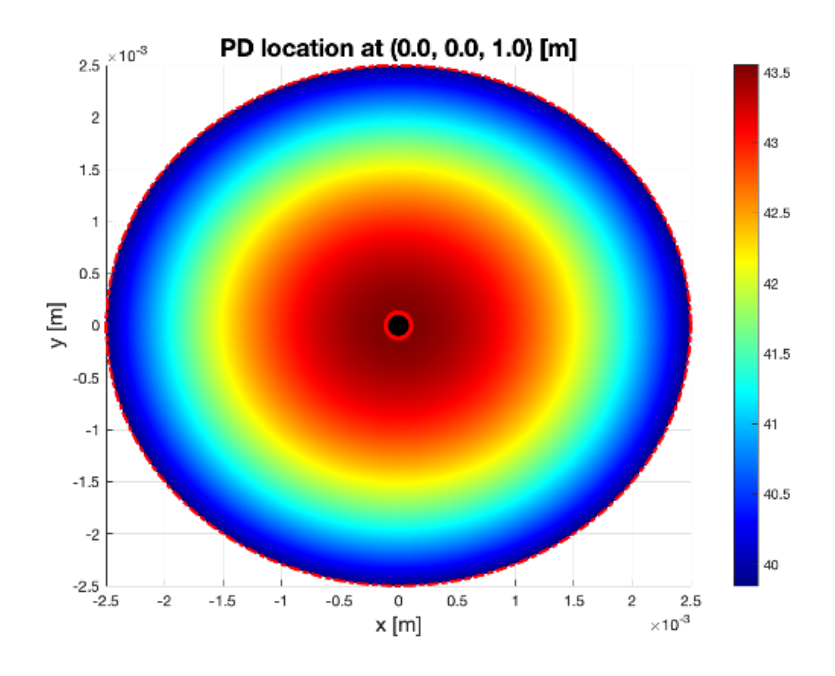


Figure B.5: Intensity distribution ($\theta_{\text{FWHM}} = 0.4^{\circ}$) over the PD area at (1.5, 1.5, 1) [m], with the maximum intensity point I_{max} , and the PD center (beam pointing position) indicated.

marked points (peak and PD center) at (0, 0, 1) [m] and (1.5, 1.5, 1.5) [m], respectively. Note that at (0, 0, 1) [m], the offset is zero and two points match.

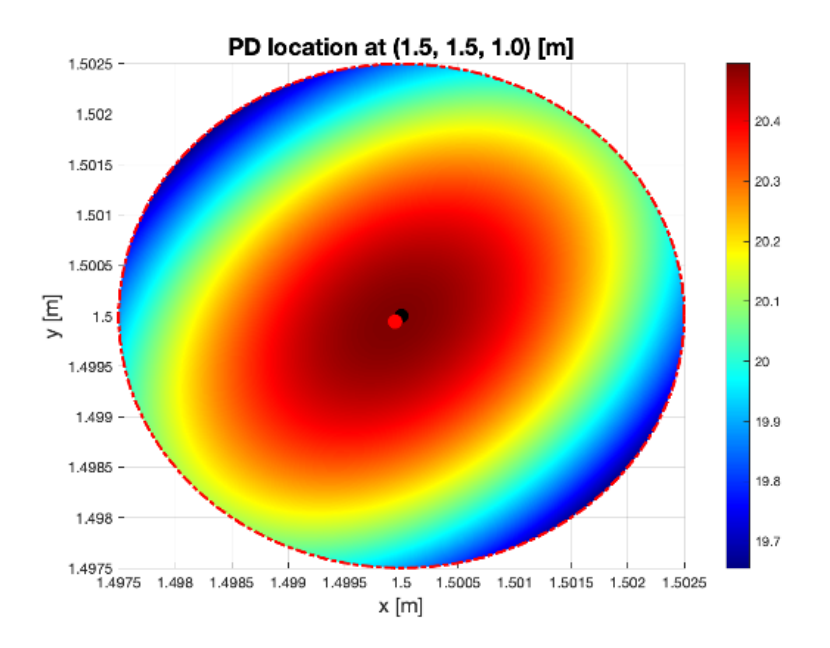


Figure B.6: Intensity distribution ($\theta_{\text{FWHM}} = 0.4^{\circ}$) over the PD area at (0, 0, 1) [m], with the maximum intensity point I_{max} , and the PD center (beam pointing position) indicated.

Appendix C

Analytical Expression of Beam Spot and Localization Accuracy

The objective is to derive mathematical expressions for the elliptical beam spot shape, and localization accuracy. According to (3.6), (x_s, y_s) can be calculated as

$$x_s^{(i)} = r_s^{(i)} \cos\left(\theta_s^{(i)}\right) + x_{s0}$$
 (C.1a)

$$y_s^{(i)} = r_s^{(i)} \sin\left(\theta_s^{(i)}\right) + y_{s0},$$
 (C.1b)

where (x_{s0}, y_{s0}) is the starting position of spiral search, $\theta_s^{(1)} = 0$, and $\theta_s^{(i)}$ can be obtained from (3.9). Fig. C.1 shows the geometry of the elliptical beam spot footprint on the XY plane, where the user is located. In this figure, \mathcal{Z} , is called the intersection distance, which is the distance from the AP to the XY plane at $z = z_{rx}$ where the beam (cone) intersects horizontally. Moreover, θ can be calculated from (3.4), T_z is AP height, the point $S = (x_s, y_s)$ is spiral search discrete point according to (C.1), the point P is elliptical spot center, $\omega(\mathcal{Z})$ is beam radius at distance \mathcal{Z} , ℓ is distance between S and center of cone (beam) base at distance \mathcal{Z} , $\alpha_b/2$ is beam divergence angle, and points A, B, C, D are selected for geometrical calculation in the following. To begin, \mathcal{Z} is calculated as

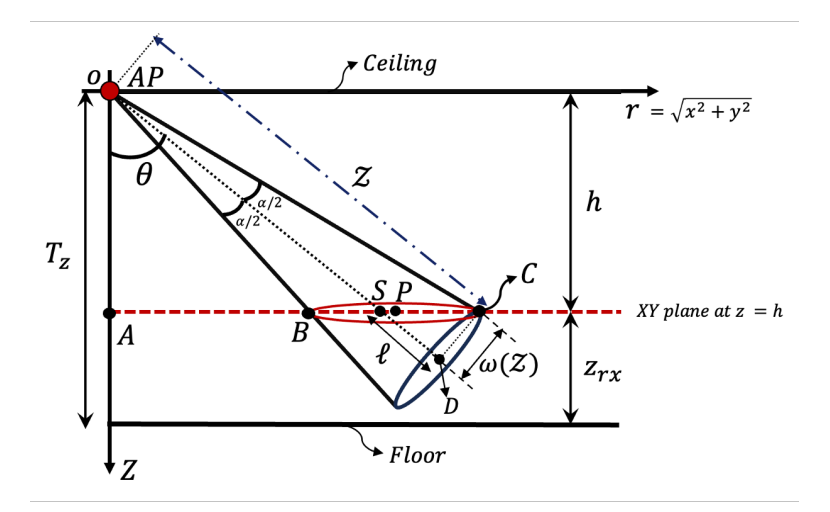


Figure C.1: Geometry of pointed beam and the intersection with XY plane at height z=h, resulting in elliptical beam spot footprint

$$l = \omega(\mathcal{Z}) \tan(\theta), \qquad (C.2)$$

$$\cos(\theta) = \frac{h}{\mathcal{Z} - \ell},\tag{C.3}$$

$$\mathcal{Z} = \frac{h}{\cos(\theta)} + l = \frac{h}{\cos(\theta)} + \omega(\mathcal{Z})\tan(\theta)$$
 (C.4a)

$$\Rightarrow \mathcal{Z} = \frac{h}{\cos(\theta)} + \omega_0 \tan(\theta) \sqrt{1 + \left(\frac{\lambda \mathcal{Z}}{\pi \omega_0^2}\right)^2}, \qquad (C.4b)$$

solving the equation results in

$$\mathcal{Z} = \frac{-\frac{h}{\cos(\theta)} + \omega_0 \tan(\theta) \sqrt{-\frac{\lambda^2 \tan^2(\theta)}{\pi^2 \omega_0^2} + \frac{h^2 \lambda^2}{\pi^2 \omega_0^2 \cos^2(\theta)} + 1}}{\frac{\lambda^2 \tan^2(\theta)}{\pi^2 \omega_0^2} - 1}.$$
 (C.5)

The pointed IR beam is modeled as a cone according to [73]; thus, the equation of a vertical cone can be expressed as

$$r_b(z, \mathcal{Z}) = \frac{w(\mathcal{Z})}{\mathcal{Z}} z,$$
 (C.6a)

$$x_b = r_b \cos(t) \,, \tag{C.6b}$$

$$y_b = r_b \sin(t) \,, \tag{C.6c}$$

$$z_b = \frac{\mathcal{Z}}{w(\mathcal{Z})} \sqrt{x_b^2 + y_b^2}, \qquad (C.6d)$$

where $t \in [0, 2\pi]$, and $0 \le z \le \mathcal{Z}$. Moreover according to (2.20)

$$\tan\left(\frac{\alpha_b}{2}\right) = \sqrt{\frac{2}{\ln(2)}} \tan\left(\frac{\theta_{\text{FWHM}}}{2}\right)$$

$$= \frac{\omega(\mathcal{Z})}{\mathcal{Z}}.$$
(C.7)

The rotated cone (beam) equation can be calculated as

$$\begin{bmatrix} x_{rot} \\ y_{rot} \\ z_{rot} \end{bmatrix} = R_z R_y \begin{bmatrix} x_b \\ y_b \\ z_b \end{bmatrix}, \tag{C.8}$$

where R_z , and R_y are rotation matrices with respect to z-axis and y-axis respectively, and θ, φ can be obtained from (3.4), (3.5) respectively. Thus

$$\begin{bmatrix} x_{rot} \\ y_{rot} \\ z_{rot} \end{bmatrix} = \begin{bmatrix} \cos \varphi & -\sin \varphi & 0 \\ \sin \varphi & \cos \varphi & 0 \\ 0 & 0 & 1 \end{bmatrix} \begin{bmatrix} \cos \theta & 0 & \sin \theta \\ 0 & 1 & 0 \\ -\sin \theta & 0 & \cos \theta \end{bmatrix} \begin{bmatrix} x_b \\ y_b \\ z_b \end{bmatrix}, \quad (C.9)$$

$$\begin{bmatrix} x_{\text{rot}} \\ y_{\text{rot}} \\ z_{\text{rot}} \end{bmatrix} = \begin{bmatrix} x_b \cos \theta \cos \varphi - y_b \sin \varphi + z_b \sin \theta \cos \varphi \\ x_b \sin \varphi \cos \theta + y_b \cos \varphi + z_b \sin \theta \sin \varphi \\ -x_b \sin \theta + z_b \cos \theta \end{bmatrix}.$$
 (C.10)

Since beam intersects with the horizontal plane, $z_{rot} = h$. As a result

$$z_{rot} = h = -x_b \sin \theta + z_b \cos \theta$$

$$\Rightarrow -\frac{\omega(\mathcal{Z})}{\mathcal{Z}} z_b \cos(t) \sin \theta + z_b \cos \theta = h$$

$$\Rightarrow z_b = \frac{h}{\cos \theta - \frac{\omega(\mathcal{Z})}{\mathcal{Z}} \sin \theta \cos(t)}.$$
(C.11)

By substituting z_b in (C.6) and updating (C.10), the following is obtained

$$x_{\text{spot}} = \frac{\omega(\mathcal{Z})}{\mathcal{Z}} \left(\frac{h}{\cos(\theta) - \frac{\omega(\mathcal{Z})}{\mathcal{Z}}} \sin(\theta) \cos(t) \right)$$

$$\times \left(\cos(t) \cdot \cos(\theta) \cos(\varphi) - \sin(t) \sin(\varphi) + \frac{\mathcal{Z}}{\omega(\mathcal{Z})} \sin(\theta) \cos(\varphi) \right), \qquad (C.12a)$$

$$y_{\text{spot}} = \frac{\omega(\mathcal{Z})}{\mathcal{Z}} \left(\frac{h}{\cos(\theta) - \frac{\omega(\mathcal{Z})}{\mathcal{Z}}} \sin(\theta) \cos(t) \right)$$

$$\times \left(\cos(t) \cdot \sin(\varphi) \cos(\theta) - \sin(t) \cos(\varphi) + \frac{\mathcal{Z}}{\omega(\mathcal{Z})} \sin(\theta) \sin(\varphi) \right). \qquad (C.12b)$$

where $(x_{\text{spot}}, y_{\text{spot}})$ are points of elliptical beam spot footprint on XY plane at $z = z_{rx}$. Based on Fig. C.1, the following holds

$$\tan\left(\theta + \frac{\alpha_b}{2}\right) = \frac{AC}{h} \tag{C.13}$$

$$\tan\left(\theta - \frac{\alpha_b}{2}\right) = \frac{AB}{h} \tag{C.14}$$

$$\Rightarrow BC = AC - AB$$

$$= h\left(\tan\left(\theta + \frac{\alpha_b}{2}\right) - \tan\left(\theta - \frac{\alpha_b}{2}\right)\right). \tag{C.15}$$

After simplifying the equation, the result is

$$BC = \frac{2h \cdot \sin(\alpha_b)}{\cos(2\theta) + \cos(\alpha_b)}$$

$$= 2b.$$
(C.16)

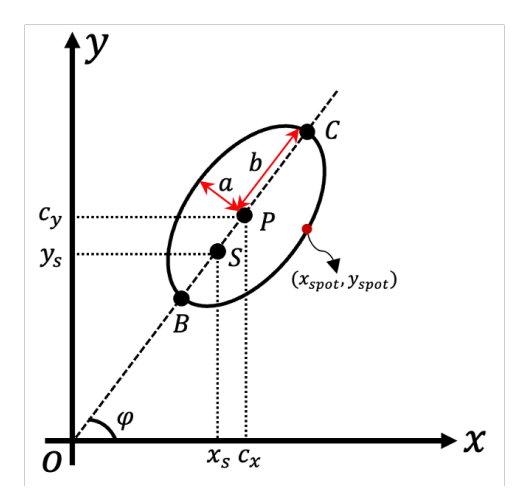


Figure C.2: The elliptical beam spot footprint on XY plane which is 2D demonstration of Fig. C.1

In $\triangle SDC$ (see Fig. C.1), the angle at vertex C is equal to θ due to the Triangle Similarity Theorem applied to $\triangle OAS$ and $\triangle SDC$. Thus,

$$\cos \theta = \frac{\omega(\mathcal{Z})}{SC}$$

$$\Rightarrow SC = \frac{\omega(\mathcal{Z})}{\cos(\theta)}.$$
(C.17)

Moreover, SP = SC - b, therefore,

$$SP = \frac{\omega(\mathcal{Z})}{\cos(\theta)} - \frac{h\sin(\alpha_b)}{\cos(2\theta) + \cos(\alpha_b)}.$$
 (C.18)

According to the 2D view of the beam spot footprint as illustrated in Fig. C.2, the center of elliptical spot is $P = (c_x, c_y)$, hence

$$SP = \sqrt{(c_x - x_s)^2 + (c_y - y_s)^2}.$$
 (C.19)

Furthermore, from Fig. C.2, since P, S forms a line that passes through the origin, consequently,

$$C_y = \frac{y_s}{x_s} C_x. (C.20)$$

Hence, by substituting (C.20) into (C.19), the following is obtained:

$$C_x^2 - 2x_sC_x + x_s^2\left(1 - \frac{SP^2}{x_s^2 + y_s^2}\right) = 0.$$
 (C.21)

By substituting (C.18) and solving the equation, the following result is obtained

$$\begin{cases}
C_x = x_s \left(1 \pm \frac{1}{\sqrt{x_s^2 + y_s^2}} \left(\frac{w(\mathcal{Z})}{\cos(\theta)} - \frac{h \sin(\alpha_b)}{\cos(2\theta) + \cos(\alpha_b)} \right) \right) \\
C_y = y_s \left(1 \pm \frac{1}{\sqrt{x_s^2 + y_s^2}} \left(\frac{w(\mathcal{Z})}{\cos(\theta)} - \frac{h \sin(\alpha_b)}{\cos(2\theta) + \cos(\alpha_b)} \right) \right)
\end{cases}$$
(C.22)

Note that $|c_x| > |x_s|, |c_y| > |y_s|$. The equation of the elliptical spot footprint can be determined as

$$\frac{((x - c_x)\cos\varphi + (y - c_y)\sin\varphi)^2}{a^2} + \frac{((x - c_x)\sin\varphi - (y - c_y)\cos\varphi)^2}{b^2} = 1.$$
 (C.23)

By considering an arbitrary point on the beam spot (e.g., $x_{\text{spot}}, y_{\text{spot}}$ at t = 0), the semi-minor axis of the ellipse in Fig. C.2, a, can be expressed as

$$a = \sqrt{\frac{\left(\left(x_{\text{spot}} - c_x\right)\cos\varphi + \left(y_{\text{spot}} - c_y\right)\sin\varphi\right)^2}{1 - \frac{\left(x_{\text{spot}} - c_x\right)\sin\varphi - \left(y_{\text{spot}} - c_y\right)\cos\varphi\right)^2}{b^2}}}.$$
(C.24)

When user detects a received power higher than a threshold power, it sends ACK to AP. In a geometric point of view, this means the user is covered by the beam spot footprint. Therefore, the user must be inside the beam spot. Thus, the geometrical condition for the ACK signal is given by

$$\frac{((x_{rx} - c_x)\cos\varphi + (y_{rx} - c_y)\sin\varphi)^2}{a^2} + \frac{((x_{rx} - c_x)\sin\varphi - (y_{rx} - c_y)\cos\varphi)^2}{b^2} < 1.$$
(C.25)

In the spiral search in simulation, the parameters in (C.25) (that is, (c_x, c_y) , φ , a, b) are kept updated iteratively until the condition is met for a certain (x_{rx}, y_{rx}) . The total number of updates gives the total number of spots, N, required to localize the user.

Note that N is equal to total number of $\Delta \theta^{(i)}$ values.

To evaluate an analytical expression for $D_{\text{max}} < \epsilon$, from Fig. C.2, the maximum distance between the beam pointing position $S = (x_s, y_s)$ and the user location (x_{rx}, y_{rx}) is denoted by SC, where SC = SP + b. Therefore, the maximum localization error, D_{max} , can be considered equal to SC. However, to impose a stricter condition on localization accuracy, $D_{\text{max}} = b$ is adopted to ensure that the user cannot be located at the very edge of the farthest beam spot. Consequently, from (C.16),

$$D_{\max} = \frac{h \sin(\alpha_b)}{\cos(2\theta) + \cos(\alpha_b)}$$

$$= \frac{h \cdot \sin\left(2 \tan^{-1}\left(\frac{\omega(\mathcal{Z})}{\mathcal{Z}}\right)\right)}{\cos(2\theta) + \cos\left(2 \tan^{-1}\left(\frac{\omega(\mathcal{Z})}{\mathcal{Z}}\right)\right)}.$$
(C.26)

By substituting (C.7) into (C.26) and simplifying, the following is obtained

$$D_{\text{max}} = \frac{2h \cdot \sqrt{\frac{2}{\ln(2)}} \tan\left(\frac{\theta_{\text{FWHM}}}{2}\right)}{\cos(2\theta) + 1 + \frac{2}{\ln(2)} \tan^2\left(\frac{\theta_{\text{FWHM}}}{2}\right) (\cos(2\theta) - 1)} \leqslant \varepsilon.$$
 (C.27)

To get the θ_{FWHM} that satisfies the condition $D_{\text{max}} \leq \epsilon$, (C.27) can be expressed as

$$\frac{2}{\ln(2)}(\cos(2\theta) - 1)\tan^2\left(\frac{\theta_{\text{FWHM}}}{2}\right) - \frac{2h}{\varepsilon} \cdot \sqrt{\frac{2}{\ln(2)}} \tan\left(\frac{\theta_{\text{FWHM}}}{2}\right) + (\cos(2\theta) + 1) \geqslant 0.$$
(C.28)

Solving (C.26) for θ_{FWHM} yields

$$\theta_{\text{FWHM, min}} = 2 \tan^{-1} \left(\sqrt{\frac{\ln(2)}{2}} \cdot \frac{1}{\cos(2\theta) - 1} \left(\frac{h}{\varepsilon} - \left(\sqrt{\left(\frac{h}{\varepsilon}\right)^2 + \sin^2(2\theta)} \right) \right) \right), \quad (C.29)$$

given that $\theta \neq 0$. The $\theta_{\text{FWHM,min}}$ is defined as the minimum θ_{FWHM} that is required to achieve the localization accuracy of $D_{\text{max}} \leq \epsilon$. Considering the largest spot for the

M.A.Sc. Thesis - Hamed Hosseinnejadazad McMaster University - ECE Department

farthest position in the room at (2.5, 2.5), $\cos(2\theta) = -0.515$, therefore,

$$\theta_{\text{FWHM}} \leqslant 2 \tan^{-1} \left(-0.3886 \left(\frac{2}{\varepsilon} - \sqrt{\frac{4}{\varepsilon^2} + 0.734} \right) \right).$$
 (C.30)

Note that the farthest location in this setup depends on the specific room dimensions. The equation for the required $\theta_{\rm FWHM}$ given in (C.29) is a general formula for achieving the desired localization accuracy ϵ , while (C.30) reflects the calculation for the dimensions of this particular setup. The general form in (C.29) can be applied to any room dimensions. As long as the user can detect the received signal from the AP and the AP can receive the ACK feedback from the user, the room dimensions for the proposed DBS scheme (localization and tracking) can be extended.

Appendix D

Appendix: Simulation Results

Comparing Approximate and

Exact Received Power

Calculations

This appendix presents simulation results comparing data rate while tracking user obtained from the approximate received power calculation from (2.42) with the exact data rate obtained from integration of the Gaussian beam profile over the PD area, provided in Appendix B when user is moving from center of the room to the corner (i.e., along a linear path).

Figure D.1 illustrates differences for DBS, cellular, and ideal schemes as the user moves with a constant speed of $v_{\rm user} = 1\,m/s$. The difference between the curve corresponding to ${\rm FWHM_{ideal, exact}}$ and ${\rm FWHM_{ideal, approx}}$, which represent the ideal tracking scheme, is small near the center of room but increases as the user moves toward the corner due to the growing beam spot size and increase in offset between position of maximum intensity and center of PD (where the beam is pointed in the ideal scheme)

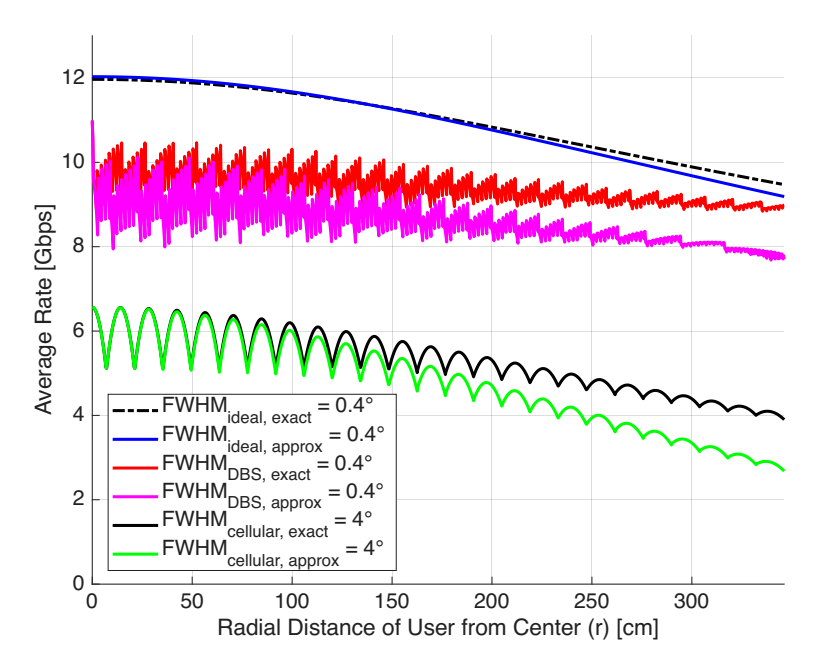


Figure D.1: Comparison of DBS, cellular, and ideal schemes in terms of average rate versus radial distance from the room center. Results compare the exact received power calculated from (B.8) with the approximate received power estimated using (2.42).

as discussed in Appendix B. For the DBS scheme, a similar trend is observed where the difference between the approximate and exact methods becomes significant at greater distances, with the exact calculation (FWHM_{DBS, exact} curve) showing improved performance in terms of achievable rate compared to FWHM_{DBS, approx} curve. The cellular scheme also exhibits increasing differences with distance.

Bibliography

- [1] Hossein Kazemi, Elham Sarbazi, Michael Crisp, Taisir El-Gorashi, Jaafar Mohamed Hamad Elmirghani, Richard Vincent Penty, Ian H. White, Majid Safari, Harald Haas, A novel terabit grid-of-beam optical wireless multi-user access network with beam clustering, arXiv preprint arXiv:2404.04443, 2024.
- [2] Ton Koonen, Fausto Gomez-Agis, Frans Huijskens, Ketemaw Addis Mekonnen, Zizheng Cao, Eduward Tangdiongga, High-capacity optical wireless communication using two-dimensional IR beam steering, *Journal of Lightwave Technology*, vol. 36(19), 4486–4493, 2018.
- [3] Marco Giordani, Michele Polese, Marco Mezzavilla, Sundeep Rangan, Michele Zorzi, Toward 6G networks: Use cases and technologies, *IEEE Communications magazine*, vol. 58(3), 55–61, 2020.
- [4] Emilio Calvanese Strinati, Sergio Barbarossa, Jose Luis Gonzalez-Jimenez, Dimitri Ktenas, Nicolas Cassiau, Luc Maret, Cedric Dehos, 6G: The next frontier: From holographic messaging to artificial intelligence using subterahertz and visible light communication, *IEEE Vehicular Technology Magazine*, vol. 14(3), 42–50, 2019.
- [5] 3GPP, "Study on scenarios and requirements for next generation access technologies (Release 15)," 3rd Generation Partnership Project (3GPP), 3GPP TR 38.913, version 15.0.0, 2018, https://www.3gpp.org/ftp/Specs/archive/38_series/38.913/38913-f00.zip.

- [6] Xuemin Shen, Jie Gao, Mushu Li, Conghao Zhou, Shisheng Hu, Mingcheng He, Weihua Zhuang, Toward immersive communications in 6G, Frontiers in Computer Science, vol. 4, 1068 478, 2023.
- [7] Huiyi Weng, Wei Wang, Zhiwei Chen, Zhu Bowen, Fan Li, A review of indoor optical wireless communication, in *Photonics*, MDPI AG, vol. 11, 2024, 722.
- [8] Ke Wang, Ampalavanapillai Nirmalathas, Christina Lim, Efstratios Skafidas, High-speed optical wireless communication system for indoor applications, IEEE Photonics Technology Letters, vol. 23(8), 519–521, 2011.
- [9] Ton Koonen, Fausto Gomez-Agis, Zizheng Cao, Ketemaw Mekonnen, Frans Huijskens, Eduward Tangdiongga, Indoor ultra-high capacity optical wireless communication using steerable infrared beams, in 2017 International Topical Meeting on Microwave Photonics (MWP), IEEE, 2017, 1–4.
- [10] Ton Koonen, Ketemaw Mekonnen, Zizheng Cao, Frans Huijskens, Ngoc Quan Pham, Eduward Tangdiongga, Ultra-high-capacity wireless communication by means of steered narrow optical beams, *Philosophical Transactions of the Royal Society A*, vol. 378(2169), 20190192, 2020.
- [11] Zhihong Zeng, Mohammad Dehghani Soltani, Majid Safari, Harald Haas, A VC-SEL array transmission system with novel beam activation mechanisms, *IEEE Transactions on Communications*, vol. 70(3), 1886–1900, 2021.
- [12] Harald Haas, Jaafar Elmirghani, Ian White, Optical wireless communication, 2020.
- [13] Joseph Mitchel Kahn, John Robert Barry, Wireless infrared communications, *Proceedings of the IEEE*, vol. 85(2), 265–298, 1997.
- [14] Steve Hranilovic, Frank R. Kschischang, A pixelated MIMO wireless optical communication system, IEEE Journal of Selected Topics in Quantum Electronics, vol. 12(4), 859–874, 2006.

- [15] Henderson, Roy and Schulmeister, Karl, Laser safety. CRC Press, 2003.
- [16] Haas, Harald and Yin, Liang and Wang, Yunlu and Chen, Cheng, What is LiFi?

 Journal of Lightwave Technology, vol. 34(6), 1533–1544, 2015.
- [17] Toshihiko Komine, Masao Nakagawa, Fundamental analysis for visible-light communication system using LED lights, *IEEE Transactions on Consumer Electronics*, vol. 50(1), 100–107, 2004.
- [18] Parth H. Pathak, Xiaotao Feng, Pengfei Hu, Prasant Mohapatra, Visible light communication, networking, and sensing: A survey, potential and challenges, IEEE communications surveys & tutorials, vol. 17(4), 2047–2077, 2015.
- [19] Damith Karunatilaka and Fahad Zafar and Vidhyasaharan Kalavally and Rajendran Parthiban, LED-based indoor visible light communications: State of the art, IEEE Communications Surveys & Tutorials, vol. 17(3), 1649–1678, 2015.
- [20] Mohammad S. Islim and Stefan Videv and Harald Haas, Towards 10 Gb/s orthogonal frequency division multiplexing-based visible light communication using a GaN violet micro-LED, *IEEE Photonics Technology Letters*, vol. 29(6), 576–579, 2017.
- [21] R. Bian, D. Tsonev, and H. Haas, 15.73-Gb/s visible light communication with off-the-shelf LEDs, *IEEE Photonics Technology Letters*, vol. 28(22), 2511–2514, 2016.
- [22] Yi Liu, Ali Wajahat, Rui Chen, Nikos Bamiedakis, Michael Crisp, Ian H. White, Richard Vincent Penty, High-capacity optical wireless VCSEL array transmitter with uniform coverage, in *Proc. SPIE 12413, Free-Space Laser Communications* XXXV, vol. 12413, 2023, 124130J.
- [23] Dong Ho Kwon, Seong Hoon Yang, Seong Kyu Han, Modulation bandwidth enhancement of white-LED-based visible light communications using electrical

- M.A.Sc. Thesis Hamed Hosseinnejadazad McMaster University ECE Department
 - equalizations, in *Proc. SPIE 9387, Broadband Access Communication Technologies IX*, vol. 9387, 2015, 93870W.
- [24] Eric Fred Schubert, Jong Kyu Kim, Light-emitting diodes, *Optics Express*, vol. 14(13), 6297–6310, 2006.
- [25] Steve Hranilovic, Wireless Optical Communication Systems. New York, NY: Springer, 2004.
- [26] Silvija T. Jivkova, Borislav A. Hristov, Mohsen Kavehrad, Power-efficient multispot-diffuse multiple-input-multiple-output approach to broad-band optical wireless communications, *IEEE Transactions on Vehicular Technology*, vol. 53(3), 882–889, 2004.
- [27] Frank Mederer, Ingo Ecker, Jürgen Joos, Markus Kicherer, Hans J. Unold, Karl J. Ebeling, Martin Grabherr, Roland Jäger, Robert King, Dieter Wiedenmann, High performance selectively oxidized VCSELs and arrays for parallel high-speed optical interconnects, *IEEE Transactions on Advanced Packaging*, vol. 24(4), 444–449, 2001.
- [28] Kenichi Iga, Surface-emitting laser-its birth and generation of new optoelectronics field, *IEEE Journal of Selected Topics in Quantum Electronics*, vol. 6(6), 1201–1215, 2000.
- [29] Anders Larsson, Advances in VCSELs for communication and sensing, *IEEE Journal of selected topics in quantum electronics*, vol. 17(6), 1552–1567, 2011.
- [30] Jing Zhang, Feng Liu, Thermal radiation properties of cool pigmented coatings for IR reflectance, *International Journal of Wireless and Mobile Technologies* (IJWMT), vol. 11(1), 1–7, 2021.
- [31] Xiaojie Zhou, Jianlin Zhao, Infrared-reflective coatings for energy-efficient buildings: A review, *Energy and Buildings*, vol. 214, 109 870, 2020.

- [32] Hany Elgala, Raed Mesleh, Harald Haas, Indoor optical wireless communication: Potential and state-of-the-art, *IEEE Communications Magazine*, vol. 49(9), 56–62, 2011.
- [33] American Society of Heating, Refrigerating and Air-Conditioning Engineers, ASHRAE Handbook—Fundamentals (2009): Emissivity and Absorptance Values, ASHRAE, 2009.
- [34] Farhad Khozeimeh, Steve Hranilovic, Dynamic spot diffusing configuration for indoor optical wireless access, *IEEE Transactions on Communications*, vol. 57(6), 1765–1775, 2009.
- [35] Fritz R. Gfeller, Urs Bapst, Wireless in-house data communication via diffuse infrared radiation, *Proceedings of the IEEE*, vol. 67(11), 1474–1486, 2005.
- [36] Shunji Kishimoto, Avalanche photodiodes as fast X-ray detectors, *Journal of Synchrotron Radiation*, vol. 5(3), 275–279, 1998.
- [37] Elham Sarbazi, Hossein Kazemi, Majid Safari, Harald Haas, Imaging angle diversity receiver design for 6G optical wireless communications: Performance tradeoffs and optimisation, in *GLOBECOM 2023-2023 IEEE Global Communications Conference*, IEEE, 2023, 5555–5560.
- [38] Mohammad Dehghani Soltani and Hossein Kazemi and Elham Sarbazi and Taisir E. H. El-Gorashi and Jaafar M. H. Elmirghani and Richard V. Penty and Ian H. White and Harald Haas and Majid Safari, High-Speed Imaging Receiver Design for 6G Optical Wireless Communications: A Rate-FOV Trade-Off, *IEEE Transactions on Communications*, vol. 71(2), 1024–1043, 2023.
- [39] Elham Sarbazi, Hossein Kazemi, Michael Crisp, Taisir El-Gorashi, Jaafar Mohamed Hamad Elmirghani, Richard Vincent Penty, Ian H. White, Majid Safari, Harald Haas, Design and optimization of high-speed receivers for 6G optical wireless networks, *IEEE Transactions on Communications*, vol. 72(2), 971–990, 2023.

- [40] Sylvester Aboagye, Telex Magloire Nkouatchah Ngatched, Alain Roland Ndjiongue, Octavia Adriana Dobre, Harold Vincent Poor, RIS-assisted visible light communication systems: A tutorial, *IEEE Communications Surveys & Tutorials*, vol. 25(1), 251–288, 2022.
- [41] Thomas Kamalakis, Panagiotis Kanakis, Adonis Bogris, Vasilis Dalakas, Georgia Dede, Designing coherent optical wireless systems for high speed indoor telecom applications, *Optics Communications*, vol. 358, 35–44, 2016.
- [42] Jin Tao, Quan You, Chao Yang, Zile Li, Liangui Deng, Mian Wu, Ming Luo, Lin Wu, Chao Li, Zichen Liu, others, Beam-steering metasurfaces assisted coherent optical wireless multichannel communication system, *Nanophotonics*, vol. 12(17), 3511–3518, 2023.
- [43] British Standards Institution, Safety of Laser Products: Equipment Classification and Requirements. British Standards Institution, 2021.
- [44] Nurul Aini Amran, Mohammad Dehghani Soltani, Majid Safari, Link blockage analysis for indoor optical wireless communications, in *GLOBECOM 2023-2023 IEEE Global Communications Conference*, IEEE, 2023, 5568–5573.
- [45] Newport Corporation, URS precision stepper motor rotation stages, Accessed: December 20, 2024. [Online]. Available: https://www.newport.com/f/urs-stepper-rotation-stages.
- [46] Thorlabs Incorporated, LSK-GR08/12 Galvo-resonant scanner and controller, https://www.thorlabs.com/newgrouppage9.cfm?objectgroup_id=11579, Accessed: 2025-06-18, 2025.
- [47] Sercalo Microtechnology, MEMS mirrors, Accessed: December 20, 2024. [Online]. Available: https://www.sercalo.com/products/mems-mirrors/mm160110-2.
- [48] Preciseley Microtechnology, *MEMS tilting mirrors*, Accessed: December 20, 2024. [Online]. Available: https://preciseley.com.

- [49] Thorlabs, Exulus spatial light modulators, Accessed: December 20, 2024. [Online].

 Available: https://www.thorlabs.com/newgrouppage9.cfm?objectgroup_id=
 10378.
- [50] Holoeye Photonics AG, Amplitude spatial light modulators, Accessed: December 20, 2024. [Online]. Available: https://holoeye.com/products/spatial-light-modulators/amplitude-slms/.
- [51] Texas Instruments, DLPLCR55EVM Evaluation Module for DLP5500 DMD, https://www.ti.com/tool/DLPLCR55EVM, Accessed: 2025-06-18, 2025.
- [52] Martijn J. R. Heck, Highly integrated optical phased arrays: Photonic integrated circuits for optical beam shaping and beam steering, *Nanophotonics*, vol. 6(1), 93– 107, 2017.
- [53] Jie Sun, Erman Timurdogan, Ami Yaacobi, Ehsan Shah Hosseini, Michael Reed Watts, Large-scale nanophotonic phased array, *Nature*, vol. 493(7431), 195–199, 2013.
- [54] Xiaosheng Zhang, Kyungmok Kwon, Johannes Henriksson, Jianheng Luo, Ming Cheng Wu, A large-scale microelectromechanical-systems-based silicon photonics LiDAR, *Nature*, vol. 603(7900), 253–258, 2022.
- [55] Anthony Malotaux Johannes Koonen, Chang Wook Oh, Eduward Tangdiongga, Reconfigurable free-space optical indoor network using multiple pencil beam steering, in 2014 OptoElectronics and Communication Conference and Australian Conference on Optical Fibre Technology (OECC/ACOFT), IEEE, 2014, 204–206.
- [56] Ton Koonen, Joanne Oh, Ketemaw Mekonnen, Zizheng Cao, Eduward Tangdiongga, Ultra-high capacity indoor optical wireless communication using 2Dsteered pencil beams, *Journal of Lightwave Technology*, vol. 34(20), 4802–4809, 2016.

- [57] Zhi Li, Yicong Li, Zihan Zang, Yaqi Han, Lican Wu, Mutong Li, Qian Li, Hai-Yan Fu, LiDAR integrated IR OWC system with the abilities of user localization and high-speed data transmission, *Optics Express*, vol. 30(12), 20796–20808, 2022.
- [58] Ahmad Adnan Qidan, Taisir El-Gorashi, Jaafar Mohamed Hamad Elmirghani, Towards terabit LiFi networking, arXiv preprint arXiv:2111.13784, 2021.
- [59] Hossein Kazemi and Elham Sarbazi and Mohammad Dehghani Soltani and Taisir Elmiligi El-Gorashi and Jaafar Mohammed Hassan Elmirghani and Richard Valentine Penty and Ian Hugh White and Majid Safari and Harald Haas, A terabit-per-second indoor mimo optical wireless backhaul system using vcsel arrays, IEEE Transactions on Communications, vol. 70(6), 3995–4012, 2022.
- [60] Fan Liu, Yifan Cui, Chunsheng You, Jie Xu, Tao Qing Siong Quek, Harold Vincent Poor, Integrated sensing and communications: Toward dual-functional wireless networks for 6G and beyond, *IEEE Journal on Selected Areas in Communications*, vol. 40(6), 1728–1767, 2022.
- [61] Zhi Zhang, Fan Liu, Yu Han, Christos Masouros, Harold Vincent Poor, Lajos Hanzo, Enabling integrated sensing and communication in 6G: Architecture, applications, and challenges, *Proceedings of the IEEE*, vol. 111(2), 232–252, 2023.
- [62] Yuan Zhuang, Luchi Hua, Longning Qi, Jun Yang, Pan Cao, Yue Cao, Yongpeng Wu, John Thompson, Harald Haas, A survey of positioning systems using visible LED lights, IEEE Communications Surveys & Tutorials, vol. 20(3), 1963–1988, 2018.
- [63] Puxi Lin, Xubin Hu, Yukui Ruan, Huaping Li, Junjian Fang, Yongchun Zhong, Huadan Zheng, Junbin Fang, Zoe Lin Jiang, Zhe Chen, Real-time visible light positioning supporting fast moving speed, *Optics Express*, vol. 28(10), 14503– 14510, 2020.

- [64] Sverre Holm, Ultrasound positioning based on time-of-flight and signal strength, in 2012 International Conference on Indoor Positioning and Indoor Navigation (IPIN), IEEE, 2012, 1–6.
- [65] Sverre Holm, Hybrid ultrasound-RFID indoor positioning: Combining the best of both worlds, in 2009 IEEE International Conference on RFID, IEEE, 2009, 155– 162.
- [66] Lev Azarkh, Jean-Paul Maria Gerardus Linnartz, Accelerated beam searching for optical wireless communication system with slow feedback channel, in 2023 IEEE 34th Annual International Symposium on Personal, Indoor and Mobile Radio Communications (PIMRC), IEEE, 2023, 1–6.
- [67] Diederick C. Niehorster, Li Li, Markus Lappe, The accuracy and precision of position and orientation tracking in the HTC vive virtual reality system for scientific research, i-Perception, vol. 8(3), 2017, Article ID: 2041669517708205.
- [68] John E. Greivenkamp, Field Guide to Geometrical Optics (SPIE Field Guides).
 Bellingham, WA: SPIE Press, 2004, ISBN: 9780819452941.
- [69] Matthew S. Brennesholtz, Liquid lens technology, *Information Display*, vol. 35(2), 10–14, 2019.
- [70] Paul F. McManamon, A review of phased-array steering for narrow-band electrooptical systems, *Proceedings of the IEEE*, vol. 97(6), 1078–1096, 2009.
- [71] Christian Jansen, Bernhard Steiger, Fabian Böhm, Advanced optics for automotive LIDAR systems, *Advances in Optical Technologies*, vol. 2021, 1–18, 2021.
- [72] Long Wu, Zhenhua Yu, Chen Gong, Zhengyuan Xu, Effect of optimal Lambertian order for cellular indoor optical wireless communication, *IEEE Journal on Selected Areas in Communications*, vol. 34(4), 894–906, 2016, Receiver plane set at 1 m above floor.

- [73] Bahaa Eldin Abdelsalam Saleh, Malvin Carl Teich, Fundamentals of photonics. john Wiley & sons, 2019.
- [74] Safety of laser products—part 1: Equipment classification and requirements, 2nd, IEC 60825-1, International Electrotechnical Commission (IEC), Geneva, Switzerland, 2001.
- [75] International Commission on Non-Ionizing Radiation Protection, Guidelines on limits of exposure to laser radiation, *Health Physics*, vol. 79(4), 431–440, 2000.
- [76] Hamamatsu Photonics, G8931 Series: Photomultiplier Tubes, https://www.hamamatsu.com/content/dam/hamamatsu-photonics/sites/documents/99_SALES_LIBRARY/ssd/g8931_series_kapd1018e.pdf, [Online; accessed October 23, 2024], 2024.
- [77] Govind Padmanabhan Agrawal, Lightwave Technology: Telecommunication Systems. John Wiley & Sons, 2005.
- [78] Sunghwan Shin, Utkarsh Sharma, Haohua Tu, Woonggyu Jung, Stephen Allen Boppart, Characterization and analysis of relative intensity noise in broadband optical sources for optical coherence tomography, *IEEE Photonics Technology Letters*, vol. 22(14), 1057–1059, 2010.
- [79] Mohammad Dehghani Soltani, Hossein Kazemi, Elham Sarbazi, Harald Haas, Majid Safari, Optimal imaging receiver design for high-speed mobile optical wireless communications, in 2022 IEEE international conference on communications workshops (ICC workshops), IEEE, 2022, 01–06.
- [80] Jean Armstrong, OFDM for optical communications, Journal of Lightwave Technology, vol. 27(3), 189–204, 2009.
- [81] Cheng Chen, Dushyantha Athukorala Basnayaka, Harald Haas, Downlink performance of optical attocell networks, *Journal of Lightwave Technology*, vol. 34(1), 137–156, 2015.

- [82] Mohammad Dehghani Soltani, Xiping Wu, Majid Safari, Harald Haas, Bidirectional user throughput maximization based on feedback reduction in LiFi networks, IEEE Transactions on Communications, vol. 66(7), 3172–3186, 2018.
- [83] Svilen Dimitrov, Harald Haas, Optimum signal shaping in OFDM-based optical wireless communication systems, in 2012 IEEE Vehicular Technology Conference (VTC Fall), IEEE, 2012, 1–5.
- [84] Svilen Ivanov Dimitrov, Harald Haas, Information rate of OFDM-based optical wireless communication systems with nonlinear distortion, *Journal of Lightwave Technology*, vol. 31(6), 918–929, 2012.
- [85] W. contributors, *IEEE 802.11bb*, https://en.wikipedia.org/wiki/IEEE_802.11bb, Accessed: 2025-08-12.
- [86] I Gusti Putu Purwita, Mohammad Dehghani Soltani, Majid Safari, Harald Haas, Terminal orientation in OFDM-based LiFi systems, IEEE Transactions on Wireless Communications, vol. 18(1), 430–444, 2019.
- [87] Mohammad Dehghani Soltani, I Gusti Putu Purwita, Iman Tavakkolnia, Harald Haas, Majid Safari, Impact of device orientation on error performance of LiFi systems, *IEEE Access*, vol. 7, 41 690–41 701, 2019.
- [88] Jing Shao, Feng Hu, Xiang Xu, Yan Zheng, Xianfeng Chen, Angle-insensitive optical wireless communication using retro-reflective transceivers with liquid crystal shutters, *Optics Express*, vol. 26(14), 18340–18350, 2018.
- [89] Cheng Chen, Rui Bian, Harald Haas, Omnidirectional transmitter and receiver design for wireless infrared uplink transmission in LiFi, in 2018 IEEE International Conference on Communications Workshops (ICC Workshops), Ieee, 2018, 1–6.
- [90] Inventables, Stepper Motor NEMA 23, Web page, Regular price US\$55.00, 2025. [Online]. Available: https://www.inventables.com/products/steppermotor-nema-23.

- [91] Optics Focus, Motorized rotation stage (mor-100-30), https://optics-focus.com/motorized-rotation-stage-p-522.html, Accessed: 2025-06-18, 2025.
- [92] Edmund Optics, *Galvanometers*, Accessed: December 20, 2024. [Online]. Available: https://www.edmundoptics.com/c/galvanometers/1279/.
- [93] Thorlabs, Galvanometer mirror positioning systems, https://thorlabs.com/newgrouppage9.cfm?objectgroup_id=3258, Accessed: 2024-12-25, 2024.
- [94] Thorlabs Incorporated, EXULUS-HD4 phase-only spatial light modulator, https://www.thorlabs.com/thorproduct.cfm?partnumber=EXULUS-HD4, Accessed: 2025-06-19, 2025.
- [95] Joseph W. Goodman, Introduction to Fourier Optics, 3rd. Greenwood Village,CO: Roberts and Company Publishers, 2005, ISBN: 978-0974707723.
- [96] Shin, Seungwoo and Kim, Kyoohyun and Yoon, Jonghee and Park, YongKeun, Active illumination using a digital micromirror device for quantitative phase imaging, Optics letters, vol. 40(22), 5407–5410, 2015.
- [97] Edmund Optics, TECHSPEC Risley Prism Mount, https://www. edmundoptics.com/p/25mm-dia-0-26-risley-prism-mount/3128, Accessed: 2025-06-19, 2025.
- [98] Mingyu Tan, James Smith, Alex Lee, Bo Chen, Rajesh Kumar, Laura Johnson, Priya Gupta, Yifan Zhao, Sanjay Patel, Thuy Nguyen, A fully integrated lidaron-chip system, *Nature*, vol. 603, 616–620, 2022.
- [99] NSR Gayatri, Yi-Hsuan Lin, Silvano Donati, San-Liang Lee, Simplified beam steering and fast error compensation of optical phased arrays by using a novel weighted-grouping algorithm, *IEEE Access*, vol. 12, 63701–63712, 2024.
- [100] Pierre Maidment, Development of an integrated multispectral LIDAR in silicon photonics, MASc Thesis, University of British Columbia, 2023.

- [101] Gerald Hechenblaikner, Analysis of performance and robustness against jitter of various search methods for acquiring optical links in space, *Applied Optics*, vol. 60(13), 3936–3946, 2021.
- [102] Charles Hindman and Lawrence Robertson, Beaconless satellite laser acquisition
 modeling and feasibility, in MILCOM 2004 2004 IEEE Military Communications Conference, 2004, 41–46.
- [103] Xin Li, Siyuan Yu, Jing Ma, Liying Tan, Analytical expression and optimization of spatial acquisition for intersatellite optical communications, *Optics Express*, vol. 19(3), 2381–2390, 2011.
- [104] Patrick Van Hove, Vincent Wai S. Chan, Spatial acquisition algorithms and systems for optical ISL, ICC 1983-Integrating Communication for World Progress, vol. 3, 1208–1214, 1983.
- [105] Michael Scheinfeild, Norman S. Kopeika, Raviv Melamed, Acquisition system for microsatellites laser communication in space, in Free-Space Laser Communication Technologies XII, SPIE, vol. 3932, 2000, 166–175.
- [106] Matthew David Higgins, Roger John Green, Mark Stuart Leeson, A genetic algorithm method for optical wireless channel control, *Journal of Lightwave Technology*, vol. 27(6), 760–772, 2009.
- [107] Evgeny Khorov, Anton Kiryanov, Andrey Lyakhov, Giuseppe Bianchi, A tutorial on IEEE 802.11 ax high efficiency WLANs, *IEEE Communications Surveys & Tutorials*, vol. 21(1), 197–216, 2018.
- [108] Mirrorcle Technologies, Dual-Axis Quasi-static MEMS Mirror Datasheet A5L2.2-6400, Point-to-point precision 0.2 mdeg, 2021. [Online]. Available: https://www.rxelectronics.es/datasheet/6e/emmm161-ab-w-ep.pdf.

- [109] David R. Gozzard and Lyle E. Roberts and James T. Spollard and Paul G. Sibley and Daniel A. Shaddock, Fast beam steering with an optical phased array, *Optics Letters*, vol. 45(13), 3793–3796, 2020.
- [110] Meadowlark Optics, 1024×1024 LCOS spatial light modulator data sheet, Phase ripple as low as 0.2% (0.002π rad) to $\sim 2\%$ (0.02π rad), 2024. [Online]. Available: https://www.meadowlark.com/wp-content/uploads/2025/01/SLM-HSP-UHSP-1024-x-1024-Data-Sheet-0624.pdf.
- [111] X. Zhang, "High-performance FMCW LiDAR with MEMS optical beam scanner," University of California, Berkeley, EECS Department, Tech. Rep. UCB/EECS-2023-26, 2023, Measured FWHM beam divergence ≈ 0.050° × 0.049°. [Online]. Available: https://www2.eecs.berkeley.edu/Pubs/TechRpts/2023/EECS-2023-26.pdf.
- [112] Cheng-Lin Tsao, Yueh-Ting Wu, Wanjiun Liao, Jia-Chun Kuo, Link duration of the random way point model in mobile ad hoc networks, in *IEEE Wireless Communications and Networking Conference*, 2006. WCNC 2006., IEEE, vol. 1, 2006, 367–371.
- [113] Elham Sarbazi, Hossein Kazemi, Mohammad Dehghani Soltani, Majid Safari, Harald Haas, Design tradeoffs of non-imaging angle diversity receivers for 6G optical wireless access networks, in GLOBECOM 2022-2022 IEEE Global Communications Conference, IEEE, 2022, 419–424.
- [114] Toshimasa Umezawa, Atsushi Matsumoto, Kouichi Akahane, Shinya Nakajima, Naokatsu Yamamoto, Large submillimeter high-speed photodetector for large aperture FSO receiver, *IEEE Journal of Selected Topics in Quantum Electronics*, vol. 28(2: Optical Detectors), 1–9, 2021.

- [115] Chen Chen, Wen-De Zhong, Dehao Wu, Zabihollah Ghassemlooy, Wide-FOV and high-gain imaging angle diversity receiver for indoor SDM-VLC systems, *IEEE Photonics Technology Letters*, vol. 28(19), 2078–2081, 2016.
- [116] Gregory F. Welch, Gary F. Bishop, An introduction to the Kalman filter, in *ACM SIGGRAPH 2001: Course 8 (Course Notes)*, 2001.
- [117] John B. Pearson and Edwin B. Stear, Kalman filter applications in airborne radar tracking, IEEE Transactions on Aerospace and Electronic Systems, (3), 319–329, 1974.
- [118] Lvwen Huang, Siyuan Chen, Jianfeng Zhang, Bang Cheng, Mingqing Liu, Real-time motion tracking for indoor moving sphere objects with a LiDAR sensor, Sensors, vol. 17(9), 1932, 2017.
- [119] Yongjun Guo, Yuhao Guo, Chunshu Li, Hao Zhang, Xiaoyan Zhou, Lin Zhang, Integrated optical phased arrays for beam forming and steering, Applied Sciences, vol. 11(9), 4017, 2021.
- [120] Ahmed Taha Hussein, Mohammed Talal Alresheedi, Jaafar Mohamed Hamad Elmirghani, 20 Gb/s mobile indoor visible light communication system employing beam steering and computer generated holograms, *Journal of Lightwave Technology*, vol. 33(24), 5242–5260, 2015.
- [121] Xiaosheng Zhang, Ming Cheng Wu, Andrew Scott Michaels, Johannes Henriksson, Beam-steering system based on a MEMS-actuated vertical-coupler array, US Patent 11,441,353, 2022.
- [122] Abdelrahman Samir Elgamal and Osama Zeyad Aletri and Ahmad Adnan Qidan and Taisir Elmiligi El-Gorashi and Jaafar Mohammed Hassan Elmirghani, Reinforcement learning for resource allocation in steerable laser-based optical wireless systems, in 2021 IEEE Canadian Conference on Electrical and Computer Engineering (CCECE), IEEE, 2021, 1–6.

- [123] Rizwana Ahmad, Hossein Kazemi, Elham Sarbazi, Harald Haas, Joint position and orientation estimation in VCSEL-based LiFi networks: A deep learning approach, in 2023 IEEE Global Communications Conference (GLOBECOM), Kuala Lumpur, Malaysia: IEEE, 2023, 3676–3681.
- [124] Mohammad Dehghani Soltani, Ardimas Andi Purwita, Zhihong Zeng, Harald Haas, Majid Safari, Modeling the random orientation of mobile devices: Measurement, analysis and LiFi use case, *IEEE Transactions on Communications*, vol. 67(3), 2157–2172, 2018.
- [125] Sylvester Aboagye, Telex Magloire Nkouatchah Ngatched, Alain Roland Ndjiongue, Octavia Adriana Dobre, Hyundong Shin, Liquid crystal-based RIS for VLC transmitters: Performance analysis, challenges, and opportunities, IEEE Wireless Communications, vol. 31(4), 98–105, 2023.
- [126] Alain Roland Ndjiongue, Telex Magloire Nkouatchah Ngatched, Octavia Adriana Dobre, Harald Haas, Re-configurable intelligent surface-based VLC receivers using tunable liquid-crystals: The concept, Journal of Lightwave Technology, vol. 39(10), 3193–3200, 2021.
- [127] Sylvester Aboagye, Telex Magloire Nkouatchah Ngatched, Octavia Adriana Dobre, Alain Roland Ndjiongue, Intelligent reflecting surface-aided indoor visible light communication systems, *IEEE Communications Letters*, vol. 25(12), 3913–3917, 2021.
- [128] Yiming Huo, Xiaodai Dong, Nuwan Ferdinand, Distributed reconfigurable intelligent surfaces for energy-efficient indoor terahertz wireless communications, *IEEE Internet of Things Journal*, vol. 10(3), 2728–2742, 2022.
- [129] Alain Roland Ndjiongue, Telex Magloire Nkouatchah Ngatched, Octavia Adriana Dobre, On the capacity of RIS-assisted intensity-modulation optical channels, *IEEE Communications Letters*, vol. 26(2), 389–393, 2021.

- [130] Alain Roland Ndjiongue, Telex Magloire Nkouatchah Ngatched, Octavia Adriana Dobre, Harald Haas, Digital RIS (DRIS): The future of digital beam management in RIS-assisted OWC systems, Journal of Lightwave Technology, vol. 40(16), 5597–5604, 2022.
- [131] Ruixin Yang and Shuai Ma and Zihan Xu and Hang Li and Xiaodong Liu and Xintong Ling and Xiong Deng and Xun Zhang and Shiyin Li, Spectral and energy efficiency of DCO-OFDM in visible light communication systems with finite-alphabet inputs, *IEEE Transactions on Wireless Communications*, vol. 21(8), 6018–6032, 2022.